Instituto Interuniversitario de Reconocimiento
Molecular y Desarrollo Tecnológico

València, March 2017

Hybrid silica materials for detection of toxic species and clinical diagnosis

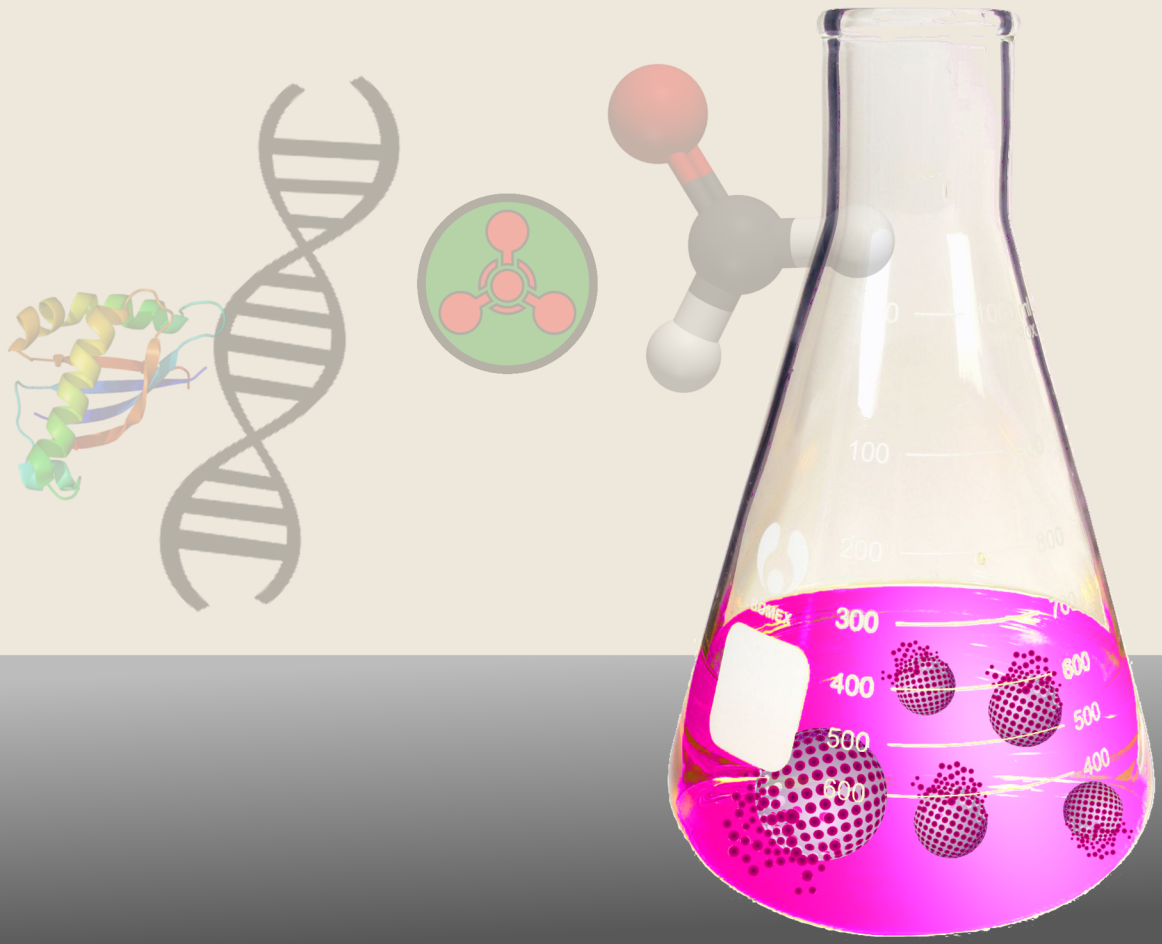

Ph. D. Thesis

Submitted by:
Lluís Pascual i Vidal

Ph. D. Supervisors:
Dr. Félix Sancenón Galarza
Prof. Ramón Martínez Máñez

UNIVERSITAT POLITÈCNICA DE VALÈNCIA

Hybrid silica materials for detection of toxic species and clinical diagnosis

PhD. THESIS

Submitted by
Lluís Pascual i Vidal

PhD. Supervisors:
Dr. Félix Sancenón Galarza
Prof. Ramón Martínez Máñez

València, **March 2017**

Instituto Interuniversitario de Reconocimiento Molecular y Desarrollo Tecnológico

FÉLIX SANCENÓN GALARZA, PhD in Chemistry and Lecturer at the *Universitat Politècnica de València*, and RAMÓN MARTÍNEZ MÁÑEZ, PhD in Chemistry and Professor at the *Universitat Politècnica de València*,

CERTIFY:

That the work *"Hybrid silica materials for detection of toxic species and clinical diagnosis"* has been developed by **Lluís Pascual i Vidal** under their supervision in the Instituto de Reconocimiento Molecular y Desarrollo Tecnológico (IDM) de la *Universitat Politècnica de València*, as a thesis Project in order to obtain the international degree of PhD in Chemistry at the *Universitat Politècnica de València.*

València, March 2017.

Prof. Ramón Martínez Máñez

Dr. Félix Sancenón Galarza

Als meus pares, **l'exemple**,
al meu iaio, **la voluntat**,
a la meua iaia**, l'estima**,
i a Isabel, **el refugi**.

"Costa molt d'aconseguir una certesa,
i encara sempre és interina."
Joan Fuster i Ortells

"Autoritätsdusel ist der größte Feind der Wahrheit."
(El respecte acrític per l'autoritat és el major enemic de la veritat)
Albert Einstein

"You look at science (or at least talk of it) as some sort of demoralising invention of man, something apart from real life, and which must be cautiously guarded and kept separate from everyday existence. But science and everyday life cannot and should not be separated."
Rosalind Franklin

Agraïments
Aknowledgements

I per fi ha aplegat el dia, sembla mentida. Més que témer el moment, crec que l'esperava amb una mescla d'incertesa pel futur i de motivació per ser capaç de superar aquesta etapa. I ací hem aplegat, més de cinc anys després, al moment d'assentar-se per posar blanc sobre negre la merescuda gratitud a totes i tots aquells que m'han acompanyat i han fet que tot açò siga possible. Mil gràcies!

Primerament voldria donar-li les gràcies als meus directors, Ramón i Félix. A Ramón per haver-me fet un lloc al grup de investigació, per donar-me la oportunitat de fer ciència al més alt nivell i per haver-me ensenyat tantes coses del món acadèmic i d'aquest ofici d'*artesans de la matèria*. I a Fèlix per la paciència, pel seu temps i per tot el que he après al seu costat. Han sigut moltes hores assegut al teu despatx intentant resoldre els maldecaps que ens produïa cada projecte i crec que quedaré en un deute perpetu per tanta ajuda i per oferir-me la teua companyia. Gràcies als dos per fer-ho tot possible.

Així tampoc em puc oblidar dels meus primers mestres en açò de la investigació: Marga i Boro. Allà en l'edifici blanc de Burjassot donava els meus primers passets d'allò que ha sigut la meua manera de viure tots estos anys gràcies a ells, i a Ana i Pablo. I també a Juan que em va ensenyar mil i una coses durant la meua primera etapa al IDM i ha sigut durant tot este temps un important referent tant a nivell personal com professional. Així com a Loles i Joserra que sempre han estat al costat, treballant i disposats a donar els consell que han fet falta. No m'oblide de Luis i totes les nombroses converses que he tingut el gust de compartir amb ell fent de la feina del dia a dia quelcom menys pesat, gracias tio! I de Pedro, quants materials per analitzar i quanta feina li hem donat tots aquests anys. Moltes gràcies a tots!

Ralph, I also want to thank you for taking care of me when I was in Rio de Janeiro. I think we did a great job there and I appreciate a lot that professional and personal experience with you, all your students and your partners. Eu vou tentar escrever isto no meu melhor *portunhol*, por favor desculpem os meus erros gramaticais. Obrigado gente por tudo o que vocês fizeram por mim lá. A Cristal que me abriu as portas do lab de farmácia e ajudou a fazer e caracterizar os materiais, a Marta e Fagner pelas provas de SPECT, a Suyene que me mostrou como trabalhar com os ratos e a Luis Filipe, Thamires e Sara pela sua ajuda e companhia no lab. Ah! I gracias a Fiorella por compartir conmigo la experiencia de ser los extranjeros del lab. Muito obrigado a todos vocês! Hablando de mi estancia no puedo (ni debo, ni quiero) olvidarme de dar las gracias a mis otros compañeros en la otra cara de aquella experiencia. Leonel, que suerte cuando me escribiste al anuncio para compartir piso, no habría encontrado compañeros mejores. Gracias por tus

consejos, por tu predisposición para todo, por tu tranquilidad y por los libros que me diste. Conociéndote y sabiendo todo lo que has trabajado te va a llegar un futuro brillante más pronto que tarde, no lo puedo imaginar de otra manera. Así que puede que la siguiente vez que hablemos ya sea de doctor a doctor, creo que ya te lo dije alguna vez pero te lo mereces todo. I Julio, Julito, ¡qué bueno que apareciste! Seguro que sin ti mi experiencia *na cidade maravilhosa* hubiera sido muy distinta y seguro mucho más aburrida. Bueno te daría gracias por muchas cosas pero sobretodo resaltaré que gracias por lo que compartimos y por alimentarme (bueno a mí y a Leo) durante aquellos meses. A ver si pronto te atreves a cruzar el charco y nos vemos por aquí cerquita.

Em queden, com no, tots els meus companys, que han anat passant pel laboratori. Intentaré anar agrupant-vos d'alguna manera que sou moltíssims! Espere no deixar-me a ningú (jeje). Comence agraint a Inma: fuiste mi primera jefa, cuanto miedo me metieron Juan y Román hasta que llegaste y luego, Bueno, digamos que conseguí adaptarme. Muchas gracias por haber estado a mi lado y por toda la ayuda que me has dado. A Elena per encarregar-te tantes vegades de coordinar tot allò que havíem de fer i posar una miqueta de ordre en el meu cas particular. A Carmen per haver-me escoltat tantes vegades i haver-me transmès tantes de les mil coses que saps, ha sigut un plaer. A Estela que, tot i no haver coincidit tant de temps, has sigut tot un exemple a seguir per la dedicació i per eixa passió per la feina que tens i que encomanes a tot el teu voltant. A Édgar per ser un company i una persona formidable, d'eixos que sempre estan disposats a tirar una mà a qualsevol, i sobretot per ser el millor comunicador que he conegut fins ara, mai he vist ningú capaç d'explicar les coses millor que tu. A Mari Carmen per eixa manera tan genial que vàrem tindre de conèixer-nos treballant junts a La Fe, però també perquè després has sigut un recolzament genial.

Com hem començat amb la gent que més coses m'ha ensenyat ara toca anomenar al que va ser el meu mestre Jedi i mentor al laboratori quan vaig entrar: Alesandro, el italiano. Cuantas cosas tuve la suerte de compartir contigo amigo y cuanto te he echado de menos desde que regresaste a Italia. He de confesar que sin ti se habla mucho menos de futbol en el lab y que con el paso del tiempo Rocco y Bendedicto han perdido sus lugares de honor en tu (nuestra) vitrina. Pero sé que todos estos cambios han sido para mejor. Il migliore auguri a te, Claudia e Matilde. Grazie maestro! I si començava amb la primera jefa, ara li toca el torn a la última: Gracias Andrea por acompañarme en este último tramo, sabes bien que los últimos repechos de esta subida de montaña se me han hecho bastante duros pero sin esos cafés y momentos de compañerismo que me has regalado hubiera sido casi una subida imposible.

Tampoc vull deixar de banda a la resta de gent que ja estava al grup quan vaig aplegar i que, tot i compartir menys moments i experiències, també han estat ahí quan ha fet falta. Gràcies Maria, Yoli, Patri, Inma Candel i Cris Sanfeliu. Ha sigut un plaer conèixer-vos i compartir un trosset d'aquesta etapa amb vosaltres.

El següent grup que m'agradaria destacar es tota la gent de diversos indrets del món que he tingut la sort de conèixer i que m'han ensenyat tantíssimes maneres diferents de vore i entendre el món. Especialment m'enrecorde d'Isabel i aquella batalla conjunta que vàrem lliurar junts contra els materials amb oligos. ¡Cuan ingratos nos hemos portado y que poco hablamos últimamente! Quiero que sepas que he tenido siempre muy presente aquellas charlas de cultura y política que teníamos y que esta tesis tiene una gran parte de ti también. Sameh amigo, creo que has sido el compañero que más cercano he sentido durante toda esta etapa, me has enseñado mucho, creo que más de lo que imagines. جَزيّلاً شُكراً Gracias también a Luis Enrique, Krishanu, Ravi, Asha, Manoharan, Ismael, Hazem, Anita, Pavel i Rafa. Amelia, Mª Elena y Carol también entráis en este grupo de internacionales aunque a vosotras yo creo que prácticamente ya os puedo contar como valencianas, no creéis? Muchas gracias amigas! Y me quedan las nuevas incorporaciones Tania y Andy, mucha suerte en esta nueva aventura que emprendéis.

Gràcies també a la resta de predocs del lab: Ángela (la que millor ha aconseguit domar als oligos), Lorena, Alba (sort al trivial!), Toni, Mónica, Irene, Bea (la madrileña inagotable), Santi, Xente (ara eres el nou amo del lab 1.2), Luis Pla (el meu *tocayo*), Iris, Elisa, Adrián i Bea de Luis. Ànim que ja veieu que al final la tesi sí que s'acaba. Als nous post docs, Sara y Borja y a Marta. I a les profes, Ana i Cristina Marín, també va ser un plaer treballar amb vosaltres. I a Cris de la Torre (la atleta oficial!) que tu també ho tens ahí. Ha sigut un plaer compartir tantes coses amb vosaltres!

Em queden un parell de companys més al laboratori d'arquitectura. José Manuel que és tot un exemple de determinació i Roman gràcies per haver-me ensenyat i ajudat a muntar i reparar aparells diversos, falta em feia. I també els companys d'altres grups del departament, en especial Raúl, Rafa Bellesteros, Óscar (organizador de eventos deportivos), Juanfran, Juan Carlos, Andrea i, com no, Herme (espere no perdre't la pista mai loco!).

Anem acabant, i ara toca el torn a tots els meus comboieros i les meues comboiantes que han plenat de plans i activitats ludicofestives la realització de la tesi. En especial a Mar, amb qui he anat de la maneta pràcticament tot este període (des de que començarem amb el màster de sensors) i que t'has comportat sempre com una gran companya i una molt bona amiga, el meu millor recolçament. A Núria, amb qui coincidisc en tantes coses que era inevitable fer-se tan amics, moltes gràcies

bonica! A CrisGi per eixa alegria contagiosa i eixe somriure inesborrable. A Dani per intentar posar un poquet de trellat. A Almu per la seua energia imparable. A Neus i Carles de Borbotó city. A Marian, la profe de mates. I a Maria (molta sort en el últim tram del master!).

I ja per finalitzar em queda agrair-li-ho a la meua família. Als meus pares que han sigut sempre un exemple constant, un mirall i una ajuda quan ha fet falta. A ells els dec el cuquet per fer ciència i crec que a ma mare més, perquè alguna raó deu haver per a que m'agrade així la química. Al meu iaio Domingo, perquè és una persona lluitadora, treballadora i sobretot honesta com cap altra. La teua figura sempre ha deixat una emprenta ben forta en mi que crec és la responsable de l'impuls per voler fer les coses sempre ben fetes. A la meua iaia Rosita, que ha esta cuidant-nos a tots sempre i això m'ha ensenyat, més que cap altra cosa, el valor de ser responsable i cuidar el teu entorn. Al meu germà perquè sempre és una via d'escapada amb qui parlar de coses diferents a allò que és el meu dia a dia. I per últim a Buck, per eixa companyia còmplice estos mesos d'escriptura i a Isabel, pilar i refugi, bàlsam constant i necessari per poder seguir endavant, junts, contra les fatigues quotidianes. Gràcies per aguantar-me i acompanyar-me tots aquests anys.

Sou els millors penya!

Abstract

The present PhD thesis entitled "*Silica Hybrid Materials for detection of toxic species and clinical diagnosis*" is focused on the design and synthesis of new hybrid materials, using different silica supports as inorganic scaffolds, with applications in recognition, sensing and diagnostic protocols.

The first chapter of the PhD thesis is devoted to the definition and classification of hybrid materials, relying on concepts of Nanotechnology, Supramolecular and Materials Chemistry. State of art of this field of knowledge is described using numerous examples of applications for molecular recognition, especially about gated materials. In the second chapter, the general and specific objectives of the PhD thesis are presented.

The third chapter shows the synthesis, characterization and sensing performances of hybrid silica nanoparticles for the chromogenic detection of formaldehyde. Commercially available silica nanoparticles are functionalized with thiol and polyamine moieties. These hybrid nanoparticles were used for the chromogenic recognition of formaldehyde using a blue squaraine indicator. In the absence of formaldehyde, suspensions of the functionalized nanoparticles are able to bleach the blue squaraine solutions due to a reaction between the grafted thiol moieties and the added dye. In the presence of formaldehyde, -SH moieties onto the surface reacts with this molecule with the subsequent inhibition of thiol-squaraine reaction. As a consequence suspension remains blue and formaldehyde is detected. These nanoparticles allows detection of formaldehyde in a selective and sensitive fashion in aqueous and in gas phase.

The fourth chapter deals with the preparation of acetylcholinesterase capped mesoporous silica nanoparticle that are used for the selective and sensitive sensing of diisopropylfluorophosphate (DFP), a nerve agent mimic. Mesoporous silica nanoparticles are prepared and the pores loaded with rhodamine B dye. Then, the external surface of the loaded nanoparticles is functionalized with a pyridostigmine derivative (a reversible inhibitor of acetylcholinesterase enzyme). Finally the pores are capped upon acetylcholinesterase addition (by coordination with the grafted inhibitor). In the absence of DFP nanoparticles are tightly closed whereas in the presence of nerve agent simulant pore opening and dye release is observed (due to preferential coordination of DFP with the enzyme active sites and detachment from the nanoparticles surface). In an extension of the previous results, nanoparticles functionalized with a neostigmine derivative are prepared and characterized and its controlled release features studied in the presence of several acetylcholinesterase inhibitors.

The selective recognition of *Mycoplasma fermentans* genomic DNA using capped mesoporous silica nanoparticles is presented in chapter fifth. Sensing nanodevices are based on mesoporous silica nanoparticles loaded with rhodamine B and with the external surface functionalized with isocyanatopropyl moieties. Then, a short DNA sequence was covalently attached to the surface of the nanoparticles through the formation of urea linkages. Finally, the pores were capped by adding a single stranded oligonucleotide which is a highly conserved sequence of the 16S ribosomal subunit of the mycoplasma species genome. Aqueous suspensions of the DNA-capped nanoparticles showed negligible dye release. However, only in the presence of *Mycoplasma fermentans* genomic DNA the pores are opened and a marked rhodamine B release is observed. Using these nanoparticles a limit of detection as low as 70 DNA copies μL^{-1} is achieved.

The sixth chapter of this PhD thesis presents the synthesis and characterization of mesoporous silica nanoparticles coated with MUC1 aptamer (able to recognize MUC1 glycoprotenin, presented in certain cancer types) and radiolabeled with ^{99m}Tc radioisotope. Mesoporous silica nanoparticles were loaded with safranine O and its external surface functionalized with aminopropyl moieties. Then, the pores are capped upon addition of MUC1 aptamer. These MUC1 aptamer capped nanoparticles are internalized by MDA-MB-231 cancer cells (which overexpressed MUC1 glycoprotein) and released the entrapped dye. In a step forward, MUC1 aptamer capped nanoparticles are radiolabeled with ^{99m}Tc and used for image cancerous lesions in mice using SPECT.

Finally, in the seventh chapter the conclusions of this PhD thesis are exposed and commented.

Resum

La present tesi doctoral titulada "*Silica Hybrid Materials for detection of toxic species and clinical diagnosis*" està enfocada al disseny i síntesi de nous materials híbrids utilitzant diferents suports inorgànics basat en sílice, amb aplicacions en protocols de reconeixement, sensat i diagnòstic.

El primer capítol de la tesi està dedicat a la definició i classificació dels materials híbrids , basant-se en conceptes de Nanotecnologia, Química Supramolecular i Química dels Materials. L'estat del art d'aquest camp de coneixement es descriu utilitzant nombroses exemples de aplicacions per a reconeixement molecular, especialment sobre materials de tipus porta molecular. En el segon capítol es presenten els objectius generals i específics de la present tesi.

El tercer capítol presenta la síntesi, caracterització i capacitats sensores de nanopartícules híbrides de sílice per a la detecció de formaldehid. Nanopartícules silícies comercials es funcionalitzen amb grups tiol i poliamina. Estes nanopartícules híbrides han sigut utilitzades per al reconeixement cromogènic de formaldehid utilitzant un indicador blau de escuaridina. En absència de formaldehid, suspensions de nanopartícules son capaces de decolorar les dissolucions blaves de escuaridina degut a una reacció entre els tiols inserits i el colorant afegit. En presència de formaldehid els grups –SH de la superfície reaccionen amb esta molècula amb la conseqüent inhibició de la reacció tiol-escuaridina. Com a conseqüència la suspensió roman blava i el formaldehid es detecta. Estes nanopartícules permeten la detecció de formaldehid de forma sensitiva i selectiva en dissolució i en fase gas.

El quart capítol de la tesi tracta de la preparació de nanopartícules mesoporoses de sílice tapades amv acetilcolinesterasa que són utilitzades per al sensat selectiu i sensitiu de diisopropilfluorofosfat (DFP), un simulant de gas nerviós. Nanopartícules mesoporoses de sílice es preparen i els seus porus es carreguen amb rodamina B. Llavors, la superfície externa de les nanopartícules carregades es funcionalitzen amb un derivat de piridostigmina (un inhibidor reversible de l'enzim acetilcolinesteras). Finalment els porus es tapen amb la addició de acetilcolinesterasa (per coordinació del inhibidor inserit). En absència de DFO, les nanopartícules romanen tancades mentre que en la presència del simulant d'agent nerviós els porus s'obrin i s'observa l'alliberament del colorant (degut a la preferència de coordinació dels centres actius de l'enzim amb el DFP i el desancoratge de la superfície de les nanopartícules). En una extensió dels resultats comentats, es preparen nanopartícules funcionalitzades amb un derivat de neostigmina per a caracteritzar-les i estudiar els seus processos d'alliberació controlada en presència de diferents inhibidors d'acetilcolinesterasa.

El reconeixement selectiu d'ADN genòmic de *Mycoplasma fermentans* utilitzant nanopartícules mesoporoses de sílice es presenta en el quint capítol. Nanodispositius sensors basats en nanopartícules mesoporoses de sílice carregades amb rodamina B i amb la superfície externa funcionalitzada amb grups propilisocianat. Llavors, una seqüència curta d'ADN s'ancora covalentment a través de la formació d'enllaços urea. Finalment, els porus es tapen afegint un oligonucleòtid de cadena simple, el qual està composat per una seqüència altament conservada de la subunitat ribosomal 16S del genoma d'aquesta espècie concreta de micoplasma. Suspensions aquoses de nanopartícules tapades amb oligonucleòtids presenten una alliberació negligible de colorant. No obstant, solament en presència d'ADN genòmic

de *Mycoplasma fermentans* els porus s'obrin i s'observa una marcada lliberació de rodamina B. Utilitzant estes nanopartícules es va aplegar a un límit de detecció tan baix com 70 còpies d'ADN per μL.

El sisè capítol de este tesi presenta la síntesi i caracterització de nanopartícules mesoporoses de sílice recobertes amb aptámers de MUC1 (capaços de reconèixer la glicoproteïna MUC1, present en cert tipus de càncer) i marcades amb radioisòtops de ^{99m}Tc. Nanopartícules mesoporoses de sílice es carregaren amb safranina O i la seua superfície externa es funcionalitza amb grups amina. Llavors, els porus es tapen mitjançant l'addició de l'aptámer MUC1. Aquestes nanopartícules tapades amb l'aptámer varen ser internalitzades per cèl·lules canceroses MDA-MB-231 (les quals sobrexpressen glicoproteïna MUC1) i l'alliberació del colorant. Anant un pas més enllà, les nanopartícules tapades amv l'aptàmer de MUC 1 es radiomarquen amb ^{99m}TC i són utilitzades per a la imatge de lesions canceroses en ratolins utilitzant SPECT.

Finalment, en el seté capítol s'exposen les conclusions de la tesi.

Resumen

La presente tesis doctoral titulada "*Silica Hybrid Materials for detection of toxic species and clinical diagnosis*" está enfocada al diseño y síntesis de nuevos materiales hibridos usando diferentes soportes inorgánicos basados en sílice, con aplicaciones en protocolos de reconocimiento, sensado y diagnóstico.

El primer capítulo de la tesis está dedicado a la definición y clasificación de los materiales híbridos, basándose en conceptos de Nanotecnología, Química Supramolecular y Química de Materiales. El estado del arte de este campo de conocimiento se describe usando numerosas aplicaciones para reconocimiento molecular, especialmente sobre materiales de tipo puerta molecular. En el segundo capítulo se presentan los objetivos generales y específicos de la presente tesis.

El tercer capítulo presenta la síntesis, caracterización y capacidades sensoras de nanopartículas híbridas de sílice para la detección de formaldehído. Nanopartículas silíceas comerciales se funcionalizan con grupos tiol y poliamina. Estas nanopartículas híbridas han sido usadas para el reconocimiento cromogénico de formaldehído usando un indicador azul de escuaridina. En ausencia de formaldehído, suspensiones de nanopartículas son capaces de decolorar las disoluciones azules de escuaridina debido a una reacción entre los tioles insertados y el colorante añadido. En presencia de formaldehído, los grupos -SH de la superficie reaccionan con esta molécula con la consiguiente inhibición de la reacción tiol-escuaridina. Como consecuencia la suspensión permanece azul y el formaldehído es detectado. Estas nanopartículas permiten la detección de formaldehído de manera sensitiva y selectiva en disolución y fase gas.

El cuarto capítulo trata de la preparación de nanopartículas mesoporosas de sílice tapadas con acetilcolinesterasa que son usadas para el sensado selectivo y sensitivo de diisopropilfluorofosfato (DFP), un simulante de gas nervioso. Nanopartículas mesoporosas de sílice se preparan y sus poros se cargan con rodamina B. Entonces, la superficie externa de las nanopartículas cargadas se funcionalizan con un derivado de piridostigmina (un inhibidor reversible de la enzima acetilcolinesterasa). Finalmente los poros se tapan con la adición de acetilcolinesterasa (por coordinación con el inhibidor insertado). En ausencia de DFP, las nanopartículas permanecen cerradas mientras que en la presencia del simulante de agente nervioso los poros se abren y se observa la liberación del colorante (debido a la preferencia de coordinación de los sitios activos de la enzima con el DFP y el desanclaje de la superficie de las nanopartículas). En una extensión de los resultados comentados, se preparan nanopartículas funcionalizadas con un derivado de neostigmina para caracterizarlas y estudiar sus procesos de liberación controlada en presencia de distintos inhibidores de acetilcolinesterasa.

El reconocimiento selectivo de ADN genómico de *Mycoplasma fermentans* usando nanopartículas mesoporosas de sílice se presenta en el quinto capítulo. Nanodispositivos sensores basados en nanopartículas de sílice mesoporosa cargadas con rodamina B y con la superficie externa funcionalizada con grupos isocianatopropilo. Entonces, una secuencia corta de ADN se ancla covalentemente a la superficie de las nanopartículas a través de la formación de enlaces urea. Finalmente, los poros se tapan añadiendo un oligonucleótido de cadena simple el cuál está formado por una secuencia altamente conservada de la subunidad ribosomal 16S del genoma de esta especie concreta de micoplasma. Suspensiones acuosas de nanopartículas tapadas con oligonucleótido presentan una liberación insignificante de colorante. Sin embargo, sólo en presencia de ADN

genómico de *Mycoplasma fermentans* los poros se abren y se observa una marcada liberación de rodamina B. Usando estas nanopartículas se llegó a un límite de detección tan bajo como 70 copias de ADN por μL.

El sexto capítulo de esta tesis presenta la síntesis y caracterización de nanopartículas mesoporosas de sílice recubiertas con aptámeros de MUC1 (capaces de reconocer la glicoproteína MUC1, presente en ciertos tipos de cáncer) y marcadas con radioisótopos de ^{99m}Tc. Nanopartículas mesoporosas de sílice se cargaron con safranina O y su superficie externa se funcionaliza con grupos amino. Entonces, los poros se tapan mediante la adición del aptámero MUC1. Estas nanopartículas tapadas con el aptámero son internalizadas por células cancerosa MDA-MB-231 (las cuáles sobreexpresan glicoproteína MUC1) y liberación del colorante cargado. Dándo un paso más adelante, las nanopartículas tapadas con el aptámero de MUC1 se radiomarcan con ^{99m}Tc y son usadas para la imagen de lesiones cancerosas en ratones usando SPECT.

Finalmente, en el séptimo capítulo se exponen las conclusiones de la tesis.

Publications

This thesis and other collaboration have resulted in the following scientific publications:

Pascual, L.; Baroja, I.; Aznar, E.; Sancenón, F.; Marcos, M. D.; Murguía, J. R.; Amorós, P.; Rurack, K.; Martínez-Máñez, R. Oligonucleotide-Capped Mesoporous Silica Nanoparticles as DNA-Responsive Dye Delivery Systems for Genomic DNA Detection. *Chem. Commun.* **2015**, *51* (8), 1414–1416.

El Sayed, S.; Pascual, L.; Licchelli, M.; Martínez-Máñez, R.; Gil, S.; Costero, A. M.; Sancenón, F. Chromogenic Detection of Aqueous Formaldehyde Using Functionalized Silica Nanoparticles. *ACS Appl. Mater. Interfaces* **2016**, *8* (23), 14318–14322.

Pascual, L.; Sayed, S. El; Martínez-Máñez, R.; Costero, A. M.; Gil, S.; Gaviña, P.; Sancenón, F. Acetylcholinesterase-Capped Mesoporous Silica Nanoparticles That Open in the Presence of Diisopropylfluorophosphate (a Sarin or Soman Simulant). *Org. Lett.* **2016**, *18* (21), 5548–5551.

Agostini, A.; Mondragón, L.; Pascual, L.; Aznar, E.; Coll, C.; Martínez-Máñez, R.; Sancenón, F.; Soto, J.; Marcos, M. D.; Amorós, P.; et al. Design of Enzyme-Mediated Controlled Release Systems Based on Silica Mesoporous Supports Capped with Ester-Glycol Groups. *Langmuir* **2012**, *28* (41), 14766–14776.

Bataller, R.; Campos, I.; Alcañiz, M.; Gil-Sánchez, L.; García-Breijo, E.; Martínez-Máñez, R.; Pascual, L.; Soto, J.; Vivancos, J.-L. A Humid

Electronic Nose Based on Pulse Voltammetry: A Proof-of-Concept Design. *Sensors Actuators B Chem.* **2013**, *186*, 666–673.

Campos, I.; Pascual, L.; Soto, J.; Gil-Sánchez, L.; Martínez-Máez, R. An Electronic Tongue Designed to Detect Ammonium Nitrate in Aqueous Solutions. *Sensors* **2013**, *13* (10), 14064–14078.

Agostini, A.; Campos, I.; Milani, M.; Elsayed, S.; Pascual, L.; Martínez-Máñez, R.; Licchelli, M.; Sancenón, F. A Surfactant-Assisted Probe for the Chromo-Fluorogenic Selective Recognition of GSH in Water. *Org. Biomol. Chem.* **2014**, *12* (12), 1871-1874.

El Sayed, S.; Pascual, L.; Agostini, A.; Martínez-Máñez, R.; Sancenón, F.; Costero, A. M.; Parra, M.; Gil, S. A Chromogenic Probe for the Selective Recognition of Sarin and Soman Mimic DFP. *ChemistryOpen* **2014**, *3* (4), 142–145.

Olguín, C.; Laguarda-Miró, N.; Pascual, L.; García-Breijo, E.; Martínez-Mañez, R.; Soto, J. An Electronic Nose for the Detection of Sarin, Soman and Tabun Mimics and Interfering Agents. *Sensors Actuators B Chem.* **2014**, *202*, 31–37.

Pascual, L.; Campos, I.; Bataller, R.; Olguín, C.; García-Breijo, E.; Martínez-Mañez, R.; Soto, J. A "humid Electronic Nose" for the Detection of Nerve Agent Mimics; a Case of Selective Sensing of DCNP (a Tabun Mimic). *Sensors Actuators B Chem.* **2014**, *192*, 134–142.

Sancenón, F.; Pascual, L.; Oroval, M.; Aznar, E.; Martínez-Máñez, R. Gated Silica Mesoporous Materials in Sensing Applications. *ChemistryOpen* **2015**, *4* (4), 418–437.

Aznar, E.; Oroval, M.; Pascual, L.; Murguía, J. R.; Martínez-Máñez, R.; Sancenón, F. Gated Materials for On-Command Release of Guest Molecules. *Chem. Rev.* **2016**, *116* (2), 561–718.

Pascual, L.; Campos, I.; Vivancos, J.-L.; Quintás, G.; Loras, A.; Martínez-Bisbal, M. C.; Martínez-Máñez, R.; Boronat, F.; Ruiz-Cerdà, J. L. Detection of Prostate Cancer Using a Voltammetric Electronic Tongue. *Analyst* **2016**, *141* (15), 4562–4567.

Cerqueira-Coutinho, C.; Vidal, L. P.; Pinto, S. R.; Santos-Oliveira, R. Drug Metabolism: Comparison of Biodistribution Profile of Holmium in Three Different Compositions in Healthy Wistar Rats. *Applied Radiation and Isotopes* **2016**, 112, 27-30.

Pascual, L.; Sancenón, F.; Martínez-Máñez, R.; Barja-Fidalgo, T. C.; da Silva, S. V.; Sousa-Batista, A. de J.; Cerqueira-Coutinho, C.; Santos-Oliveira, R. Mesoporous Silica as Multiple Nanoparticles Systems for Inflammation Imaging as Nano-Radiopharmaceuticals. Microporous Mesoporous Mater. **2017**, 239, 426–431.

Abbreviations and Acronyms

AChE	*Acetylcholinesterase*
AFM	*Atomic force microscope*
AMF	*Alternating magnetic field*
APC	*2,4-bis-(4-dialkylaminophenyl)-3-hydroxy-4-alkylsulfanylcyclobut-2-one groups*
APTES	*(3-aminopropyl)triethoxysilane (APTES)*
ATP	*Adenosine 5′-triphosphate (ATP)*
AuNPs	*Gold nanoparticles*
BET	*Brunauer, Emmett and Teller*
BJH	*Barret, Joyner and Halenda*
BSA	*Bovine serum albumin*
CBPQT^{4+}	*Cyclobis(paraquat-p-phenylene)*
CD	*Cyclodextrin*
CLSM	*Confocal laser scanning microscopy*
COLO 205	*Human Caucasian colon adenocarcinoma*
CP[5]A	*Carboxylatopillar[5]arene*
CTAB	*Hexadecyltrimethylammonium bromide*
DCNP	*Diethyl cyanophophonate*
DCP	*Diethyl chlorophosphate*
DFP	*Diisiopropyl fluorophosphate*
DNA	*Deoxyribonucleic acid*
DNP	*Dinitrophenyl*
dsDNA	*Double stranded DNA*
DTNB	*5,5′-dithiobis(2-nitro)benzoic acid*
DTT	*Dithiothreitol*
EDX	*Energy dispersive X-ray spectroscopy*
FA	*Folic acid*
FITC	*Fluorescein isothiocyanate*
GFP	*Green fluorescent protein*
GOS	*Galacto-oligosaccharide polymer*
Gox	*Glucose oxidase*
GSH	*Glutathione*
GTP	*Guanosine 5'-triphosphate*
H640	*Hypotriploid human cell line*

Hep G2	*Human liver cancer cell line*
Hep2	*Human epithelial type 2 cell line*
HIFU	*High intensity focused ultrasound*
ICS	*Ion-channel sensors*
IUPAC	*International Union of Pure and Applied Chemistry*
L929	*L929 mouse fibroblast cell line*
LCST	*Lower critical solution temperature*
LOD	*Limit of detection*
MCF-10-A	*Michigan Cancer Foundation - 10 (human breast epithelial) cell line*
MCF-7	*Michigan Cancer Foundation - 7 cells*
MCM	*Mobil Composition of Matter*
MDA-MB-231	*Invasive ductal carcinoma breast cancer cells*
MES	*2-(N-morpholino)ethanesulfonic acid*
MPTS	*3-(mercaptopropyl) trimethoxysilane*
MRI	*Magnetic resonance imaging*
MSNs	*Mesoporous silica nanoparticles*
MTT	*(3-(4,5-Dimethylthiazol-2-yl)-2,5-Diphenyltetrazolium Bromide)*
MUC1	*Mucin 1 glycoprotein*
NIR	*Near infrared*
NMR	*Nuclear magnetic resonance*
NOTA	*1,4,7-triazacyclononane-triacetic acid*
OP-1	*Dimethylmethyl phosphonate*
OP-2	*Diethyl (2-cyanoethyl) phosphonate*
OP-3	*Diethyl (methylthiomethyl) phosphonate*
OP-4	*Dimethyl chlorothiophosphate*
OP-5	*Ethyl dichlorophosphate*
PBS	*Phosphate buffer saline*
PDAC	*Pancreatic ductal adenocarcinoma*
PEG	*Polyethylene glycol*
PEI	*Polyethyleneimine*
PET	*Positron emission tomography*
PETE	*Polyethylene terephthalate*
PFH	*Perfluorohexane*
PMOs	*Periodic mesoporous organosilicas*
PVPON	*Polyvinyl pyrollidone*

PXRD	*Powder X-ray diffraction*
RNA	*Ribonucleic acid*
SC[4]A	*Sulfonatocalix[4]arene*
SKOV3	*Ovarian carcinoma cells*
SNTs	*Silica nanotubes*
SPECT	*Single emission photon computed tomography*
SPIONPs	*Superparamagnetic iron oxide nanoparticles*
SQ	*Squaraine dye*
ssDNA	*Single stranded DNA*
STM	*Scanning tunneling microscope*
sulfo-EMCS	*N-(ε-maleimidocaproyloxy) sulfosuccinimide ester*
TATP	*Triacetone triperoxide*
TEM	*Transmission electron microscopy*
TEOS	*Tetraethylorthosilica*
Tetryl	*2,4,6-trinitrophenyl methylnitramine*
TGA	*Thermogravimetric analysis*
TGF-β	*Transforming growth factor beta*
TLCT	*True liquid-crystal templating*
TMOS	*Tetramethylorthosilica*
TNF-α	*Tumor necrosis factor a*
TNT	*2,4,6-trinitrotoluene*
TRIS	*Tris(hidroxymethyl)aminomethane*
TTF	*Tetrathiafulvalene*
US	*Ultrasound*
US EPA	*Us environmental protection agency*
UV	*Ultraviolet*
UV-Vis	*Ultraviolet-visible*
VX2	*Rabbit tumor cell line*
X-DC	*X-linked Dyskeratosis Congenita*

Table of Contents

Chapter 1:

Elemental concepts

1. Introduction

This thesis is based on the development of functional mesoporous silica-based hybrid nanomaterials. In this general introduction, fundaments of nanotechnology will be briefly described to further focus on the description of mesoporous silica-based supports, their classification and a picture of selected examples to illustrate their unique features and technological potential.

1.1 Nanotechnology and nanomaterials

29th December 1959, annual meeting of the American Physical Society at Caltech: "There's plenty room at the bottom". Under this title, Nobel laureate physicist Richard Feynman gave a premonitory talk where he defined the conceptual principles of this not yet discovered revolutionary field of knowledge. In his own words:

"Nature has been working at the level of atoms and molecules for millions of years, so why do we not?[…] The principles of physics, as far as I can see, do not speak against the possibility of maneuvering things atom by atom. It is not an attempt to violate any laws; it is something, in principle, that can be done; but in practice, it has not been done because we are too big."[1]

The first known use of the term of **nanotechnology** is attributed to Professor Norio Taniguchi, that defined it in 1974 as: "production technology to get extra high accuracy and ultra-fine dimensions, that is, the preciseness and fineness on the order of 1 nm, 10^{-9} m, in length."[2] In the following years prodfessor Eric Drexler developed a deeper therotical corpus that was eventually summarized in its book *Engines of creation: the coming era of nanotechnology*. These theoretical contributions were reinforced in a dialectical way with the impact of incoming new technologies able to act at a molecular or atomic level, specially scanning tunneling microscopy (STM) and the atomic force microscopy (AFM) developed by the Nobel prize winner Gerd Binnig.[3]

[1] Feynman, R. *Caltech Engineering & Science* **1960**, *23*, 22.

[2] Taniguchi, N. in *Proc. Intl. Conf. Prod. Eng. Tokyo, Part II, Japan Society of Precision Engineering.*; **1974**.

[3] Wilson, Mick; Kannangara, Kamali; Smith, Geoff; Simmons, Michelle; Raguse, B. *NANOTECHNOLOGY: Basic Science and Emerging Technologies; Chapman & Hall/CRC*, **2002**.

Nowadays, our knowledge on nanotechnology has been hugely improved and now the term is commonly defined as "the construction and use of functional structures designed from atomic or molecular scale with at least one characteristic dimension measured in nanometers. Their size allows them to exhibit new and significantly improved physical, chemical, and biological properties, phenomena, and processes. Thus, nanotechnology can be defined as research and development that involves measuring and manipulating matter at the atomic, molecular, and supramolecular levels at scales measured in approximately 1–100 nm in at least one dimension."[4] Figure 1 instructs in what means this range.

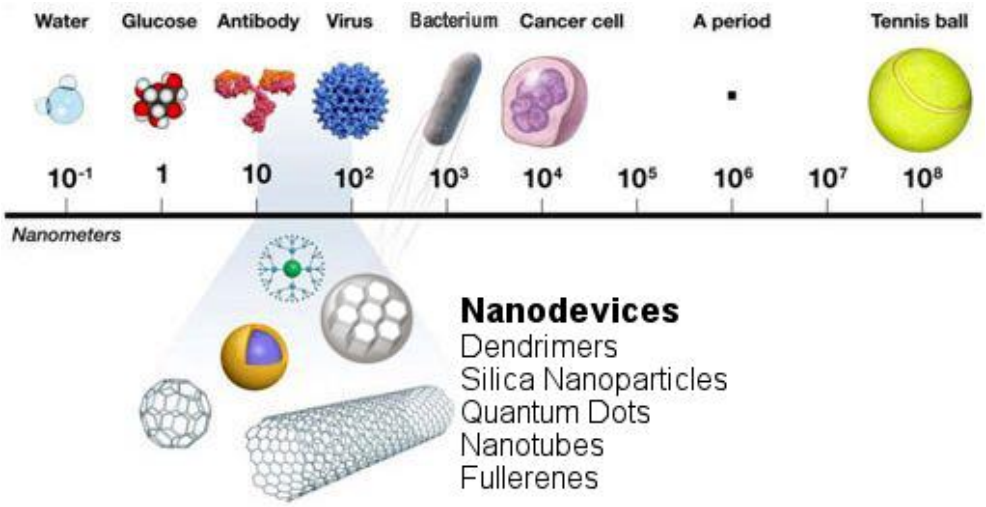

Figure 1. Scale illustration to compare range of sizes of objects, biomolecules and nanomaterials.

Nanotechnology literally means any technology performed on nanoscale range that has applications in the real world and we can found several of them being developed on almost every research field and industrial area such as materials science, electrical and electronic engineering, surface

[4] Narendra, K.; Kumbhat, S. *Essentials in Nanoscience and Nanotechnology*; John Wiley & Sons, **2016**.

science, catalysis, colloid science, ceramic and chemical engineering, coatings and adsorbents, drug delivery, polymer science and engineering, nanomedicine, metallurgy and powder technology, device and chip engineering, biomimetics, pharmacy, biotechnology, etc.

In the basis of every nanotechnology definition, relies an essential concept: development of **nanomaterials**. To prepare devices able to operate in a range of nanometers, development and characterization of materials and supporting structures of that size, namely nanomaterials, is needed. These can be definded as "a set of substances where at least one dimension is approximately less than 100 nm. However, organizations in some areas such as environment, health, and consumer protection favor a larger size range from 0.3 to 300 nm to define nanomaterials. This larger size range allows more research and a better understanding of all nanomaterials and also allows to know whether any particular nanomaterial shows concerns for human health or not and in what size range."[4]

A large amount of nanomaterials are already applied for several purposes in different fields such as biotechnology, medicine, electronics, chemistry or photonics among others. Carbon nanomaterials as fullerene or graphene structures; nanoparticles or nanorods composed of silica, metals or metal oxides; quantum dots; dendrimers; metallic or organic nanowires and natural nanomaterials as cellulose fibers, wax crystals on lotus leaf or the coloured structure of butterfly wings are only a small taste of these revolutionary materials.[5]

[5] Rurack, K., Martínez-Máñez, R. *The Supramolecular Chemistry of Organic-Inorganic Hybrid Materials*; John Wiley & Sons, **2010**.

1.2 Hybrid materials

Hybrid materials are composed by two constituents (within a size in the range of nanometers or even angstroms) in a synergetic way. One of the components tends to be inorganic and the other organic so we can refer to them as **organic-inorganic hybrid materials**. Oftentimes, these materials are obtained by the anchoring of functional (organic) groups into nanoscopic inorganic materials as supporting platforms.

In words of professor Clément Sanchez "hybrid organic inorganic materials are not simply physical mixtures. They can be broadly defined as nano-composites with (bio)organic and inorganic components, intimately mixed where at least one of the component domains has a dimension ranging from a few Å to several nanometers. Consequently the properties of hybrid materials are not only the sum of the individual contributions of both phases, but the role of their inner interfaces could be predominant." [6]

A usual division of these materials separes them into two different classes: materials where both components are embedded only using non-covalent interactions (class I) or materials where both phases are linked by covalent bonds (class II). In the face of a better understanding of the materials presented on this PhD thesis all the examples described will correspond to class II hybrid materials.

Hybrid materials offer interesting features for molecular recognition applications. Several examples of these kind of systems can be found on literature.[7] Some of the principal advantages of these systems are summarized herein:

[6] Sanchez, C. *J. Mater. Chem.* **2005**, *15*, 3557.

[7] a) Kim, H. J.; Lee, M. H.; Mutihac, L.; Vicens, J.; Kim, J. S. *Chem. Soc. Rev.* **2012**, *41*, 1173.

- Receptors can be organized in a more or less compact monolayer (depending on the degree of the surface functionalization). Due to this, the movement of the different molecular units is reduced and this generates new collective proceses that improve the features of the recognition process, such as "surface chelate effect" with monodentate ligands or an increase on the "effective concentration" on the solids.
- It is possible to carry out subsequent anchoring processes to obtain a solid surface functionalized with different organic molecules and modulate their properties according to the nature of the anchored functional groups.
- Leaching processes involving the receptor are avoided.
- If the solid support is functionalized with a receptor that could give reversible coordination processes it can be reused several times without lost of their recognition features.

1.2.1 Silica-based hybrid materials

Among others, silica is one of the most popular scaffold used for the development of organic-inorganic hybrid materials for sensing and recognition protocols.[8] There are plenty of forms of silica nanomaterials useful for the development of these nanodevices, thus we will broadly classify these supports in two groups:

- **2D silica-based hybrid materials**: Involving all solids in which the recognition process occurs over a planar surface (i.e. solid nanoparticles,[9] nanotubes,[10] thin layers,[11] etc.)

- **3D silica based hybrid materials**: Involving all solids in which the recognition process is affected by other effects depending on the material shape such as the diffusion rate or the accessibility to receptors (i.e. mesoporous nanoparticles,[12] mesoporous thin films,[13] mesoporous nanorods,[14] hollow nanoparticles,[15] etc.).

[8] a) Han, W. S.; Lee, H. Y.; Jung, S. H.; Lee, S. J.; Jung, J. H. *Chem. Soc. Rev.* **2009**, *38*,1904. b) Nicole, L.; Boissière, C.; Grosso, D.; Quach, A.; Sanchez, C. *J. Mater. Chem.* **2005**, *15*, 3598.

[9] Brasola, E.; Mancin, F.; Rampazzo, E.; Tecilla, P.; Tonellato, U. *Chem. Commun.* **2003**, *2*, 3026.

[10] Lee, S. J.; Lee, S. S.; Lee, J. Y.; Jung, J. H. *Chem. Mater.* **2006**, *18*, 4713.

[11] a)Ding, L.; Cui, X.; Han, Y.; Lü, F.; Fang, Y. *J. Photochem. Photobiol. A Chem.* **2007**, *186*, 143.b) Marques, M. E.; Mansur, A. A. P.; Mansur, H. S. *Appl. Surf. Sci.* **2013**, *275*, 347.

[12] Descalzo, A. B.; Jiménez, D.; el Haskouri, J.; Beltrán, D.; Amorós, P.; Marcos, M. D.; Martínez-Máñez, R.; Soto, J. *Chem. Commun.* **2002**, 562.

[13] Nicole, L.; Boissière, C.; Grosso, D.; Hesemann, P.; Moreau, J.; Sanchez, C. *Chem. Commun.* **2004**, 20, 2312.

[14] Yang, X.; He, D.; He, X.; Wang, K.; Tang, J.; Zou, Z.; He, X.; Xiong, J.; Li, L.; Shangguan, J. *ACS Appl. Mater. Interfaces* **2016**, *8*, 20558.

[15] Guardado-Alvarez, T. M.; Chen, W.; Norton, A. E.; Russell, M. M.; Connick, W. B.; Zink, J. I. *Nanoscale* **2016**, *8*, 18296.

1.3 2D silica-based hybrid materials

The easiest way to obtain a functional hybrid material is using the planar surface of the inorganic scaffold and anchor onto the surface organic moieties. In the case of silica these inorganic supports usually are the surface of nanoparticles or thin layers.

Organic modification of silica materials have been reported using differents methodologies and procedures depending on the solid used. However, referring to planar silica hybrid materials the most common strategy to orderly functionalize their surface is using trialkoxysilane derivatives. Surface of silica materials contains a great concentration of structural defects in form of silanol (Si-OH) groups. These silanols can easily react with trialkoxysilane derivatives ($(R'O)_3$-Si-R) by nucleofilic substitution reaction providing new organic functionalities to the prepared hybrid material. In the case of planar hybrid supports this condensation is generally produced once the silica scaffold is prepared (post-functionalization) in a procedure known as **grafting**. In this **grafting procedure** a suspension of the required quantity of the solid in an anhydrous solvent is reacted with the functional silane precursor (see figure 2). The presence of the silanol groups on the silica scaffold surface guarantees the formation of a covalent bond between the trialkoxysilane precursors and the solid surface. Functionalization techniques of silica materials will be deeply described in the next section refered to 3D silica-based hybrid materials.

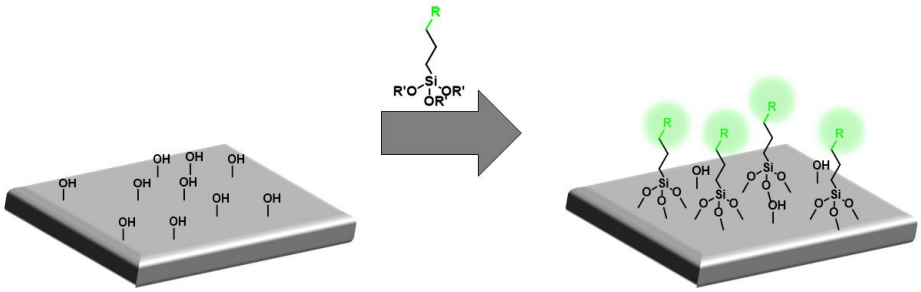

Figure 2. Schematic representation of silica surface functionalization by grafting procedure.

1.3.1 2D Hybrid materials for molecular recognition

As commented before, anchoring certain functional organic molecules onto the surface of an inorganic scaffold is one of the main ways to obtain hybrid materials, which can be used for sensing and molecular recognition purposes. Preorganization of the receptors over a surface induce an enhancement of the local concentration in a dense monoloyer of binding sites in a specific orientation maximizing the capability of interaction with the analyte. Simpliest way for that strategy is to anchor the organic receptors in a planar area as the surface of a nanoparticle or over a film of material.

In this way, an interesting example was provided by Dubertret and coworkers using cluster gold nanoparticles (AuNPs), single-stranded DNA molecules (ssDNA) and a collection of commonly used fluorophores.[16] The material prepared consisted on a ssDNA with a hairpin-loop structure connected through the 5'- end side to AuNPs. Besides, the 3'-end side is

[16] Dubertret, B.; Calame, M.; Libchaber, a J. *Nat. Biotechnol.* **2001**, *19*, 365.

functionalzed with a fluorophore (fluorescein, rhodamine 6G, Texas red, or cyanine-5). Due to the hairpin conformation fluorophore and AuNPs remain very near in space activating a distance-depending quenching process of the fluorescence (primarily from a nonradiative energy transfer). No significant differences of the quenching efficiencies were observed for the fluorophores tested. In presence of a complementary DNA strand the conformation of this hybrid material changes due to DNA hybridization. In this final conformation the fluorophore is displaced away from the gold nanoparticle deactivating the quenching process and increasing the fluorescence over several thousands (see figure 3). Also the capability of the system to detect a single nucleotide mismatch was also proof.

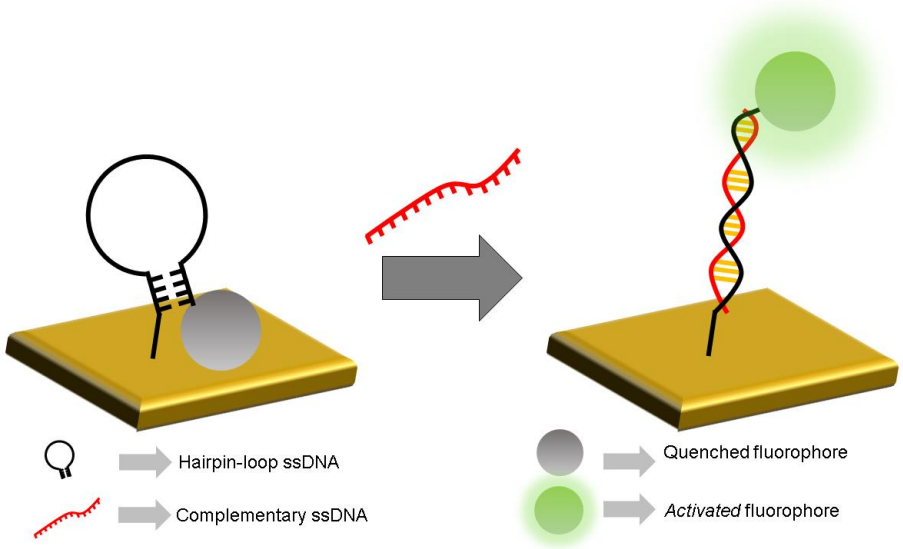

Figure 3. Recognition of a DNA complementary strand using a hybrid material based on AuNPs derivatized on its surface with a DNA hairpin.

Beating with hybrid materials using solid silica supports, some interesting examples were reported by Montalti's group. In a first work silica nanoparticles, covered with dansyl moieties on its surface, were applied for pH determination.[17] Authors demonstrated that protonation of dansyl units not only quenched its own fluorescence but also the surrounding unprotonated ones. In this case, the preorganization of functional units over the surface of the hybrid material resulted in a signal amplification effect not observable on the isolated components. Taking a step further Montalti and coworkers developed another silica hybrid material for sensing metal ions. For this purpose, silica nanoparticles were functionalized with a dansyl derivative bearing a polyamine receptor unit.[18] Addition of Cu^{2+}, Co^{2+} or Ni^{2+} at nanomolar concentrations produced a strong quenching of the fluorescence due to coordination with metal ions (see figure 4). Each ion was capable of quenching the emission of several fluorophores. At this respect, a single Cu^{2+} cation induces an emission decrease equivalent to deactivation of 13 dansyl moieties. A similar system was designed by Ding and coworkers for sensing Cu^{2+} with the same components but using glass slides as supports.[11a] Also *Brasola et al.* reported a system based on the same principle but with the organic units (dansylamide as fluorophore and picolinamide as receptor unit) grafted separately onto the surface of silica nanoparticles.[9]

[17] Montalti, M.; Prodi, L.; Zaccheroni, N.; Falini, G. *J. Am. Chem. Soc.* **2002**, *124*, 13540.
[18] Montalti, M.; Prodi, L.; Zaccheroni, N. *J. Mater. Chem.* **2005**, *15*, 2810.

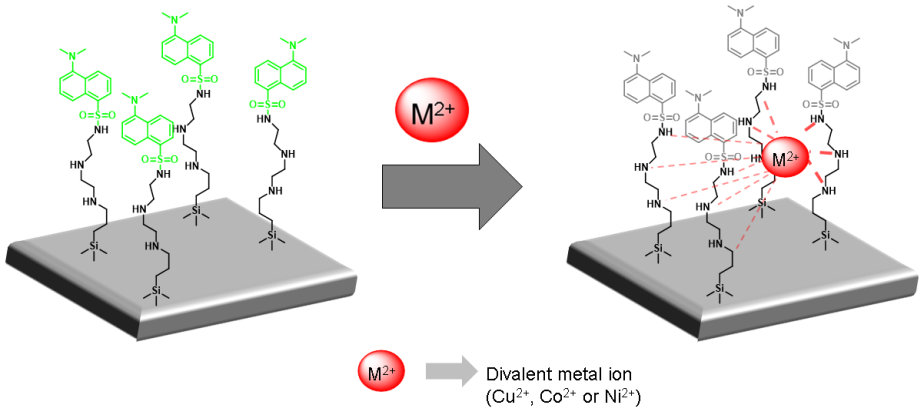

Figure 4. Detection of Cu^{2+}, Co^{2+} and Ni^{2+} divalent metal ions using silica nanoparticles functionalized with dansyl moieties.

Several examples of hybrid materials for the colorimetric detection of surfactants can be also found on the literature. In a first example, Martínez-Máñez and coworkers developed silica nanoparticles grafted with a merocyanine derivative and thiourea as anion receptor. Interaction between thiourea moieties and long chain carboxylates induced a change on the polarity of the nanoparticles surface (due to the hydrophobic tails of these organic targets). This hydrophobic environment induces the cyclization of merocyanine units to the spirocyclic form. As a result, a modulation of color from pink to pale yellow was observed and monitorized. In a more advanced system the same authors applied a similar hybrid material for anionic surfactants detection using a two-step recognition protocol.[19] In this case silica nanoparticles were functionalized with an imidazolium derivative (obtained by reaction of *N*-methylimidazole with triethoxysilylchloropropane). In a first step, suspended nanoparticles were able to selectively coordinate lauryl sulfate by electrostatic interaction between their sulfate moieties and the imidazolium receptors. Consequently

[19] Coll, C.; Martínez-Máñez, R.; Marcos, M. D.; Sancenón, F.; Soto, J. *Angew. Chemie - Int. Ed.* **2007**, *46*, 1675.

surfactants remained attached to the surface forming a self-assembled monolayer with a remarkable hydrophobic character. Due to this hydrophobicity in a second step methylene blue was added to the suspension and adsorbed on this monolayer colouring the solid and bleaching the suspension (see figure 5). In a further work, the authors extended this strategy to also detect cationic surfactants using sulfonate units as receptors grafted onto the silica surface.

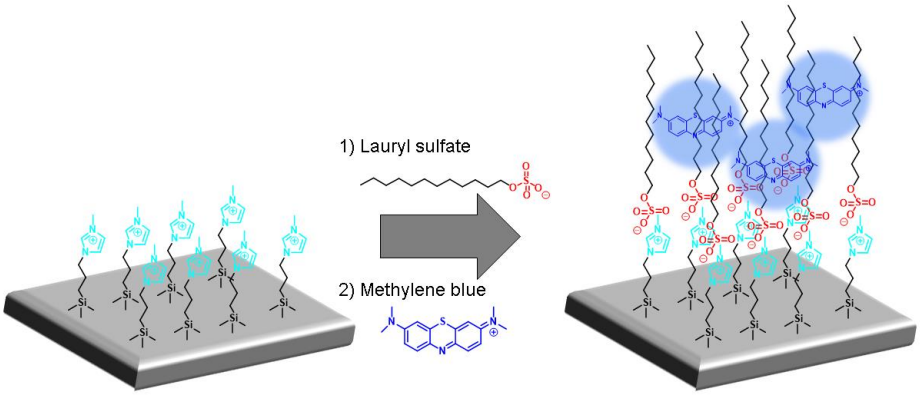

Figure 5. Detection of lauryl sulfate in a two-step procedure using silica nanoparticles functionalized with imidazolium groups (for surfactant recognition) and methylene blue (for reveal).

1.3.2 Ion-channel sensors (ICS)

Ion-channel sensors is a term coined by Suwagara and Umezawa and largely applied in electrochemical sensing. Main principles of these systems consisted in mimicking natural transmembrane and intracellular signaling processes. The binding of signaling ions and molecules to their receptors in bilayer membranes is reproduced onto the electrode surface by forming lipid bilayers, self-assembled monolayers or even some polymeric coatings with the specific molecular receptors incorporated.[20] Flux of a concrete electroactive marker to the electrode surface is controlled by the coordination of the target analyte with these receptors.

First ion-channel sensor described uses a glassy carbon electrode coated by synthetic lipid mono- and multilayers by means of the Langmuir-Blodgett technique. Voltammetry studies determined the permeability of this thin layers to electroactive marker ions depending on the polarity of the bilayer headgroup.[21] For instance, using didodecyl phosphate lipid bilayers (that contains a phosphate head group) an electronegative marker (as $[Fe(CN)_6]^{4-}$) was not able to penetrate into the bilayer and do not reach the electrode surface. But if certain cations such as Ca^{2+}, Mg^{2+} or Ba^{2+} were added $[Fe(CN)_6]^{4-}$ becomes able to diffuse reaching the electrode surface (see figure 6). Thus this technique can be applied for the electrochemical determination of the mentioned cations. The opposite result was observed when using positevely charged dimethyldioctadecylammonium bromide bilayer and

[20] Sugawara, M.; Hirano, A.; Bühlmann, P.; Umezawa, Y. *Bull. Chem. Soc. Jpn.* **2002**, *75*, 187. b) Bühlmann, P.; Aoki, H.; Xiao, K. P.; Amemiya, S.; Tohda, K.; Umezawa, Y. *Electroanalysis* **1998**, *10*, 1149.

[21] Sugawara, M.; Kojima, K.; Sazawa, H.; Umezawa, Y. *Anal. Chem.* **1987**, *59*, 2842.

$Ru(bpy)^{2+}$ marker. In this case, perchlorate anion was succesfully determined by the same procedure.

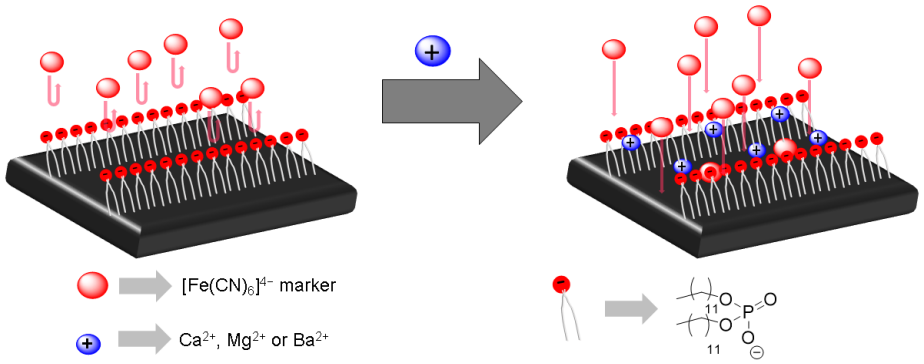

Figure 6. Glassy carbon electrode ICS for the detection of certain cations (for a better understanding only the upper part of the lipid bilayer was drawn).

In the example described above, channel opening was achieved by modifying the electrostatic character of the electrode surface allowing the electrochemical marker to diffuse along the intermolecular voids formed in the molecular receptors layer. Other ICS systems use macrocyclic molecular receptors (such as cyclodextrins (CDs), crown-ethers or calixarenes) which provide intramolecular channels that can be blocked when the target analyte forms a coordination complex. Furthermore some ICS have been applied for detecting biomolecules like antibodies, nucleotides or even specific DNA strands.[22]

[22] a) Aoki, H.; Bühlmann, P.; Umezawa, Y. *Electroanalysis* **2000**, *12*, 1272. b)Bühlmann, P.; Amemiya, S.; Xiao, K. P.; Umezawa, Y.; Nishizawa, S. *J. Incl. Phenom. Mol. Recognit. Chem.* **1998**, *32*, 151. c) Willner, I.; Blonder, R.; Dagan, A. *J. Am. Chem. Soc.* **1994**, *116*, 9365. d) Sugawara, M.; Hirano, A.; Buhlmann, P.; Umezawa, Y. *Bull. Chem. Soc. Jpn.* **2002**, *75*, 187.

1.3.3 Optical ICS based on silica nanoparticles

The research group of professor Martínez-Màñez developed a strategy to translate the principles of electrochemical ion-channel sensors for colorimetric sensing of different compounds.[23] In a general approach, the surface of silica nanoparticles is bifunctionalized with a nucleophilic unit (thiol moieties) and a receptor agent able to coordinate with the analyte. This receptor controls the acces of a chromogenic marker to the reactive thiolated surface. As chromogenic marker a water-soluble derivative of squaraine sensitive to thiols was selected. This chromogenic marker produce an intense blue color in solution but when react with thiols the colour is rapidly bleached. First material and sample were mixed and the analyte (when present) is anchored to the receptor unit preventing flow of the chromogenic marker to thiols. Persistance of the blue color in solution indicates a positive presence of the targeted analyte. Bleaching of the solution, on the contrary, indicates a negative presence of the analyte.

In a first example, silica nanoparticles were bifunctionalized using an imidazolium containing trialkoxysilane derivative and 3-(mercaptopropyl) trimethoxysilane (MPTS).[24] Imidazolium groups over the surface are able to coordinate anionics surfactants (such as lauryl sulfate) blocking the acces of the chromogenic marker (a squaraine derivative) to the thiol reactive surface (see figure 7). If there is not any anionic surfactant, when the squaraine derivative is added to the nanoparticles suspension, a quickly bleaching of the solution was observed. On the contrary when anionic surfactants are

[23] a) Climent, E.; Calero, P.; Marcos, M. D.; Martínez-Máñez, R.; Sancenón, F.; Soto, J. *Chem. - A Eur. J.* **2009**, *15*, 1816. b) Climent, E.; Casasús, R.; Marcos, M. D.; Martínez-Máñez, R.; Sancenón, F.; Soto, J. *Chem. Commun.* **2008**, *45*, 6531.

[24] Climent, E.; Giménez, C.; Marcos, M. D.; Martínez-Máñez, R.; Sancenón, F.; Soto, J. *Chem. Commun.* **2011**, *47* , 6873.

present, the squaraine-thiol reaction is inhibited and the solution remains with an intense blue colour. Using this procedure determination of lauryl sulfate was comparable to the results obtained using a standard analytical methodology (methylene blue method).

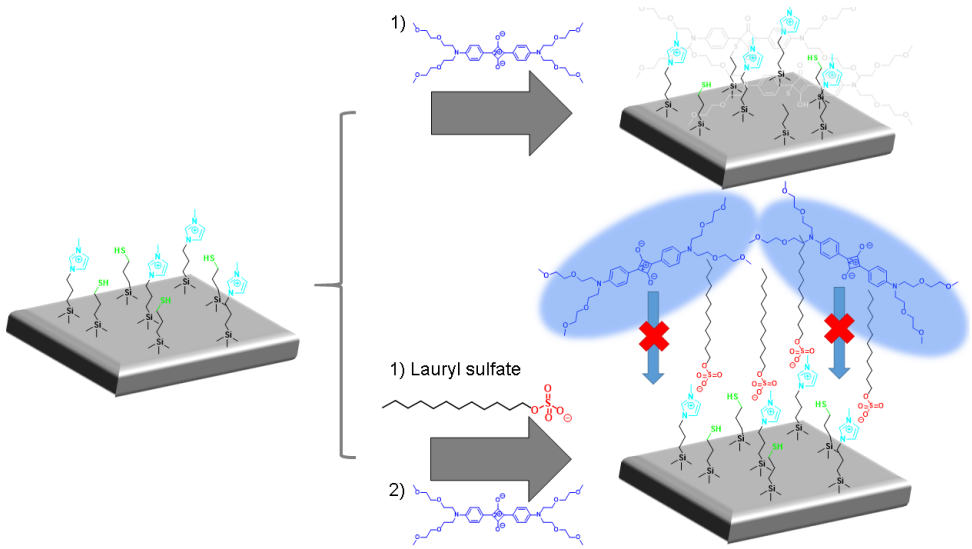

Figure 7. Detection of lauryl sulfate using optical ICS based on silica nanoparticles functionalized with thiol groups and imidazolium receptors.

In another work, the same authors designed silica nanoparticles based on the same principles for the optical detection of nerve agents.[25] For this purpose silica nanoparticles were functionalized with (3-mercaptopropyl)triethoxysilane and 3-[bis-(2-hydroxyethyl)amino] propyltriethoxysilane. Hydroxyl moieties are able to react with the organophoshate-type nerve agent mimics and, when this occurred, the acces of the optical marker to the thiol reactive surface was blocked (see figure 8). This procedure was successfully applied in 1:1 acetonitrile water solutions for the chromo-fluorogenic recognition of diethyl cyanophophonate

[25] Climent, E.; Martí, A.; Royo, S.; Martínez-Máñez, R.; Marcos, M. D.; Sancenón, F.; Soto, J.; Costero, A. M.; Gil, S.; Parra, M. *Angew. Chemie Int. Ed.* **2010**, *49*, 5945.

(DCNP), diethyl chlorophosphate (DCP) or diisiopropyl fluorophosphate (DFP). Also the detection of DFP in the vapor phase was successfully achieved using silica dipsticks containing the functionalized nanoparticles onto a polyethylene terephthalate (PETE) film. In a more recent work, also using optical ICS, the same authors achieved the detection of carbon dioxide in gas phase.[26]

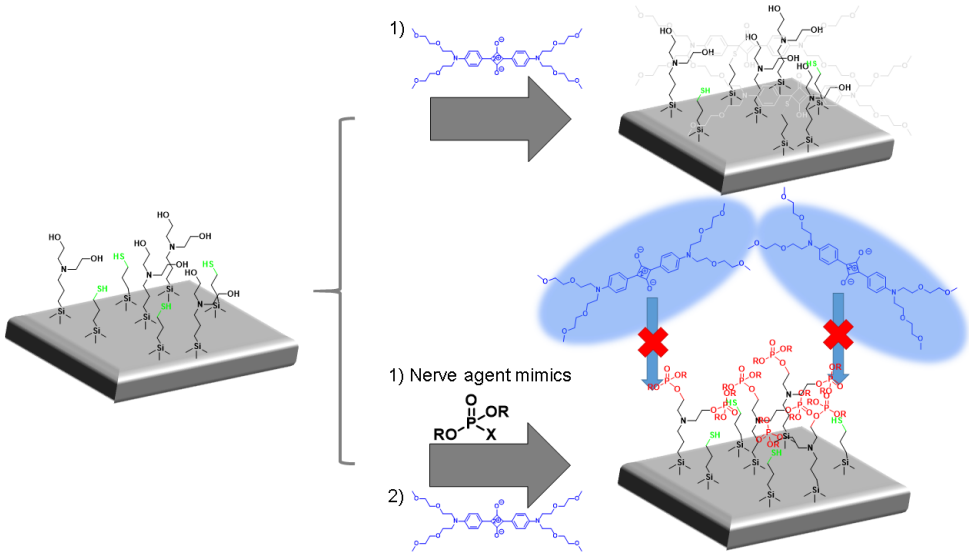

Figure 8. Detection of nerve agent mimics using optical ICS based on silica nanoparticles functionalized with thiol groups and hydroxyl moieties.

[26] Climent, E.; Agostini, A.; Moragues, M. E.; Martínez-Máñez, R.; Sancenón, F.; Pardo, T.; Marcos, M. D. *Chem. - A Eur. J.* **2013**, *19*, 17301.

1.4 3D silica-based hybrid materials

Using 3D-architectured inorganic supports improves exponentially the repository of possibilities to design new functional nanodevices. Exists a wide range of silica materials structures able to incorporate novel potential features onto hybrid materials (i.e. control of special acces to certain region, flux control inside channels, double functionalization in the inner and outer regions of the material, etc.) with respect to the possibilities of planar silica materials. The next sections will focus on the use of mesoporous silica scafolds which are the most vastly used nowadays despite the existence of other 3D materials applied or applicable in this area.

1.4.1 Mesoporous Silica Materials

Mesoporous materials are refered to those containing regular pores of an intermediate size. International Union of Pure and Applied Chemistry (IUPAC) classifies pore sizes into three main categories: *micro*- pores, *meso*-pores and *macro*-pores. Characterized by pore sizes smaller than 2 nm, between 2 and 50 nm, and larger than 50 nm respectively (see table 1).[27] Among them, thanks to their large internal surface area, microporous and mesoporous materials are attracting considerable research attention for applications in catalysis,[28] filtration and separation,[29] gas adsorption and

[27] a) Yuan, Z.-Y.; Su, B.-L.; Zeng, H. C.; Mueller, U.; Pastre, J.; Puetter, H.; Schubert, M.; Schierle-Arndt, K.; Teich, F. *J. Mater. Chem.* **2006**, *16*, 623. b) Murray, R.; Gill, M. *MRS Bull.* **1994**, *19*, 1122.

[28] De Vos, D. E.; Dams, M.; Sels, B. F.; Jacobs, P. A *Chem. Rev.* **2002**, *102*, 3615–3640.

[29] Cavenati, S.; Grande, C. A.; Lopes, F. V. S.; Rodrigues, A. E. *Microporous Mesoporous Mater.* **2009**, *121*, 114.

storage,[30] enzyme immobilization,[31] biomedical tissue regeneration,[32] drug delivery[33] and chemical/biochemical sensing.[34] Some emblematic microporous materials are crystalline framework solids (such as zeolites, pore size about 3-10 Å),[35] particular metallophosphates (pore size about 10-12 Å)[36]or cacoxenite (pore size of 14 Å).[37]

Table 1. IUPAC classification of pore size

Pore deifintion	*Pore Diameter (nm)*
Macropores	> 50
Mesopores	2-50
Micropores	< 2

In 1992 *Mobil Oil co.* developed some of the most well-kown meso-structured materials.[38] In particular they gave birth to a new family of mesoporous silica based materials known as M41S phases. The best-known representatives of this class of materials include the silica solid MCM-41 (Mobile Crystalline Material with a hexagonal arrangement of the mesopores), MCM-48 (with a cubic arrangement of mesopores) and MCM-

[30] a) Kruk, M.; Jaroniec, M. *Chem. Mater.* **2001**, *13*, 3169. b) Corma, A.; Moliner, M.; Díaz-Cabañas, M. J.; Serna, P.; Femenia, B.; Primo, J.; García, H. *New J. Chem.* **2008**, *32*, 1338. c) Ispas, C.; Sokolov, I.; Andreescu, S. *Anal. Bioanal. Chem.* **2009**, *393*, 543.

[31] Carlsson, N.; Gustafsson, H.; Thörn, C.; Olsson, L.; Holmberg, K.; Åkerman, B. *Adv. Colloid Interface Sci.* **2014**, *205*, 339.

[32] Vallet-Regí, María; Colilla, Montserrat; Izquierdo-Barba, I. *J. Biomed. Nanotechnol.* **2008**, *4*, 1.

[33] Slowing, I. I.; Trewyn, B. G.; Giri, S.; Lin, V. S.-Y. *Adv. Funct. Mater.* **2007**, *17*,1225.

[34] a) Kilian, K. A.; Böcking, T.; Gaus, K.; Gal, M.; Gooding, J. J. *ACS Nano* **2007**, *1* (4), 355. b) Jane, A.; Dronov, R.; Hodges, A.; Voelcker, N. H. *Trends Biotechnol.* **2009**, *27* (4), 230.

[35] Davis, M. E.; Saldarriaga, C.; Montes, C.; Garces, J.; Crowdert, C. *Nature* **1988**, *331*, 698.

[36] Estermann, M.; McCusker, L. B.; Baerlocher, C.; Merrouche, A.; Kessler, H. *Nature* **1991**, *352*, 320.

[37] Moore, P. B.; Shen, J. *Nature* **1983**, *306*, 356.

[38] Kresge, C. T.; Leonowicz, M. E.; Roth, W. J.; Vartuli, J. C.; Beck, J. S. *Nature* **1992**, *359*, 710.

50 (with a lamellar structure).[39] Among this family of materials, MCM-41 and analogues are the most used for developing hybrid materials. The unique characteristics of MCM-41 such as homogeneous pore size (ranging from approximately 2 to 10 nm), a high pore volume (in the order of 1 $cm^3 g^{-1}$) and a very high specific surface area (between 500 and 1000 $m^2 g^{-1}$) brought to its use in wide range of applications. Moreover, those materials are featured by high chemical inertness and thermal stability. It is worth noting that the synthetic procedure to obtain MCM-41 is quite simple and requires inexpensive and nonhazardous precursors.

The peculiarity of presenting all the characteristics mentioned above makes these materials ideal supports for adsorption processes of relatively small molecules and enables them to be suitable platforms for the preparation of molecular recognition or switching systems for controlled release protocols and sensing applications (*vide infra*).

1.4.1.1 *Synthesis of mesoporous silica materials*

Silica (as well as alumina) mesoporous materials have been widely investigated with the aim of obtaining ordered materials with larger pores than those found in microporous zeolites. The usual method for building up a system that presents a high ordered mesoporous structure with homogeneous pore dimensions required two main components:

- A *template* acting as structure-directing agent of the porous network.

[39] Beck, J. S.; Vartuli, J. C.; Roth, W. J.; Leonowicz, M. E.; Kresge, C. T.; Schmitt, K. D.; Chu, C. T. W.; Olson, D. H.; Sheppard, E. W.; McCullen, S. B.; Higgins, J. B.; Schlenker, J. L. *J. Am. Chem. Soc.* **1992**, *114*, 10834.

- A *polymeric precursor* able to self-organize around the template and, upon polymerization, build up the final rigid structure.

In the case of silica based scaffolds generally a surfactant (able to form a micellar structure) is used as template and tetraethyl- (TEOS) or tetramethylorthosilica (TMOS) are usually used as silica precursors. As reported above, the adjective mesoporous refers to a pore diameter between 2-50 nanometers and does not consider the phase of the final mesoporous ordered network. Depending on factors such as concentration and dimensions of the surfactant, temperature, pH solution, ionic force, etc. different shaped materials can be obtained according to the aggregation of the micelles. The second aspect that can be controlled deals with the dimensions of the final pores. In this case the longer the hydrophobic surfactant cue the bigger the final pore, because the intermediate micelle will present bigger size. This last statement has some limitation because if the surfactant hydrophobic cue is too long a bilayer or a vesicle could be formed and this does not allows obtaining the desired template for the preparation of a mesoporous material. Once obtained the surfactant-based template the silica precursor is added to the reaction mixture. In the correct conditions of pH and temperature the polymerization reaction takes place around the template giving origin to a *high ordered periodic porous net*. The final step is the elimination of the surfactant by aerobic calcinations or adequate solvent extraction.

Researchers have described two different mechanisms, involved on the formation process of these composite materials. In the first one, named as True Liquid-Crystal Templating (TLCT) mechanism, the concentration of the surfactant is very high and, as a consequence, a lyotropic liquid-crystalline phase is formed without requiring the presence of the precursor of the

inorganic framework.[40] The other mechanism considers that liquid-crystalline phase is formed even at lower concentrations of surfactant molecules, for example, in a cooperative self-assembly of the template molecules and the added inorganic species.[41]

Using this procedure, the original approach has been extended by a number of variations. As an example, the use of tri-block copolymer templates under acidic conditions was employed to prepare the so-called SBA (Santa Barbara Amorphous) silica phases,[42] whereas the use of cationic surfactants, such as hexadecyltrimethylammonium bromide (CTAB) was originally used in the synthesis of the first M41S materials, obtaining the hexagonal (MCM-41), the cubic (MCM-48) and lamellar (MCM-50) forms cited above.

Perhaps, the most famous, widely-studied and best known silica-based mesoporous inorganic scaffold is MCM-41. The first step of the synthesis consists in the preparation of the template for the attainment of the final hexagonal mesoporous phase (see figure 9). To obtain this template a water solution of CTAB is prepared. Thus, as reported above, in the correct conditions of temperature, pH and concentration the surfactant firstly self-organizes into micelles and secondly micelles give origin to hexagonal shaped supra-micellar aggregates. Once obtained the required template, the polymeric precursor (TEOS) is added to the solution and, at basic pH, it polymerizes around the template giving rise to the final mesoporous scaffold with its pores full of surfactant. This is a critical step, because depending on certain reaction parameters (temperature, polymeric precursor

[40] Attard, G. S.; Glyde, J. C.; Göltner, C. G. *Nature* **1995**, *378*, 366.

[41] Monnier, A.; Schuth, F.; Huo, Q.; Kumar, D.; Margolese, D.; Maxwell, R. S.; Stucky, G. D.; Krishnamurty, M.; Petroff, P.; Firouzi, A.; Janicke, M.; Chmelka, B. F. *Science* **1993**, *261* , 1299.

[42] a) Zhao, D. *Science* **1998**, *279*, 548. b) Zhao, D.; Huo, Q.; Feng, J.; Chmelka, B. F.; Stucky, G. D. *J. Am. Chem. Soc.* **1998**, *120*, 6024.

concentration and reaction time) the particle morphology can be tuned from micrometric and heterogeneous particles to create various forms, including thin films, spherical nanoparticles or monoliths.[43] Final step consists in, as explained before, removal of surfactant by aerobic calcination or by extraction with adequate solvents obtaining the final mesoporous inorganic scaffold. The obtained material presents cylindrical unidirectional empty channels arranged in a hexagonal distribution. Using CTAB as template a pore size of approximately 2-3 nm of diameter is obtained.

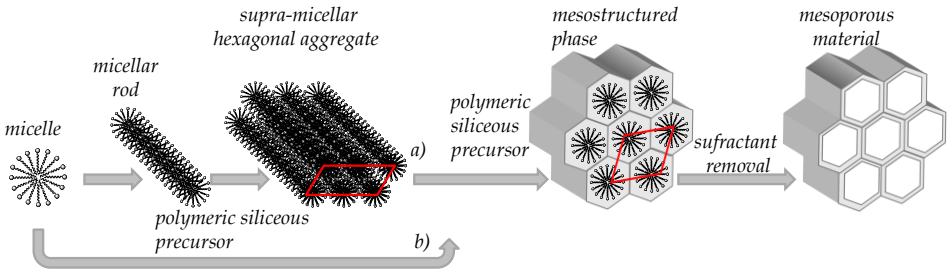

Figure 9. Schematic representation of MCM-41 template synthesis: a) true liquid-crystal template mechanism: the liquid crystal phase is intact before the inorganic precursor is added. b) cooperative liquid-crystal mechanism, where addition of the inorganic precursor mediates the ordering of the surfactant micelles.

The principal advantage of this synthetic method is that the high grade of homogeneity of the initial elements is transmitted to the final material, showing a system of pores not only homogeneous in size but also in form and regularity.

[43] a) Chan, H. B. S.; Budd, P. M.; Naylor, T. deV. *J. Mater. Chem.* **2001**, *11*, 951. b) Cai, Q.; Luo, Z.-S.; Pang, W.-Q.; Fan, Y.-W.; Chen, X.-H.; Cui, F.-Z. *Chem. Mater.* **2001**, *13*, 258. c) Huh, S.; Wiench, J. W.; Yoo, J.-C.; Pruski, M.; Lin, V. S.-Y. *Chem. Mater.* **2003**, *15*, 4247. d) Naik, S. P.; Fan, W.; Yokoi, T.; Okubo, T. *Langmuir* **2006**, *22*, 6391. e) Kobler, J.; Möller, K.; Bein, T. *ACS Nano* **2008**, *2*, 791.

1.4.1.2 *Functionalization of mesoporous silica materials*

The further step toward the preparation of organic-inorganic hybrid materials is the functionalization of the inorganic silica-based mesoporous scaffold. As commented before, silica can be easily functionalized taking advantage of the high concentration of structural defects in the form of silanol (Si-OH) groups present in its surface. These silanols can easily react with trialkoxysilane derivatives ($(R'O)_3$-Si-R) to give a nucleophilic substitution reaction and generate organic−inorganic nanocomposites. The features of these hybrid materials can be finely tuned taking into account the chemical nature of the functional groups contained on the selected tritalkoxyslane. This functionalization endow the hybrid materials with specific capabilities. In addition, the anchored groups can contain one or more reactive atoms, which can be later chemically modified on the surface of the scaffold. Three main procedures for the synthesis of the organic-inorganic mesoporous hybrid materials have been described: [44]

- ***grafting procedure***: This procedure was briefly described for the functionalization of planar silica surfaces in the past section. As a postsynthetic method requires the surfactant to be removed before functionalization. By the way, this technique present the potential advantage (depending on the application seeked) of functionalizing preferentlly the outer surface of the material and the pore entrances (see figure 10). In fact, bearing in mind the distribution of the reactive silanols group in the mesoporous scaffold, the trialkoxysilane derivatives have a preference to react with the silanol (Si-OH) groups most accessible. Therefore, the organosilanes react preferentially at

[44] Vinu, A.; Hossain, K. Z.; Ariga, K. *J. Nanosci. Nanotechnol.* **2005**, *5*, 347.

the pore openings during the initial stages of the synthetic process, and the diffusion of further molecules into the inner surface of the pores can be impaired. This lead to a non-homogeneous distribution of the organic groups with the pores having a lower degree of functionalization.

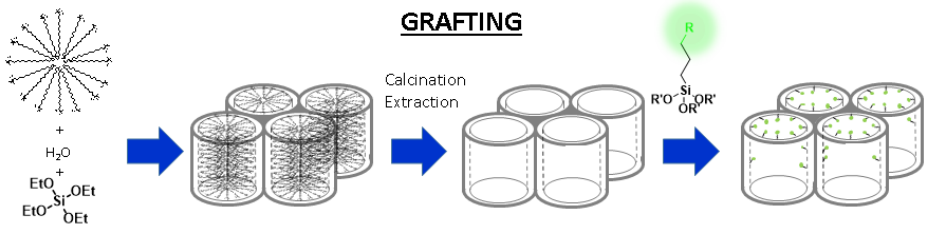

Figure 10. Schematic representation of functionalization of MCM-41 skeleton through grafting procedure

- ***co-condensation procedure***: This procedure consists in the simultaneous condensation of silica and organosilica precursors. Stein and coworkers achieved the formation of an organic monolayer of 3-mercaptopropyl groups inside of the pores of MCM-41, as shown in figure 11, in a work considered the first example of co-condensation functionalization of the MCM-41 inorganic scaffold.[45] In this case, in basic hydrolytic conditions, trialkoxysilane precursors react rapidly with the oligomeric silane (TEOS) to form the final frame structure, in which the organic groups R are bonded to silicon atoms of the inorganic scaffold wall and can therefore interact with

[45] Lim, M. H.; Blanford, C. F.; Stein, A. *Chem. Mater.* **1998**, *10*, 467.

chemical species eventually present inside the pores. In this case the final extraction of the surfactant can not be performed by aerobic calcination, because this procedure would lead to the oxidative degradation of the organic groups. Thus, the common procedure in this case to eliminate the surfactant template is by liquid extraction.

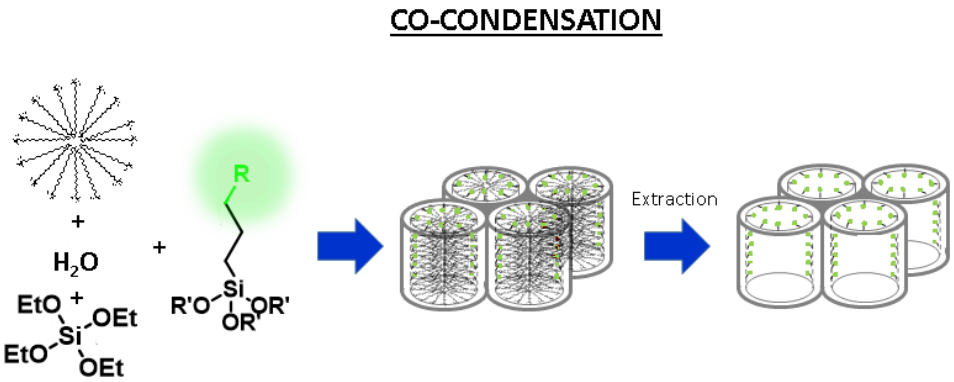

Figure 11. Schematic representation of co-condensation synthetic procedure for MCM-41.

The co-condensation method usually leads to a homogeneous distribution of the trialkoxysilane derivatives along the material particles and between the surface thereof and the inner surface corresponding to the channels and cavities. Moreover, the co-condensation method allows the incorporation of a relatively large amount of functional groups.

- **Periodic Mesoporous Organosilicas (PMOs):** Another way to incorporate organic compounds onto silicas is the production of PMOs. The preparation of these materials requires a procedure similar to co-condensation but using bridging bis-silylated trialkoxysilane agents. This procedure allows to incorporate organic groups as components of the material structure by the use of single-

source organosilica precursors (see figure 12). First example of PMOs was discovered by three independent groups at the same year.[46]

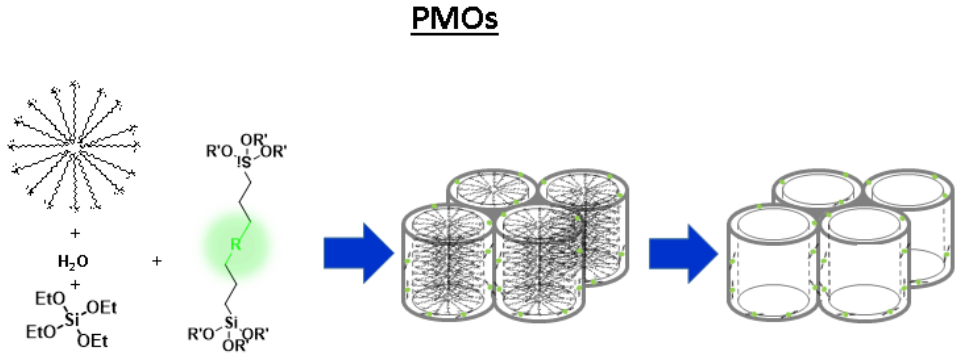

Figure 12. Schematic representation of PMOs formation.

These materials can have large inner surface areas (up to 1800 $m^2\ g^{-1}$) as well as high thermal stability but generally exhibit completely disordered pore systems.[47]

The grafting method is the most commonly used because of the existence of several practic problems related to the co-condensation and PMOs synthesis. For example, the degree of mesoscopic order of the final materials decreases when concentration of the organic silane increases. Moreover, in co-condensation procedures, the incorporated organic groups can lead to a reduction in the pore diameter, pore volume, and specific surface areas. In addition, almost only extractive methods can be used to remove the template in these cases.

[46] a) Ozin, G. A.; Asefa, T.; MacLachlan, M. J.; Coombs, N. *Nature 402*, 867. b) Melde, B. J.; Holland, B. T.; Blanford, C. F.; Stein, A. *Chem. Mater.* **1999**, *11*, 3302. c) Inagaki, S.; Guan, S.; Fukushima, Y.; Ohsuna, T.; Terasaki, O. *J. Am. Chem. Soc.* **1999**, *121*, 9611.

[47] Hatton, B.; Landskron, K.; Whitnall, W.; Perovic, D.; Ozin, G. A. *Acc. Chem. Res.* **2005**, *38*, 305.

1.5 Gated Materials[48]

Mesoporous silica materials described above are the most common scaffolds for developing molecular gated hybrid solids, also known as **gated materials**. These kind of hybrid supports have attracted the attention of researchers from several fields. Gated materials are constructed for the purpose of finely tune the movement of chemical or biochemical species from voids of porous supports to a solution, and vice versa, in response to a predefined stimulus. Taking into account this concept, several research groups have been involved in the synthesis and characterization of imaginative nanodevices in which the delivery of a certain cargo stored in a container can be triggered by applying selected external stimulus. Such gated materials are composed mainly of two subunits: (i) a porous inorganic support in which a cargo is loaded and (ii) certain molecular or supramolecular entities, generally grafted onto the external surface, which can control mass transport from pores (see Figure 13). When dealing with the inorganic support, one of the most commonly used materials for preparing gated nanodevices is mesoporous solids. Mesoporous supports can be prepared in different forms that range from micrometric to nanometric, and have tailor-made pores (2-10 nm in diameter) and a very large specific surface areas (up to 1200 m^2 g^{-1}).[49] Given these remarkable features, mesoporous materials have a huge loading capacity and can store not only small but also a wide variety of medium-sized molecules such as proteins, oligonucleotides and nucleic acids. These supports are also

[48] Aznar, E.; Oroval, M.; Pascual, L.; Murguía, J. R.; Martínez-Máñez, R.; Sancenón, F *Chem. Rev.* **2016**, *116*, 561. *Reprinted (adapted) with permission of Chemical Reviews. Copyright © 2016 American Chemical Society.*

[49] a) Valtchev, V.; Tosheva, L. *Chem. Rev.* **2013**, *113*, 6734. b) Stein, A. *Adv. Mater.* **2003**, *15*, 763.

chemically inert under a wide range conditions and are easily functionalized using well-known chemistries.[50] Another key point when designing such gated nanodevices is the selection of gating entities. In line with this, imaginative molecular and supramolecular concepts have been developed to allow the controlled release of a wide range of entrapped cargos. There is a long list of clever approaches, where the driving force to switch gating mechanisms between an open state and a closed state take advantage of electrostatic or supramolecular interactions, the rupture/formation of covalent bonds, or changes in the physical properties of molecules or macromolecules.[51] Different used stimuli to trigger guest release are; light, temperature, alternating magnetic fields (AMF), ultrasounds, redox chages, pH modulations, the presence of (bio)molecular and enzymes.

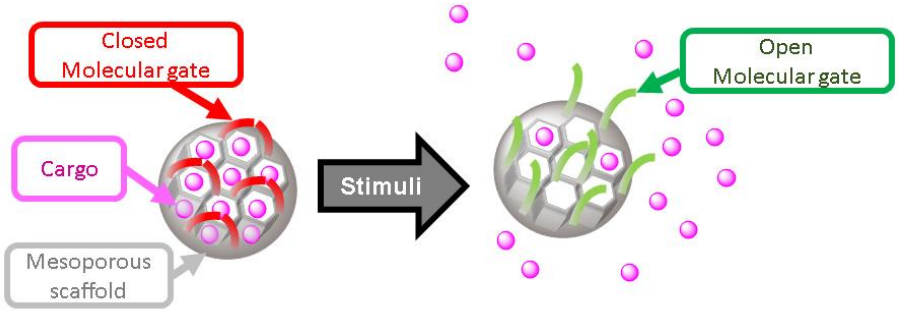

Figure 13. Schematic representation of a molecular gate for on-command controlled release.

[50] a) Soler-Illia, G. J. A. A.; Azzaroni, O. *Chem. Soc. Rev.* **2011**, *40*, 1107. b) Fuchs, A. V; Kotman, N.; Andrieu, J.; Mailaender, V.; Weiss, C. K.; Landfester, K. *Nanoscale* **2013**, *5*, 4829. c) Kickelbick, G. *Angew. Chemie Int. Ed.* **2004**, *43*, 3102.

[51] a) Saha, S.; Leung, K. C. F.; Nguyen, T. D.; Stoddart, J. F.; Zink, J. I. *Adv. Funct. Mater.* **2007**, *17*, 685. b) Angelos, S.; Johansson, E.; Stoddart, J. F.; Zink, J. I. *Adv. Funct. Mater.* **2007**, *17*, 2261. c) Wang, F.; Liu, X.; Willner, I. *Angew. Chem. Int. Ed. Engl.* **2015**, *54*, 1098. d) Song, N.; Yang, Y.-W. *Chem. Soc. Rev.* **2015**, *44*, 3474. e) Wang, G.; Zhang, J. *J. Photochem. Photobiol. C Photochem. Rev.* **2012**, *13*, 299. e) Braunschweig, A. B.; Northrop, B. H.; Stoddart, J. F. *J. Mater. Chem.* **2006**, *16*, 32. f) Trewyn, B. G.; Giri, S.; Slowing, I. I.; Lin, V. S.-Y. *Chem. Commun.* **2007**, *114*, 3236. g) Aznar, E.; Martínez-Máñez, R.; Sancenón, F. *Expert Opin. Drug Deliv.* **2009**, *6*, 643. h) Park, C.; Kim, H.; Kim, S.; Kim, C. *J. Am. Chem. Soc.* **2009**, *131*, 16614. i)Yang, Y.-W. *Medchemcomm* **2011**, *2*, 1033.

Gated nanochemistry has demonstrated the possibility of achieving new advanced pre-designed functions by means of mass transport control. The most studied application of such systems is related with controlled release protocols especially devoted to potential biomedical applications.[52] Such gated materials have also been used to develop new sensing/recognition protocols.[53] A few examples have also been reported for other applications. Nevertheless, many studies conducted to date are limited to the simple design of gated materials and there are a number of potential applications still to be explored.

The application of gated materials in the biomedical field has been boosted in the last few years because these systems allow the release of one or several drugs upon the application of external stimuli, and are promising candidates for developing new therapies to improve efficacy and safety. Moreover, anchoring biological receptors (e.g. antibodies, peptides, aptamers, carbohydrates) onto an external surface allows targeted delivery of drugs to sites such as cells and tissues that contain over-expressed receptors.[54]

[52] a) Barreto, J. A.; O'Malley, W.; Kubeil, M.; Graham, B.; Stephan, H.; Spiccia, L. *Adv. Mater.* **2011**, *23*, H18. b) Stark, W. J. *Angew. Chemie Int. Ed.* **2011**, *50*, 1242. c) Li, Z.; Barnes, J. C.; Bosoy, A.; Stoddart, J. F.; Zink, J. I. *Chem. Soc. Rev.* **2012**, *41*,, 2590. d) Doane, T. L.; Burda, C. *Chem. Soc. Rev.* **2012**, *41*, 2885.

[53] a)Coll, C.; Bernardos, A.; Martínez-Máñez, R.; Sancenón, F. *Acc. Chem. Res.* **2013**, *46*, 339. b) Sancenón, F.; Pascual, L.; Oroval, M.; Aznar, E.; Martínez-Máñez, R. *ChemistryOpen* **2015**, 4, 418.

[54] a) Lu, C. H.; Willner, B.; Willner, I. *ACS Nano* **2013**, *7*, 8320. b) Koutsopoulos, S. *Adv. Drug Deliv. Rev.* **2012**, *64*, 1459. c) Chen, Y.; Chen, H.; Shi, J. *Adv. Mater.* **2013**, *25*, 3144. d) He, Q.; Shi, J. *Adv. Mater.* **2014**, *26*, 391. e) Vallet-Regí, M.; Ruiz-Hernández, E. *Adv. Mater.* **2011**, *23*, 5177. e) Taylor-Pashow, K. M. L.; Della Rocca, J.; Huxford, R. C.; Lin, W. *Chem. Commun.* **2010**, *46*, 5832. f) Bitar, A.; Ahmad, N. M.; Fessi, H.; Elaissari, A. *Drug Discov. Today* **2012**, *17* , 1147. g) Rosenholm, J. M.; Peuhu, E.; Bate-Eya, L. T.; Eriksson, J. E.; Sahlgren, C.; Linden, M. *Small* **2010**, *6*, 1234. h) Ang, C. Y.; Tan, S. Y.; Zhao, Y. *Org. Biomol. Chem.* **2014**, *12*, 4776. i) Manzano, M.; Vallet-Regí, M. *Prog. Solid State Chem.* **2012**, *40*, 17.

Dealing with the application of gated material in sensing/recognition protocols, the key point is to prepare systems capable of responding specifically to a certain target molecule which could modulate delivery of an indicator (e.g. dye or fluorophore).[54b] The recognition protocol which uses these "gated materials" clearly differs from the classic supramolecular "binding site-signaling subunit" paradigm because it detaches the recognition event from the signaling step. This makes signaling independent of the host-guest stoichiometry and sometimes allows signal amplification.[55] Additionally, the approach is highly flexible given the possible selection of different porous supports, distinct selective binding sites and a wide range of indicator molecules.

Despite of drug delivery and sensing are largely the most exploited fields, gated materials are capable of much more. One raising application is using them for *in vivo* imaging diagnostic techinques. It can be done via loading and release of imaging agents or via incorporating these agents embedded or grafted onto the material. In the first case, the most common strategy is to follow the release of a fluorescent drug or marker. In the second, other techniques such as Magnetic Resonance Imaging (MRI) can be used incorporating paramagnetic elements to the porous material. Moreover, certain biological receptors are grafted onto the external surface for targeting purposes. These nanodevices are capable of targeting selected cells or tissues to avoid the premature degradation of the entrapped cargo, and also facilitate the transfer of the payload across the cell membrane. Presence of markers also allows the release process and the accumulation of the gated nanodevice in target tissues to be traced in real time. [56] These

[55] Martinez-Manez, R.; Sancenon, F.; Hecht, M.; Biyikal, M.; Rurack, K. *Anal. Bioanal. Chem.* **2011**, *399*, 55.

[56] a) Ambrogio, M. W.; Thomas, C. R.; Zhao, Y.-L.; Zink, J. I.; Stoddart, J. F. *Acc. Chem. Res.* **2011**, *44* , 903. b) Xie, J.; Lee, S.; Chen, X. *Adv. Drug Deliv. Rev.* **2010**, *62*, 1064. c) Rai, P.; Mallidi, S.; Zheng,

materials, combined with drug delivery capabilities, reveals a new approach with great potential impact in biomedicine: the mixing of specific therapeutic systems with advanced diagnostic techniques (**theranostic** nanodevices).

X.; Rahmanzadeh, R.; Mir, Y.; Elrington, S.; Khurshid, A.; Hasan, T. *Adv. Drug Deliv. Rev.* **2010**, *62*, 1094. d) Rosenholm, J. M.; Sahlgren, C.; Linden, M. *Curr. Drug Targets* **2011**, *12*, 1166. e) Rosenholm, J. M.; Sahlgren, C.; Linden, M. *Nanoscale* **2010**, *2*, 1870. f) Fu, L. B.; Zhuang, J. Y.; Lai, W. Q.; Que, X. H.; Lu, M. H.; Tang, D. P. *J. Mater. Chem. B* **2013**, *1*, 6123. g) Chen, Y.-C.; Huang, X.-C.; Luo, Y.-L.; Chang, Y.-C.; Hsieh, Y.-Z.; Hsu, H.-Y. *Sci. Technol. Adv. Mater.* **2013**, *14*, 44407.

1.5.1 Drug delivery applications of gated materials

In terms of number of publications, drug delivery systems are the principal application of these gated materials. High loading capacity for storage a large amount of drug, its easy functionalization with biodirecting agents and a great variety of stimuli to selectively open and release the cargo makes gated materials an ideal candidate for targeted therapies (see figure 14).

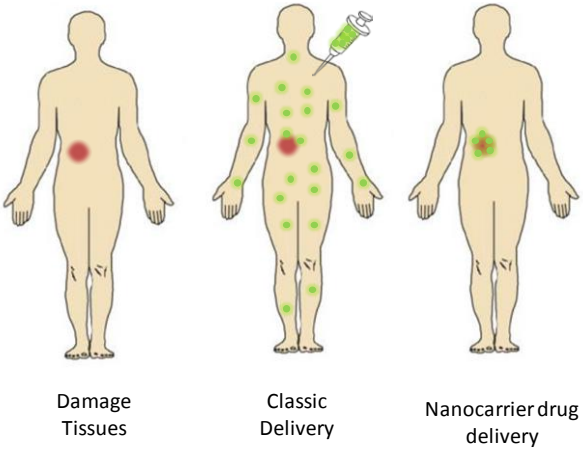

Figure 14. Scheme of ideal targeted drug delivery compared with classic delivery of drugs.

Stimuli used to activate drug delivery can be divided as internal if the system takes advantage of a biological process for the release (i.e. overexpression of a enzyme, pHs changes in the targeted area, molecular recognition by antibodies or aptamers, presence of redox active biomolecules, etc) or external if the strategy consists in apply several techniques to induce the release on a specific region in a specific moment (i.e. light irradiation, application of alternate magnetic fields, ultrasounds, etc). Another way to classify these systems is via their opening mechanism. Some of them acts as a nanovalves that produce the release via a conformational

change of the molecular gate (reversible opening) and others requires the deattachment of a blocking agent via the rupture of a covalent bond or another intermolecular force (irreversible opening). Main difference resides in the fact that nanovalves release can be reverted and stopped (allowing the possibility of an on-command dosage) while in the second group the process becomes irreversible.

1.5.1.1 *Reversible drug delivery systems (nanovalves)*

The first example of a gated material, based on the use of the photodimerization of coumarin, was developed by Fujiwara and co-workers in 2003. Coumarin undergoes a [2+2] photodimerization in which there is a cycloaddition reaction that involves carbon-carbon double bonds of two neighboring molecules to result in a cyclobutane dimer.[57] Photodimerization is performed in the presence of light and is, in most cases, a reversible process that can be controlled by selecting the irradiation wavelength. The gate of Fujiwara's work consisted in 7-[(3-triethoxysilyl)propoxy]coumarin groups attached to an MCM-41 support. The pores of the coumarin-functionalized hybrid material were loaded with selected cargos (phenanthrene, cholestane and progesterone), and were then capped by irradiation with > 310 nm light that triggered the photodimerization process as depicted in Figure 15. Capped solids showed no cargo release, however, when the system was irradiated with 250 nm UV-light pore opening, and cargo release was observed. Later in 2010, coumarin was also used as a gate on mesoporous bioactive glasses.[58] The authors loaded the pores of

[57] a) Mal, N. K.; Fujiwara, M.; Tanaka, Y. *Nature* **2003**, *421*, 350. b) Mal, N. K.; Fujiwara, M.; Tanaka, Y.; Taguchi, T.; Matsukata, M. *Chem. Mater.* **2003**, *15*, 3385.

[58] Lin, H. M.; Wang, W. K.; Hsiung, P. A.; Shyu, S. G. *Acta Biomater.* **2010**, *6*, 3256.

mesoporous bioactive glasses with phenanthrene and pore outlets were functionalized with a coumarin derivative. When *n*-hexane suspensions of the material were irradiated with light of wavelength > 310 nm, negligible phenanthrene release was observed due to the formation of coumarin dimers, whereas irradiation with 250 nm light induced cargo release.

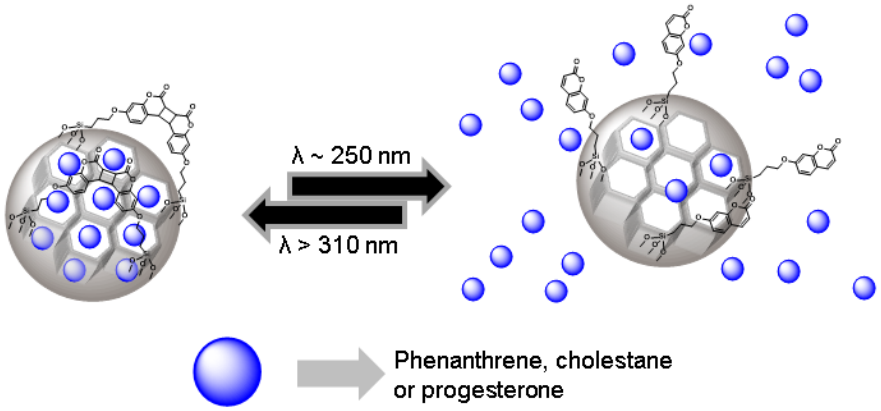

Figure 15. Scheme of the photo-driven nanovalve operated by coumarin dimerization using MSNs.

Song and coworkers developed a drug delivery system which used a co-polymer composed of *N*-isopropylacrylamide and methacrylic acid, used as cap (see Figure 16).[59] These two units conferred thermo- and pH-sensitive properties to the polymer, respectively. Mesoporous silica nanoparticles (MSNs) were selected as inorganic scaffolds and the outer surface was functionalized with methacryloxypropyl subunits. Then *N*-isopropylacrylamide and methacrylic acid were copolymerized on the external surface by seeded precipitation polymerization. Finally, fluorescein was loaded in mesopores. A second capped solid was obtained by attaching folic acid (FA) to the free carboxylic acid moieties of the polymeric chains via amide formation to improve cellular uptake. Delivery studies demonstrated

[59] Liu, X.; Yu, D.; Jin, C. S.; Song, X. W.; Cheng, J. Z.; Zhao, X.; Qi, X. M.; Zhang, G. X. *New J. Chem.* **2014**, *38*, 4830.

that cargo delivery was achieved when the temperature was raised over lower critical solution temperature (LCST) and in an acidic environment. The cellular uptake of both capped solids (with or without FA) was confirmed by confocal laser scanning microscopy (CLSM) in Hep2 cells and also by flow cytometry. When compared to A549 cells, a targeting effect to Hep2 cells was observed when the FA-functionalized capped MSNs were employed. Finally, the authors prepared two similar capped materials, but loaded with the anticancer drug cisplatin. Cell viability studies based on MTT assays were performed against Hep2 cells with free cisplatin and cisplatin loaded solids. Only a slight effect of the cisplatin was noted when using the solid without FA moieties, but evident cell death enhancement was achieved when the FA-functionalized cisplatin-loaded nanoparticles were used. Finally, the effects on tumor growth on Hep2-tumor bearing nude mice resulted in the same tendency as that observed in cell viability studies.

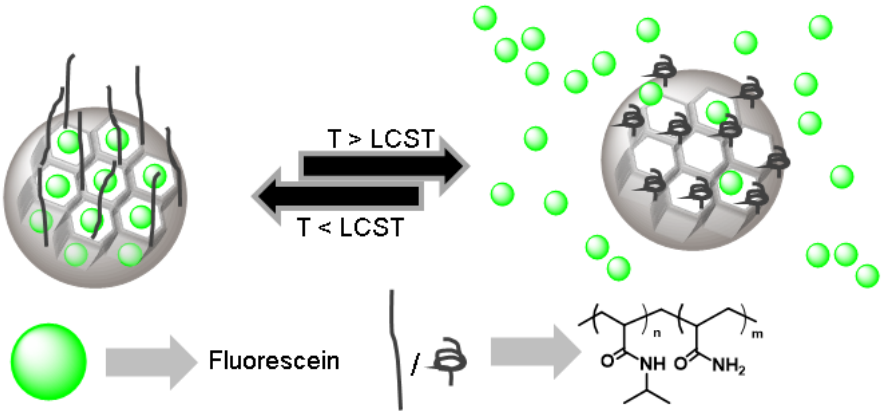

Figure 16. Scheme of a polymer-capped nanovalve operated by thermal phase transition using MSNs.

First example that used rotaxanes coupled with a redox reaction to design gated materials was reported by Stoddart, Zink and coworkers. These authors prepared MSNs loaded with $Ir(ppy)_3$ and functionalized the surface with a dinitrophenyl (DNP) derivative. Pores were capped by the formation

of an inclusion complex between the DNP derivative and cyclobis(paraquat-*p*-phenylene) ($CBPQT^{4+}$). Reduction of $CBPQT^{4+}$ by $NaCNBH_3$ resulted in the rupture of the complex and the release of the entrapped dye.[60]

Later the same authors designed a more complex system in which the $CBPQT^{4+}$ ring was able to move between a tetrathiafulvalene (TTF) station and a DNP moiety, both separated by an oligoethyleneglycol chain that incorporated a rigid terphenylene spacer.[61] In this supramolecular ensemble, the cyclophane has a preference for the TTF unit, but the oxidation of TTF by using $Fe(ClO_4)_3$ to give a TTF^{2+} dication promoted the movement of the $CBPQT^{4+}$ ring to the DNP station. When ascorbic acid was added, the TTF^{2+} unit was reduced back to the neutral TTF, which induced the return of the $CBPQT^{4+}$ ring to the TTF group (see Figure 17). This bistable[2]rotaxane unit was anchored to the MSNs via the formation of a carbamate between the hydroxyl group in the [2]rotaxane and isocyanate moieties on the silica support. The material was loaded with $Ir(ppy)_3$ or rhodamine B. The release kinetics of the gating system was performed in a PhMe:EtOH (1:1) solution (for the iridium complex) and in MeCN for rhodamine B. To complete the study, the authors synthesized another hybrid material that contained the dumbbell part of the [2]rotaxane, but without the $CBPQT^{4+}$ ring. This second material was unable to control rhodamine B release, which was delivered to the solution immediately. These results confirmed the vital role of $CBPQT^{4+}$ ring motion to control the transport of guest molecules from the pore voids to the solution.

[60] Hernandez, R.; Tseng, H. R.; Wong, J. W.; Stoddart, J. F.; Zink, J. I. *J. Am. Chem. Soc.* **2004**, *126*, 3370.

[61] Nguyen, T. D.; Tseng, H. R.; Celestre, P. C.; Flood, A. H.; Liu, Y.; Stoddart, J. F.; Zink, J. I. *Proc. Natl. Acad. Sci. U. S. A.* **2005**, *102*, 10029.

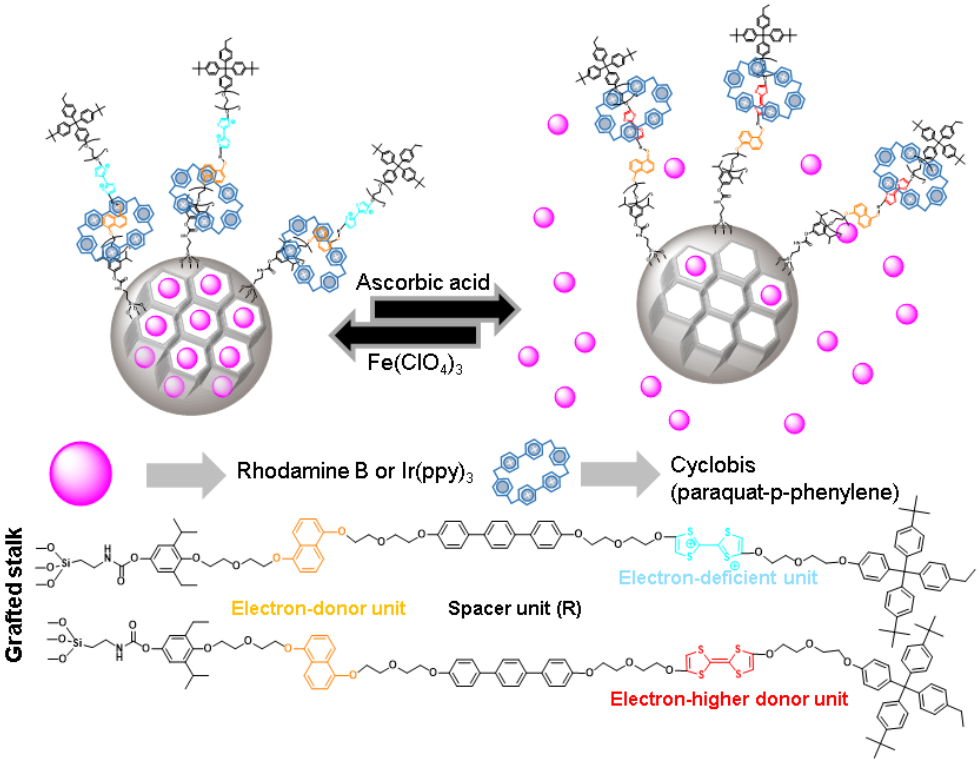

Figure 17. Scheme of a bistable[2]rotaxane capped nanovalve operated by redox agents using MSNs (spacer units are simplifacated as R).

1.5.1.2 *Irreversible drug delivery systems*

In a complete work, *Lin et al.* prepared capped MSNs and studied their use for DNA and drug co-delivery into plants.[62] In a first attempt, the external surface of MSNs was functionalized with mercaptopropyl moieties. The resulting thiol groups were reacted with 2-(pyridyldisulfanyl) ethylamine and then fluorescein isothiocyanate (FITC) was used for labeling MSNs by urea bond formation. Afterward a layer of triethyleneglycol was anchored to improve the biocompatibility and suspendability of MSNs (see

[62] Torney, F.; Trewyn, B. G.; Lin, V. S. Y.; Wang, K. *Nat. Nanotechnol.* **2007**, *2*, 295.

Figure 18). A DNA plasmid that contained a green fluorescent protein gene was used for coating the solid on the triethyleneglycol layer, and its capability for gene transfection was successfully tested in protoplasts. However, the described nanoparticles proved useless for gene transfection in plant tissues by a gene gun system. Thus in another step, a different material was prepared using MSNs grafted with MPTS and reacted with 2-(pyridyldisulfanyl) ethylamine. Instead of labeling with FITC, MSNs were loaded with fluorescein and capped with AuNPs coated with 11-mercaptoundecanoic acid through the formation of amide bonds. Anchored AuNPs were coated with the DNA plasmid. These new materials were successfully tested in tissue plants by gene gun techniques. DNA plasmid internalization produced green fluorescent protein (GFP)-expressing foci and was viewed on tobacco cotyledons bombarded with the system. Fluorescein delivery was also observed given the reduction of disulfide bonds by dithiothreitol (DTT). Similar results were obtained when maize immature embryos were bombarded with the nanomaterial. A third solid was obtained in the same way as the previous one, but was loaded with β-oestradiol. This solid was tested in transgenic tobacco plants in which GFP expression could be detected only if β-oestradiol was present. As expected, the GFP signal was detected in the transgenic seeds germinated in DTT-containing media, which opened the gate by reducing the chemical linker to thus release the GFP inducer and the required cargo. These results demonstrated the interaction between the cargo inside MSNs and the DNA coated on AuNPs.

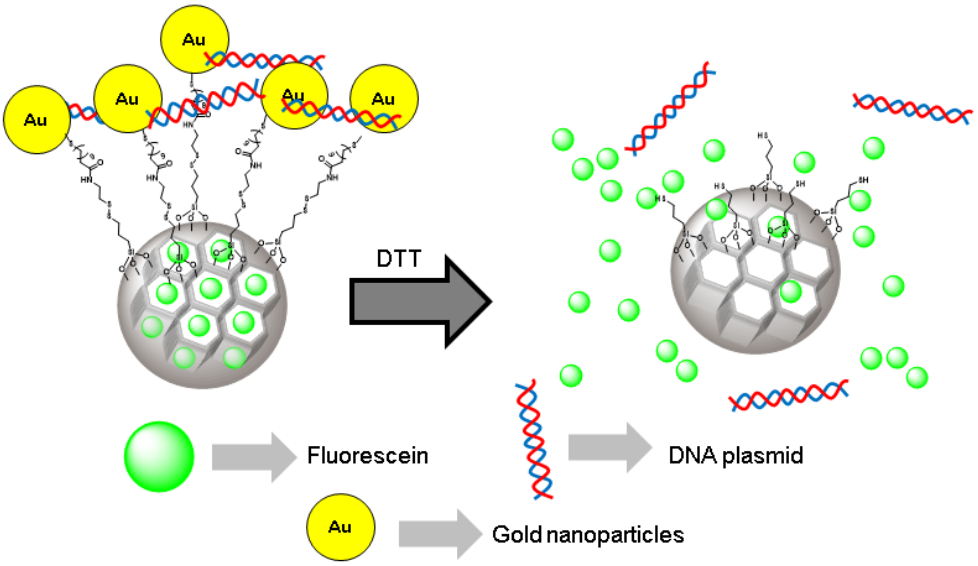

Figure 18. Scheme of a drug and DNA plasmid co-delivery sytem operated by redox agents using MSNs capped with AuNPs.

Xu et al. prepared Hollow MSNs using chitosan as cap, which was anchored to the silica surface via a reaction with (3-glycidyloxypropyl)trimethoxysilane.[63] These authors loaded pores with bovine serum albumin (BSA). Phosphate buffer saline (PBS) suspensions of loaded nanoparticles at pH 7.4 showed poor BSA release (17.4% of the entrapped protein after 100 h). However at an acidic pH (4), clear cargo delivery took place. For the *in vitro* cellular studies, the same nanoparticles were prepared, but were loaded with tumor necrosis factor α (TNF-α) instead of BSA. Antibody ab2428 (that can bind to antigen ErbB 2) was conjugated with the chitosan polymer. After conjugating the antibody (to ErbB 2) to capped MSNs, nanocarriers exhibited good performance in delivering TNF- α to MCF-7 breast cancer cells in both *in vitro* and *in vivo* (nine 3-week-old athymic nude mice). The high affinity between the

[63] Deng, Z.; Zhen, Z.; Hu, X.; Wu, S.; Xu, Z.; Chu, P. K. *Biomaterials* **2011**, *32*, 4976.

antibody and the antigen directed the system to achieve targeted delivery to cancer cells. Due to the acidic micro-environment inside solid tumors, the loaded TNF- α was gradually released from nanocarriers, which triggered apoptosis in tumor cells.

The first enzyme-driven gated MSNs, described by Zink, Stoddart and coworkers, used an esterase as a trigger.[64] These authors encircled α-CDs within polyethylene glycol (PEG) stalks anchored to MSNs, and further attached to stalks an ester-linked adamantly bulky stopper to retain α-CDs and to effectively block pores. The capped system was loaded with rhodamine B. Cargo delivery was achieved only in the presence of porcine liver esterase, which was able to hydrolyze the ester group resulting in the removal of the adamantly moiety. This allowed the dethreading of α-CDs and the subsequent cargo delivery. As control experiments, the authors synthesized a similar system which contained an amide-linked adamantyl stopper that was unable to be cleaved by esterase. In another work,[65] these authors used the same molecular gate in a novel hierarchically structured material consisting of micro-patterned mesoporous silica films, prepared by vapor-phase infiltration by a reactive wet-stamping technique.

Martínez-Máñez and coworkers reported the first example of silica nanoparticles capped with "saccharide" derivatives. In this work,[66] MSNs were loaded with $Ru(bipy)_3^{2+}$ and gated with a covalently anchored lactose derivative. Dye delivery from the aqueous suspensions of the lactose-capped material was negligible due to the formation of a dense disaccharide network, in which lactose groups were most likely linked through hydrogen-

[64] Patel, K.; Angelos, S.; Dichtel, W. R.; Coskun, A.; Yang, Y. W.; Zink, J. I.; Stoddart, J. F. *J. Am. Chem. Soc.* **2008**, *130*, 2382.

[65] Klichko, Y.; Khashab, N. M.; Yang, Y. W.; Angelos, S.; Stoddart, J. F.; Zink, J. I. *Microporous Mesoporous Mater.* **2010**, *132*, 435.

[66] Bernardos, A.; Aznar, E.; Marcos, M. D.; Martinez-Manez, R.; Sancenon, F.; Soto, J.; Barat, J. M.; Amoros, P. *Angew. Chemie-International Ed.* **2009**, *48*, 5884.

bonding interactions around pore outlets. Addition of β-D-galactosidase enzyme induced progressive cargo release, which was clearly related to the enzymatic hydrolysis of the glycosidic bond in disaccharide.

In a further work, the same authors prepared MSNs loaded with rhodamine B and functionalized the external surface with an alkylgluconamine derivative of a galacto-oligosaccharide polymer (GOS).[67] *In vitro* assays demonstrated that the capped material showed no cargo delivery, but opened in the presence of β-galactosidase (see Figure 19) due to the selective hydrolysis of the GOS cap. Moreover, the performance of the GOS-capped nanoparticles *in vitro* was also studied for the potential targeting of senescent cells, in which β-galactosidase is known to be overexpressed. For instance, when GOS nanoparticles were incubated with yeast cells, rhodamine B staining was observed only in the β-galactosidase overexpressing strains, which indicated that the molecular gate actually worked *in vitro*. It was found that GOS-capped MSNs were also selectively opened in human senescent fibroblasts from X-linked Dyskeratosis Congenita (X-DC) patients, in which β-galactosidase was overexpressed. Remarkably, no emission was detected in lung carcinoma H460 cells (in which β-galactosidase was not overexpressed), not even after 48 h. Cell viability remained unaffected in H460 and X-DC cells. The authors suggested that by choosing an appropriate cargo (a telomerase reactivation drug or a cytotoxic drug), the prevention and removal/replacement of senescent cells could be possible, which thus opens up new avenues for managing age-related diseases.

[67] Agostini, A.; Mondragon, L.; Bernardos, A.; Martinez-Manez, R.; Marcos, M. D.; Sancenon, F.; Soto, J.; Costero, A.; Manguan-Garcia, C.; Perona, R.; Moreno-Torres, M.; Aparicio-Sanchis, R.; Murguia, J. R. *Angew. Chemie-International Ed.* **2012**, *51*, 10556.

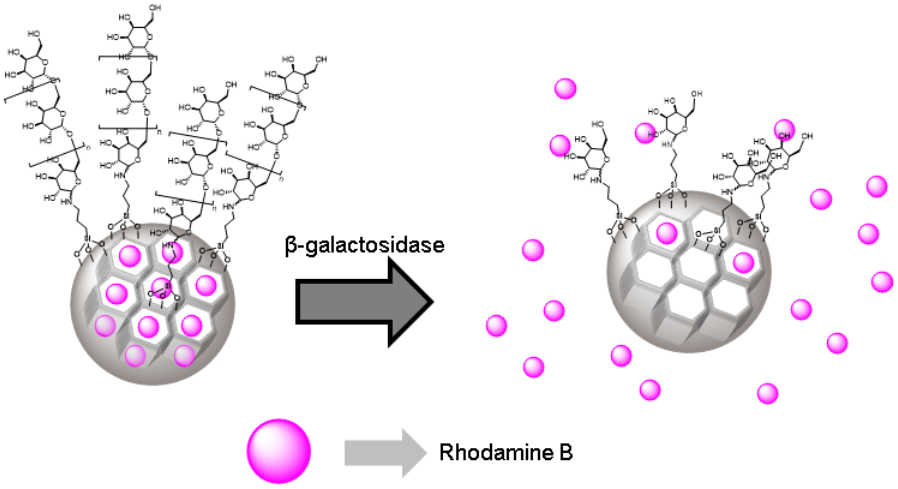

Figure 19. Scheme of drug delivery sytem opened by enzymatic action using saccharide-capped MSNs.

Raichur and coworkers designed a trypsin-driven drug delivery system prepared from MSNs and the Food and Drug Administration approved peptide drug protamine.[68] To synthesize the gated nanoparticles, the amino-functionalized MSNs were capped with protamine by a simple amine-aldehyde cross-linking reaction in which glutaraldehyde was used as a linker (see Figure 20). As model drug, diclofenac was encapsulated in pores. In release experiments, the authors found that gated MSNs exhibited minimal premature release in the absence of the trigger, whereas selective diclofenac release was observed in the presence of trypsin. These authors also investigated the system's efficacy as a carrier for the delivery of hydrophobic anticancer drugs to trypsin-overexpressing cells. In particular, trypsin and trypsin-like enzymes were seen to be overexpressed under conditions such as inflammation and cancer. Capped MSNs were loaded with antineoplasic drug curcumin and incubated with COLO205 cells at

[68] Radhakrishnan, K.; Gupta, S.; Gnanadhas, D. P.; Ramamurthy, P. C.; Chakravortty, D.; Raichur, A. M. *Part. Part. Syst. Charact.* **2014**, *31*, 449.

different time points. Nanoparticles were internalized after 1 h of incubation and intense curcumin fluorescence was observed inside cells. No significant cell fluorescence was detected in the cells incubated with curcumin and suspended in water. The ability of curcumin-loaded nanoparticles to induce cell death in COLO205 cells was also evaluated. It was noteworthy that encapsulated curcumin exhibited significantly greater anticancer activity than free curcumin.

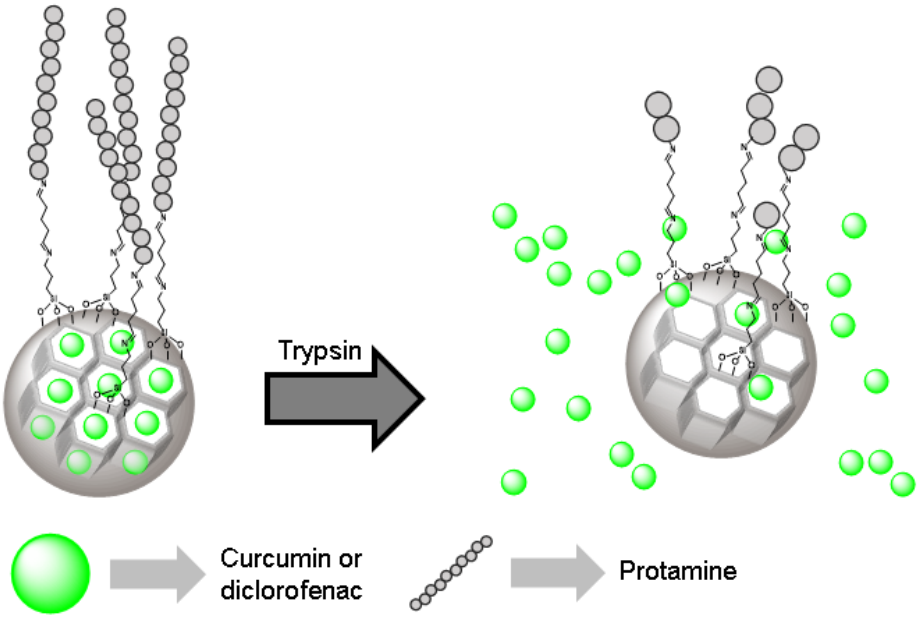

Figure 20. Scheme of protamine capped drug delivery sytem opened by protease action

1.5.2 Sensing applications of gated materials

Mesoporous gated structures can be also governed using molecular and supramolecular interactions between certain binding sites anchored on the pore outlets with species present in the solution. A wide variety of anions, cations, neutral molecules and biomolecules has been used to trigger the release of entrapped cargos from mesoporous supports. The great advantage of these molecule or biomolecule-driven systems is related with their intrinsic specificity. Only in the very restricted scenarios where the selected triggering molecule or biomolecule is present, the encapsulated cargo will be released. This opens the possibility to design precise systems for very particular applications including a specific illness. For the same reason, most gated systems described here found application in sensing processes. This strategy has demonstrated its effectiveness to detect methylmercury (CH_3Hg^+), acetylcholine or nitroaromatic explosives. Use of biomolecules in gated materials increased the spectrum of possibilities, for example, oligonucleotides led to the possibility of recognize specific DNA sequences, even genomic DNA, and also certain molecules targeted by aptamers, whereas the use of antibodies allows the very selective detection of certain molecules.

1.5.2.1 *Sensing systems based on supramolecular switches or cleavage of organic caps*

Capped MSNs designed to be opened in the presence of cations are relatively scarce. As far as we know the first reported example, which was used for sensing applications, was able to respond to the presence of CH_3Hg^+.[69] The gated material consisted of a micrometric silica mesoporous support loaded with safranin O and capped with 2,4-bis-(4-dialkylaminophenyl)-3-hydroxy-4-alkylsulfanylcyclobut-2-one groups (APC). APC were formed by the reaction of a squaraine dye and thiol units that were previously anchored on the external surface of the mesoporous solid. When CH_3Hg^+ was added to acetonitrile:toluene 4:1 v/v suspension of the APC-capped support release of entrapped safranin O was observed (see Figure 21). The uncapping derived from the reaction of CH_3Hg^+ with the thiol group on APC, resulting in the coordination of the cation to thiols, in the release of the bulky squaraine chromophore and in the delivery of the entrapped safranin O reporter. This simple chromogenic probe allowed detection of CH_3Hg^+ down to 0.5 ppm, whereas the use of standard fluorometric methods reduced the detection limit to less than 2 ppb. This system was successfully tested to determine CH_3Hg^+ in fish samples by using a simple CH_3Hg^+ extraction procedure with toluene and CH_3Hg^+ detection with the APC-capped solid. Fish samples were also spiked with cations (i.e. Na^+, K^+, Ca^{2+}, Mg^{2+}, Cu^{2+}, Ni^{2+}, Zn^{2+}, Ag^+, Pd^{2+}, Cd^{2+}, Au^{3+} and Tl^+) and various organic species such as sodium lauryl sulfate, cysteine, histamine, ethanol, heptylamine, hexanethiol, but none of those species affected the response of the capped material to CH_3Hg^+.

[69] Climent, E.; Marcos, M. D.; Martinez-Manez, R.; Sancenon, F.; Soto, J.; Rurack, K.; Amoros, P. *Angew. Chemie-International Ed.* **2009**, *48*, 8519.

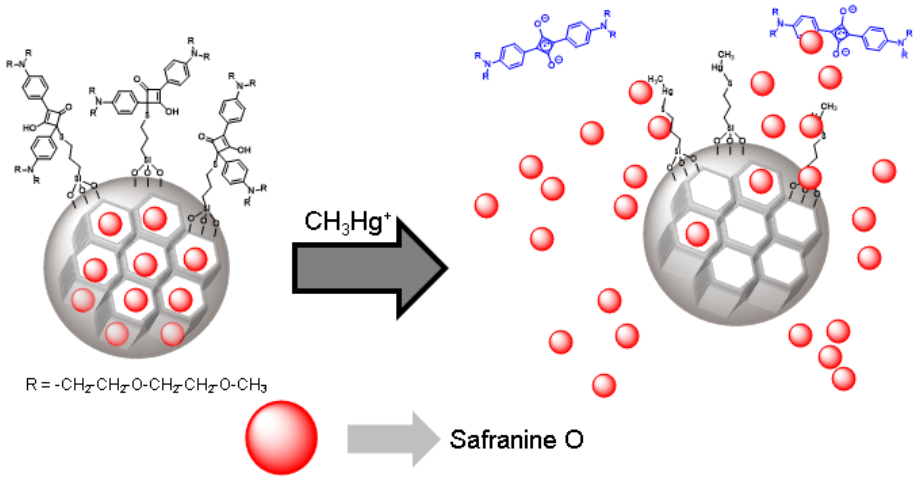

Figure 21. Recognition of methylmercury using a squaraine-capped gated material based on MSNs.

Acetylcholine was used by *Yang et al.* as trigger for uncapping gated MSNs.[70] In order to prepare the capped solid the authors functionalized the surface of MSNs with a pyridinium derivative and loaded the pores with rhodamine 6G. Finally, the pores were capped with sulfonatocalix[4]arene (SC[4]A) or carboxylatopillar[5]arene (CP[5]A) via the formation of inclusion complexes with the grafted pyridinium derivative (Figure 22). Water suspensions of both gated materials showed negligible cargo release whereas upon addition of acetylcholine a marked delivery of the dye was observed. Rhodamine 6G release was a consequence of the formation of acetylcholine-SC[4]A and acetylcholine-CP[5]A complexes. In addition, dye release from the material capped with SC[4]A was larger than that observed for the nanoparticles capped with CP[5]A, an effect that was ascribed to the difference in binding constants.

[70] Zhou, Y.; Tan, L.-L.; Li, Q.-L.; Qiu, X.-L.; Qi, A.-D.; Tao, Y.; Yang, Y.-W. *Chem. Eur. J.* **2014**, *20*, 2998.

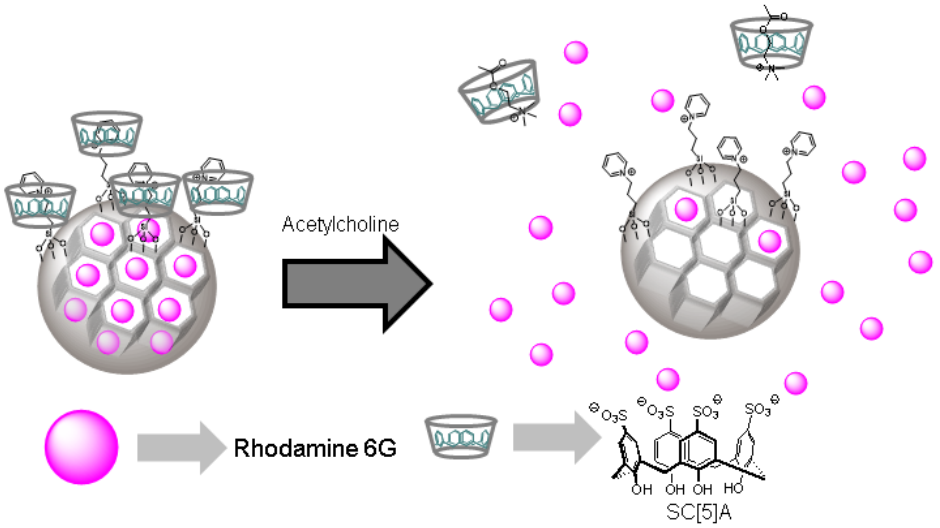

Figure 22. Recognition of acetylcholine using pseudorotaxane gated material based on MSNs.

The group of Martínez-Máñez reported several examples of capped silica mesoporous supports which were opened in the presence of nitroaromatic explosives. Moreover, the designed capped materials were used for the fluorogenic detection of these explosives.[71] As example the authors designed a silica support loaded with $Ru(bipy)_3^{2+}$ and functionalized in the surface with 3-(azidopropyl) triethoxysilane groups. Moreover a suitable pyrene derivative was attached to azido moieties by using a copper(I)-catalysed Huisgen azide/alkyne 1,3-dipolar cycloaddition click reaction leading to the formation of a 1,2,3-triazole heterocycle. In this final material, the pores were blocked due to presence of bulky pyrene moieties on the outer surface, and dye release was inhibited in acetonitrile (see Figure 23). The presence of the nitroaromatic explosives 2,4,6-trinitrophenyl methylnitramine (Tetryl) and 2,4,6-trinitrotoluene (TNT) induced the formation of pyrene–nitroaromatic

[71] Salinas, Y.; Agostini, A.; Perez-Esteve, E.; Martinez-Manez, R.; Sancenon, F.; Dolores Marcos, M.; Soto, J.; Costero, A. M.; Gil, S.; Parra, M.; Amoros, P. *J. Mater. Chem. A* **2013**, *1*, 3561.

complexes, pushing apart the bulky pyrene from the pore voids resulting in dye release. Limits of detection (LODs) of 1.4 and 11.4 ppm for Tetryl and TNT, respectively were calculated from fluorogenic studied. The authors found that other aromatic derivatives (i.e. 2,4-dinitrotoluene, *N*-methylaniline, 2-nitrotoluene, nitrobenzene) non-aromatic explosives (i.e. hexahydro-1,3,5-trinitro-1,3,5-triazine, pentaerythritoltetra nitrate), methylene blue and naphthalene were unable to uncap the pores. Moreover 2,4-dinitrotoluene was also found to be able to induce a partial release of the entrapped fluorophore but in a lesser extent.

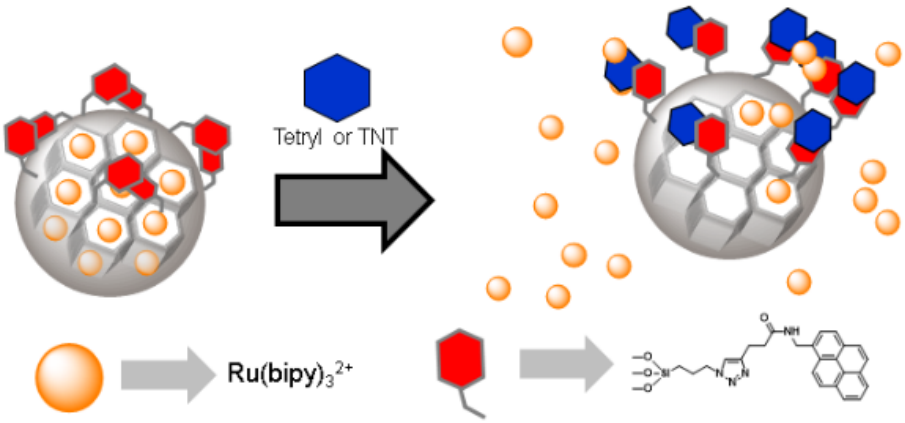

Figure 23. Recognition of nitroaromatic explosives using a pyrene-capped gated material based on MSNs.

1.5.2.2 *Sensing systems based on biomolecular interactions*

A first example of uncapping protocol triggered by biomolecules, in particular by a certain oligonucleotide, was reported by *Martínez-Máñez et al*.[72] The system was based on MSNs loaded with fluorescein and functionalized with (3-aminopropyl)triethoxysilane (APTES) in the outer surface. The oligonucleotide 5′-AAT GCT AGC TAA TCA ATC GGG-3′ was used to cap the pores through electrostatic interactions with the amines at the surface that were partially protonated at neutral pH. Cargo delivery was triggered in the presence of the complementary single strand of the capping oligonucleotide as consequence of the hybridization of both single oligonucleotides and detachment from the nanoparticles' surface as shown in Figure 24. Dye delivery was also studied in the presence of other oligonucleotides yet in all cases a poor cargo delivery was found.

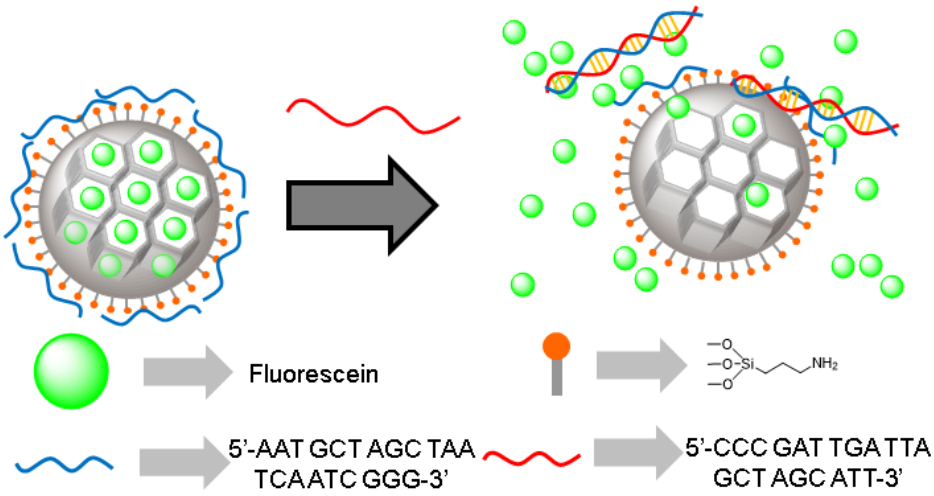

Figure 24. Recognition of complementary DNA strands using an oligonucleotide capped gated material based on MSNs.

[72] Climent, E.; Martinez-Manez, R.; Sancenon, F.; Marcos, M. D.; Soto, J.; Maquieira, A.; Amoros, P. *Angew. Chemie-International Ed.* **2010**, *49*, 7281.

Based in an analogous design the same authors prepared capped materials for the detection of genomic DNA.[73] For this purpose MSNs were loaded with rhodamine B and functionalized with APTES on the external surface. In this case it was used as the capping oligonucleotide a sequence highly conserved in the *Mycoplasma* genome that corresponds to a fragment of the 16S ribosomal RNA subunit. The system displayed no dye delivery until the addition of *Mycoplasma fermentans* genomic DNA. No cargo delivery was observed in the presence of genomic DNA from other bacteria such as *Candida albicans* or *Legionella pneumophilla*. A LOD as low as 70 DNA copies μL^{-1} was found. The capped nanoparticles were used to detect *Mycoplasma* in real contaminated cell-culture media without the use of PCR techniques.

Ozalp and coworkers used adenosine 5'-triphosphate (ATP)-aptamers to develop a gated material.[74] In their work, they used an amino-terminated oligonucleotide sequence that contained both, an ATP aptamer and a short extra sequence which was used to induce a hairpin-like structure that blocked the pores (see Figure 25). MSNs were loaded with fluorescein and functionalized in the external surface with sulfhydryl groups. The amino functionalized aptamer was then covalently anchored to the nanoparticles using the crosslinker sulfo-*N*-succinimidyl 4-maleimidobutyrate. The hairpin structure of the aptamer blocked the pores while the presence of ATP triggered the delivery of the entrapped dye. This was explained due to ATP binding that resulted in a conformational change from a duplex to a single stranded DNA of the aptamer sequence that was close to the surface of the MSNs. Interestingly similar nanoparticles capped with a mutated hairpin

[73] Climent, E.; Mondragon, L.; Martinez-Manez, R.; Sancenon, F.; Dolores Marcos, M.; Ramon Murguia, J.; Amoros, P.; Rurack, K.; Perez-Paya, E. *Angew. Chemie-International Ed.* **2013**, *52*, 8938.

[74] Ozalp, V. C.; Schaefer, T. *Chem. Eur. J.* **2011**, *17*, 9893.

did not respond to ATP, and guanosine 5′-triphosphate (GTP) was also unable to induce dye release. In a further work the same authors extended their studies and monitored the performance of aptamer-gated MSNs using circular dichroism.[75]

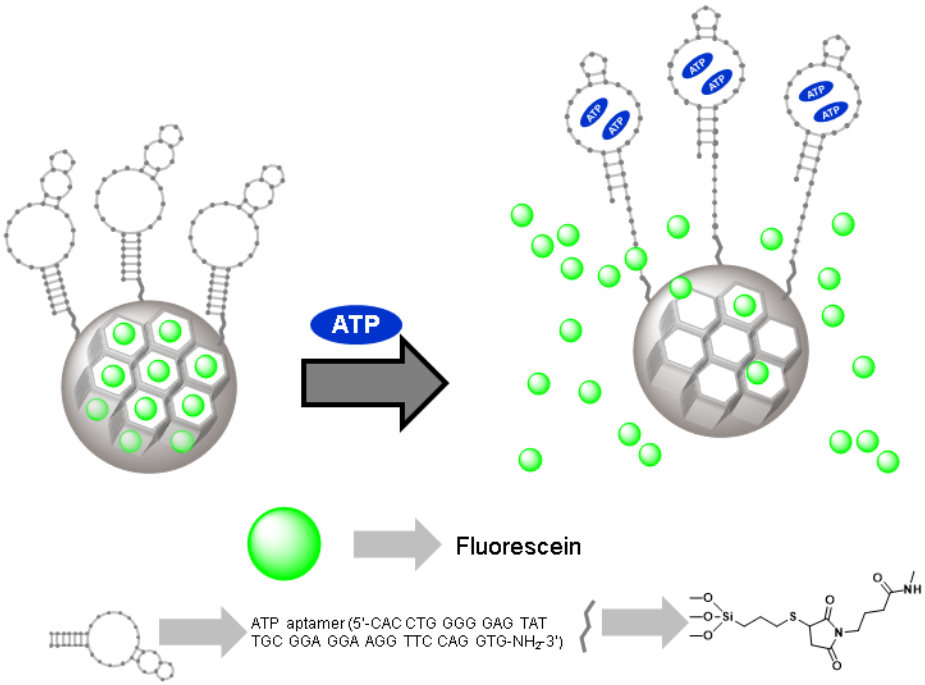

Figure 25. Recognition of ATP using an aptamer capped gated material based on MSNs.

Hernandez et al. developed amino-modified nucleolin binding aptamer (AS1411) aptamer-capped MSNs able to be opened in the presence of nucleolin.[76] For the preparation of the system, an was first prepared. Moreover in order to conjugate this aptamer to MSNs the nanoparticles' surface was first modified with MPTS and the pores loaded with fluorescein. Subsequently, sulfo-*N*-succinimidyl 4-maleimidobutyrate was attached to

[75] Ozalp, V. C.; Pinto, A.; Nikulina, E.; Chuvilin, A.; Schaefer, T. *Part. Part. Syst. Charact.* **2014**, *31*, 161.

[76] Hernandez, F. J.; Hernandez, L. I.; Pinto, A.; Schafer, T.; Ozalp, V. C. *Chem. Commun.* **2013**, *49*, 1285.

the sulfhydryl-modified nanoparticles. Finally, the amino-modified AS1411 aptamer was conjugated to the solid and capped the pores. From the *in vitro* release studies the authors found that in the presence of isolated cell membrane fragments of MDA-MB-231 cells (nucleolin positive) fluorescein was released from the capped nanoparticles. The authors found that the interaction of the aptamer with nucleotin on the surface of cancer cells induced a conformational change of the aptamer unblocking the pores and releasing the cargo. Moreover, upon aptamer binding, the MSNs internalized via receptor-mediated endocytosis resulting in dye release.

Willner and co-workers prepared different DNA-capped MSNs able to be opened in the presence of certain biomarkers.[77] MSNs were functionalized with aminopropyl moieties and the amino groups in the surface were used for grafting selected single stranded DNA sequences using sulfo-EMCS as covalent cross-linker. In the first material the DNA-**1** sequence was anchored. DNA-**1** contained a tailored base sequence that generated at room temperature a hairpin structure that blocked the pore entrances. DNA-**1** also included a single stranded loop for the recognition of a nucleic acid biomarker (i.e. 5′-AGT GTG CAA GGG CAG TGA AGA CTT GAT TGT-3′). The pores were loaded with rhodamine B. Treatment of the DNA-**1**-capped MSNs with the biomarker induced the opening of the hairpin forming a duplex structure that also blocked the pores inhibiting dye release. Addition of Exo III enzyme induced the hydrolysis of the 3′-end of **1** allowing the release of the entrapped rhodamine B and the biomarker which induced the opening of additional capped pores. The same approach was used by grafting the single stranded DNA sequence **2** and as biomarker 5′-ATC CTC AGC TTC G-3′. Both DNA formed a duplex structure that was able to cap

[77] Zhang, Z. X.; Balogh, D.; Wang, F. A.; Sung, S. Y.; Nechushtai, R.; Willner, I. *ACS Nano* **2013**, *7*, 8455.

the pores and inhibit dye release. In this case the duplex included a programmed sequence for the specific nicking of one base. Upon addition of Nb.BbvCl enzyme the duplex was dissociated because of the nicking of the grafted DNA strand that resulted in the release of the biomarker and the entrapped rhodamine B. Another gated material was obtained by the grafting sequence DNA-**3**, which formed a hairpin structure, and also incorporated an ATP-aptamer conjugated with other sequence that ensured that Exo III enzyme was unable to hydrolyze. Upon addition of ATP, the hairpin formed by DNA-**3** opened and the 3′end formed a duplex structure with the 5′ domain that was hydrolyzed by Exo III. This hydrolysis induced the release of the entrapped dye and ATP which induced the opening of additional gated pores. The same methodology was used to prepare a material able to release the entrapped dye and ATP by grafting DNA-**4**, which contained an ATP-aptamer and a fragment able to be hydrolyzed by Nb.BbvCl enzyme. Finally, the material capped with the DNA-**3** was loaded with CPT and its internalization in MDA-MB-231 (breast cancer cells) and MCF-10a (normal breast cells) studied. The capped nanoparticles were internalized by endocytosis and induced a 65% cell death in MDA-MB-231 after 48 h whereas only a cell death of 25% was observed for MCF-10a cells. These results were consistent with the fact that cancer cells have a high ATP concentration which induced an enhanced opening of the gated material.

Climent et al.[78] developed antibody-capped support for the selective detection of finasteride. In this case, the silica mesoporous material was loaded with rhodamine B and functionalized with *N*-(*t*-butyl)- 3-oxo-(5a,17b)-4-aza-androst-1-ene-17-carboxamide groups, which was a similar molecule to finasteride. The addition of polyclonal antibodies for finasteride

[78] Climent, E.; Martinez-Manez, R.; Maquieira, A.; Sancenon, F.; Dolores Marcos, M.; Brun, E. M.; Soto, J.; Amoros, P. *ChemistryOpen* **2012**, *1*, 251.

induced the capping of the pores due to the interaction with the anchored hapten-like derivative. The addition of finasteride to water suspensions of the antibody-capped material resulted in the displacement of the antibody and release of the cargo. Moreover, the amount of dye delivered was found to be proportional to finasteride concentration and a LOD of 20 ppb was calculated. Selectivity studies showed that only finasteride, among other steroids (such as testosterone, metenolone and 16-β-hydroxystanozolol), was able to induce a significant uncapping process. Furthermore, the material was used to detect finasteride in spiked samples of urine and recovery ranges from 94% to 118% were observed.

Using a similar protocol a new antibody-gated system for the detection of peroxide-based explosive triacetone triperoxide (TATP) was developed.[79] In this work, MSNs were loaded with the dye sulforhodamine B and the external surface was functionalized with an appropriate hapten-like molecule and the system was capped using a TATP-selective polyclonal antibody. A remarkable and highly selective uncapping of the pores with the subsequent cargo delivery in the presence of TATP was observed in phosphate-buffered saline (pH 7.4) as depicted in figure 26. TATP was detected at concentrations as low as 12.5 ppb using this protocol. Moreover the authors also demonstrated that the capped-MSNs could be integrated into a lateral-flow assay. Using this latter procedure a limit of detection of 15 ppb for TATP was calculated. It was also found that other common explosives such as TNT, hexogen, nitropenta, octogen, nitroguanidine and hexamethylenetriperoxide diamine did not induce cargo delivery.

[79] Climent, E.; Groninger, D.; Hecht, M.; Walter, M. A.; Martinez-Manez, R.; Weller, M. G.; Sancenon, F.; Amoros, P.; Rurack, K. *Chem. Eur. J.* **2013**, *19*, 4117.

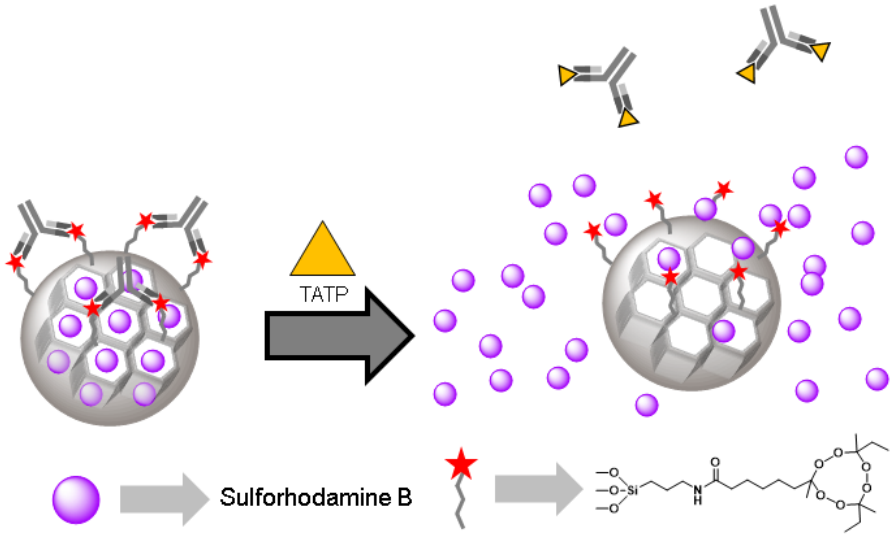

Figure 26. Recognition of TATP using an antibody capped material based on MSNs.

Lu and co-workers developed gated MSNs that were able to deliver an entrapped cargo in the presence of glucose.[80] MSNs were functionalized with prop-2-yn-1-yl(3-(triethoxysilyl)propyl)carbamate and then the inhibitor D-(+)-glucosamine was grafted through a click chemistry reaction. The pores were loaded with rhodamine B and capped by the addition of glucose oxidase (GOx) enzyme through the formation of a complex with the grafted inhibitor. Aqueous suspensions of the capped material showed negligible cargo release whereas the presence of glucose induced a clear dye release. The observed delivery was proportional to the amount of glucose added, and it was consequence of a displacement reaction of the GOx due to the presence of the glucose substrate. Cargo delivery in the presence of glucose was selective and the authors confirmed that other monosaccharides tested (i.e. fructose, mannose and galactose) induced no payload release.

[80] Chen, M.; Huang, C.; He, C.; Zhu, W.; Xu, Y.; Lu, Y. *Chem. Commun.* **2012**, *48*, 9522.

Villalonga and coworkers developed MSNs in which an enzyme also acted as cap, however in this case the uncapping process was triggered by the product obtained by the enzyme's activity on glucose.[81] MSNs were loaded with $Ru(bipy)_3^{2+}$ and the external surface functionalized with 3-iodopropyltrimethoxysilane that was further transformed to 1-propyl-1-*H*-benzimidazole groups through a nucleophilic substitution reaction using benzimidazole. The pores were finally capped with an active CD-modified glucose oxidase(CD-GOx) through the formation of inclusion complexes between the CDs groups in CD-GOx and the propylbenzymidazole stalks attached to the solid support (see Figure 27). In their study, the authors confirmed that dye delivery was induced when glucose was present in the solution due to displacement of CD-GOx as consequence of CD-GOx-induced oxidation of glucose to gluconic acid and the subsequent protonation of the benzimidazole group. The authors found a linear response to glucose in the $1x10^{-2}$-$1x10^{-4}$ mol L^{-1} range and a LOD of $1.5x10^{-4}$ mol L^{-1} which was in the range of other glucose detection systems. The response to glucose was selective and the presence of other saccharides such as mannose, fructose, galactose, maltose and saccharose at a concentration of $1x10^{-3}$ mol L^{-1} induced no cargo delivery.

[81] Aznar, E.; Villalonga, R.; Gimenez, C.; Sancenon, F.; Dolores Marcos, M.; Martinez-Manez, R.; Diez, P.; Pingarron, J. M.; Amoros, P. *Chem. Commun.* **2013**, *49*, 6391.

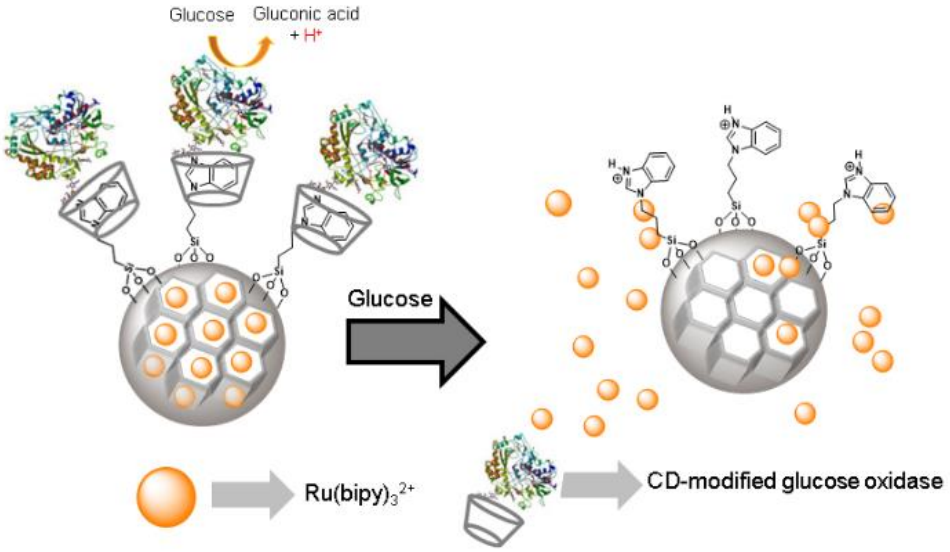

Figure 27. Recognition of glucose using an enzyme capped and operated gated material based on MSNs.

In a further work[82] the same authors demonstrated that the gating mechanism and different effector ensembles can be integrated in a unique system based in the use of Janus-type nanoparticles having opposing Au and mesoporous silica faces. In particular, the porous network of the silica face was loaded with $Ru(bipy)_3^{2+}$ and the external surface grafted with 3-(2-aminoethylamino)propyltrimethoxysilane. Additionally, the gold side was functionalized with thiol modified urease enzyme. Aqueous solution (acetate buffer pH 5) of the Janus nanoparticles showed negligible cargo release because the polyamines were protonated and the molecular gate was closed. In the presence of urea a clear delivery of the entrapped ruthenium complex was found. This release was a consequence of the urease-catalyzed

[82] Villalonga, R.; Diez, P.; Sanchez, A.; Aznar, E.; Martinez-Manez, R.; Pingarron, J. M. *Chem. Eur. J.* **2013**, *19*, 7889.

hydrolysis of urea into CO_2 and NH_3 that induced an increase in the pH of the local environment. With this increase the polyamines became deprotonated and subsequently the gates were opened.

1.5.3 Imaging applications of gated materials

During the last years a novel challenge has overcome to the field of nanomedicine: development of theranostic agents with diagnostic and therapeutic applications at the same time. These system make capable to treat and detect or trace a certain disease using the same agent. The most common strategy is to use imaging techniques by including a specific imaging agent in the nanomaterial structure. Regarding to gated materials most of the system reported until today can be followed by fluorescence imaging when a fluorescent drug is used as a cargo. However, there are only a few reports dealing with the testing of this strategy in *in vivo* animal models. Different strategies are based on including paramagnetic nanoparticles in the core of the structure or loading them with ultrasound-sensitive compounds. Other imaging techniques such as thermal imaging or radiological imaging as positron emission tomography (PET) or single emission photon computed tomography (SPECT) have been barely explored in gated nanoparticles.

Meng et al.[83] developed an engineered approach for the pancreatic ductal adenocarcinoma (PDAC) stromal barrier through the combined use of a liposome that contained gemcitabine and MSNs coated with polyethyleneimine(PEI)-PEG. The authors electrostatically attached PEI to MSNs and the polymer was also used to anchor PEG. Finally, a small

[83] Meng, H.; Zhao, Y.; Dong, J. Y.; Xue, M.; Lin, Y. S.; Ji, Z. X.; Mai, W. X.; Zhang, H. Y.; Chang, C. H.; Brinker, C. J.; Zink, J. I.; Nel, A. E. *ACS Nano* **2013**, *7*, 10048.

molecule inhibitor of the transforming growth factor (TGF-β) beta signalling pathway, LY364947, was attached to the PEI polymer through H-bonding interactions (Figure 28). PBS suspensions of MSNs at pH 7.4 showed negligible LY364947 release, whereas delivery was marked when pH was lowered to 5.5. An optimal liposome design was achieved by using a transmembrane ammonium sulfate gradient to trap gemcitabine inside the liposome. TGFβ delivery to the PDAC tumor site was explored in nude mice BxPC3 xenografts. These xenografts are known to elicit a dense infiltrating stroma, which surrounds nests of cancer cells and also covers tumor blood vessel fenestrations. Due to the acidic pH environment of the tumor stroma, the LY364947-coated nanoparticles were firstly used for the pH-dependent LY364947 delivery to inhibit the TGF-β receptor signaling in the xenograft. As a result of TGF-β signaling blockage, pericyte differentiation and attachment to endothelial cells were also prevented. This allowed liposomal gemcitabine carrier access through the open vascular fenestrations, and the ability to increase gemcitabine delivery. This two-wave approach allowed the effective shrinkage of the tumor xenografts beyond 25 days compared to the treatment only with free drug or gemcitabine -loaded liposomes.

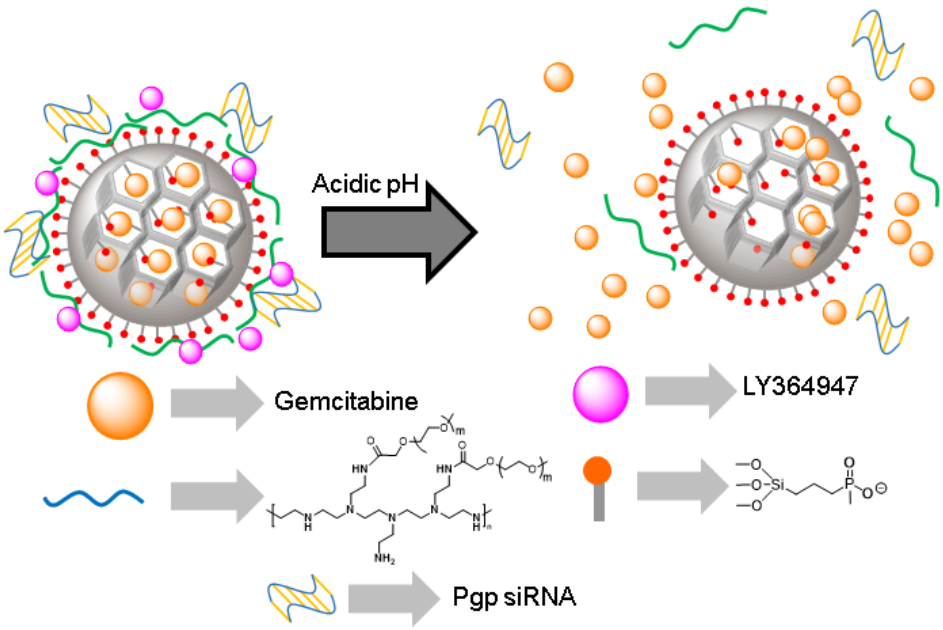

Figure 28. Acidic responsive double drug and siRNA delivery using a PEI-capped gated material. MSN were prepared by co-condensation.

Son et al. used silica nanotubes (SNTs) as inorganic scaffold which were functionalized in the open end with a gold nano-ring through a seed-mediated Au growth reaction.[84] Then, the nanotubes were loaded with doxorubicin and capped upon addition of 1-octadecanethiol groups that were grafted into the surface of the gold nano-ring yielding a hydrophobic cap that disabled the diffusion of the entrapped doxorubicin. Addition of glutathione (GSH) induced nanotube opening with the subsequent release of the entrapped cargo. The substitution of 1-octadecanethiol by GSH changed the hydrophobic character around the nanotube entrance to a more hydrophilic allowing the release of the polar doxorubicin. Doxorubicin release from the nanotubes was studied by real-time live-cell fluorescence

[84] Wang, L.; Kim, M.; Fang, Q.; Min, J.; Jeon, W. Il; Lee, S. Y.; Son, S. J.; Joo, S.-W.; Lee, S. B. *Chem. Commun.* **2013**, *49*, 3194.

spectroscopy in the multi-drug resistant human breast carcinoma MCF-7/ADR cell line. Preincubation of cells with GSH ethyl ester was used to enhance intracellular GSH concentration. Under these conditions, an increase in intracellular fluorescence intensity was found after 24 h. Similar results were independently obtained in A549 cells. To further characterise the doxorubicin-loaded capped SNTs an in vivo experiment was performed. The SNTs were administered via injection into MCF-7/ADR xenografted mice. Remarkably, total fluorescence intensities increased after treating mice with GSH, showing that the release of doxorubicin appeard to increase by two orders of magnitude. Furthermore, an in vivo tumour growth test indicated an increased reduction using doxorubicin-loaded capped SNTs.

Gaberscek et al. developed different redox-responsive delivery systems, all of which were based on the use of β-CDs, which were anchored to the silica surface via different linkers.[85] MSNs were functionalized with APTES and then reacted with (*N*-succinimidyl 3-(2-pyridyldithio)propionate , 4-(succinimidyloxycarbonyl)-α-(2-pyridyldithio)toluene or 4-(succinimidyl oxycarbonyl)-α-methyl-α-(2-pyridyldithio)toluene to provide systems with three levels of hindrance around disulfide bonds. Pores were loaded with rhodamine B as a model drug and molecule monothio-β-CD or perthio-β-CD were used as capping agents through a reaction with the pyridyldithio groups of the thiol-containing linkers, which resulted in the formation of disulfide linkages. Capped systems were tested in a non reducing environment and showed slight leakage, whereas addition of DTT allowed clear cargo release. The delivery of entrapped dye was dependent on the level of hindrance induced by the substituents around the disulfide bond. Increased hindrance caused the release rate to lower. To evaluate the

[85] Nadrah, P.; Maver, U.; Jemec, A.; Tisler, T.; Bele, M.; Drazic, G.; Bencina, M.; Pintar, A.; Planinsek, O.; Gaberscek, M. *ACS Appl. Mater. Interfaces* **2013**, *5*, 3908.

teratogenicity of synthesized materials, *in vivo* experiments on zebra fish (*Daniorerio*) were performed. To avoid excessive animal testing, only the system that exhibited the largest amount of rhodamine B release (that containing the ethylene linker) was evaluated, along with two concentrations of capped MSNs. No tested sample affected hatching of larva on day 4 post-fertilization in all the samples. Likewise, no effects on fish length were detected at the same time point. The system neither significantly affected embryo development and survival, nor were signs of cell death detected. These data confirmed the non-teratogenicity of the nanomaterial.

Kim and coworkers prepared ultrasmall (7 nm) superparamagnetic iron oxide nanoparticles (SPIONPs) that formed ca. 59-nm clusters with the assistance of polyacrylic acid. Then clusters were coated with a 18-nm silica shell with polyvinyl pyrollidone (PVPON) moieties on the external surface, and pores were loaded with gemcitabine. In another step, an etching process was run with sodium hydroxide in order to obtain pores of around 5 nm. Finally, temperature-sensitive hydroxypropyl cellulose was grafted onto the surface by hydrogen bonding interactions with PVPON groups (see Figure 29).[86] In a first step, the authors studied the release of gemcitabine at two different temperatures (37 ^{o}C and 45 °C). Heating magnetic gated particles and subsequent gemcitabine release were investigated in PBS by amplying an Alternating Magnetic Filed (AMF) at 199 kHz (175 Oe). At both temperatures, a two-phase release pattern was monitored by UV-Vis spectroscopy, with an initial fast "burst" release followed by a sustained release period. The cumulative release was significantly higher at 45 °C. At this temperature, grafted hydroxypropyl cellulose (LCST 41 °C) collapsed, which allowed entrapped drug release. The authors also confirmed the "on-

[86] Kim, D. H.; Guo, Y.; Zhang, Z. L.; Procissi, D.; Nicolai, J.; Omary, R. A.; Larson, A. C. *Adv. Healthc. Mater.* **2014**, *3*, 714.

off" behavior of the gated solid by repeated temperature-driven release cycles run at 37 ºC and 43 ºC. *In vitro* cell viability studies, performed in pancreatic cancer PANC-1 cells, indicated that cell growth was significantly inhibited upon the simultaneous application of an AMF and gemcitabine delivery compared with gemcitabine or magnetic hyperthermia alone. The delivery of injected gemcitabine-loaded nanomaterial in PANC-1 xenografts in nude mice was viewed by both MRI and fluorescent imaging techniques. Combinations of AMF with intra-tumoral injections of the gated system induced a significant increase in apoptosis compared to the tumors treated with nanocarrier injections alone.

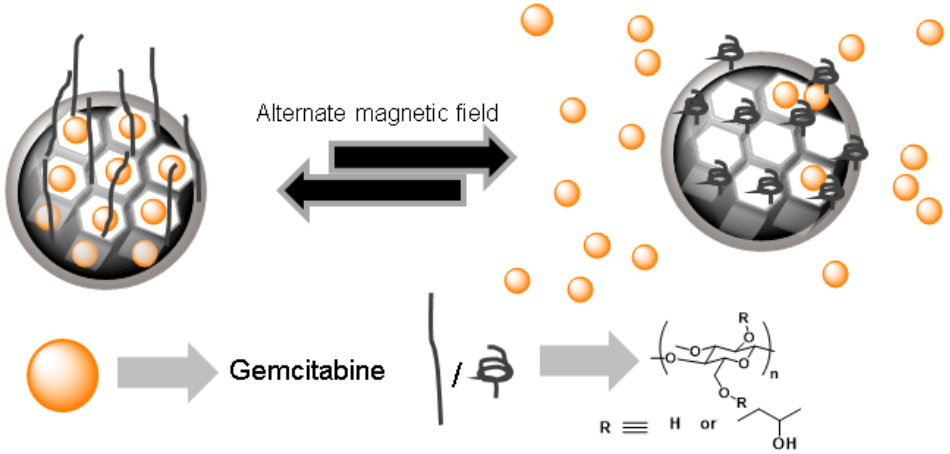

Figure 29. Thermal nanovalve operated by an alternate magnetic field based on SPIONPs-core MSNs. SPIONPs core is drawn in black.

Lin and coworkers prepared Hollow MSNs and incorporated into the internal cavity Gd_2O_3:Eu^{3+} luminescent nanoparticles.[87] After preparing the inorganic support, the hollow voids were filled with the monomers *N*-isopropylacrylamide and acrylic acid amide, and were then subjected to

[87] Kang, X.; Cheng, Z.; Yang, D.; Ma, P.; Shang, M.; Peng, C.; Dai, Y.; Lin, J. *Adv. Funct. Mater.* **2012**, *22*, 1470.

polymerization by a photo-induced process. This formed a copolymer inside the voids between the external mesoporous silica shell and the internal Gd_2O_3:Eu^{3+} luminescent nanoparticles. Indomethacin, a nonsteroidal anti-inflammatory drug commonly used to reduce fever, pain, stiffness and swelling, was selected to study drug release from the capped system. The release behavior of indomethacin was clearly temperature-dependent as drug release was triggered at 45 °C and release stopped at 20 °C. The authors indicated that the drug release rate could be regulated by the change in temperature due to the composite nanocarrier's unique architecture. This release was attributed to the polymer shrinking that opened the porous network with the subsequent drug release. Cell viability assays in mouse L929 fibroblasts showed that the nanomaterial presented good biocompatibility. Intracellular uptake of the fluorescein-loaded system in the ovarian carcinoma SKOV3 cell line was confirmed by flow cytometry and CLSM. The system had the potential to serve as a T1-NMR contrast agent given the existence of Gd^{3+} ions.

Chen et al. coated Hollow MSNs with AuNPs through the *in situ* reduction of Au^{3+} by $NaBH_4$. Pyrene dye, used as model drug, and ultrasound-sensitive liquid perfluorohexane (PFH) were loaded into inner cavities. Finally, thiol-functional PEG was grafted onto the surface of the attached.[88] Application of ordinary ultrasound irradiation triggered the release of the loaded drug through the alteration of acoustic and thermal properties of the attached AuNPs. Irradiation of the nanocarrier with ultrasound converted PFH liquid into small bubbles, which promoted the appearance of cavitations which, in turn, also conferred the nanomaterial with contrast-intensified ultrasound imaging properties (see figure 30).

[88] Wang, X.; Chen, H.; Zheng, Y.; Ma, M.; Chen, Y.; Zhang, K.; Zeng, D.; Shi, J. *Biomaterials* **2013**, *34*, 2057.

Ultrasound-guided (US) high intensity focused ultrasound (HIFU) therapy *ex vivo* and *in vivo* with the nanomaterial was found to be highly efficient on rabbit VX2 xenograft tumor ablation due to the high thermal energy accumulation and increased mechanical/thermal effects. The system induced significant cytoclasis and enhanced drug release, served as contrast-intensified US imaging agent, and enabled efficient US-guided HIFU tumor ablation therapy. Therefore, this nanosystem could be used as a theranostic platform for contrast-intensified US imaging, combined chemotherapy and efficient HIFU tumor ablation.

The same authors functionalized the external surface of mesoporous silica nanocapsules with APTES and amines were further reacted with a maleimide PEG-*N*-hydroxysuccinimide ester. Afterward, anticancer drug camptothecin-11 and ultrasound-sensitive PFH were co-loaded into pores. Subsequently, a thiol-functionalized hyaluronic acid was synthesized and conjugated to PEG through maleimide-thiol coupling.[89] When treating the material with chloramine-T, hyaluronic acid was cross-linked with disulfide bonds. The potential nanocarrier application was tested in hepatocellular carcinoma Hep G2 tumor-bearing nude mice. The results indicated that the nanomaterial could serve as a nanotheranostic agent with a tumor targeting function via binding and CD44 receptor-mediated endocytosis. This, in turn, facilitated the enhanced accumulation of the system and, as a result, led to specifically intensified ultrasound imaging in the hepatocellular carcinoma Hep G2 tumor-bearing nude mice tumor area. *In vivo* results also showed that the system accomplished enhanced HIFU ablation efficacy of tumors by the PFH gasification in the nanocarrier.

[89] Wang, X.; Chen, H.; Zhang, K.; Ma, M.; Li, F.; Zeng, D.; Zheng, S.; Chen, Y.; Jiang, L.; Xu, H.; Shi, J. *Small* **2014**, *10*, 1403.

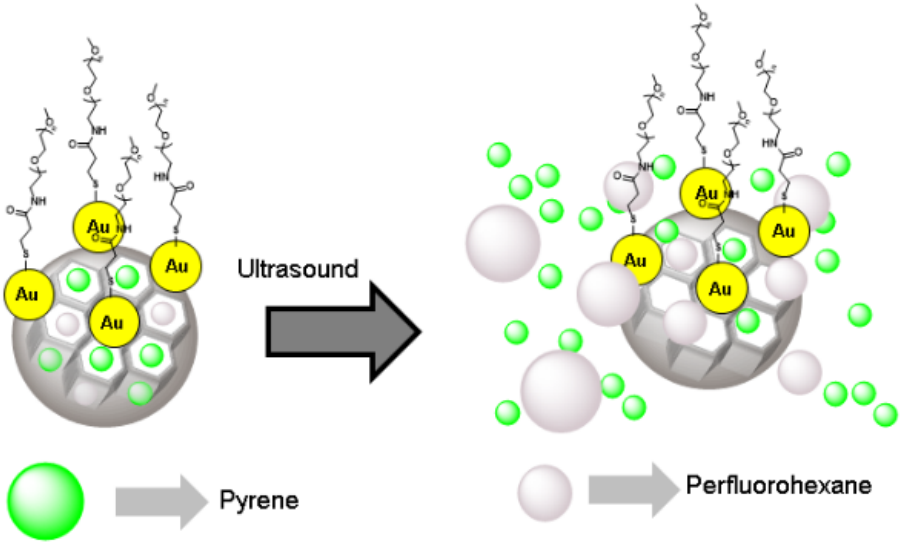

Figure 30. Dual loaded MSNs capped with gAuNPs applied for ultrasound induced drug delivery and ultrasound imaging.

Few examples existed of gated materials for thermal or photothermal imaging. A near infrared (NIR) fluorescence-responsive drug nanocarrier reported by Zhang and co-workers was also applied for thermal imaging.[90] Nanomaterial was obtained from mesoporous silica-coated $Cu_{1.8}S$ nanoparticles loaded with curcumin and functionalized by APTES. A DNA double helix containing a thiolated strand and a biodirecting strand with AS1411 aptamer and binding sites for doxorubicin was anchored through sulfosuccinimidyl 4-(*N*-maleimidomethyl) cyclohexane-1- carboxylate chemistry. This double-stranded DNA structure was suitable to coordinate with doxorubicin. Application of a NIR laser (980 nm) causes the nanoparticle heating and produce the release of the drug and the

[90] Zhang, Y.; Hou, Z.; Ge, Y.; Deng, K.; Liu, B.; Li, X.; Li, Q.; Cheng, Z.; Ma, P.; Li, C.; Lin, J. *ACS Appl. Mater. Interfaces* **2015**, *7* , 20696.

deattachment of DNA. Cell experiments on MCF-7 (targeted cells) and HEK-293 (control cells) demonstrated the affinity of the system to nucleolin. *In vivo* experiments involving tumor-bearing Balb/c mice also demonstrated the capability of the nanocomposite as a photothermal imaging agent.

A common imaging techniques which has not been combined yet with gated materials is PET and SPECT imaging (that are common diagnostic procedures in medicine). These techniques have been used in combination of nanomaterials but not with gated nanodevices. Despite of these facts, there are some examples of mesoporous silica systems marked with radiolabeling agents. In several examples developed by *Chen et al.* Hollow mesoporous silica nanoparticles were used as drug carrier (doxorubicin loaded) and also functionalized with a copper chelating agent 1,4,7-triazacyclononane-triacetic acid (NOTA), and biodirecting antibodies (TRC105, which binds to CD105 on tumor neovasculature).[91] NOTA derivatives coordinates with the radionuclide ^{64}Cu achieving a radiological marker material (see figure 31). However these biodirected drug DSAdelivery systems cannot been formerly considered a gated material because the absence of stimuli-responisve molecules on the outer surface of the nanoparticles. In these examples is observed a slow and continuos delivery of doxorubicin, due to the absence of a capping agent, but this delivery is enhanced on the tumor site because of the acidic environment. Also in some case can be stimulated with laser irradiation (when nanoparticles contain CuS core). In all examples, authors performed *in vitro* and *in vivo* studies to investigate the stability, tumor targeting efficacy and

[91] a) Chen, F.; Hong, H.; Shi, S.; Goel, S.; Valdovinos, H. F.; Hernandez, R.; Theuer, C. P.; Barnhart, T. E.; Cai, W. *Sci. Rep.* **2014**, *4*, 5080. b) Chen, F.; Hong, H.; Goel, S.; Graves, S. A.; Orbay, H.; Ehlerding, E. B.; Shi, S.; Theuer, C. P.; Nickles, R. J.; Cai, W. *ACS Nano* **2015**, *9*, 3926.

specificity, biodistribution and drug delivery capability to fully explore the potential of as-developed new theranostic nanoparticles.

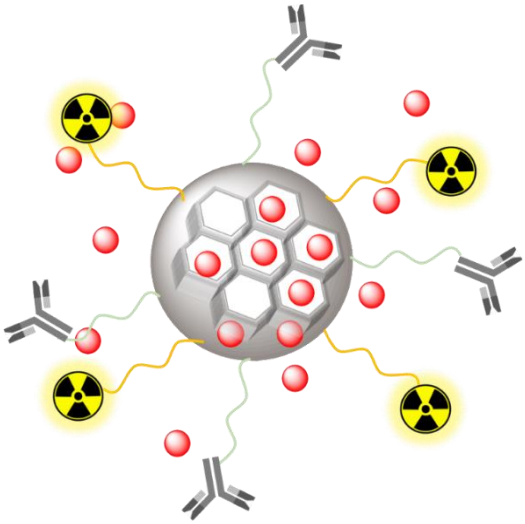

Figure 31 Doxorubicin-loaded MSNs drug delivery system biodirected by TRC105 antibody and radiolabeled with ^{64}Cu-NOTA complex.

Chapter 2:

Objectives

2. Objectives

The general objectives of the present PhD thesis are to design, fabricate and evaluate different hybrid materials based on silica supports functionalized with operative supramolecular ensembles or biomolecules. These objectives can be summarized in three general goals:

- Bring forward innovative strategies for molecular recognition, relying on concepts of supramolecular chemistry and biochemical interactions, in the fields of optical ion channel sensors (ICS) and gated materials.

- Synthesis and characterization of new functional hybrid organic-inorganic materials using solid or mesoporous silica nanoparticles as scaffolds.

- Application of these materials as sensing systems or diagnostic tools.

2.1 Objectives by chapter

The specific objectives of ***chapter three*** are:

- Design and synthesis of an optical ICS, inspired by biological ion-channels, able to selectively detect (using chromogenic changes) formaldehyde over other aldehydes.

- Characterization of the hybrid material using thermogravimetric analysis (TGA) and transmission electron microscopy (TEM). Elucidate the recognition mechanism using ^{1}H and ^{13}C-NMR spectroscopy.

- Evaluate the selectivity and sensitivity toward formaldehyde (in aqueous solution and in gas phase) of the prepared nanodevice.

The specific objectives of ***chapter four*** are:

- Design and synthesis of an acetylcholinesterase (AChE)-capped gated material based on mesoporous silica nanoparticles, loaded with the fluorophore rhodamine B and opened by the presence of the enzyme inhibitors.

- Synthesis of trialkoxysilane-containing derivatives of well-known AChE inhibitors (pyridostigmine and neostigmine) and grafting onto the external surface of rhodamine B-loaded mesoporous nanoparticles.

- Characterization of the hybrid materials prepared using powder X-ray diffraction (PXRD), TGA, TEM, N_2 adsorption-desorption isotherms, UV spectrometry and enzyme activity assays.

- Study the opening protocol of the AChE-capped nanoparticles in the presence of different enzyme inhibitors. Explore the use of AChE-capped nanoparticles for the recognition and sensing of paraoxon and DFP in real environments.

The specific objectives of ***chapter five*** are:

- Design and synthesis of a gated material based on mesoporous silica nanoparticles, loaded with the fluorophore rhodamine B and capped by a supramolecular ensemble of DNA strands able to recognize specifically *Mycoplasma fermentans* genome.
- Characterization of the hybrid material using PXRD, TGA, TEM, N_2 adsorption-desorption isotherms and elemental analysis.
- Study the recognition features of the capped material toward *Mycoplasma fermentans* genomic DNA, evaluating selectivity and sensitivity.

The specific objectives of ***chapter six*** are:

- Design and synthesis of a gated material based on mesoporous silica nanoparticles, loaded with the fluorophore safranin O and capped with MUC1 aptamer.
- Characterization of the hybrid material using PXRD, TGA, TEM, N_2 adsorption-desorption isotherms, elemental analysis and energy dispersive X-ray spectroscopy (EDX).
- Test the bio-direction and drug delivery features of the hybrid material in MUC1-expressing cancer cell lines.

- Explore the use of the capped nanoparticles radiolabeled with ^{99m}Tc as *in vivo* radioimaging agent in an animal model. Study the biodistribution of the labelled nanoparticles.

Chapter 3:

Chromogenic detection of aqueous formaldehyde using functionalized silica nanoparticles

Chromogenic detection of aqueous formaldehyde using functionalized silica nanoparticles

Sameh El Sayed, [†,‡,§,II,⊥] Lluis Pascual, [†,‡,§,⊥] Maurizio Licchelli, [II*] Ramón Martínez-Máñez, [†,‡,§*] Salvador Gil[†,§,⊥] Ana M. Costero[†,§,⊥] and Félix Sancenón[†,‡,§]

[†] *Instituto de Reconocimiento Molecular y Desarrollo Tecnológico (IDM), Unidad Mixta Universidad Politécnica de Valencia-Universidad de Valencia, Spain.*

[‡] *Departamento de Química, Universidad Politécnica de Valencia, Camino de Vera s/n, 46022, Valencia, Spain. E-mail: rmaez@qim.upv.es.*

[§] *CIBER de Bioingeniería, Biomateriales y Nanotecnología (CIBER-BNN).*

[II] *Dipartimento di Chimica, Università di Pavia, via Taramelli 12, I-27100 Pavia, Italy. E-mail: maurizio.licchelli@unipv.it.*

[⊥] *Departamento de Química Orgánica, Universitat de València, Dr. Moliner 50, 46100, Burjassot, Valencia, Spain.*

Received: March 16, 2016
Accepted: June 2, 2016
Published online: June 2, 2016

Abstract

Silica nanoparticles functionalized with thiol reactive units and bulky polar polyamines were used for the selective colorimetric detection of formaldehyde. The reaction of thiols groups in the nanoparticles surface with a squaraine dye resulted in loss of the π-conjugation of the chromophores, and the subsequent bleaching of the solution. However, when formaldehyde was present in the suspension, the thiol-squaraine reaction was inhibited and a chromogenic response was observed. A selective response to formaldehyde was observed only when the thiol and polyamine groups were anchored to the silica surface. The observed selective response was ascribed to the fact that bulky polyamines generate a highly polar environment around thiols, which were only able to reaction with the small and polar formaldehyde, but not with other aldehydes. The sensing nanoparticles showed a limit of detection (LOD) for formaldehyde of 36 ppb in water.

Aldehydes are pollutants in every-day life as they are employed in chemical adhesives and are side-products of several industrial processes or imperfect combustions (tobacco smoke, automotive exhaust, etc.). Among aldehydes, formaldehyde is widely used in household materials, and adhesives which bind veneers, particle board and pressed wood products. Formaldehyde is also used in the manufacture of paints, textiles and paper. However, it is an strong irritant of mucous membranes and eyes and is, therefore, highly dangerous as an indoor pollutant. The International Agency for Research on Cancer (IARC) elevated, in 2006, the cancer classification of formaldehyde to "carcinogenic to humans".[1] Formaldehyde has been implied by the IARC to be a causative agent of nasopharyngeal cancer and leukemia in humans.[2] Low formaldehyde levels (1–3 ppm) can induce irritation in nose and eyes, and levels above 10 ppm cause much

discomfort.[3] The US EPA gives a reference dose (RfD) for chronic oral exposure of 0.2 mg/kg bodyweight/day.[4] Feron and co-workers estimated that formaldehyde amounts by consumption food products is ca. in the 1.5 and 14 mg/person/day range.[5]

After considering the above-mentioned facts, formaldehyde detection has been explored profoundly in the last few years. To this end, techniques such as cataluminescence,[6,7] different spectroscopies,[8-10] gas chromatography,[11,12] chemoresistivity,[13] organic-inorganic hybrid materials,[14] bio-sensing,[15] field effect gas sensors,[16] quartz micro balances,[17,18] and amperometric electrochemical cells[19] have been developed.

As an alternative to these classical costly time-consuming techniques,[20,21] the use of chromogenic and fluorogenic probes for formaldehyde detection has recently emerged.[22-25] All reported probes have been designed using the chemodosimeter paradigm, and most employ the well-known reaction between nucleophilic alkyl and aryl amines with the electrophilic carbon of formaldehyde. These sensing systems are designed so that, upon the reaction with formaldehyde, color and/or emission changes are induced. However some of these probes are not completely selective to formaldehyde and other aldehydes also display chromo-fluorogenic changes. Optical probes are attractive for the use of simple instrumentation, their high sensitivity, their ability to work at ambient temperature, and the possibility of target analyte detection "in situ" using relatively simple assays. [22-25]

Following our interest in the preparation and applications of hybrid organic-inorganic materials in sensing and recognition protocols,[26-28] we described herein the use of functionalized silica nanoparticles for chromogenic formaldehyde sensing in both solutions and air. Of the various available silica supports, we selected silica nanoparticles because of their simple preparation, known surface functionalization, and high stability in

both organic solvents and water. The sensory material we developed used the well-known ion-channel approach introduced, some years ago, by Umezawa for electrochemical sensors.[29] In our version, the silica nanoparticles external surface was decorated with thiol moieties as reactive units, which underwent a nucleophilic substitution reaction with formaldehyde. The optical response arose from the competitive reaction of thiol moieties with the central electron-deficient 4-membered ring of a blue squaraine dye (SQ) or with formaldehyde. In the absence of formaldehyde, the reaction of thiol moieties with the SQ resulted in loss of the π-conjugation of the dye, and the subsequent bleaching of the solution. Yet in the presence of formaldehyde, thiols were expected to react with the –CHO group, which would further inhibit SQ-thiol coupling and result in a chromogenic response (see Figure 1).

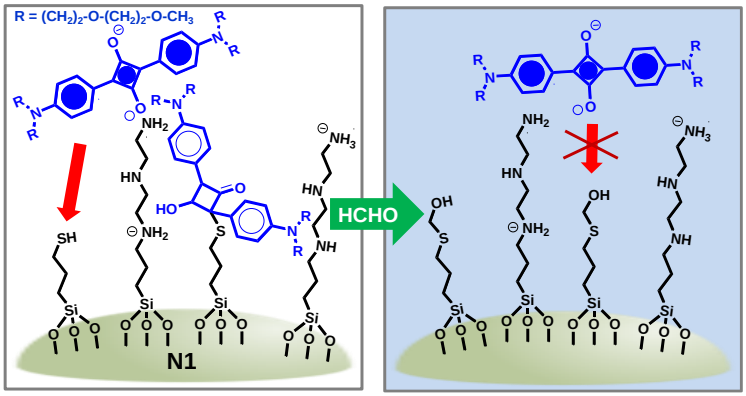

Figure 1. Colorimetric detection of formaldehyde using **N1** nanoparticles.

In order to improve selectivity toward formaldehyde, it was envisioned that grafting additionally bulky polar molecules onto the nanoparticle's surface would enhance the reactivity of the thiol groups to sterically less hindered aldehydes. For this purpose, we selected 3-[2-(2-aminoethylamino)

ethylamino]propyltrimethoxysilane as a large polar group, which was also anchored to the surface of nanoparticles. We were aware that amines can also react with aldehydes to yield the corresponding imines. However, due to the greater nucleophilic character of thiols, the formaldehyde reaction with thiols was expected to occur preferentially. Amines were also expected to be partially protonated under the experimental conditions (neutral pH), this rendering them less nucleophilic.

Silica nanoparticles coated with thiol and amino groups (**N1**) were obtained upon the reaction with 3-[2-(2-aminoethylamino) ethylamino]propyltrimethoxysilane and (3-mercaptopropyl) trimethoxysilane at a 10:1 molar ratio following a similar procedure to that reported by Montalti and co-workers.[30] In this procedure, silica nanoparticles were heated (80ºC) in a water:ethanol:acetic acid (1:2:1) solution in the presence of coating subunits (see Supporting Information for details). Solid **N1** was characterized using standard techniques (thermogravimetic analysis and transmission electron microscopy). Other molar ratios were tested, but the final supports were less selective. The organic contents in the final **N1** nanoparticles were assessed by thermogravimetric studies and elemental analysis, and amounted to 0.54 mmol/g of SiO_2 for polyamine and 0.033 mmol/g of SiO_2 for thiols. Solid **N1** presented and average coverage of ca. 1.75 molecules/nm^2 (1.65 of which are triamines and 0.10 are thiols). Based on the value of the specific surface of the silica nanoparticles (ca. 200 $m^2\ g^{-1}$) and the organic matter content, an average distance between grafted molecules of about 5.7 Å was calculated.

For the sake of comparison, only the thiol-coated nanoparticles (**N2**) were synthesized using (3-mercaptopropyl)trimetoxysilane and a similar procedure to that described above. The thiol content in **N2** was evaluated by

thermogravimetric measurements and elemental analysis, and amounted to 1.10 mmol/g SiO_2.

The reactivity of solid **N1** with SQ was tested in the absence and presence of formaldehyde. In a typical experiment, **N1** was suspended in phosphate-buffered saline (PBS, 0.01 M, pH 7.0). Then the suspension of nanoparticles was mixed with formaldehyde and stirred for 5 min. Finally, an acetonitrile solution of SQ was added, and the changes at 642 nm (SQ visible band) were monitored according to time. The same protocol was carried out with **N1** suspensions in the absence of formaldehyde. The obtained results are shown in Figure 2, where we can see a gradual decrease in absorbance at 642 nm in the absence of formaldehyde, which indicated that the reaction between thiols and SQ occurs. However in the presence of formaldehyde, the thiol-SQ reaction was highly inhibited. This inhibition was ascribed to the reaction of thiols with formaldehyde, which yielded weakly nucleophilic (alkylthio)methanol moieties that were unable to react with SQ.

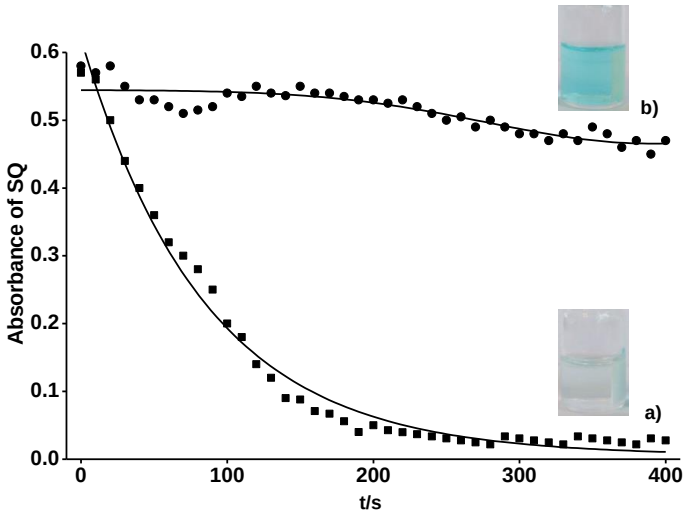

Figure 2. Absorbance at 642 nm (SQ band) versus time for PBS (0.01 M, pH 7.0) suspensions of **N1** and SQ alone (a) and in the presence of formaldehyde 0.1 mM (b).

In a second step, the chromogenic response of **N1** nanoparticles in the presence of formaldehyde, acetaldehyde, propionaldehyde, butyraldehyde, acetone, salicylaldehyde and 4-aminobenzoic acid was tested following the same protocol described above. The response obtained using the **N1** nanoparticles was extremely selective, and only addition of formaldehyde was able to clearly inhibit the thiol-SQ reaction. Selectivity of **N1** toward formaldehyde could be explained by bearing in mind that the grafting of bulky polyamines onto the nanoparticle surface generates a highly polar environment around thiols and, as a result, only formaldehyde, i.e. the more electrophilic and smallest of aldehydes tested, was able to access the nanoparticle's surface and react with grafted thiols. The required presence of polyamines to obtain a selective response to formaldehyde is clearly evidenced when comparing the response of **N1** with that of **N2**. For the latter, the four tested aliphatic aldehydes were also able to inhibit the thiol-SQ reaction to some extent (see Figure 3). **N2** was clearly not selective to

formaldehyde, and the different degree of thiol-SQ reaction inhibition with the tested aldehydes was tentatively attributed to the different electrophilic character of the carbonyl group in them (formaldehyde > acetaldehyde > propionaldehyde > butyraldehyde).

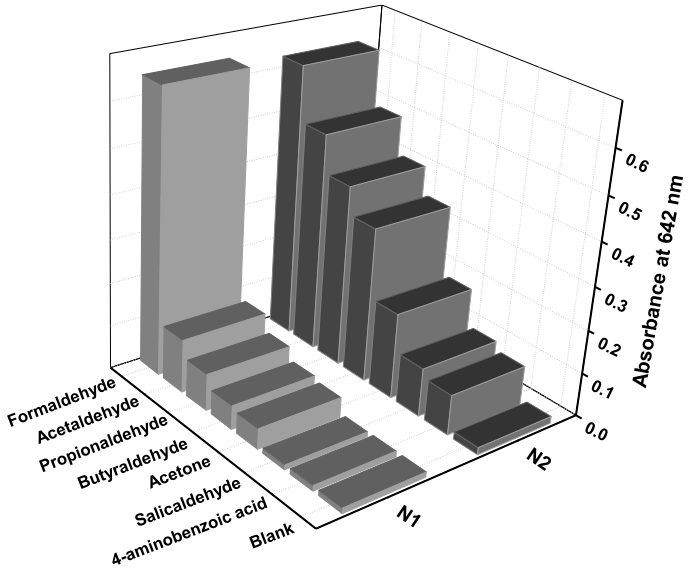

Figure 3. Absorbance at 642 nm (SQ band) for the PBS (0.01 M, pH 7.0) suspensions of nanoparticles **N1** and **N2** in the presence of selected aldehydes, ketones and carboxylic acids (0.1 mM) after 10 min.

In another experiment, the PBS solutions that contained the same quantity of 3-mercaptopropanol and diethylenetriamine as the content of thiol and polyamine in **N1** were mixed with formaldehyde, acetaldehyde, propionaldehyde and butyraldehyde, stirred for 5 min and SQ was added. Under these conditions the reaction between SQ and 3-mercaptopropanol was inhibited in the presence of all the tested aldehydes due to the formation of the corresponding alkylthio derivatives that were unable to react with SQ. More importantly this experiment demonstrated that a simple mixture of

amine, thiol and SQ was unable to induce a chemoselective response to formaldehyde, and preorganizing the amine and thiol groups on the silica surface was necessary to observe a selective response.

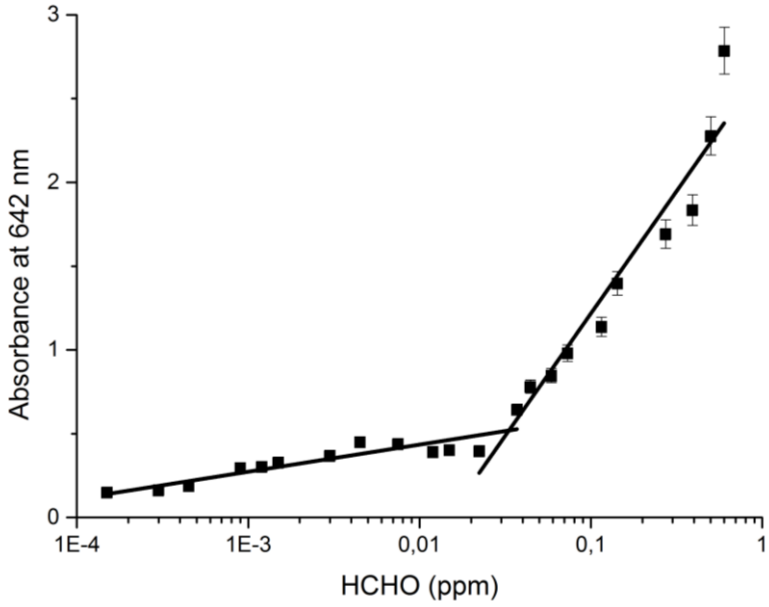

Figure 4. Absorbance at 642 nm for the PBS (0.01 M, pH 7.0) suspensions of **N1** in the presence of increasing amounts of formaldehyde and 15 min after adding SQ.

Then the sensitivity of the N1 nanoparticles was assessed. To do this, the chromogenic response of the PBS suspensions of the **N1** nanoparticles upon the addition of increasing amounts of formaldehyde was studied. The SQ dye absorption at 642 nm was gradually enhanced with increasing formaldehyde concentrations (see the Supporting Information). From the titration profile, an LOD of 1.2 μM (36 ppb) for formaldehyde was determined (see Figure 4).

Figure 5. Photograph of a 1.0 cm x 2.0 cm silica dipstick immersed into 2 ml of PBS (0.01 mM, pH 7.0) and with 0.18 ml of SQ (acetonitrile, 1.0 x 10^{-4} M). The right-hand stick was previously immersed into formaldehyde (1 mM) for 5 min, whereas the left-hand foil was directly immersed into PBS-SQ solution.

In order to enhance the applicability of our chromogenic system to detect formaldehyde, we prepared test strips by the simple functionalization of coated silica PET films with 3-[2-(2-aminoethylamino) ethylamino]propyltrimethoxysilane and (3-mercaptopropyl)trimethoxysilane (see the Supporting Information for details). In a typical test, functionalized sticks were immersed into PBS (pH 7.4) that either contained formaldehyde or did not (0.1 mM) for 5 min. Then SQ was added and the solution was stirred for 15 min. As seen in Figure 5, the solution of the stick that was reacted with formaldehyde remained blue, whereas clear bleaching was observed for the untreated foil.

The mechanism of the formaldehyde-selective colorimetric response observed was assessed by the ^{13}C MAS NMR measurements taken with the **N2** nanoparticles which were selected for the sake of clarity due to the absence of polyamine moieties. Figure 6 shows the chemical shifts in ppm of the different carbon atoms of the organic moieties grafted onto the external surface of nanoparticles, and ^{13}C MAS NMR of **N2** exhibited two signals

centered at 11.5 (-Si-$\underline{C}H_2$-CH_2-CH_2-SH) and 28.2 ppm (two carbons overlapped -Si-CH_2-$\underline{C}H_2$-$\underline{C}H_2$-SH). When **N2** reacted with formaldehyde, the signal centered at 28.2 ppm split into two new signals at 23.4 and 33.9 ppm and a new carbon appeared at 70.0 ppm, which was ascribed to an alkylthio methanol group. Similar information was obtained from the NMR studies carried out with **N1** (see the Supporting Information). Also, the reaction of SQ with thiol moieties in **N2** was studied by ^{13}C MAS NMR measurements (see the Supporting Information).

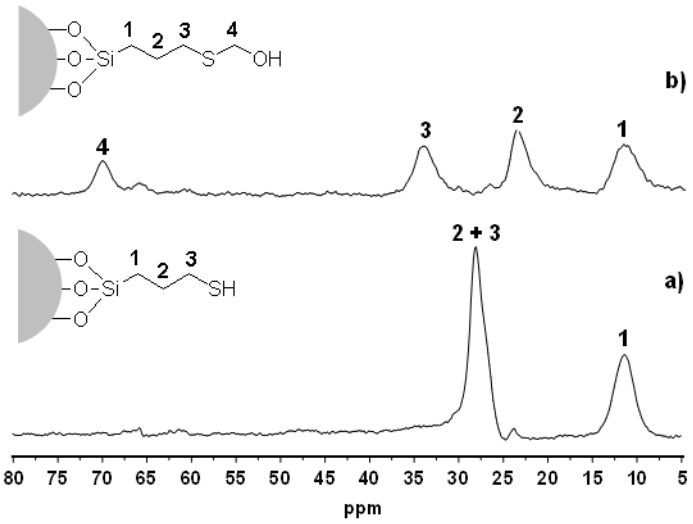

Figure 6. The ^{13}C MAS NMR spectra of the **N2** nanoparticles (a) before and (b) after being exposed to formaldehyde.

The sensing features of the **N1** nanoparticles to formaldehyde are remarkable when compared with other chromo-fluorogenic molecular probes described in the literature (see the Supporting Information for more details). In particular, the **N1**-SQ system only required 5 min to give a chromogenic response, whereas the reaction times for the other probes typically fell within the 6-180 min range.[22-25] When using the **N1** nanoparticles, the LOD for formaldehyde (0.036 ppm) was lower than those reported for other published probes (0.15-105 ppm).[22-25] We also observed

that the **N1** nanoparticles could be stored for 6 months with no evident loss of sensing features.

In summary, we prepared silica nanoparticles (**N1**) functionalized with thiols and polyamines for the selective chromogenic recognition of formaldehyde *vs.* other aldehydes. The sensing mechanism arises from the formaldehyde-induced inhibition of a thiol-SQ reaction after reacting formaldehyde with thiol groups. A selective response to formaldehyde was only observed when the thiols and polyamine groups were anchored to the silica surface. Bulky polyamines generated a highly polar environment around thiols, which were only able to reaction with the small and polar formaldehyde, but not with other aldehydes. Sensing material **N1** showed a LOD for formaldehyde of 36 ppb in water. The probe is very easy to prepare yet it is highly selective.

Acknowledgements

Financial support from the Generalitat Valencia (Project PROMETEOII/2014/047) and the Spanish Government (Project MAT2015-64139-C4-1-R) is gratefully acknowledged. S. E. is grateful to the Generalitat Valenciana for his Santiago Grisolia fellowship. Ll. P. thanks the Universidad Politécnica de Valencia for his grant.

REFERENCES

1 IARC Monographs on the Evaluation of Carcinogenic Risks to Humans, **2006**, *88*, 39.

2 Baan, R.; Grosse, Y.; Straif, K.; Secretan, B.; El Ghissanni, F.; Bouvard, V.; Benbrahim-Tallaa, L.; Guha, N.; Freeman, C.; Galichet, L.; Collagno, V. *Lancet Oncol.* **2009**, *10*, 1143.

3 Wang, J.; Liu, L.; Cong, S. –Y.; Qi, J. –Q.; Xu, B. –K. *Sens. Actuators, B* **2008**, *134*, 1010.

[4] US Environmental Protection Agency (US EPA). Formaldehyde (CASRN 50-00-0). Integrated Risk Information System. Document 0419. Washington (DC), USA, **1998**.

[5] Feron, V. J.; Til, H. P.; DeVrijer, F.; Woutersen, R. A.; Cassee, F. R.; van Bladeren, P. J. *Mutat. Res.* **1991**, *259*, 363.

[6] Yang, P.; Lau, C. W.; Liang, J. Y.; Lu, J. Z.; Liu, X. *Luminescence* **2007**, *22*, 473.

[7] Can, X. O.; Zhang, Z. Y.; Zhang, X. R. *Sens. Actuat. B* **2004**, *99*, 30.

[8] Bicanic, D.; Persijn, S.; Taylor, A.; Cozijnsen, J.; van Veldhuyzen, B.; Lenssen, G.; Wegh, H. *Rev. Sci. Instrum*. **2003**, *74*, 690.

[9] Moeskops, B. W. M.; Steeghs, M. M. L.; van Swam, K.; Cristescu, S. M.; Scheepers, P. T. J.; Harren, F. J. M. *Physiol. Meas*. **2006**, *27*, 1187.

[10] Bunkoed, O.; Davis, F.; Kanatharana, P.; Thavarungkul, P.; Higson, S. P. J. *Anal. Chim. Acta* **2010**, *659*, 251.

[11] Ohata, H.; Otsuka, M.; Ohmori, S. *J. Chromatogr., Biomed. Appl*. **1997**, *693*, 297.

[12] Li, Z.; Jacobus, L. K.; Wuelfing, W. P.; Golden, M.; Martin, G. P.; Reed, R. A. *J. Chromatogr. A* **2006**, *1104*, 1.

[13] Shi, D.; Wei, L.; Wang, J.; Zhao, J.; Chen, C.; Xu, D.; Geng, H.; Zhang, Y. *Sens. Actuators, B* **2013**, *177*, 370.

[14] Itoh, T.; Matsubara, I.; Shin, W.; Izu, N.; Nishibori, M. *Sens. Actuators, B* **2008**, *128*, 512.

[15] Mitsubayashi, K.; Matsunaga, H.; Nishio, G.; Toda, S.; Nakanishi, Y.; Saito, H.; Ogawa, M.; Otsuka, K. *Sens. Actuators, B* **2005**, *108*, 660.

[16] Lofdahl, M.; Utaiwasin, C.; Carlsson, A.; Lundstrom, I.; Eriksson, M. *Sens. Actuators, B* **2001**, *80*, 183.

[17] Zhu, Y.; Li, H.; Zheng, Q.; Xu, J.; Li, X. *Langmuir* **2012**, *28*, 7843.

[18] Heil, C.; Windscheif, G. R.; Braschohs, S.; Florke, J.; Glaser, J.; Lopez, M.; Muller-Albrecht, J.; Schramm, U.; Bargon, J.; Vogtle, F. *Sens. Actuators, B* **1999**, *61*, 51.

[19] Jacquinot, P.; Hodgson, A. W. E.; Muller, B.; Wehrli, B.; Hauser, P. C. *Analyst* **1999**, *124*, 871.

[20] Allouch, A.; Guglielmino, M.; Bernhardt, P.; Serra, C. A.; Le Calvé, S. *Sens. Actuat. B* **2013**, *181*, 551.

[21] Chung, P. –R.; Tzeng, C. –T.; Ke, M. –T.; Lee, C. –Y. *Sensors* **2013**, *13*, 4468.

[22] Li, Z.; Xue, Z.; Wu, Z.; Han, J.; Han, S. *Org. Biomol. Chem*. **2011**, *9*, 7652.

[23] Zhoua, W.; Dong, H.; Yan, Y.; Shi, C.; Yu, M.; Wei, L.; Li, Z. *Sens. Actuators, B*. **2015**, *209*, 664.

[24] Brewer, T. F.; Chang, C. J. *J. Am. Chem. Soc*. **2015**, *137*, 10886.

[25] Roth, A.; Li, H.; Anorma, C.; Chan, J. *J. Am. Chem. Soc.* **2015**, *137*, 10890.

[26] Climent, E.; Agostini, A.; Moragues, M. E.; Martínez-Máñez, R.; Sancenón, F.; Pardo, T.; Marcos M. D. *Chem. Eur. J*. **2013**, *19*, 17301.

[27] Climent, E.; Martí, A.; Royo, S.; Martínez-Máñez, R.; Marcos, M. D.; Sancenón, F.; Soto, J.; Costero, A. M.; Gil, S.; Parra, P. *Angew. Chem. Int. Ed*. **2010**, *49*, 5945.

[28] El Sayed, S.; Milani, M.; Licchelli, M.; Martínez-Máñez, R.; Sancenón, F. *Chem. Eur. J*. **2015**, *21*, 7002.

[29] Sugawara, M.; Kojima, K.; Sazawa, H.; Umezawa, Y. *Anal. Chem.* **1987**, *59*, 2842.

[30] Montalti, M.; Prodi, L.; Zaccheroni, N.; Falini, G. *J. Am. Chem. Soc.* **2002**, *124*, 13540.

Supporting Information

Chromogenic detection of aqueous formaldehyde using functionalized silica nanoparticles

Sameh El Sayed, [†,‡,§,II,‖] Lluis Pascual, [†,‡,§,‖] Maurizio Licchelli, [II*] Ramón Martínez-Máñez, [†,‡,§*] Salvador Gil[†,§,⊥] Ana M. Costero[†,§,⊥] and Félix Sancenón[†,‡,§]

[†] *Instituto de Reconocimiento Molecular y Desarrollo Tecnológico (IDM), Unidad Mixta Universidad Politécnica de Valencia-Universidad de Valencia, Spain.*

[‡] *Departamento de Química, Universidad Politécnica de Valencia, Camino de Vera s/n, 46022, Valencia, Spain. E-mail: rmaez@qim.upv.es.*

[§] *CIBER de Bioingeniería, Biomateriales y Nanotecnología (CIBER-BNN).*

[II] *Dipartimento di Chimica, Università di Pavia, via Taramelli 12, I-27100 Pavia, Italy. E-mail: maurizio.licchelli@unipv.it.*

[⊥] *Departamento de Química Orgánica, Universitat de València, Dr. Moliner 50, 46100, Burjassot, Valencia, Spain.*

Experimental section

A 30% suspension of ludox silica nanoparticles AS-30 colloidal silica was purchased from Sigma-Aldrich. Solvents were absolute grade and were purchased from Scharlab. Organosiloxane derivatives 3-[2-(2 aminoethylamino) ethylamino] propyltrimethoxysilane and (3-mercaptopropyl)trimethoxysilane were provided by Aldrich. Thermogravimetric analyses were carried out on a TGA/SDTA 851e Mettler Toledo balance. Transmission Electron Microscopy (TEM) images were obtained with a Philips CM10 that operated at 20 KeV. The samples for TEM were prepared by spreading a drop of nanoparticles solution in H_2O onto standard carbon-coated copper grids (200 mesh). UV-visible spectroscopy was carried out with a Lambda 35 UV/Vis Spectrometer (Perkin Elmer Instruments). ^{1}H and ^{13}C-NMR spectra were acquired in a BRUKER ADVANCE III (400 MHZ).

Preparation of coated silica N1 nanoparticles

Coated silica **N1** nanoparticles were prepared using the corresponding trialcoxysilane derivatives following the procedures reported by Montalti and coworkers.[1] Ludox silica nanoparticles AS-30, 18±2 nm average diameter, were added (12 mL) to a solution that contained acetic acid (60 mL), water (60 mL) and ethanol (100 mL). Then a mixture of 3-[2-(2-aminoethylamino) ethylamino]propyltrimethoxysilane (1.63 mmol) and (3-mercaptopropyl)trimethoxysilane (0.1636 mmol) was added to the suspension of nanoparticles. The mixture was heated to 80^{o}C for 48 h and solvents were evaporated. The functionalized nanoparticles (**N1**) were precipitated by centrifugation, washed with water and acetone, and dried at 70^{o}C.

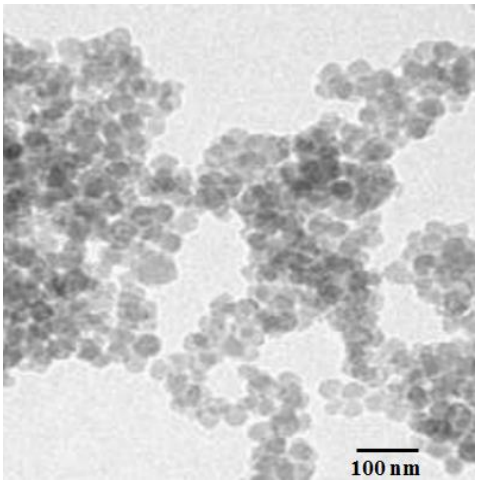

Figure S1. TEM image of **N2** hybrid nanoparticles.

Preparation of coated silica N2 nanoparticles

Coated silica **N2** nanoparticles were prepared using the corresponding trialcoxysilane derivatives following the procedures reported by Montalti and coworkers.[1] Ludox silica nanoparticles AS-30, 18±2 nm average diameter, were added (12 mL) to a solution that contained acetic acid (60 mL), water (60 mL) and ethanol (100 mL). Then (3-mercaptopropyl)trimethoxysilane (1.75 mmol) were added to the suspension of the nanoparticles. The mixture was heated to 80ºC for 48 h and solvents were evaporated. Functionalized **N2** were precipitated by centrifugation, washed with water and acetone, and dried at 70ºC. Figure S1 shows a TEM image of the final **N2** nanoparticles.

Preparation of test strips

Sensory test strips were prepared using commercially available silica gel plastic sheets for thin layer chromatography (Merck TLC silica gel 60 F_{254}). A silica gel rectangle (2 x 5 cm) was immersed into acetonitrile (20 mL) that contained 3-[2-(2-aminoethylamino)ethylamino]propyltrimethoxysilane

(1.63 mmol) and (3-mercaptopropyl)trimethoxysilane (0.16 mmol), and was then stirred at room temperature for 48 h. After this time, the silica rectangle was dried in air for 2 h. From the elemental analysis and the thermogravimetric measurements, the amounts of thiol (0.21 mmol/g SiO_2) and polyamine (0.97 mmol/g SiO_2) in the strips were measured.

TGA measurements

Thermogravimetric analyses were carried out under an air flow at a heating rate of 10ºC/minute within the 30-1000ºC interval. The final solid was maintained at 1000ºC for 30 minutes. Thermogravimetric studies with **N2** in the absence and presence of formaldehyde were carried out. In the thermogram of **N2** three clearly defined zones were observed: (i) from 30ºC to 150ºC, assigned to loss of water and organic solvents; (ii) from 150ºC to 800ºC, assigned to the organic matter attached to the nanoparticle surface; (iii) from 800ºC to 1000ºC, assigned to the condensation of silanol groups. The thermograms of **N2** in the presence of formaldehyde showed a similar behavior, but a greater loss of organic matter was obtained in this case (see Figure S2). This higher organic content was related with the formation of (alkylthio)methanol groups after formaldehyde reaction with the grafted thiols.

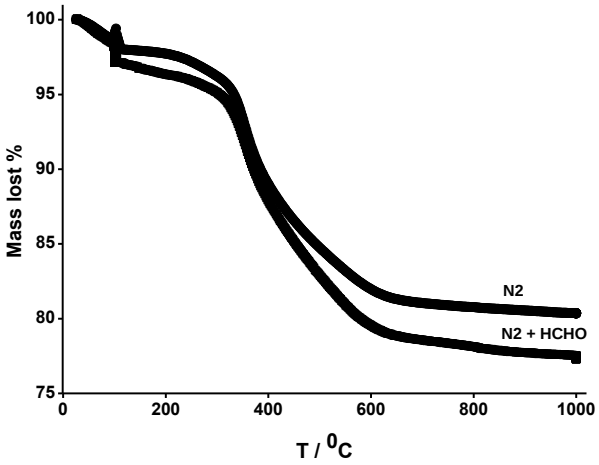

Figure S2. Mass loss (%) in the **N2** nanoparticles in the absence and presence of formaldehyde.

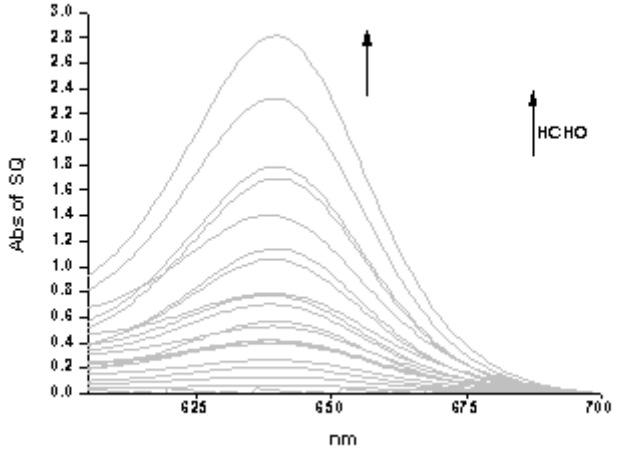

Figure S3. Absorbance at 642 nm (SQ band after 20 min of addition) of the SQ added to the PBS (0.01 M, pH 7.0) suspensions of **N1** when increasing the formaldehyde concentration.

NMR measurements

In order to fully understand the sensing mechanism, ^{1}H NMR studies with the D_2O solutions of 3-[2-(2 aminoethylamino) ethylamino] propyltrimethoxysilane and (3-mercaptopropyl)trimethoxysilane alone and in the presence of increasing quantities of formaldehyde were carried out. The ^{1}H NMR spectra of (3-mercaptopropyl)trimethoxysilane (Figure S4) showed signals of the propyl chain at ca. 0.90, 1.75 and 2.60 ppm (for the methylene connected to Si, the central methylene group and the protons of the carbon directly linked with the thiol moiety, respectively). Addition of increasing quantities of formaldehyde induced the progressive substitution of the signal centered at 2.60 ppm for two new resonances at 2.76 and 4.65 ppm. This latter signal partly overlapped the water signal, but was clearly visible upon heating at 4.80 ppm (see Figure S5). The observed shifts could be ascribed to a nucleophilic attack of thiol to the electrophilic carbon of the formaldehyde that yielded an (alkylthio)methanol moiety. The formation of the –S-CH_2-OH group was clearly confirmed by the appearance of a methylene carbon centered at 64.6 ppm (see Figure S6). The HSQC measurements (see Figure S7) also confirmed the reaction between thiol and formaldehyde. The possible reaction between polyamines and formaldehyde when solid **N1** was used was rejected because the ^{1}H and ^{13}C NMR experiments carried out with 3-[2-(2-aminoethylamino)ethylamino]propyltrimethoxysilane and formaldehyde in D_2O gave minor signal changes (data not shown).

^{13}C MAS NMR of the **N1** nanoparticles alone (see Figure S8) showed signals centered at ca. 12, 23 and 27 ppm, which could be ascribed to the methylene linked with the Si atoms, the central methylene group of the propyl chain and the carbon directly linked with the thiol moieties, respectively. A very broad signal within the 35-55 ppm range was observed

and attributed to the methylene groups directly connected with nitrogen atoms. The most remarkable change, observed when the **N1** nanoparticles were reacted with formaldehyde, was the appearance of a signal centered at 76.2 ppm, ascribed to a methylene directly connected with a sulfur atom and a hydroxyl moiety.

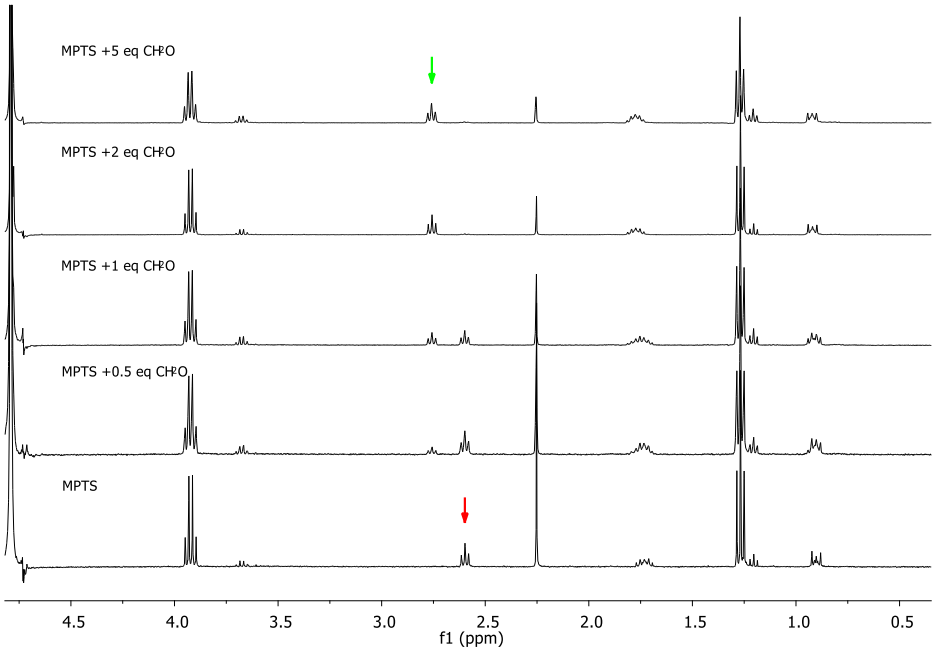

Figure S4. The ^{1}H NMR spectra of (3-mercaptopropyl)trimethoxysilane upon increasing formaldehyde concentrations.

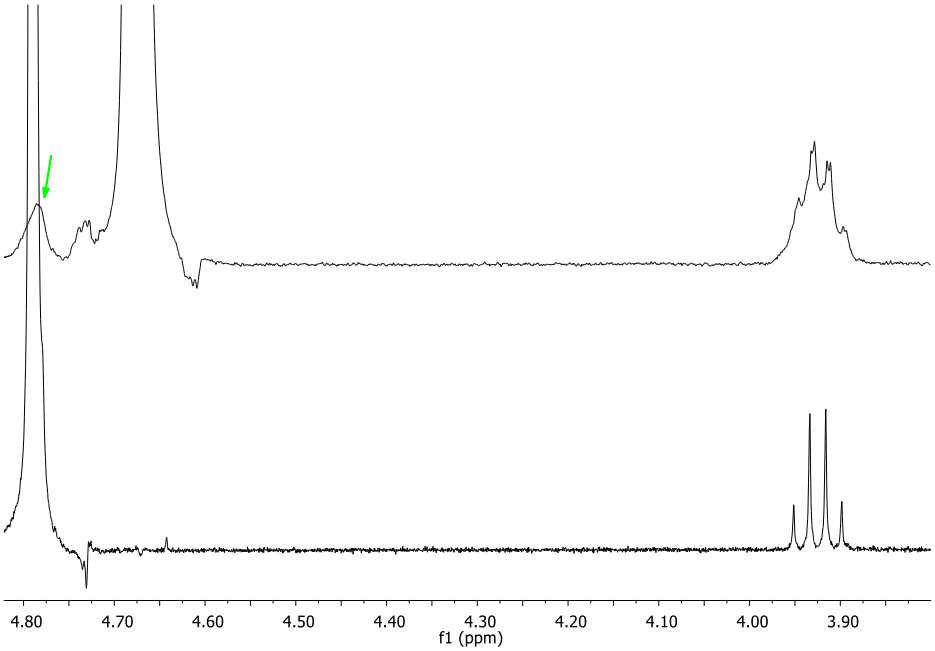

Figure S5. The ^{1}H NMR spectra of the product obtained upon the reaction between (3-mercaptopropyl)trimethoxysilane and formaldehyde (down) at 25°C and (up) at 35°C.

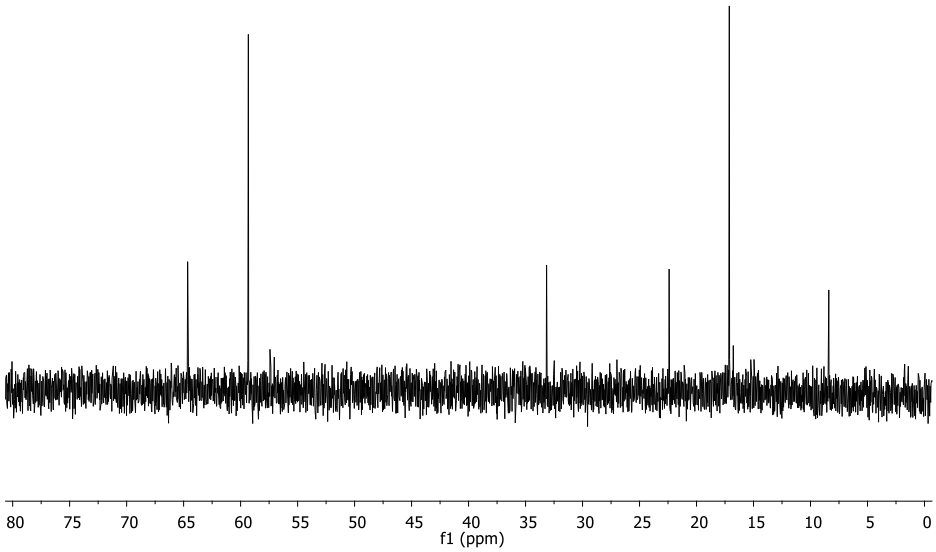

Figure S6. The 13C NMR spectra of the product formed upon the reaction of (3-mercaptopropyl)trimethoxysilane with formaldehyde.

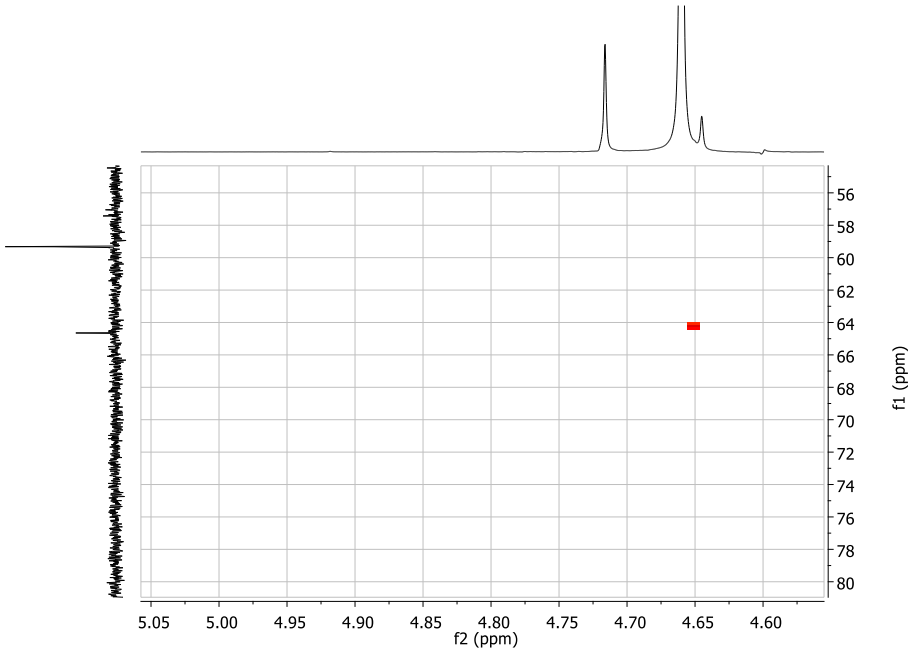

Figure S7. The HSQC NMR spectra of the product formed upon the reaction of (3-mercaptopropyl)trimethoxysilane with formaldehyde.

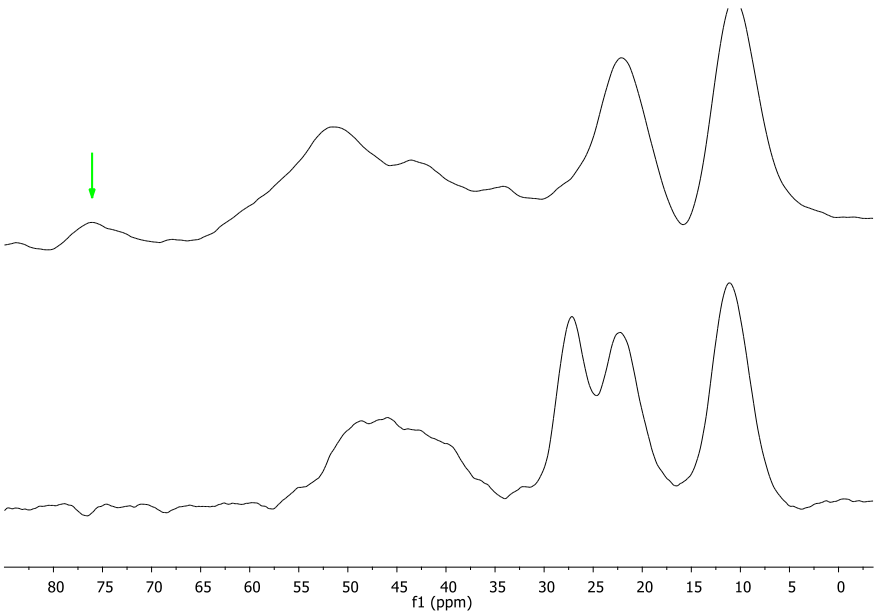

Figure S8. The ^{13}C MAS NMR spectra of the **N1** nanoparticles (down) before and (up) after the reaction with formaldehyde.

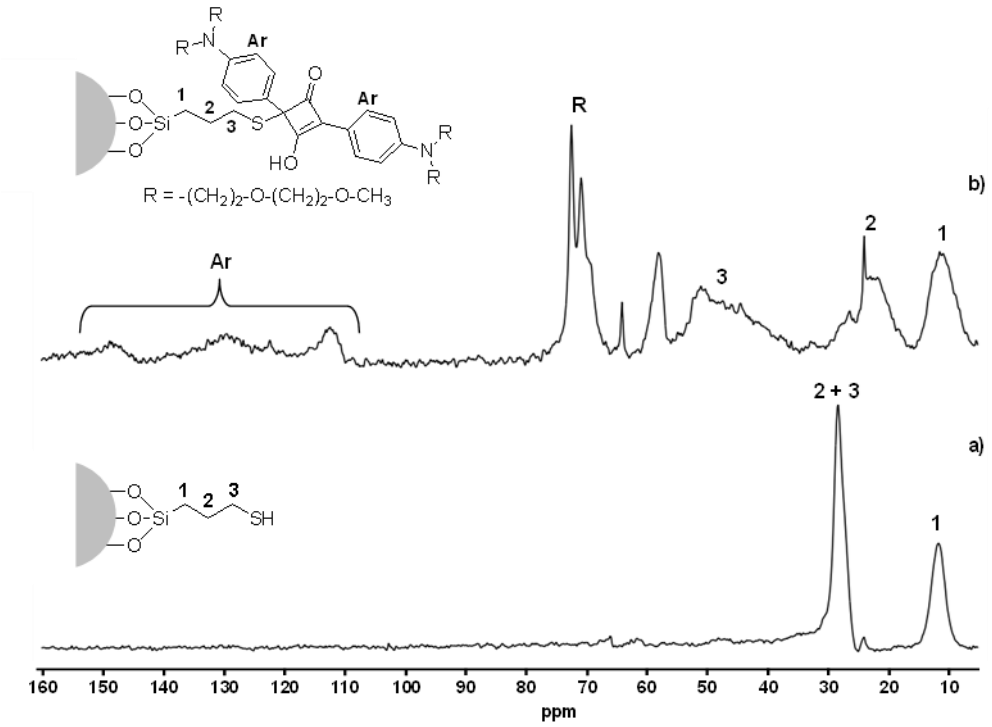

Figure S9. The ^{13}C MAS NMR spectra of the **N2** nanoparticles (a) before and (b) after the reaction with SQ dye.

The reaction of SQ with the thiol moieties, located onto the surface of **N1** and **N2** nanoparticles, was assessed by means of ^{13}C NMR measurements. At this respect, **N1** and **N2** nanoparticles were suspended in acetonitrile and then an excess of SQ dissolved in the same solvent was added. After 24 h, nanoparticles were filtered off and washed with acetonitrile and water. Finally, ^{13}C NMR MAS measurements of the nanoparticles reacted with SQ was carried out. The results obtained with **N2** nanoparticles (selected for the sake of clarity) are showed in Figure S9. As could be seen, upon reaction of the thiol subunits with SQ dye, signals of aromatic carbons appeared in the 110-150 ppm interval. These signals were clearly ascribed to the aromatic carbons of the SQ dye grafted onto the nanoparticle surface. Also, a

resonance at ca. 70 ppm appeared that was ascribed to the oligoethylene glycol chains. The appearance of the aromatic signals clearly pointed to a nucleophilic addition reaction of the thiols to the central electron deficient cyclobutane ring of the SQ dye.

Table S1. The sensing features of the published formaldehyde chromo-fluorogenic probes.

Sensor	Solvent	Selectivity	Time (min)	LOD (ppm)	Reference
N- (rhodamine B)-deoxylactam-ethylenediamine	DMF	formaldehyde hexanaldehyde 4-hydroxybenzaldehyde	90	105	*Org. Biomol. Chem.* **2011**, *9*, 7652
2-amidyl-3-(3-amidly- 1*H*-benzo[d]imidazolyl) -pyridine	water-ethanol 99:1	not reported	6	0.18	*Sens. Actuat. B.* **2015**, *209*, 664
homoallylamine-containing fluorescent probe	PBS buffer	formaldehyde	120	0.15	*J. Am. Chem. Soc.* **2015**, *137*, 10886
julolidine-based silicon rhodol fluorescent probe	PBS buffer	formaldehyde	180	0.30	*J. Am. Chem. Soc.* **2015**, *137*, 10890
Silica nanoparticles functionalized with thiol and amine moieties/squaraine dye	PBS buffer	formaldehyde	5	0.036	This paper

REFERENCES

[1] Montalti, M.; Prodi, L.; Zacheronni, N.; Falini, G. *J. Am. Chem. Soc.* **2002**, *124*, 13540.

Chapter 4:

Acetylcholinesterase-capped Mesoporous Silica Nanoparticle for detecting its inhibitors

Acetylcholinesterase capped mesoporous silica nanoparticles that open in the presence of diisopropylfluorophosphate (a Sarin or Soman simulant)

Lluís Pascual, [†,‡,§] Sameh El Sayed,[⊥] Ramón Martínez-Máñez,*[†,‡,§] Ana M. Costero,[†,§,||] Salvador Gil,[†,§,||] Pablo Gaviña[†,§,||] and Félix Sancenón*[†,‡,§]

[†] *Instituto de Reconocimiento Molecular y Desarrollo Tecnológico (IDM), Unidad Mixta Universidad Politécnica de Valencia-Universidad de Valencia, Spain.*

[‡] *Departamento de Química, Universidad Politécnica de Valencia, Camino de Vera s/n, 46022, Valencia, Spain. E-mail: rmaez@qim.upv.es.*

[§] *CIBER de Bioingeniería, Biomateriales y Nanotecnología (CIBER-BNN).*

[⊥] *Dipartimento di Chimica, Università di Pavia, via Taramelli 12, I-27100 Pavia, Italy. E-mail: maurizio.licchelli@unipv.it.*

[||] *Departamento de Química Orgánica, Universitat de València, Dr. Moliner 50, 46100, Burjassot, Valencia, Spain.*

Received: September 16, 2016
Accepted: October 18, 2016
Published online: October 18, 2016

Reprinted with permission from
Org. Lett. **2016**, *18,* 5548

Abstract

Mesoporous silica nanoparticles (MSNs) loaded with rhodamine B and capped with acetylcholinesterase are able to be selectively opened and deliver their cargo in the presence of nerve agent simulant diisopropyl fluorophosphate (DFP).

Nowadays, unfortunately, nerve agents have become a matter of concern for our society. Their use as chemical weapons in indiscriminate attacks carried out by terrorists and in armed conflicts boosted the interest of the international community on these lethal molecules.[1,2] Nerve agents are hazardous species because can disrupt certain functions of nervous system.[3–5] In this respect, nerve agents are known to cause severe toxicity because are able to inhibit acetylcholinesterase enzyme with the subsequent accumulation of acetylcholine in synaptic junctions, hindering muscle relaxation.[6] In addition, nerve agents are easily synthesized, and their indiscriminate use by terrorist organizations has directed interest toward remediation and detection studies of these lethal chemicals.[7–13]

The preparation of smart nanodevices based on mesoporous silica scaffolds (in the form of micro- or nanoparticles) has attracted much attention in recent years.[14–18] Mesoporous silicas present interesting features, such as large surface area, inertness, ease of functionalization using well-known alkoxysilane chemistries and presence of a highly ordered porous network.[19] One recently developed appealing concept that uses mesoporous scaffolds is the design of gated mesoporous materials. To prepare these gated systems, the pores of the inorganic scaffold are loaded with selected cargoes, and the external surface functionalized with certain (bio)molecules or supramolecular ensembles able to control the release of entrapped species upon the application of triggering stimuli. These gated materials have been

extensively used for the controlled release of drugs [20–24] and, more recently in sensing and diagnostic applications.[25–31]

In relation to nerve gases, the use of gated mesoporous supports is especially appealing and, for instance, the design of capped solids able to be selectively opened in the presence of a certain nerve agent in an aqueous environment can be envisioned. Such devices have not been developed, but applications may be found, for instance, in remediation protocols (via the delivery of molecules able to hydrolyze nerve agents),[32,33] as early detection systems (releasing a reporter in the presence of nerve agents)[34] or the release of a certain antidote.

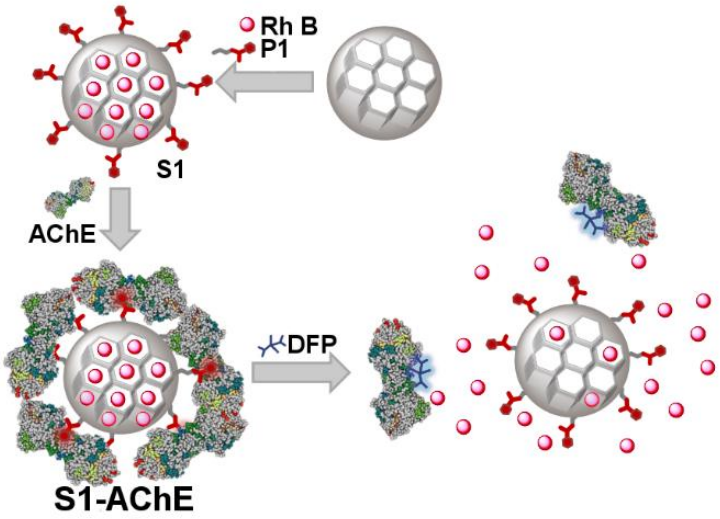

Scheme 1. Schematic representation of the sensing paradigm for DFP detection using solid **S1-AChE**.

In order to design such delivery systems, capable of being selectively opened in the presence of certain nerve gases, we focused herein on the use of mesoporous silica materials and enzymes. Enzymes are highly valuable molecules as they have proven exquisite selectivity in the design of advanced gated devices for on-command delivery applications.[23,35–40] In fact, several

enzyme-driven capped materials have been recently described, applied mainly for controlled release protocols in which a given cap is hydrolyzed in the presence of a certain enzyme.[15] In contrast, there are very few examples in which enzymes themselves are used as caps.[41]

Based on these concepts, we report herein the preparation of mesoporous silica nanoparticles (MSNs) capable of selectively opening and releasing an entrapped cargo (we selected a dye as a proof of concept) in the presence of DFP, which is a mimic of nerve agents Sarin or Soman. We employed the acetylcholinesterase (AChE) enzyme as the cap, rhodamine B as the cargo and directed experiments to detect DFP in aqueous environments. The design of the system is shown in Scheme 1. MSNs were firstly loaded with the rhodamine B dye and the surface was grafted with **P1**, a derivative of pyridostigmine, which is a well-known AChE inhibitor.[6] The interaction between **P1** and AChE was expected to block pores and avoid the entrapped dye from leaking. We speculated that the presence of a stronger AChE inhibitor, such as DFP, would induce a displacement of the enzyme from the solid surface and result in cargo release (see Scheme 1).

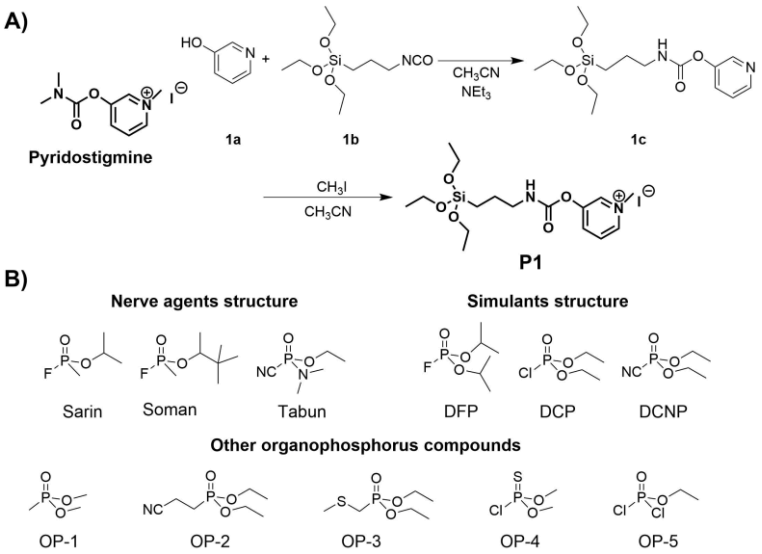

Scheme 2. A) Structure of the AChE inhibitor pyridostigimine and synthesis of **P1**. B) Chemical structure of nerve agent simulants and other organophosphorus derivatives tested.

MSNs were synthesized according to reported procedures.[42] The pores of the calcined mesoporous scaffold were loaded with fluorophore rhodamine B by simply stirring a suspension of nanoparticles in a concentrated acetonitrile solution of the dye. In another step, the external surface of nanoparticles was functionalized with pyridostigmine derivative **P1** to yield solid **S1**. **P1** was obtained by a 2-step procedure (see Scheme 2). In a first step 3-hydroxypyridine (**1a**) was reacted with (3-isocyanatopropyl)triethoxysilane (**1b**) to yield carbamate derivative **1c**. In a second step, the pyridine moiety in **1c** was quaternized upon the reaction with methyl iodide to yield **P1** (see Supporting Information) for further details). The final solid, **S1-AChE**, was prepared by suspending **S1** in an aqueous solution of AChE (TRIS buffer at pH 8.0) for 30 min (see Supporting Information). UV-visible studies of the solution before and after the capping

process allowed us to estimate that an amount of 250±40 μmols g^{-1} AChE was attached to the final solid.

The starting MSNs and solid **S1** were characterized following standard procedures (see Supporting Information for details). Powder X-ray diffraction (PXRD) and transmission electron microscopy (TEM), carried out on the starting MSNs, clearly showed the presence of a mesoporous structure that persisted in solid **S1** regardless of the loading process with rhodamine B and further functionalization with **P1** (see Figure 1). From the thermogravimetric and elemental analyses, rhodamine B (0.012 mmol/g SiO_2) and **P1** (0.93 mmol/g SiO_2) contents were determined. Table 1 lists the main structural properties (BET specific surface area, pore volumes and pore sizes) for the starting MSNs and **S1** obtained from the N_2 adsorption-desorption measurements (see Supporting Information for N_2 adsorption-desorption isotherms for calcined MCM-41 and **S1** and pore size distribution of calcined MCM-41 nanoparticles). The size of MSNs was assessed by TEM images, which gave an average particle diameter of 100±8 nm (see Figure 1).

The activity of AChE in **S1-AChE** was measured using the Elman´s assay and amounted to 1.97 U mg^{-1} (see Supporting Information for details). Remarkably the activity of the enzyme in **S1-AChE** was significantly reduced when compared to the free enzyme (101.41 U mg^{-1}) due to the coordination of the enzyme active site with the **P1** inhibitor.

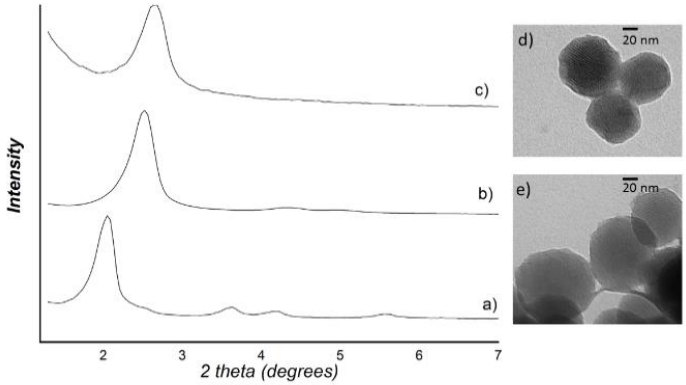

Figure 1. Left: Powder X-ray patterns of (a) MCM-41 as synthesized; (b) calcined MCM-41; (c) solid **S1**. Right: TEM images of (d) calcined MCM-41 and (e) solid **S1**.

Table 1. BET-specific surface values, pore volumes, and pore sizes calculated from the N2 adsorption-desorption isotherms.

solid	S_{BET} ($m^2\ g^{-1}$)	BJH pore size[a,c] (nm)	total pore volume[b] ($cm^3\ g^{-1}$)
MCM-41	747,5	2.45	0.334
S1	65,9	-	0.027

[a] Pore size was estimated by the BJH model, applied to the adsorption branch of the isotherm. [b,c] Pore volumes and pore sizes were associated with only intraparticle mesopores.

In a typical experiment, **S1-AChE** (500 µg) was suspended in TRIS buffer and the resulting suspension was divided into two parts. Both mixtures were diluted with TRIS until a final volume of 1 mL. Then 3 µL of DFP or water were added to suspensions. In both cases suspensions were stirred at room temperature, aliquots were extracted at certain times and the solid was removed by centrifugation. Dye delivery to the bulk solution was easily

detected by monitoring the emission band of rhodamine B at 572 nm upon excitation at 555 nm. The cargo release profile is shown in Figure 2. It can be seen that, in the absence of DFP, a poor rhodamine B release was found (less than 5% after 15 min and ca. 25% after 90 min). However, when DFP was present, a remarkable cargo delivery was observed (ca. 80% of maximum dye release after 15 min). The release of the entrapped rhodamine B was attributed to a preferential coordination of DFP with the active site of AChE enzyme. In fact it has been reported that DFP displays a stronger interaction with the AChE enzyme (half the maximal inhibitory concentration (IC_{50}) for DFP is 120 nM)[43] than that shown by pyridostigmine derivative **P1** (IC_{50} for pyridostigmine is 330 nM).[44] Moreover, the partial delivery of rhodamine B observed in the absence of DFP was ascribed to the fact that **P1** (as pyridostigmine) is a reversible inhibitor of AChE enzyme. As a consequence, a slow enzymatic hydrolysis of **P1** occurs with subsequent detachment of enzyme from the surface and dye release.

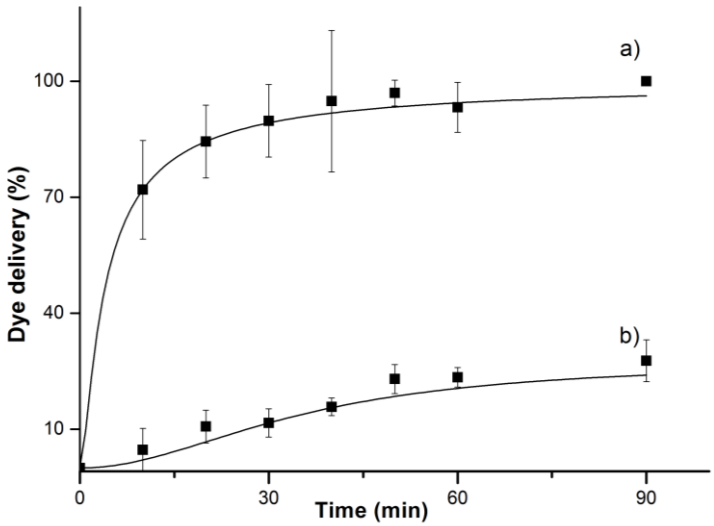

Figure 2. Kinetics of the release of rhodamine B from solid **S1-AChE** (a) in the presence of DFP and (b) in the absence of DFP.

Cargo release from **S1-AChE**, in the absence and in the presence of DFP, was monitored at pH 8.0 because this is the optimal proton concentration for the AChE enzyme. However, following a similar procedure, cargo release from **S1-AChE** was also studied at pH 4.0 and 6.0 (see Supporting Information). Cargo release profiles at these pHs were quite similar to that found at pH 8.0. However, at pH 4.0 and 6.0, in the absence of DFP, a greater pore closure was observed, and in the presence of DFP, the release of rhodamine B was reduced at short times when compared with the delivery profiles at pH 8. These observations are most likely due to the lower AChE enzymatic activity at acidic pH.

To assess the selective aperture of **S1-AChE** with DFP, the fluorogenic response of **S1-AChE** in the presence of other nerve agent simulants and some other organophosphorus compounds was tested (see Scheme 2 for chemical structures). Figure 3 shows the emission of rhodamine B in the solution at 572 nm 15 min after adding these organophosphorous derivatives (1000 ppm) to the buffered suspensions of **S1-AChE**. It is apparent from Figure 3 that **S1-AChE** is highly selective for DFP, whereas other simulants such as DCP, DCNP, and other organophosphorous derivatives such as OP1-OP5, were unable to induce remarkable cargo delivery.

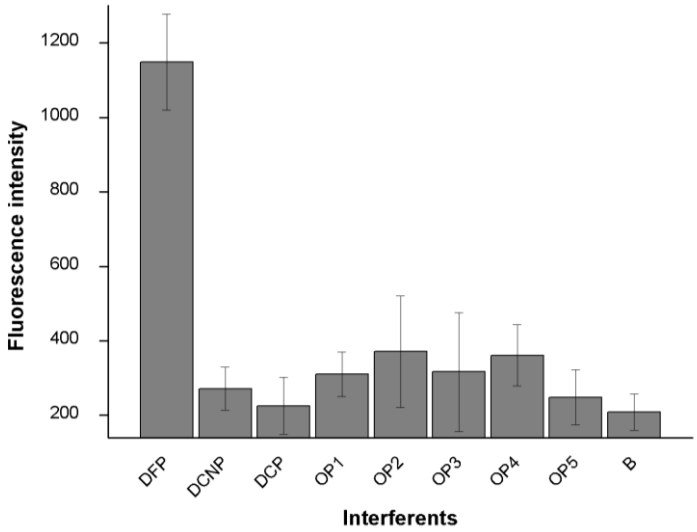

Figure 3. Emission intensity of rhodamine B at 572 nm (excitation at 555 nm) released from solid **S1-AChE** (TRIS, pH 8.0) in the presence of selected organophosphorous derivatives (1000 ppm) after 15 min after addition.

In order to test sensitivity in terms of the cargo release of **S1-AChE** for DFP, the fluorogenic response obtained upon the addition of increasing quantities of this nerve agent simulant (after 15 min) was tested. As seen in Figure 4, a clear correlation between DFP concentration and rhodamine B release was observed, which agreed with an uncapping protocol that involved AChE displacement from the surface of MSNs. From the titration profile shown in Figure 4, a limit of detection (LOD) for DFP as low as 0.28 ppm was determined.

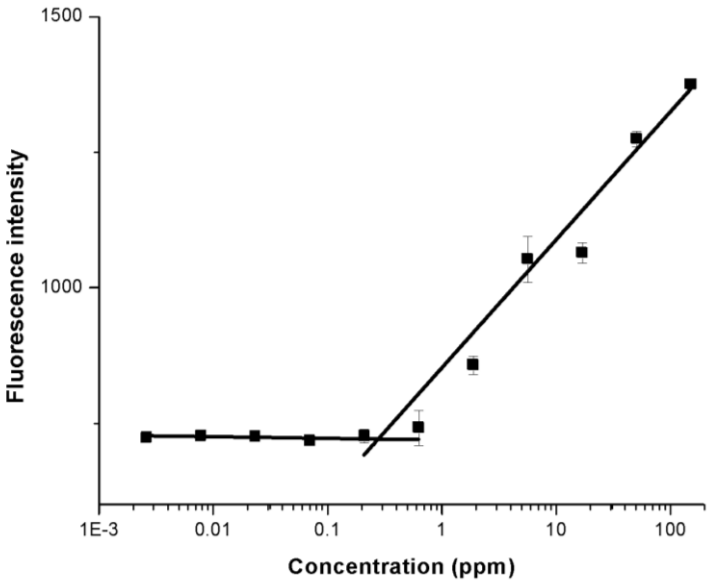

Figure 4. Release of rhodamine B from solid **S1-AChE** in the presence of different amounts of DFP in TRIS buffer at pH 8.0 15 min after addition.

Sensing features of **S1-AChE** for the detection of DFP in aqueous environments are similar to other reported probes (see Supporting Information). **S1-AChE** displays a remarkable selectivity toward DFP and slower response time (15 min), when compared with other probes, which are in the range of few minutes (from 0.5 to 5). The slower response observed with **S1-AChE** was ascribed to several factors. In this respect, in order to detach AChE from the surface of the solid, DFP must first displace **P1**. Then, once DFP-AChE pair is formed, the rhodamine dye must diffuse from the porous structure to the bulk solution. This multistep mechanism is slower than that in other probes reported in the literature. Besides, the LOD of other published chemosensors ranged from 21 ppt to 147 ppm with the measured for **S1-AChE** nanoparticles (0.28 ppm) located in the lower part of the interval.

Finally, in order to assess the use of **S1-AChE** for DFP detection in a more realistic setting, we measured cargo release profiles from **S1-AChE** in tap water (pH 7.65, 637 μS cm^{-1}) in the absence and in the presence of DFP (3μL). The obtained profiles were quite similar to those found in buffered solutions (see Supporting Information) pointing toward a possible use of **S1-AChE** solid for the detection of DFP in real competitive media.

In summary, we report herein the synthesis, characterization and delivery behavior of a new hybrid material functionalized with a pyridostigmine derivative and capped with AChE. The gated support is only able to open and deliver the cargo in the presence of nerve agent simulant DFP among other simulants and organophosphorous derivatives. As a proof of concept, we used this material for sensing DFP in aqueous solution by employing reporter rhodamine B as the cargo. The fluorogenic response obtained in the presence of DFP is a consequence of competitive DFP binding with the active site of the AChE, which resulted in cargo delivery. The response of capped nanoparticles is highly selective and sensitive to DFP with an LOD of 0.28 ppm. Despite our particular application to detect DFP, we believe that the design of materials capable of selectively delivering a cargo in the presence of nerve agents has enormous potential for preparing smart materials for other applications in which delivery of remediation molecules or antidotes when nerve gases are present might be of much relevance. Studies along these lines are currently being carried out in our laboratory.

Acknowledgements

Financial support from the Spanish Government and FEDER funds (Project MAT2015-64139-C4-1) and the Generalitat Valencia (Project PROMETEOII/2014/047) is gratefully acknowledged. Ll. P. is grateful to the Universitat Politécnica de Valencia for his grant.

REFERENCES

1 Kelle, A. *Int. Aff.* **2013**, *89*, 143.

2 Cardoza, R. *Anu. Colomb. Derecho Int.* **2015**, *8*, 17.

3 Wheelis, M. *Pure Appl. Chem.* **2002**, *74*, 2247.

4 Augerson, W. S. *Chem. Biol. Warf. Agents* **2000**, 99.

5 *Chemical Warfare Agents* Ed.: S. M. Somani, Academic Press, London, **1992**.

6 Rang, H. P.; Dale, M.; Ritter, J. M.; Flower, R. J.; Henderson, G. *Rang & Dale's Pharmacology*, 8th ed.; Elsevier Churchill Livingstone: London, England, **2015**.

7 Ajami, D.; Rebek, J. *Org. Biomol. Chem.* **2013**, *11*, 3936.

8 El Sayed, S.; Pascual, L.; Agostini, A.; Martínez-Máñez, R.; Sancenón, F.; Costero, A. M.; Parra, M.; Gil, S. *ChemistryOpen* **2014**, *3*, 142.

9 Eubanks, L. M.; Dickerson, T. J.; Janda, K. D. *Chem. Soc. Rev.* **2007**, *36*, 458.

10 Hiscock, J. R.; Sambrook, M. R.; Wells, N. J.; Gale, P. A. *Chem. Sci.* **2015**, *6*, 5680.

11 Singh, V. V; Wang, J. *Nanoscale* **2015**, *7*, 19377.

12 Smith, B. M. *Chem. Soc. Rev.* **2008**, *37*, 470.

13 Pascual, L.; Campos, I.; Bataller, R.; Olguín, C.; García-Breijo, E.; Martínez-Mañez, R.; Soto, J. *Sensor. Actuat. B-Chem.* **2014**, *192*, 134.

14 Alberti, S.; Soler-Illia, G. J. A. A.; Azzaroni, O. *Chem. Commun.* **2015**, *51*, 6050.

[15] Aznar, E.; Oroval, M.; Pascual, L.; Murguía, J. R.; Martínez-Máñez, R.; Sancenón, F. *Chem. Rev.* **2016**, *116*, 561.

[16] Li, Z.; Barnes, J. C.; Bosoy, A.; Stoddart, J. F.; Zink, J. I. *Chem. Soc. Rev.* **2012**, *41*, 2590.

[17] Lu, C. -H.; Willner, I. *Angew. Chem. Int. Ed.* **2015**, *54*, 12212.

[18] Slowing, I. I.; Trewyn, B. G.; Giri, S.; Lin, V. S. -Y. *Adv. Funct. Mater.* **2007**, *17*, 1225.

[19] Rurack, K.; Martínez-Mánez, R. *The Supramolecular Chemistry of Organic-Inorganic Hybrid Materials*; Wiley-VCH Verlag, **2010**.

[20] Lee, J.; Kim, H.; Kim, S.; Lee, H.; Kim, J.; Kim, N.; Park, H. J.; Choi, E. K.; Lee, J. S.; Kim, C. *J. Mater. Chem.* **2012**, *22*, 14061.

[21] Torney, F.; Trewyn, B. G.; Lin, V. S. -Y.; Wang, K. *Nat. Nanotechnol.* **2007**, *2*, 295.

[22] Mal, N. K.; Fujiwara, M.; Tanaka, Y. *Nature* **2003**, *421*, 350.

[23] Agostini, A.; Mondragon, L.; Bernardos, A.; Martínez-Mañez, R.; Marcos, M. D.; Sancenón, F.; Soto, J.; Costero, A. M.; Manguan-Garcia, C.; Perona, R.; Moreno-Torres, M.; Aparicio-Sanchis, R.; Murguía, J. R. *Angew. Chem. Int. Ed.* **2012**, *51*, 10556.

[24] Meng, H. A.; Xue, M.; Xia, T. A.; Zhao, Y. L.; Tamanoi, F.; Stoddart, J. F.; Zink, J. I.; Nel, A. E. *J. Am. Chem. Soc.* **2010**, *132*, 12690.

[25] a) Sancenón, F.; Pascual, L.; Oroval, M.; Aznar, E.; Martínez-Mañez, R. *ChemistryOpen*, **2015**, 4, 418; b) Aznar, E.; Martínez-Máñez, R.; Sancenón, F. *Expert Opin. Drug Del.* **2009**, 6, 643; c) Tang, D.; Lin, Y.; Zhou, Q.; Lin, Y.; Li, P.; Niessner, R.; Knopp, D. *Anal. Chem.* **2014**, *86*, 11451.

[26] Zhao, Y. N.; Trewyn, B. G.; Slowing, I. I.; Lin, V. S. -Y. *J. Am. Chem. Soc.* **2009**, *131*, 8398.

[27] Climent, E.; Mondragon, L.; Martínez-Mañez, R.; Sancenón, F.; Marcos, M. D.; Murguía, J. R.; Amoros, P.; Rurack, K.; Perez-Paya, E. *Angew. Chem. Int. Ed.* **2013**, *52*, 8938.

[28] Zhang, Z. X.; Balogh, D.; Wang, F. A.; Willner, I. *J. Am. Chem. Soc.* **2013**, *135*, 1934.

[29] Hernandez, F. J.; Hernandez, L. I.; Pinto, A.; Schafer, T.; Ozalp, V. C. *Chem. Commun.* **2013**, *49*, 1285.

[30] Salinas, Y.; Martínez-Máñez, R.; Jeppesen, J. O.; Petersen, L. H.; Sancenón, F.; Marcos, M. D.; Soto, J.; Guillem, C.; Amoros, P. *ACS Appl. Mater. Interfaces* **2013**, *5*, 1538.

[31] Oroval, M.; Climent, E.; Coll, C.; Eritja, R.; Avino, A.; Marcos, M. D.; Sancenón, F.; Martínez-Máñez, R.; Amoros, P. *Chem. Commun.* **2013**, *49*, 5480.

[32] Candel, I.; Marcos, M. D.; Martínez-Máñez, R.; Sancenón, F.; Costero, A. M.; Parra, M.; Gil, S.; Guillem, C.; Perez-Pla, F.; Amoros, P. *Micropor. Mesopor. Mat.* **2015**, *217*, 30.

[33] Barba-Bon, A.; Martínez-Mañez, R.; Sancenón, F.; Costero, A. M.; Gil, S.; Perez-Pla, F.; Llopis, E. *J. Hazard. Mater.* **2015**, *298*, 73.

[34] Candel, I.; Bernardos, A.; Climent, E.; Marcos, M. D.; Martínez-Máñez, R.; Sancenón, F.; Soto, J.; Costero, A. M.; Gil, S.; Parra, M. *Chem. Commun.* **2011**, *47*, 8313.

[35] Agostini, A.; Mondragon, L.; Pascual, L.; Aznar, E.; Coll, C.; Martínez-Máñez, R.; Sancenón, F.; Soto, J.; Marcos, M. D.; Amoros, P.; Costero, A. M.; Parra, M.; Gil, S. *Langmuir* **2012**, *28*, 14766.

[36] Radhakrishnan, K.; Tripathy, J.; Gnanadhas, D. P.; Chakravortty, D.; Raichur, A. M. *RSC Adv.* **2014**, *4*, 45961.

[37] Park, C.; Kim, H.; Kim, S.; Kim, C. *J. Am. Chem. Soc.* **2009**, *131*, 16614.

[38] Villalonga, R.; Díez, P.; Sánchez, A.; Aznar, E.; Martínez-Máñez, R.; Pingarron, J. M. *Chem. Eur. J.* **2013**, *19*, 7889.

[39] Coll, C.; Mondragon, L.; Martínez-Máñez, R.; Sancenón, F.; Marcos, M. D.; Soto, J.; Amoros, P.; Perez-Paya, E. *Angew. Chem. Int. Ed.* **2011**, *50*, 2138.

[40] Patel, K.; Angelos, S.; Dichtel, W. R.; Coskun, A.; Yang, Y. W.; Zink, J. I.; Stoddart, J. F. *J. Am. Chem. Soc.* **2008**, *130*, 2382.

[41] (a) Chen, M. J.; Huang, C. S.; He, C. S.; Zhu, W. P.; Xu, Y. F.; Lu, Y. F. *Chem. Commun.* **2012**, *48*, 9522. (b) Aznar, E.; Villalonga, R.; Giménez, C.; Sancenón, F.; Marcos, M. D.; Martínez-Máñez, R.; Díez, P.; Pingarrón, J. M.; Amorós, P. *Chem. Commun.* **2013**, *49*, 639. (c) Díez P.; Sánchez, A.; de la Torre, C.; Gamella, M.; Martínez-Ruíz, P.; Aznar, E.; Martínez-Máñez, R.; Pingarrón, J. M.; Villalonga, R. *ACS Appl. Mater. Interfaces* **2016**, *8*, 7657.

[42] (a) Kresge, C. T.; Leonowicz, M. E.; Roth W. J.; Vartuli, J. C.; Beck, J. S. *Nature* **1992**, *359*, 710. (b) El Haskouri, J.; Ortiz de Zarate, D.; Guillem, C.; Latorre, J.; Caldés, M.; Beltán, A.; Beltrán, D.; Descalzo, A. B.; Rodríguez-López, G.; Martínez-Máñez, R.; Marcos, M. D., Amorós P. *Chem. Commun*. **2002**, 330.

[43] Al, E. T.; Chan, K.; Jensen, N.; Brien, P. J. O. *J. Appl. Toxicol.* **2008**, *28*, 608.

[44] Lorke, D. E.; Hasan, M. Y.; Nurulain, S. M.; Shafiullah, M.; Kuca, K.; Petroianu, G. A. *J. Appl. Toxicol.* **2011**, *31*, 515.

Supporting Information

Acetylcholinesterase capped mesoporous silica nanoparticles that open in the presence of diisopropylfluorophosphate (a Sarin or Soman simulant)

Lluís Pascual, [†,‡,§] Sameh El Sayed,[⊥] Ramón Martínez-Máñez,*[†,‡,§] Ana M. Costero,[†,§,||] Salvador Gil,[†,§,||] Pablo Gaviña[†,§,||] and Félix Sancenón*[†,‡,§]

[†] *Instituto de Reconocimiento Molecular y Desarrollo Tecnológico (IDM), Unidad Mixta Universidad Politécnica de Valencia-Universidad de Valencia, Spain.*

[‡] *Departamento de Química, Universidad Politécnica de Valencia, Camino de Vera s/n, 46022, Valencia, Spain. E-mail: rmaez@qim.upv.es.*

[§] *CIBER de Bioingeniería, Biomateriales y Nanotecnología (CIBER-BNN).*

[⊥] *Dipartimento di Chimica, Università di Pavia, via Taramelli 12, I-27100 Pavia, Italy. E-mail: maurizio.licchelli@unipv.it.*

[||] *Departamento de Química Orgánica, Universitat de València, Dr. Moliner 50, 46100, Burjassot, Valencia, Spain.*

General techniques: Powder X-ray diffraction (PXRD), thermogravimetric analysis (TGA), elemental analysis, transmission electron microscopy (TEM), N_2 adsorption-desorption, UV-visible (UV-vis) and fluorescence spectroscopy were employed to characterize synthesized materials. PXRD measurements were taken on a D8 Advance diffractometer using CuKα radiation (Philips, Amsterdam, The Netherlands). Thermogravimetric analyses were carried out on a TGA/SDTA 851e balance (Mettler Toledo, Columbus, OH, USA) in an oxidizing atmosphere (air, 80 mL min^{-1}) with a heating program: gradient of 393-1273 K at 10°C min^{-1}, followed by an isothermal heating step at 1273°C for 30 min. TEM images were obtained with a 100 kV CM10 microscope (Philips). N_2 adsorption-desorption isotherms were recorded with a Tristar II Plus automated analyzer (Micromeritics, Norcross, GA, USA). The samples were degassed at 120°C in vacuum overnight. The activation step at 120°C in vacuum overnight was carried out only with calcined MCM-41 and with **S1** (loaded with rhodamine B, with **P1** grafted onto the external surface of the nanoparticles and without enzyme). Specific surface areas were calculated from the adsorption data within the low pressure range using the Brunauer, Emmett and Teller (BET) model. Pore size was determined following the Barret, Joyner and Halenda (BJH) method. Fluorescence spectroscopy measurements were taken on a Felix 32 Analysis, version 1.2 (Build 56, Photon Technology International, Birmingham, NJ, USA), and by a JASCO FP-8500 spectrophotometer. High-resolution mass spectra were recorded in the positive ion mode with a VG-AutoSpec mass spectrometer.

Chemicals: Tetraethylorthosilicate (TEOS), *n*-cetyltrimethylammonium bromide (CTAB), sodium hydroxide, (3-isocyanatopropyl)triethoxysilane, 3-hydroxypyridine, methylene iodide, triethylamine, rhodamine B, acetonitrile, tris(hidroxymethyl)aminomethane (TRIS), hydrochloric acid,

diisopropyl fluorophosphate (DFP), diethyl chlorophosphate (DCP), diethyl cyanophosphonate (DCNP), dimethylmethyl phosphonate (OP-1), diethyl (2-cyanoethyl) phosphonate (OP-2), diethyl (methylthiomethyl) phosphonate (OP-3), dimethyl chlorothiophosphate (OP-4) and ethyl dichlorophosphate (OP-5) were purchased from Sigma-Aldrich Química (Madrid, Spain). All the products were used as received.

Synthesis of MCM-41 mesoporous nanoparticles: NaOH (2.00 mol L^{-1}, 3.5 mL) was added to a solution of CTAB (1.00 g, 2.74 mmol) in deionized H_2O (480 mL). The solution temperature was adjusted to 80°C and then TEOS (5.00 mL, 2.57 × 10^{-2} mol) was added dropwise to the surfactant mixture. The mixture was stirred for 2 h to give a white precipitate. The solid was isolated by centrifugation and washed with deionized H_2O and EtOH, and then dried at 60°C for 12 h to give MCM-41. In order to remove the template phase, MCM-41 was calcined at 550°C in an oxidizing atmosphere.

Synthesis of 1c: 3-hydroxypyridine (**1a**; 0.5 g, 5.26 mmol) was dissolved in CH_3CN (20 mL) and then (3-isocyanatopropyl)triethoxysilane (**1b**; 1.3 mL, 5.26 mmol) was added to the solution. A catalytic amount of triethylamine (110 μL) was added. The mixture was kept under stirring at room temperature for 4 h. The intermediate product (**1c**; 1.71 g, 5 mmol, 95%) was isolated, as light yellow oil, by evaporating the solvent in a rotary evaporator. ^{1}H NMR (400 MHz, $CDCl_3$) δ 8.43 (s, 1H), 8.42 (br m, 1H), 7.54 (d, J=8.8 Hz 1H), 7.3 (t, J=6.5 Hz, 1H), 5.59 (br s, 1H), 3.83 (q, 6H), 3.29 (t, J=6.6 Hz 2H), 1.72 (m, J=7.0 Hz 2H), 1.23 (t, J=7.0 Hz, 9H), 0.68 (t, J=7.7 Hz, 2H). ^{13}C NMR (101 MHz, $CDCl_3$) δ 154.2, 148.2, 146.4, 143.7, 129.7, 123.9, 58.9, 44.0, 23.4, 18.7, 8.2. HRMS-EI *m/z*: calcd for $C_{15}H_{27}N_2O_5Si$ 343.1684; found: 343.1688 $[M+H]^+$.

Synthesis of P1: **1c** (1.71 g, 5 mmol) was dissolved in CH_3CN (15 mL) and reacted with methylene iodide (3.3 mL, 52 mmol) for 20 h. Final product **P1** (2.3 g, 4.7 mmol, 94%) was obtained as a yellow oil by evaporating the solvent and methylene iodide using a rotary evaporator. ^1H NMR (400 MHz, $CDCl_3$) δ 9.09 (br m, 1H), 9.07 (s, 1H), 8.33 (dd, J=8.8 Hz 1H), 8.10 (t, J=6.5 Hz, 1H), 6.31 (br s, 1H), 4.68 (s, 3H), 3.84 (q, 6H), 3.29 (t, J=6.6 Hz 2H), 1.75 (m, J=7.0 Hz 2H), 1.24 (t, J=7.0 Hz, 9H), 0.69 (t, J=7.7 Hz, 2H). ^{13}C NMR (101 MHz, $CDCl_3$) δ 151.5, 150.7, 138.9, 137.8, 128.6, 128.2, 58.6, 50.1, 43.9, 22.7, 18.3, 7.7. HRMS-EI *m/z*: calcd for $C_{16}H_{29}N_2O_5Si^+$ 357.1840; found: 357.1836.

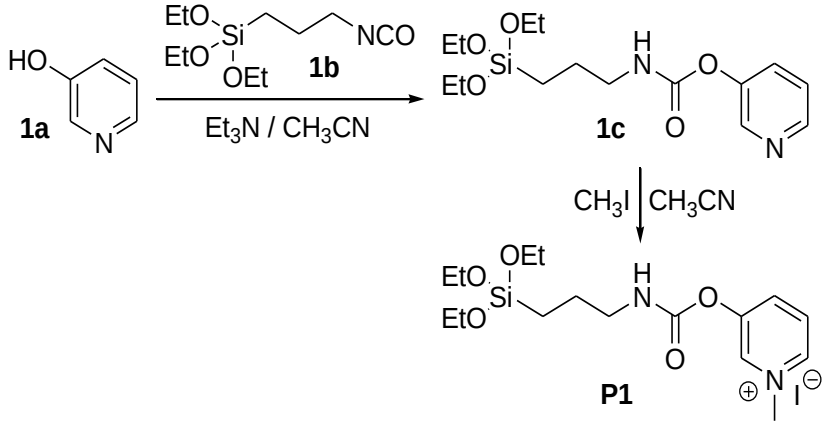

Scheme S1. Synthetic procedure to prepare alcoxysilane derivative **P1**.

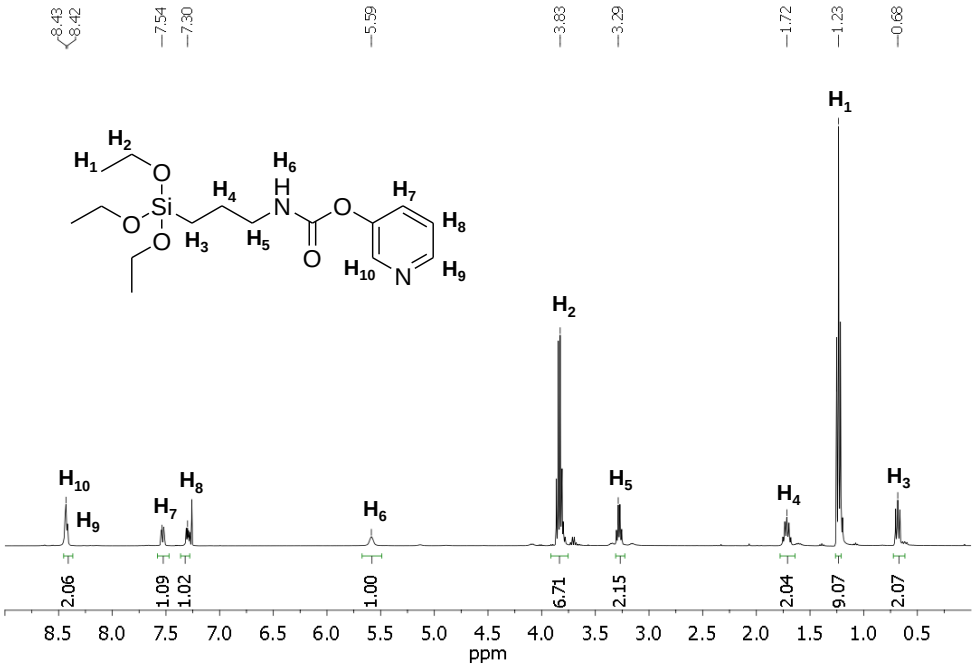

Figure S1. ^{1}H-NMR spectra of **1c** in $CDCl_3$.

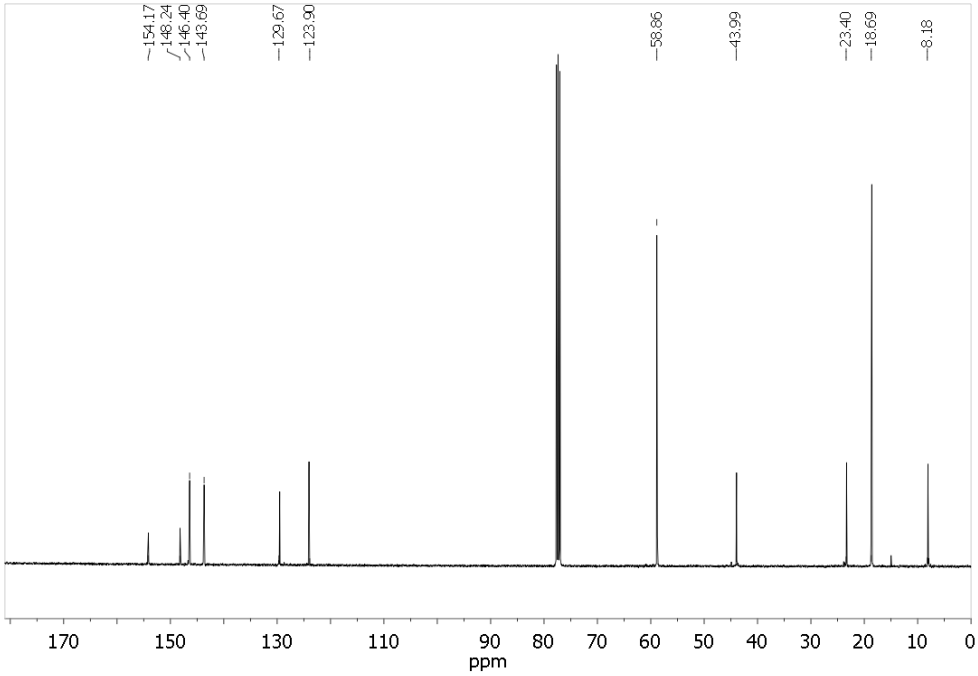

Figure S2. ^{13}C-NMR spectra of **1c** in $CDCl_3$.

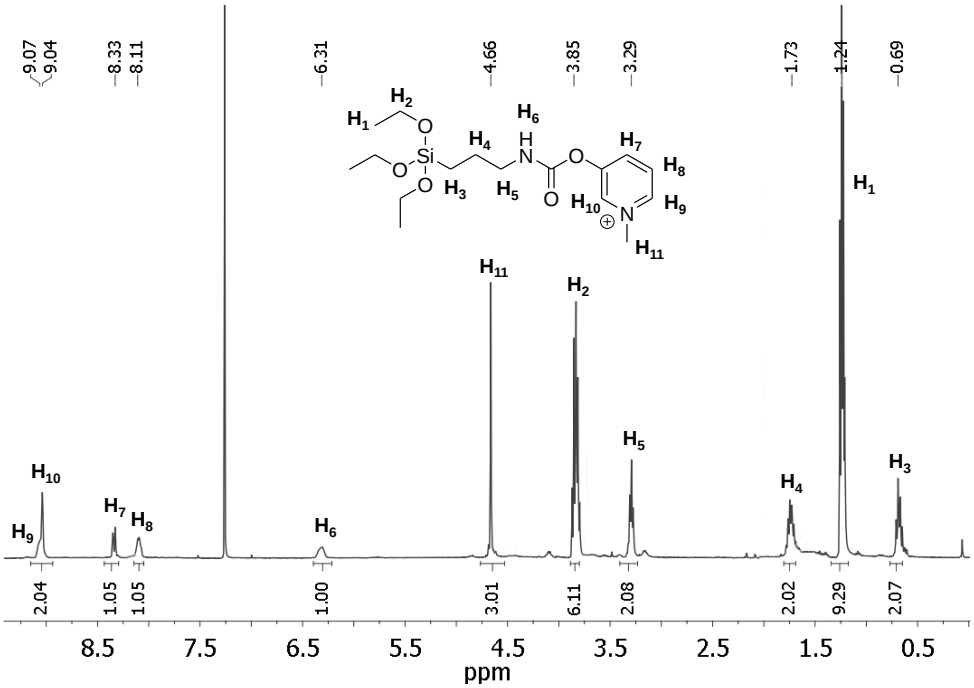

Figure S3. ^{1}H-NMR spectra of **P1** in $CDCl_3$.

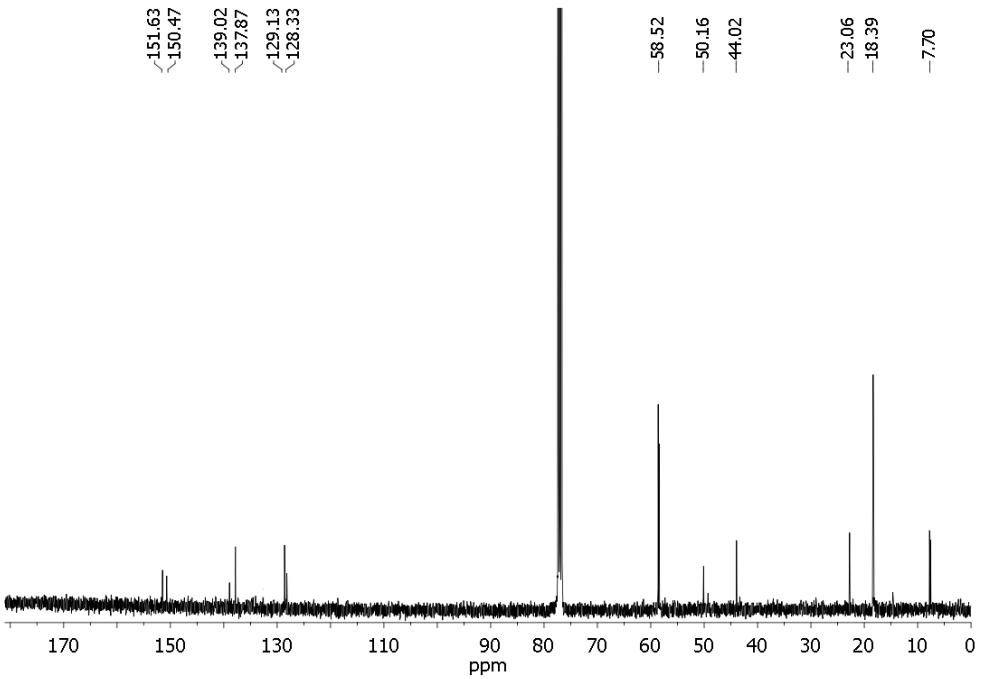

Figure S4. ^{13}C-NMR spectra of **P1** in $CDCl_3$.

Synthesis of S1: In a typical synthesis, calcined MCM-41 (200 mg) and rhodamine B (76.64 mg, 0.16 mmol) were suspended in CH_3CN (10 mL). The suspension was stirred at room temperature for 24 h in order to load MCM-41 pores. **P1** (193 mg, 0.2 mmol) was then added, and the final suspension was stirred at room temperature for 5.5 h. The resulting pink solid (**S1**) was isolated by centrifugation, rinsed 3 times with deionized water and with CH_3CN (5 mL), and then dried at 38°C for 18 h.

Synthesis of S1-AChE: In a typical experiment **S1** (500 μg) was suspended in TRIS buffer (300 μL, 100 mM, pH = 8.0) and AChE enzyme (200 μL, 2.5 μM) was added. The mixture was stirred for 30 min and then washed 3 times with TRIS buffer (1 mL, 100 mM, pH = 8.0) to eliminate the residual dye and the unattached enzyme.

Characterization of the prepared materials: The MCM-41 scaffold and mesoporous solid **S1** were characterized following standard techniques, including transmission electron microscopy (TEM), powder X-ray diffraction (PXRD) and N_2 adsorption/desorption analysis**.** The PXRD pattern of siliceous MCM-41 nanoparticles as synthesized (Figure 1 in the manuscript, curve a) shows four low-angle reflections typical of a hexagonal array, indexed as (100), (110), (200) and (210) Bragg peaks. A significant displacement of 3Å of the (100) peak in the PXRD pattern of the MCM-41 calcined nanoparticles is evident in curve b (see Figure 1 in manuscript), related to the further condensation of silanol groups in the calcination step. Finally, curve c (also in Figure 1 in manuscript) corresponds to the **S1** PXRD pattern. An intensity decrease and a broadening of the (110) and (200) reflections is observed, related to a loss of contrast from filling pore voids with rhodamine B dye.

Presence of the mesoporous structure in the final functionalized solids was confirmed by TEM analyses, in which the typical channels of the MCM-41 matrix are visualized as alternate black and white stripes (see Figure 1d and 1e in the manuscript). The figure also shows that the prepared MCM-41 and solid **S1** are obtained as spherical particles with an average diameter of 100±8 nm.

The N_2 adsorption–desorption isotherms of the calcined MCM-41 nanoparticles show an adsorption step at an intermediate P/P_0 value (0.1–0.3), which is typical of this type of solid (see Figure S5, curve a). A total pore volume of 0.334 $cm^3\ g^{-1}$ was calculated by using the BJH model on the adsorption branch of the isotherm. The application of the BET model resulted in a value for the total specific surface of 747.5 $m^2\ g^{-1}$. A pore diameter of 2.45 nm was determined by the PXRD, porosimetry and TEM studies. The N_2 adsorption–desorption isotherm of **S1** (see Figure S5, curve b) is typical of mesoporous systems with partially filled mesopores. A significant decrease in the N_2 volume adsorbed (0.027 $cm^3\ g^{-1}$) and surface area (65.9 $m^2\ g^{-1}$) were observed. BET analysis of MCM-41 calcined showed the presence of meso and micropores. Pore-size distribution plot for MCM-41 calcined nanoparticles is shown in Figure S6. As seen in the figure, pore-size distribution of MCM-41 calcined nanoparticles presented two maxima at ca. 2 and 40 nm that are ascribed to intraparticle mesopores and to micropores generated upon aggregation of the nanoparticles (textural porosity), respectively. Besides, BET linear plot for surface area calculation for calcined MCM-41 is shown in Figure S7.

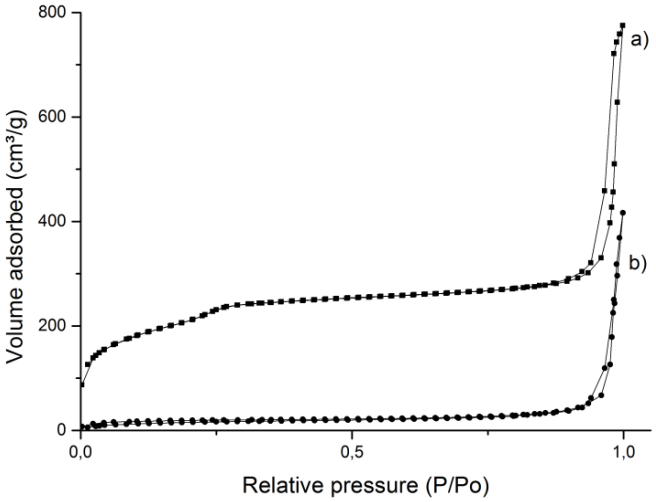

Figure S5. N_2 adsorption-desorption isotherms for calcined MCM-41 nanoparticles (a) and **S1** material (b).

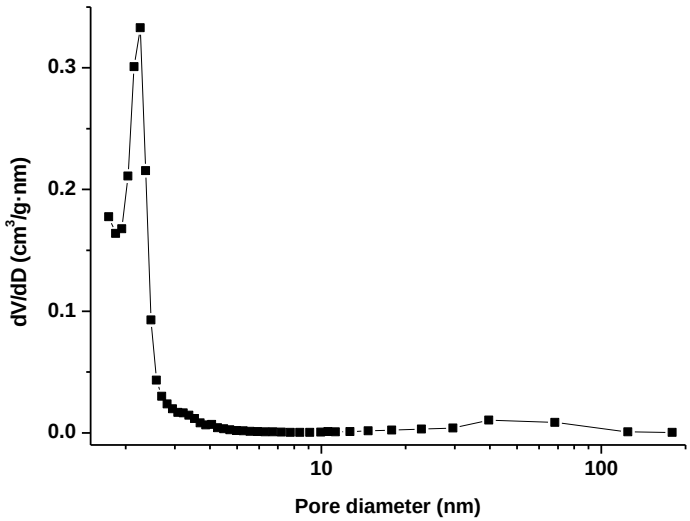

Figure S6. Pore size distribution for calcined MCM-41 nanoparticles obtained from the N_2 desorption branch of the isotherm.

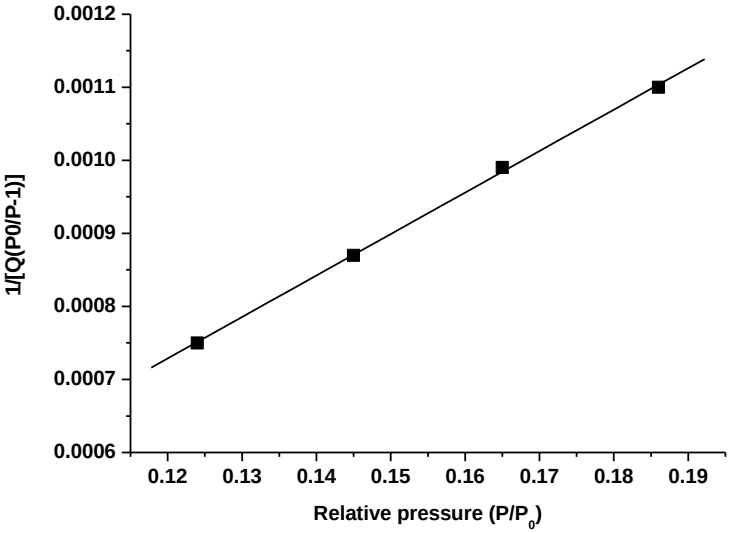

Figure S7. BET surface area plot for calcined MCM-41 nanoparticles.

The contents of **P1** and rhodamine B in the prepared solid **S1** were determined by elemental and thermogravimetric analyses, and are shown in Table S1.

Table S1. Contents of **P1** and rhodamine B (in mmol/g solid) in prepared solid **S1**.

	α_{P1} (mmol g^{-1})	$\alpha_{\text{rhodamine B}}$ (mmol g^{-1})	$\alpha_{\text{organic matter}}$ (mmol g^{-1})
S1	0.93	0.012	0.942

Release experiments of solid S1-AChE in the presence of DFP: To investigate the gating properties of **S1-AChE**, 500 µg of this solid were suspended in 400 µL of TRIS buffer (100 mM, pH = 8.0) and separated in two aliquots of 200 µL. Both samples were filled to a volume of 1250 µL with the same buffer. At the same time, 3 µL of DFP were added to one aliquot. Simultaneously, 3 µL of water (milliQ grade) were added to the remaining aliquot. Both suspensions were stirred at 25ºC for 90 min. Aliquots of 150 µL were taken at several times and centrifuged for 2 min at 12000 rpm (to remove the solid) and the fluorescence of the released rhodamine B was measured at 575 nm (λ_{exc} = 555 nm). The same procedure was used for the release experiments carried out at pH 6.0 (100 mM MES buffer) and 4.0 (100 mM acetic acid/sodium acetate buffer). The release profiles obtained are shown in Figure S8.

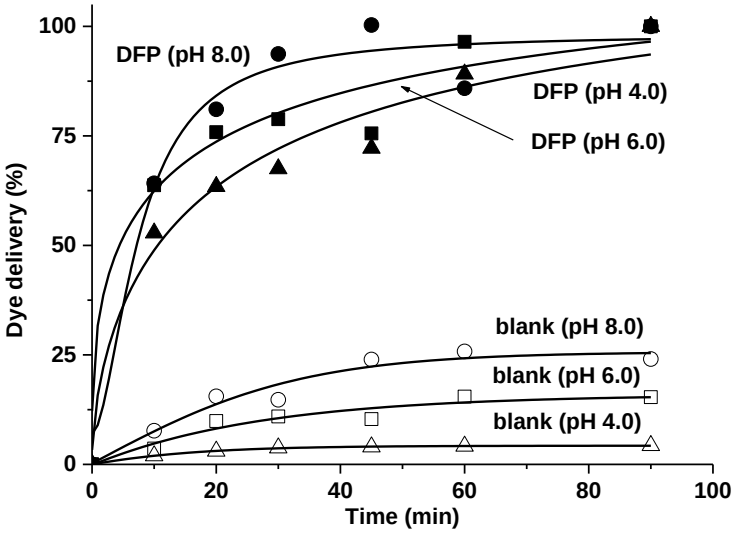

Figure S8. Rhodamine B release profiles form solid **S1-AChE** in the absence and in the presence of DFP at three different pH (8.0, 6.0 and 4.0).

Release experiments of solid S1-AChE in tap water: Solid **S1-AChE** (500 μg) was suspended in 400 μL of tap water (pH = 7.65, 673 μS cm^{-1}) and separated in two aliquots of 200 μL. Both samples were filled to a volume of 1250 μL with the same buffer. At the same time, 3 μL of DFP were added to one aliquot. Simultaneously, 3 μL of water (milliQ grade) were added to the remaining aliquot. Both suspensions were stirred at 25ºC for 90 min. Aliquots of 150 μL were taken at several times and centrifuged for 2 min at 12000 rpm (to remove the solid) and the fluorescence of the released rhodamine B was measured at 575 nm (λ_{exc} = 555 nm). The release profile obtained is shown in Figure S9.

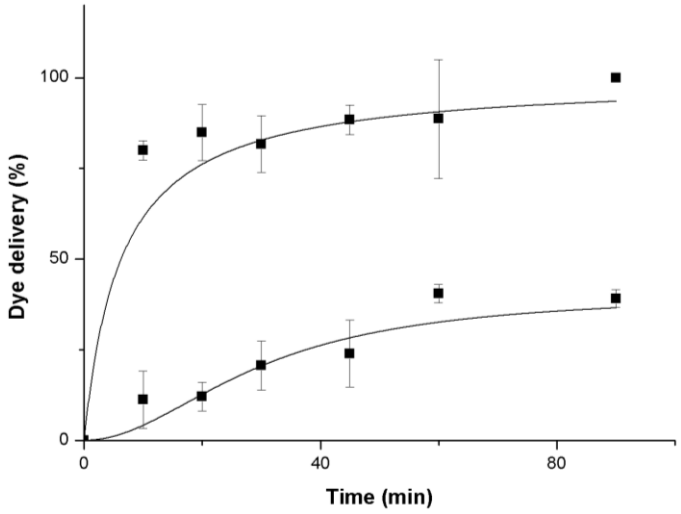

Figure S9. Rhodamine B release profiles form solid **S1-AChE** in the absence and in the presence of DFP using tap water.

Calibration curve of S1-AChE with DFP: In order to carry out these experiments, 500 μg of **S1-AChE** were suspended in 750 μL of TRIS buffer (100 mM, pH = 8.0) and divided into 15 aliquots of 50 μL each. Several water solutions of DFP that fell within a range from 0.002 to 1390 ppm were prepared and, instantaneously, 150 μL of each DFP solutions were added to

the aliquots and stirred for 15 min. One aliquot was reserved to add 150 μL of water (milliQ grade) as a blank. Then suspensions were centrifuged for 2 min at 12000 rpm (to remove the solid) and the fluorescence of the released rhodamine B was measured at 575 nm (λ_{exc} = 555 nm).

Selectivity studies with S1-AChE: In order to test the selectivity of **S1-AChE**, 500 μg of the solid were suspended in 1 mL of TRIS buffer (100 mM, pH = 8.0) and divided into 10 aliquots of 100 μL. Several water solutions of different organophosphorus compounds (DFP, DCP, DCNP and OP1-OP5, see Scheme 2 in the manuscript for chemical structures) at a concentration of 1500 ppm were prepared. Next 200 μL of the prepared solutions were added to each **S1-AChE** aliquot to obtain a final concentration of 1000 ppm. One aliquot was reserved to add 200 μL of water (milliQ grade) as a blank. After 15 min of stirring samples were centrifuged for 2 min at 12000 rpm (to remove the solid) and the fluorescence of the released rhodamine B was measured at 575 nm (λ_{exc} = 555 nm).

Enzyme activity assay: Acetylcholinesterase activity on **S1-AChE** was checked by the Ellman's assay. The test is based on the fact that thiols react with Ellman's reagent (5,5'-dithiobis(2-nitrobenzoic acid), DTNB), cleaving the disulfide bond to give 2-nitro-5-thiobenzoate (TNB^{2-}). This TNB^{2-} has a characteristic yellow colour that can be monitored by UV-visible spectrophotometry. Acetylthiocholine is used as the enzyme substrate which when hydrolysed produces the resulting thiocholine as the thiol containing molecule. In a typical assay, 900 μL of 100 mM sodium phosphate buffer (pH 7.5), 30 μL of 10 mM DTNB solution and 12 μL of acetylthiocholine (75 mM) where placed in a quartz cuvette. Then, 6 μL of either buffer (for blank) or **S1-AChE** (2.7 $mg \cdot mL^{-1}$) were added. The mixture was shaken and absorbance at 412 nm was monitored (Figure S10).

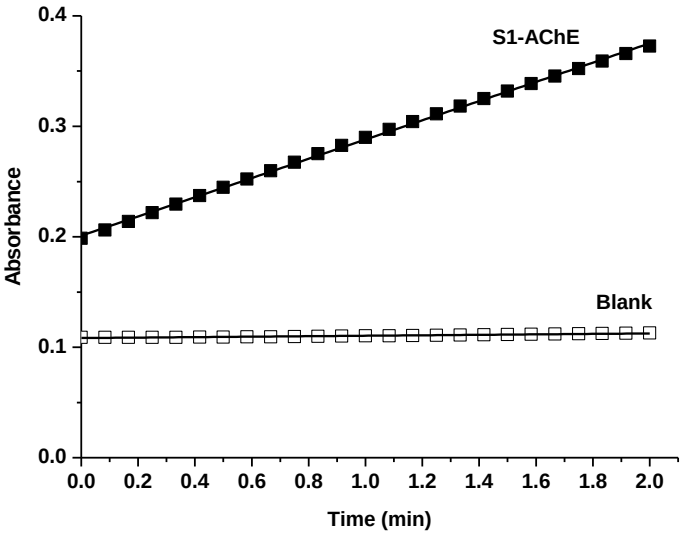

Figure S10. Monitoring of TNB^{2-} formation due to acetylcholinesterase activity on **S1-AChE**.

The acetylcholinesterase activity on **S1-AChE** was estimated to be 1.97 U mg^{-1}, by applying the following formula:

$$\frac{\text{Enzyme Units}}{\text{g}} = \frac{(\Delta - \Delta_{\text{blank}}) * V_T * F_D}{\varepsilon_{TNB} * l * V_{NPs} * C_{NPs}}$$

Where,

Δ is the slope of the graph (min^{-1})

Δ is the slope of the graph for the blank (min^{-1})

V_T is the total volume in the cuvette

ε_{TNB} is the molar extinction of TNB^{2-} at 412 nm (13,700 $M^{-1} \cdot cm^{-1}$)

L is the optical path in the cuvette (1 cm)

V_{NPs} is the volume of nanoparticles added (mL)

C_{NPs} is the concentration of nanoparticles suspension added (g/mL).

Table S2. Chromo-fluorogenic molecular probes based for nerve agent simulants detection in aqueous environments.

Probe	Mechanism	Output	Solvent	Selectivity	Time (min)	LOD	Paper
Nitrophenyl hydrazones	Phosphorylation and dehydration	Color changes	DMSO-NaOH	DCP and DFP	Not reported	Not reported	*New J. Chem.* **2005**, *29*, 1469
Eu(III) complex in Molecularly Imprinted Polymer	Binding with Eu(III)	Emission enhancement	Water pH 9.5	Sarin, Soman, VX	15-20	21-33 ppt	*Anal. Chim. Acta* **2005**, *542*, 32
Fluoresceinamine	PET-amine phosphorylation	Emission enhancement	PBS pH 7.5	DCP	0.5	Not reported	*JACS* **2006**, *128*, 5041
Azodye derivative	Hydroxyl phosphorylation and cyclization	Color changes	Acetonitrile -water 25:75	DCP, DFP, DCNP	1	16-18 ppm	*Chem. Commun.* **2008**, 6002
Azodye derivative	Hydroxyl phosphorylation and cyclization	Color changes/ Emission enhancement	Acetonitrile -MES 1:3	DCP, DFP, DCNP	1	16-18 ppm	*Chem. Asian J.* **2010**, *5*, 1573
Azopyridine derivative	Amine phosphorylation	Color changes	Acetonitrile -MES 25:75	DCNP	Few minutes	147 ppm	*Chem. Eur. J* **2011**, *17*, 6931
Triiaryl methanol derivative	Hydroxyl phosphorylation and dehydration	Color changes	Acetonitrile -water 9:1	DCNP, DFP	0.5	130 ppb (DFP); 30 ppm (DCNP)	*Chem. Eur. J* **2011**, *17*, 11994
Triaryl methanol derivatives	Hydroxyl phosphorylation and dehydration	Color changes	Acetonitrile -water 9:1	DCP, DFP, DCNP	5	0.1-125 ppm	*Eur. J. Org. Chem.* **2012**, 4937
Fluoresceinyloxime	Phosphorylation and cascade reaction	Emission enhancement	HEPES pH 7.4	DCP	Not reported	1.7 ppb	*Tetrahedron* **2014**, *70*, 2966
Silyl ether that contains stilbene derivative	Hydroxyl phosphorylation and silyl ether hydrolysis	Color changes	Water pH 8.0	DFP	0.1	5.4 ppm	*ChemOpen* **2014**, *3*, 142
BODIPY containing oxime derivative	Phosphorylation and benzonitrile formation	Emission enhancement	HEPES pH 7.4	DCNP	Not reported	15 ppm	*Chem. Commun.* **2014**, *50*, 7531
Spirobenzopyran derivative	Phosphorylation and cycle opening	Color changes/ Emission enhancement	Acetonitrile -water 1:1	DCP	0.5	1.7 ppb	*RSC Adv.* **2015**, *5*, 28996
Mesoporous silica nanoparticles capped with acetylcholinesterase	Uncapping and release of rhodamine B	Emission enhancement	TRIS pH 8.0	DFP	15	0.28 ppm	***This paper***

Table S3. Sensing solids, based on silica supports, for the chromo-fluorogenic sensing of nerve agent simulants.

Bifunctionalized silica nanoparticles	Ion channel sensor with a squaraine dye	Color changes	Acetonitrile	DFP	10	1 ppb	*Angew. Chem. Int. Ed.* **2010**, *49, 5945*
Mesoporous silica microparticles capped with hydroxyl moieties	Uncapping and release of $Ru(bipy)_3^{2+}$	Color changes	Acetonitrile	DCP, DFP, DCNP	5	15 ppm	*Chem. Commun.* **2011**, *47, 8313*
Mesoporous silica nanoparticles capped with acetylcholinesterase	Uncapping and release of rhodamine B	Emission enhance ment	Tris pH 8.0	DFP	15	0.28 ppm	*This paper*

Acetylcholinesterase-capped mesoporous silica nanoparticles controlled by the presence of inhibitors

Lluís Pascual,[a,b,c] Sameh El Sayed, [a,b,c] María D. Marcos, [a,b,c] Ramón Martínez-Máñez*[a,b,c] and Félix Sancenón[a,b,c]

[a] *Departamento de Química, Universidad Politécnica de Valencia Camino de Vera s/n, 46022, Valencia, Spain.*

[b] *Instituto Interuniversitario de Investigación de Reconocimiento Molecular y Desarrollo Tecnológico (IDM), Universitat Politécnica de Valencia, Universitat de Valencia.*

[c] *CIBER de Bioingeniería, Biomateriales y Nanomedicina (CIBER-BBN).*

Published as ASAP in Chemistry - An Asian Journal

Abstract

Two different acetylcholinesterase (AChE)-capped mesoporous silica nanoparticles (MSNs) (S1-AChE and S2-AChE) were prepared and characterized. MSNs were loaded with rhodamine B and the externa surface was functionalized with a pyridostigmine derivative P1 (yielding solid S1) or with a neostigmine derivative P2 (obtaining S2). The final capped materials were obtained by coordination of grafted P1 or P2 with AChE's active sites (to give S1-AChE and S2-AChE, respectively). Both materials were able to release rhodamine B in the presence of diisopropylfluorophosphate (DFP) or neostigmine, in a concentration dependent manner, via a competitive displacement of AChE through DFP and neostigmine coordination with the AChE's active sites. Moreover the response of S1-AChE and S2-AChE were also tested with other enzyme's inhibitors and substrates. From these studies, it is suggested that S1-AChE nanoparticles can be used for the selective detection of the nerve agent simulant DFP, whereas S2-AChE was able to sense paraoxon.

4.2.1 Introduction

In the last decades, nanotechnology has provided numerous examples of abiotic devices able to perform certain operations in response to small changes in the environment in which the nanomaterial is located. One appealing concept inside the realm of these "smart nanodevices" is the design of controlled release nanoparticles containing "molecular gates".[1] These gated nanodevices are usually formed by three subunits; i.e. (i) a suitable inorganic porous scaffold, (ii) a payload that is loaded onto the porous network and (iii) a molecular or supramolecular capping ensemble,

grafted in the outer surface of the support, which allows cargo release upon the application of an external stimuli (such as light, pH, temperature, magnetic fields, the presence of certain (bio)chemical species, etc.).[2-5]

One of the supports that has extensively been used for the preparation of gated materials is mesoporous silica nanoparticles (MSNs) owing some of their properties, such as relatively well-known functionalization chemistry (using trialkoxysilane derivatives), high stability and the presence of finely-tuned pores within the nanometric range (typically 2–3 nm).[6] Dealing with the payload, a myriad of chemical and biochemical molecules such as drugs, biomolecules, redox active species and dyes/fluorophores have been encapsulated onto MSNs-based supports.[7-11]

These gated materials have found notable applications in controlled release in biotechnological and biomedical fields,[12] especially in the drug delivery area for the potential treatment of different diseases.[13,14] Moreover, gated materials have also been applied in sensing and recognition protocols.[15] For the later application, the underlying idea is that the coordination or reaction of a certain analyte with the capping unit can modulate the delivery of a previously stored reported, usually a dye or fluorophore, from the pores to the solution, giving rise to a simple-to-detect chromo-fluorogenic signal.

From another point of view, the implementation of enzymes in gated materials has attracted great attention in recent years. For instance, enzymes can be used as triggers to induce chemical degradation of certain biomolecules used as gates allowing cargo release.[16-18] In this scenario, several examples of gated materials able to deliver an entrapped payload in the presence of esterases, amidases, azoreductases, glycosidases and other enzymes have been reported.[19-23] These materials can potentially find application in personalized biomedicine taking advantage of the

overexpression of certain enzymes in target diseases, which allow triggering pore opening and cargo release only in target tissues or organs.[24]

Besides, enzymes have also been used recently as capping subunits. In this specific use of enzymes, Martínez-Máñez and co-workers used cyclodextrin modified glucose oxidase to close the pores of mesoporous silica nanoparticles, loaded with a dye and functionalized with a benzimidazole derivative, through the formation of benzimidazole-cyclodextrin inclusion supramolecular complexes.[25] In the presence of glucose, the capping enzyme produces gluconic acid that induced benzimidazole protonation, dethreading of the supramolecular complex and dye release. In a second example, Lu and co-workers grafted glucosamine derivatives onto the external surface of mesoporous silica nanoparticles and then pores were capped with glucose oxidase through the coordination of glucosamine with the active site of the enzyme. In the presence of glucose a marked delivery of an entrapped dye was observed due to the preferential glucose binding with the glucose oxidase active site and subsequent enzyme displacement from the surface.[26] In this line, Villalonga and co-workers prepared mesoporous silica nanoparticles loaded with a dye and the external surface functionalized with a boronic acid derivative. The capped material was obtained upon addition of lactose-functionalized esterase through the formation of boronate esters between the disaccharides and the grafted boronic acids.[27] The entrapped dye was released in the presence of glucose or ethyl butyrate. Also, Ren et al also used glucose oxidase as caps, the opening protocol in this case being related with the hydrolysis of the enzyme by a protease.[28]

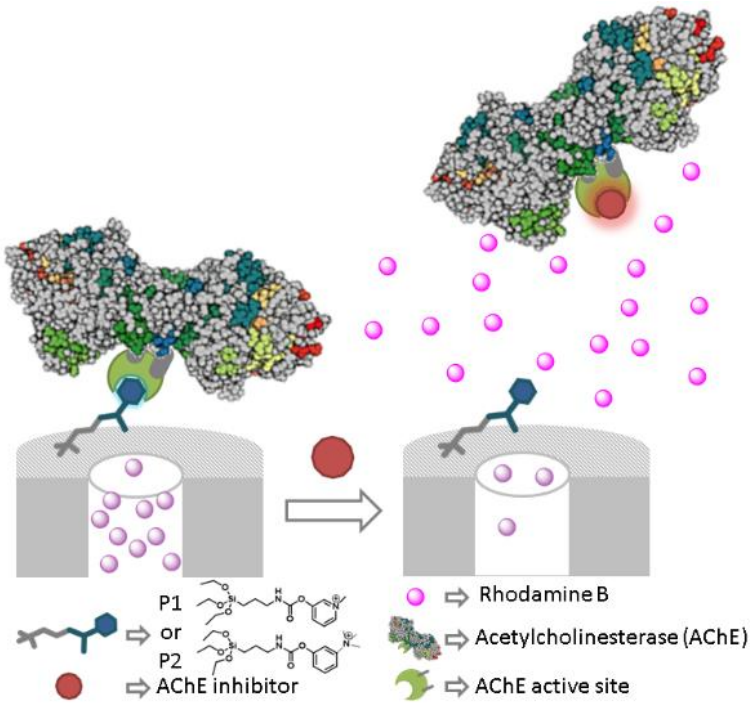

Scheme 1. Schematic representation of the opening mechanism of solid **S1-AChE** (grafted with **P1**) and solid **S2-AChE** (grafted with **P2**).

Taking into account the above mentioned facts and our interest in the development of gated nanomaterials for applications in controlled delivery and recognition/sensing protocols,[29] we report herein the use of acetylcholinesterase (AChE) as cap in the development of nanodevices that are expected to release its cargo in the presence of AChE inhibitors. For this purpose, we selected silica mesoporous nanoparticles as inorganic scaffold and loaded the pores with rhodamine B. In a second step, the external surface of the loaded nanoparticles was functionalized with two different derivatives of reversible AChE inhibitors; i.e. pyridostigmine and neostigmine (**P1** and **P2** in Scheme 1). Finally, addition of AChE induced pore capping by coordination of **P1** and **P2** with the enzyme's active sites (to obtain **S1-AChE** and **S2-AChE**, respectively). The AChE-capped solids are

expected to show "zero release" yet would deliver the cargo in the presence of other inhibitors that have more affinity for AChE enzyme (see Scheme 1). We have selected the AChE enzyme because this is a well-studied enzyme whose inhibitors (i.e. chemical warfare agents, neuroactive drugs or pesticides) are substances of interest. In fact, the capped solids **S1-AChE** and **S2-AChE** can potentially be used as probes for the selective detection of diisopropylfluorophosphate (DFP) or paraoxon, respectively (*vide infra*). A preliminary communication related with the performance of solid **S1-AChE** has been recently published by us.[30]

4.2.2 Results and discussion

Synthesis of gated nanoparticles. Two different gated materials **S1-AChE** and **S2-AChE** were prepared using mesoporous silica nanoparticles (MSNs) as inorganic scaffold.

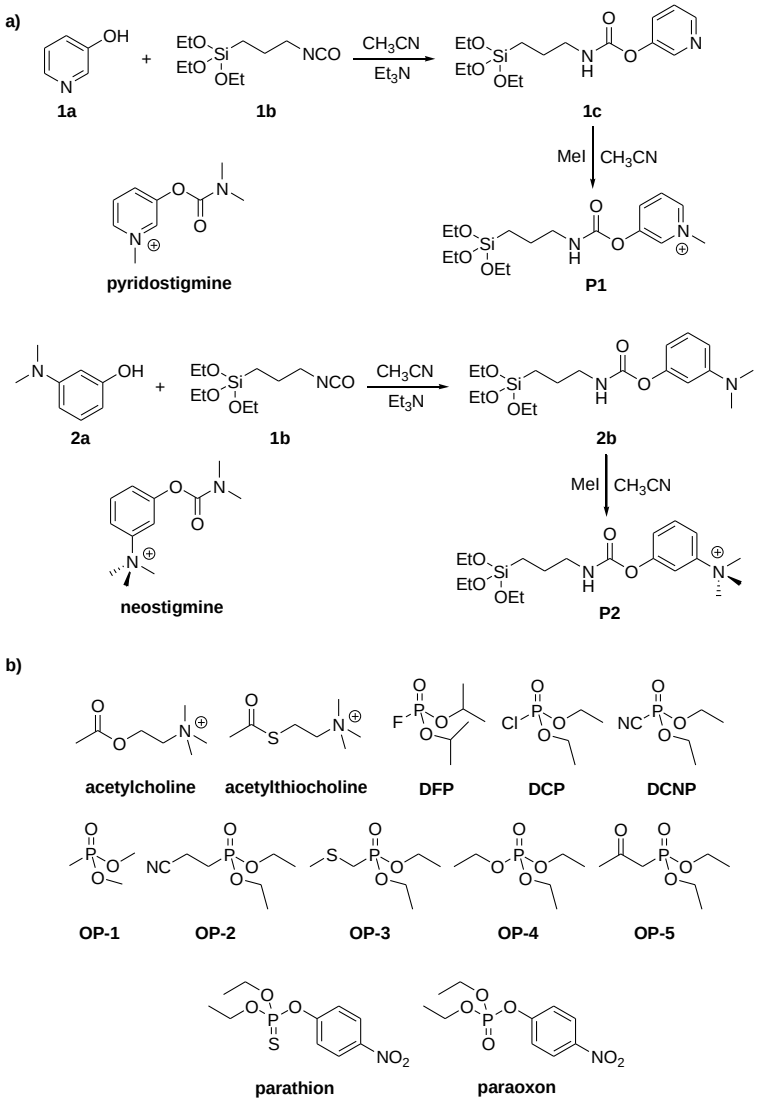

Scheme 2. a) Synthetic protocols used for the preparation of **P1** and **P2** derivatives and chemical structures of pyridostigmine and neostigmine. b) Chemical structures of the substrates and inhibitors used in this work with solids **S1-AChE** and **S2-AChE**.

MSNs were synthesized in alkaline media following well-known procedures that make use of *n*-cetyltrimethylammonium bromide (CTAB) as directing agent for condensation of the inorganic precursor

tetraethylorthosilicate (TEOS).[31] The obtained powder was washed and the surfactant was subsequently removed by calcination. Then, the pores of the MSNs were loaded with the fluorophore rhodamine B by stirring a suspension of nanoparticles in a concentrated acetonitrile solution of the dye (solid **S0**). Afterward, **P1** and **P2** were grafted onto the external surface of the loaded nanoparticles yielding solids **S1** and **S2**. Final gated nanoparticles **S1-AChE** and **S2-AChE** were prepared by suspending **S1** and **S2** in an aqueous (TRIS pH 8.0) solution of AChE for 30 min. In this step, AChE was immobilized onto the external surface of the nanoparticles, through the reversible interaction of the enzyme's active site with the grafted **P1** and **P2** inhibitors, with subsequent pore capping.

P1 is a derivative of pyridostigmine and was prepared by a two-step procedure. In the first step, 3-hydroxypyridine (**1a**) was reacted with (3-isocyanatopropyl)triethoxysilane (**1b**) yielding carbamate derivative **1c**. In a second step, the nitrogen atom of the pyridine moiety in **1c** was quaternized with methyl iodide yielding **P1** (see Scheme 2). A similar two-step synthetic protocol was used for the preparation of **P2,** which is a derivative of neostigmine, another reversible inhibitor of AChE. In this case, 3-(dimethylamino)phenol (**2a**) was reacted with (3-isocyanatopropyl)triethoxysilane (**1b**) yielding carbamate **2b**. Compound **P2** was obtained after reaction of **2b** with methyl iodide (see Scheme 2).

Materials characterization. MSNs and solids **S1** and **S2** were characterized using powder X-ray diffraction (PXRD), transmission electron microscopy (TEM), N_2 adsorption-desorption isotherms, thermogravimetric measurements and elemental analysis.

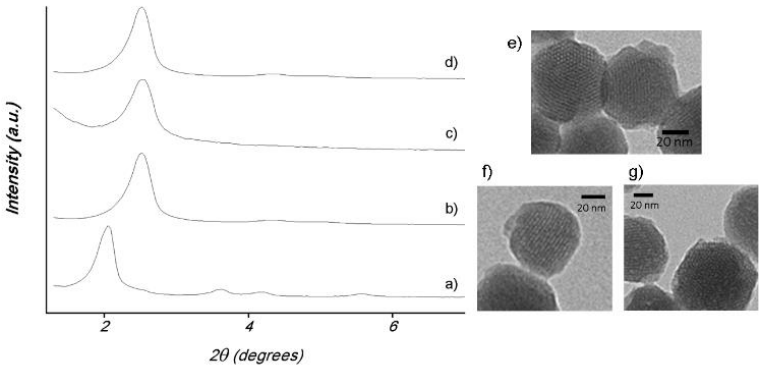

Figure 1. Left: Powder X-ray patterns of (a) as-made MSNs, (b) calcined MSNs, (c) solid **S1**, (d) solid **S2**. Right: TEM images of (e) calcined MSNs, (f) solid **S1**; (g) solid **S2**.

Table 1. BET-specific surface values, pore volumes, and pore sizes calculated from the N2 adsorption-desorption isotherms.

Solid	S_{BET} ($m^2 g^{-1}$)	BJH pore size[a] (nm)	total pore volume[b] ($cm^3 g^{-1}$)
MCM-41	747,5	2.45	0.33
S1	65,9	-	0.03
S2	137	-	0.10

[a,b] Pore volumes and pore sizes were associated with only intraparticle mesopores.

Figure 1 shows the PXRD patterns of MSNs as made (1a), calcined MSNs (1b), **S1** (1c) and **S2** (1d) solids. PXRD of as-made MSNs showed four low-angle peaks, typical of a hexagonal-ordered array of pores that can be

indexed as the (100), (110), (200) and (210) Bragg reflections. A shift of the (100) peak and a remarkable broadening of the other reflections in calcined MSNs was observed and ascribed to further condensation of silanol groups during the calcination step. For solids **S1** and **S2** the reflection (100) remained and indicated that the mesoporous structure was preserved in these solids despite the filling of the pores with rhodamine B and the anchoring of **P1** and **P2** functionalities on the nanoparticles surface. Besides, Figure 1 shows representative TEM images of calcined MSNs (1e) and solids **S1** (1f) and **S2** (1g). From these images, it can be seen that **S1** and **S2** preserve the spherical shape of the calcined nanoparticles, and a very similar average diameter of ca. 100±8 nm. In addition, the typical porosity associated with this type of inorganic support can be observed in the three materials.

N_2 adsorption-desorption studies of calcined MSNs and of **S1** and **S2** were also carried out (see Figure 2). Calcined MSNs showed a typical type IV curve that is characteristic of this mesoporous support. The curve shows the typical adsorption step at intermediate P/P_0 values (0.1–0.3) related with the nitrogen condensation inside the mesopores. The pore diameter distribution (PSD) of this sample was calculated by the Barret-Joyner-Halenda (BJH) method. A narrow BJH pore distribution and the absence of hysteresis loop in this interval suggested the existence of uniform cylindrical mesopores (pore diameter of 2.45 nm and pore volume of 0.33 $cm^3\ g^{-1}$, calculated on the adsorption branch of the isotherm). The application of the Brunauer–Emmett–Teller (BET) model gave a value of 747.5 $m^2\ g^{-1}$ for the total specific surface.

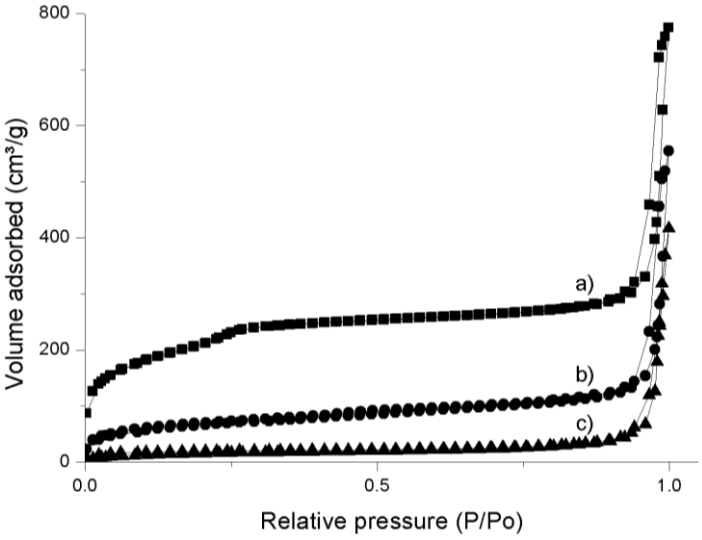

Figure 2. N_2 adsorption-desorption isotherms for (a) calcined MCM-41 nanoparticles, (b) **S2** and (c) **S1**.

The N_2 adsorption-desorption isotherms of solids **S1** and **S2** are typical of mesoporous systems with filled mesopores, and a remarkable decrease in both the adsorbed N_2 volume and the specific surface area was clearly observed (see Table 1). This reduction in the BET surface, compared with that of the MCM-41 starting material, was ascribed to the loading of pores with rhodamine B and to the functionalization of the surface with **P1** and **P2**.

Finally, the content of organic material (both rhodamine B and **P1**/**P2**) in **S1** and **S2** nanoparticles was determined by combining thermogravimetric and elemental analysis data. Results are summarized in Table 2.

Table 2. BET-specific surface values, pore volumes, and pore sizes calculated from the N_2 adsorption-desorption isotherms.

Solid	$\alpha_{\text{Inhibitor derivative}}$ (mmol g^{-1} SiO_2)	$\alpha_{\text{rhodamine B}}$ (mmol $g^{-1}SiO_2$)	$\alpha_{\text{Organic matter}}$ (% g/g)
S1	0.93	0.012	25.1
S2	0.48	0.034	17.6

The final solids, **S1-AChE** and **S2-AChE** were prepared by suspending **S1** or **S2** in an aqueous solution of AChE (TRIS buffer at pH 8.0) for 30 min (see experimental section for further details). Both final capped nanoparticles were prepared in small quantities and, for this reason, a complete characterization of the solids could not be carried out. However, UV-visible studies of the solution before and after the capping process allowed us to estimate that amounts of 250 ± 40 and 200 ± 20 μmols g^{-1} AChE were attached in **S1-AChE** and **S2-AChE**, respectively.

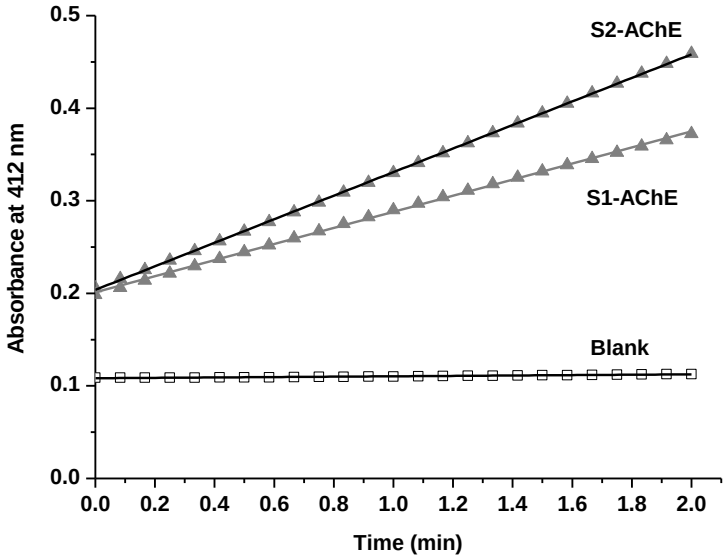

Figure 3. Absorbance at 412 nm corresponding to the TNB^{2-} formed in the Ellman's assay for AChE activity measurement in **S1-AChE** and **S2-AChE** nanoparticles.

The capping process and immobilization of the enzyme was also followed by measuring AChE activity using Ellman's assay (see Figure 3 and experimental section for details) before and after AChE attachment onto the external surface of the solids. Before grafting, AChE activity was 106.41 U mg^{-1} whereas after immobilization the activity dropped to 1.97 and 2.89 U mg^{-1} for **S1-AChE** and **S2-AChE**, respectively. This reduction in enzyme activity was attributed to the AChE immobilization in the surface by the interaction of the active sites of the enzyme with the grafted inhibitors. The low residual enzyme activity detected is tentatively ascribed to either (i) small amounts of enzyme physically adsorbed onto the external surface of the MSNs and/or (ii) the presence of two active sites in AChE which may not both be blocked by the inhibitors.

Dye delivery studies in presence of AChE inhibitors: As stated above, it is expected that the presence of inhibitors that have more affinity for ACHE than **P1** or **P2** would induce a displacement of the enzyme from the nanoparticles, with subsequent rhodamine B release. In a first step, uncapping studies were carried out with diisopropyl fluorophosphate (DFP) and neostigmine. DFP is a quasi-irreversible AChE inhibitor commonly used as nerve agent mimic. On the other hand, neostigmine is a reversible AChE inhibitor used for the treatment *myasthenia gravis*. The main differences between DFP and neostigmine in relation to their interaction with AChE are related with both, the different coordination ability to the enzyme and the inhibition mechanism. At this respect, the half maximal inhibitory concentration (IC_{50}) of DFP is 120 nM[32] whereas the value for neostigmine is 2 nM. These values reflected the higher affinity of neostigmine, when compared with DFP, for the AChE active sites. Moreover, organophosphate-based inhibitors, such as DFP, trend to covalently attach to the serine residue of the enzyme active site forming a very stable complex that can remain unaltered for hours or days. Dealing with carbamate-based inhibitors, such as neostigmine, their mode of interaction with AChE is similar to that of acetylcholine but with slower kinetics (i.e. hydrolysis will take from minutes to hours).[33]

In a typical experiment, 750 μg of **S1-AChE** were suspended in TRIS buffer (pH 8.0) and the resulting suspension was divided into 3 equal fractions. Two fractions were diluted with TRIS buffer and DFP or of neostigmine were added (final DFP and neostigmine concentration of 10 mM). The other fraction, that acted as blank, was filled with MiliQ water. The same procedure was repeated for **S2-AChE** nanoparticles. All the suspensions were stirred at room temperature, aliquots were extracted at scheduled times and the solid removed by centrifugation. Dye delivery to

the bulk solution was easily detected by monitoring the emission band of rhodamine B in the solution at 572 nm upon excitation at 555 nm. The obtained cargo release profiles are shown in Figure 4. Table 3 summarizes IC_{50} values for some inhibitors used in this work.

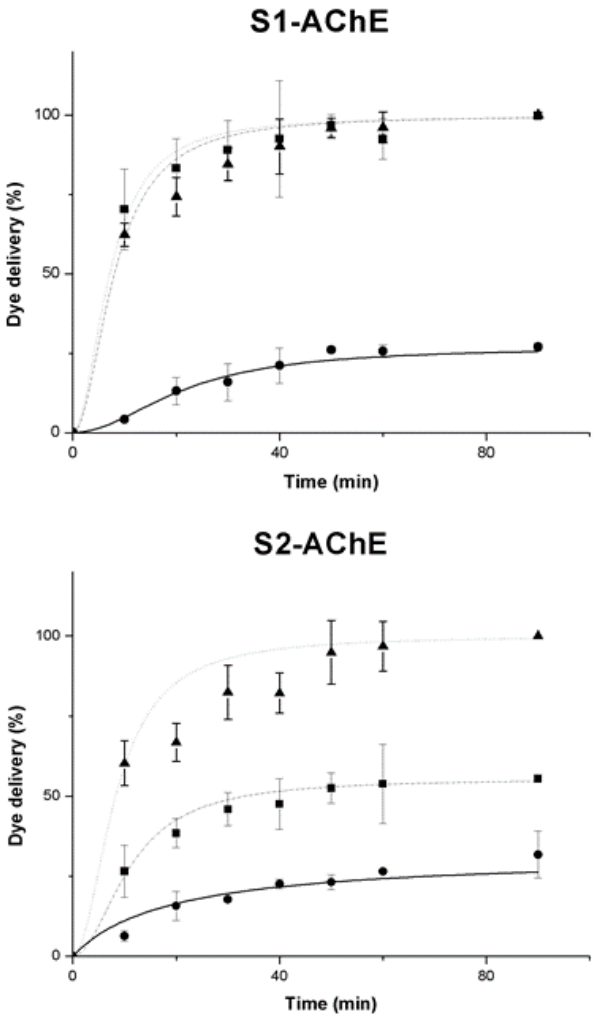

Figure 4. Kinetics of the release of rhodamine B from solids **S1-AChE** and **S2-AChE** in the absence (● blank) and in the presence of DFP (■) and neostigmine (▲).

As could be seen in Figure 4, in the absence of DFP or neostigmine, a poor rhodamine B release from solid **S1-AchE** was found (less than 5% of

maximum dye delivered after 5 min and ca. 20% after 90 min). This partial dye delivery observed in the absence of DFP and neostigmine was ascribed to the fact that **P1** (as pyridostigmine) is a reversible inhibitor of AChE enzyme. As a consequence, a slow enzymatic hydrolysis of **P1** may happen with time and subsequent detachment of AChE from the solid surface and rhodamine B release can occur. However, when DFP or neostigmine were present, a remarkable rhodamine B release was observed (ca. 80% of maximum dye delivered after 10 min). Release of the rhodamine B entrapped in the inner of the pores of **S1-AChE** solid was attributed to a preferential coordination of DFP and neostigmine with the active sites of AChE enzyme; i.e. both inhibitors (IC_{50} of 120 and 2 nM for DFP and neostigmine respectively) used displayed stronger interactions with AChE than that shown by pyridostigmine derivative **P1** (IC_{50} for pyridostigmine is 330 nM).

The release profile in hybrid materials that use enzymes as caps via interaction of the active site with anchored inhibitors, can be easily modulated by changing the chemical nature of the anchored inhibitor. This is clearly seen when the behavior of **S1-AChE** in the presence of DFP and neostigmine is compared with that of **S2-AChE**. For the later (functionalized with **P2**, a neostigmine derivative) cargo delivery profiles in the presence of DFP and neostigmine are shown in Figure 4. In the absence of DFP or neostigmine, a certain, yet poor, rhodamine B release was observed which is also tentatively ascribed to a slow enzymatic hydrolysis of **P2** derivative. In contrast, the kinetic profiles obtained in the presence of DFP or neostigmine are clearly different. As could be seen in Figure 4, DFP was unable to induce a marked AChE displacement from **S2-AChE** and only 40% of the maximum rhodamine B released was observed after 20 min. However, when neostigmine was used, nearly 90% of the dye was delivered for the same time. This different behaviour was ascribed to the interaction ability of DFP

and nesotigmine with AChE when compared to that of grafted **P2**. In fact, addition of DFP induced a moderate displacement of AChE because its IC_{50} value is higher than that of **P2** and was unable to completely detach AChE from the nanoparticles surface. On the other hand, neostigmine has an IC_{50} similar to that of **P2** and, for this reason, is able to compete for coordination with the enzyme active sites with subsequent pore opening.

Table 3. IC_{50} values from bibliography of most relevant AChE inhibitors tested or grafted on solids.[32, 34-37]

Compound	IC_{50} (nM)
Pyridostigmine (P1 precursor)	330
Neostigmine (P2 precursor)	2
DFP	120
Pox	130
Pthion	12590

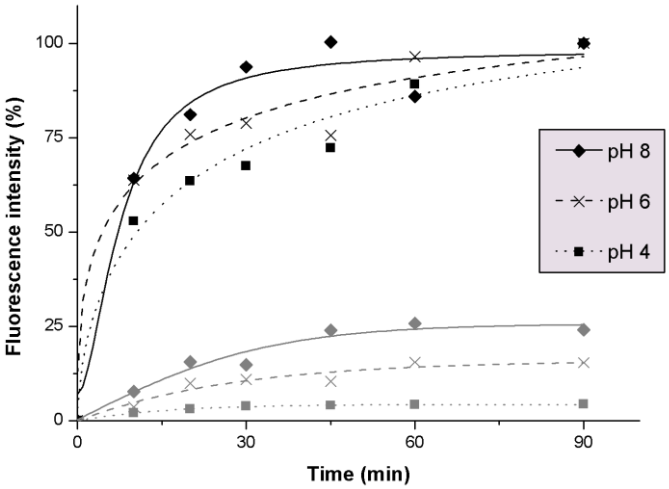

Figure 5. Rhodamine B release profiles form solid **S1-AChE** in the absence and in the presence of DFP at three different pHs. DFP response is drawn in black: pH 8.0 (♦), 6.0 (X) and pH 4.0 (■) while blanks are drawn in gray: pH 8.0 (♦), 6.0 (X) and pH 4.0 (■).

Rhodamine B release from nanoparticles **S1-AChE** and **S2-AChE** in the absence and in the presence of inhibitors was tested at pH 8.0 because this is the optimal proton concentration for the AChE enzyme. However, rhodamine B release from solid **S1-AChE** in the presence and in the absence of DFP at pH 6.0 and 4.0 was also tested following a similar procedure described above. **S1-AChE** solid was selected for this study because **P1** has the higher IC_{50} value and AChE enzyme is less effectively retained, when compared to solid **S2-AChE**. This weaker coordination of AChE to **P1** could be disrupted more easily by changes in the environment such as a change in proton concentration. Moreover, DFP was selected due to its weaker interaction with AChE when compared with neostigmine. Cargo release profiles at pH 4.0, 6.0 and 8.0 are shown in Figure 5. As can be seen in the figure, delivery profiles at pH 4.0, 6.0 and 8.0 were quite similar. The most remarkable differences, at pH 4.0 and 6.0 was an enhanced pore closure in

the absence of DFP. This reduction in the rhodamine B leakage was tentatively ascribed to the lower AChE enzymatic activity at acidic pH. Consequently, the hydrolysis rate of **P1** was also lowered and cargo delivery from **S1-AChE** decreased.

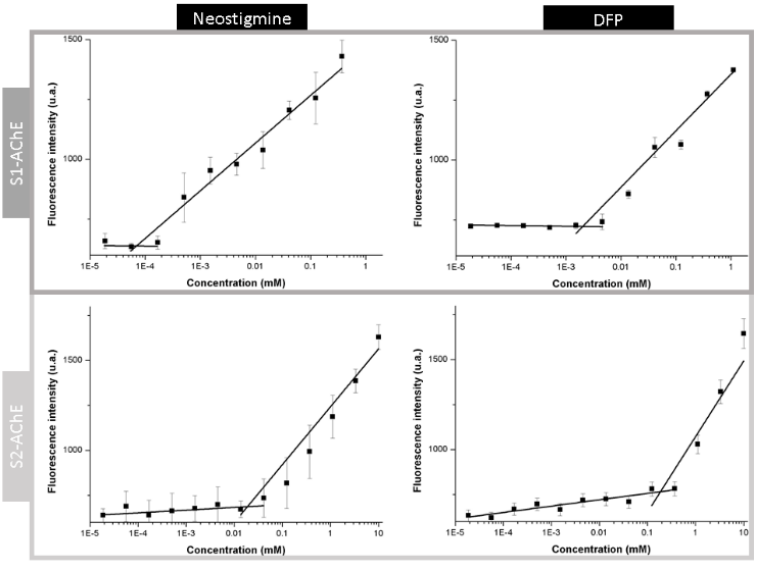

Figure 6. Emission intensity at 572 nm (excitation at 555 nm) of hodamine B release from solid **S1-AChE** and **S2-AChE** in the presence of increasing amounts of neostigmine and DFP (measured after 15 min of addition).

Once assessed the cargo delivery behavior of **S1-AChE** and **S2-AChE** nanoparticles with DFP and neostigmine, studies of payload delivery in the presence of increasing amounts of both inhibitors were carried out. The underlying idea is to assess the minimum quantity of DFP or neostigmine that induced pore opening and rhodamine B release. The corresponding titration profiles obtained for both solids with DFP and neostigmine are shown in Figure 6. From these graphics the limit of detection (LOD) for the detection of DFP and neostigmine were calculated and included in Table 4.

As can be observed from the profiles showed in Figure 6 and from the values of Table 3, the LOD for neostigmine and DFP in both solids was clearly related with the affinity of neostigmine and DFP to coordinate with AChE. Dealing with **S1-AChE** nanoparticles, the affinity of **P1** toward AChE is relatively weak and could be disrupted easily upon addition of DFP and neostigmine. Moreover, neostigimine has a stronger affinity toward AChE (IC_{50} of 2 nM) than DFP (IC_{50} of 120 nM) and, as consequence, less amount of the former was needed to induce rhodamine B release. In the case of neostigmine, a concentration as low as 110 nM is able to displace AChE from the surface of **S1-AChE**, whereas for DFP, rhodamine B release was not seen until a 3 μM concentration was reached. A similar trend were obtained with solid **S2-AChE** but in this case the amount of neostigmine and DFP that induced pore opening were higher (when compared with solid **S1-AChE**) due to the stronger affinity of **P2** toward AChE when compared with **P1**. The LOD for neostigmine and DFP using **S2-AChE** were 20 and 200 μM, respectively.

The studies shown above clearly demonstrate that AChE displacement, and pore opening, from the surface of **S1-AChE** and **S2-AChE** was a consequence of a competition between grafted (**P1** and **P2**) and free inhibitors (neostigmine and DFP) to coordinate with the active sites of the enzyme.

Selectivity studies of S1-AChE and S2-AChE nanoparticles: Once assessed the opening behavior of **S1-AChE** and **S2-AChE** in the absence and in the presence of neostigmine and DFP, we centered our attention in the study of the response of both solids in the presence of other chemical species. For this study we selected as potential AChE inhibitors and substrates; neostisgmine (NG), pyridostigmine (PG), acetylcholine (ACh),

acetylthiocholine (ASCh), diisopropyl fluorophosphate (DFP), diethyl chlorophosphate (DCP), diethyl cyanophosphonate (DCNP), parathion (Pthion), paraoxon (Pox), dimethylmethyl phosphonate (OP-1), diethyl (2-cyanoethyl)phosphonate (OP-2), diethyl (methylthiomethyl) phosphonate (OP-3), dimethyl chlorothiophosphate (OP-4) and ethyl dichlorophosphate (OP-5). Neostigmine and pyridostigmine are potent inhibitors of AChE whereas ACh and ASCh are the natural substrates of the enzyme. On the other hand, DFP, DCP and DCNP are nerve agent simulants[38] and OP1-OP5 are a family of organophosphates and phosphonates. Finally, parathion is a commonly used pesticide and paraoxon its degradation product.[39]

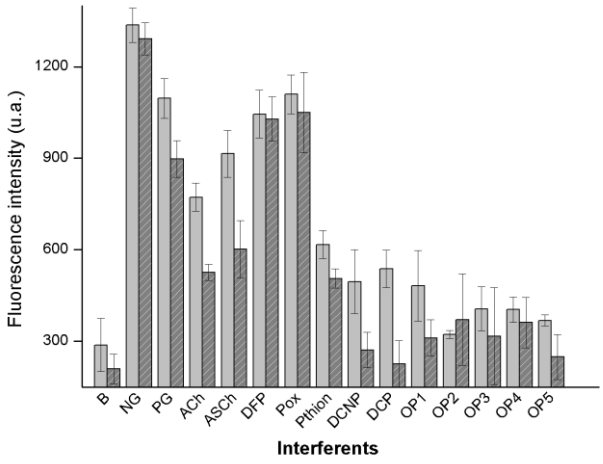

Figure 7. Emission intensity at 572 nm (excitation at 555 nm) of hodamine B release from solid **S1-AChE** and **S2-AChE** in the presence of increasing amounts of neostigmine and DFP (measured after 15 min of addition).

In a typical experiment, the release of rhodamine B from **S1-AChE** and **S2-AChE** nanoparticles in the presence of these chemicals at 5 mM concentration and after 15 min in TRIS buffer at pH 8.0 was tested. The obtained results are shown in Figure 7.

As a general trend, the fluorogenic response in terms of selectivity of **S1-AChE** is slightly better than that observed for **S2-AChE**. This fact is directly related with the strong coordinating ability of **P2** with AChE, when compared with **P1**. As seen in Figure 7, neostigmine, pyridostigmine, DFP and paraoxon induced the most marked rhodamine B release from both materials. This observation is clearly related with the fact that these chemicals display the highest affinities toward AChE enzyme. In addition, acetylcholine and acetylthiocholine were able to induce moderate rhodamine B release (higher for **S2-AChE** than for **S1-AChE**), whereas OP1-OP5 induced a very poor payload delivery which is tentatively ascribed to their low affinity for the AChE enzyme.

Table 4. Minimal concentrations of neostigmine and DFP that induced pore opening of **S1-AChE** and **S2-AChE** nanoparticles

Solid	Neostigmine (μM)	DFP (μM))
S1	0.11	3
S2	20	200

The results shown in Figure 7 suggested that **S1-AChE** and **S2-AChE** might be used for the selective fluorogenic detection of a certain chemical compound in a family of related derivatives. For instance, it is noteworthy that from all nerve agent simulants tested, only DFP induced a remarkable pore opening in both nanoparticles whereas the response obtained with the DCP and DCNP simulants was much lower. This fact pointed toward a possible use of **S1-AChE** and **S2-AChE** for the selective fluorogenic sensing

of DFP.[30] Moreover it is also of interest that both nanoparticles were able to fluorimetrically differentiate between paraoxon and parathion. Paraoxon induced a marked rhodamine B release whereas parathion response was lower. The selective detection of paraoxon is of interest because this toxic chemical is quickly produced by air-induced oxidation of parathion.[40]

4.2.3 Conclusions

In summary, we report herein the preparation of two different mesoporous silica nanoparticles loaded with rhodamine B (as model fluorophore) and capped with AChE, through the formation of supramolecular complexes with two grafted derivatives of well-known enzyme inhibitors (i.e. pyridostigmine and neostigmine). Both nanoparticles remained closed and a poor rhodamine B release was observed. However, in the presence of neostigmine and DFP, AChE was detached from the nanoparticle surface with subsequent rhodamine B release. The amount of rhodamine B release was clearly related with the affinity of the inhibitor to AChE's active sites; i.e. the larger the affinity to the enzyme, the less quantity was necessary to induce AChE detachment. It is also proposed that these capped nanoparticles could be used in sensing protocols because are able to differentiate between DFP and other nerve agent simulants (such as DCP and DCNP). In addition, paraoxon can be differentiated from its precursor parathion. These sensing features open the possibility of using these, or similar nanoparticles, for the design of chromo-fluorogenic probes for these chemical species. Moreover, in a wider context, the results presented herein may open a new way to develop MSNs-based sensing systems. The approach we have followed is general and similar materials capped with other well-known enzymes can be developed to obtain a family of gated

systems which can be selectively opened in the presence of target enzyme's inhibitors.

4.2.4 Experimental Section

General techniques: Powder X-ray diffraction (PXRD), thermogravimetric analysis (TGA), elemental analysis, transmission electron microscopy (TEM), N_2 adsorption-desorption, UV-visible (UV-vis) and fluorescence spectroscopy were employed to characterize synthesized materials. PXRD measurements were taken on a D8 Advance diffractometer using CuKα radiation (Philips, Amsterdam, The Netherlands). Thermogravimetric analyses were carried out on a TGA/SDTA 851e balance (Mettler Toledo, Columbus, OH, USA) in an oxidizing atmosphere (air, 80 mL min^{-1}) with a heating program: gradient of 393-1273 K at 10°C min^{-1}, followed by an isothermal heating step at 1273°C for 30 min. TEM images were obtained with a 100 kV CM10 microscope (Philips). N_2 adsorption-desorption isotherms were recorded with a Tristar II Plus automated analyzer (Micromeritics, Norcross, GA, USA). The samples were degassed at 120°C in vacuum overnight. Specific surface areas were calculated from the adsorption data within the low pressure range using the Brunauer, Emmett and Teller (BET) model. Pore size was determined following the Barret, Joyner and Halenda (BJH) method. Fluorescence spectroscopy measurements were taken on a Felix 32 Analysis, version 1.2 (Build 56, Photon Technology International, Birmingham, NJ, USA), and by a JASCO FP-8500 spectrophotometer.

Chemicals: Tetraethylorthosilicate (TEOS), *n*-cetyltrimethylammonium bromide (CTAB), sodium hydroxide, (3-

isocyanatopropyl) triethoxysilane, 3-hydroxypyridine, 3-(dimethylamino)phenol, methylene iodide, triethylamine, rhodamine B, tris(hidroxymethyl)aminomethane (TRIS), hydrochloric acid, neostigmine bromide, pyridostigmine bromide, parathion, paraoxon, acetylcholine, acetylthiocholine, diisopropyl fluorophosphate (DFP), diethyl chlorophosphate (DCP), diethyl cyanophosphonate (DCNP), dimethylmethyl phosphonate (OP-1), diethyl (2-cyanoethyl) phosphonate (OP-2), diethyl (methylthiomethyl) phosphonate (OP-3), dimethyl chlorothiophosphate (OP-4) and ethyl dichlorophosphate (OP-5) were purchased from Sigma-Aldrich Química (Madrid, Spain). All the products were used as received.

Synthesis of mesoporous silica nanoparticles: NaOH (2.00 mol L^{-1}, 3.5 mL) was added to a solution of CTAB (1.00 g, 2.74 mmol) in deionized H_2O (480 mL). The solution temperature was adjusted to 80°C and then TEOS (5.00 mL, 2.57×10^{-2} mol) was added dropwise to the surfactant mixture. The mixture was stirred for 2 h to give a white precipitate. The solid was isolated by centrifugation and washed with deionized H_2O and EtOH, and then dried at 60°C for 12 h to give MCM-41. In order to remove the template phase, the nanoparticles were calcined at 550°C in an oxidizing atmosphere.

Synthesis of P1: 3-hydroxypyridine (**1a**, 0.5 g, 5.26 mmol) was dissolved in CH_3CN (20 mL) and then (3-isocyanatopropyl) triethoxysilane (**1b**, 1.3 mL, 5.26 mmol) was added to the solution. A catalytic amount of triethylamine (110 µL) was added. The mixture was kept under stirring at room temperature for 4 h. The intermediate product **1c** was isolated by evaporating the solvent in a rotary evaporator. In the final step, **1c** (2.1 g, 5.26 mmol) was dissolved in CH_3CN (15 mL) and reacted with methylene iodide (3.3 mL, 52 mmol) for 20 h. Final product **P1** (1.03 g, 4.95 mmol, 94%) was obtained by evaporating the solvent and methylene iodide using a

rotary evaporator. ^{1}H NMR (400 MHz, $CDCl^{3}$) δ 9.09 (br m, 1H), 9.07 (s, 1H), 8.33 (dd, 1H), 8.10 (t, 1H), 6.31 (br s, 1H), 4.68 (s, 3H), 3.84 (q, 6H), 3.29 (t, 2H), 1.75 (m, 2H), 1.24 (t, 9H), 0.69 (t, 2H). ^{13}C NMR (101 MHz, CDCl3) δ 151.5, 150.7, 138.9, 137.8, 128.6, 128.2, 58.6, 50.1, 43.9, 22.7, 18.3, 7.7. HRMS-EI m/z: calcd for $C_9H_{21}NO_3Si$ 219.1291; found: 219.1112 ($(CH_3CH_2O)_3Si(CH_2)_3N$), calcd for $C_6H_8NO^+$ 110.0606; found: 110.0598 ($HO\text{-}C_5H_4N\text{-}CH_3^+$).

Synthesis of P2: 3-(dimethylamino) phenol (**2a**, 0.5 g, 3.64 mmol) was dissolved in CH_3CN (20 mL) and then (3-isocyanatopropyl) triethoxysilane (**2b**, 0.9 mL, 3.64 mmol) was added to the solution. A catalytic amount of triethylamine (110 μL) was added. The mixture was kept under stirring at room temperature for 4 h. The intermediate product **2c** was isolated by evaporating the solvent in a rotary evaporator. In the final step, **2c** (1.56 g, 3.64 mmol) was dissolved in CH_3CN (15 mL) and reacted with methylene iodide (3.3 mL, 52 mmol) for 20 h. Final product **P2** (1.03 g, 2.47 mmol, 68%) was obtained by evaporating the solvent and methylene iodide using a rotary evaporator. ^{1}H NMR (400 MHz, $CDCl_3$) δ 7.78 (d t, 1H), 7.61 (t, 1H), 7.55 (t, 1H), 7.27 (d t, 1H), 5.69 (s, 1H), 3.91 (s, 3H), 3.77 (q, 6H), 3.20 (t, 2H), 1.66 (m, 2H), 1.17 (t, 9H), 0.62 (t ,3H). ^{13}C NMR (101 MHz, CDCl3) δ 151.5, 150.7, 138.9, 137.8, 128.6, 128.2, 58.6, 50.1, 43.9, 22.7, 18.3, 7.7. HRMS-EI m/z: calculated for $C_{19}H_{35}N_2O_5Si^+$: 399.2310; found: 399.2419

Synthesis of S1 and S2: In a typical synthesis, calcined MSNs (200 mg) and rhodamine B (76.64 mg, 0.16 mmol) were suspended in CH_3CN (10 mL). The suspension was stirred at room temperature for 24 h in order to load MCM-41 pores. **P1** (193 mg, 0.2 mmol) or **P2** (106 mg, 0.2 mmol) were then added, and the final suspension was stirred at room temperature for 5.5 h. The resulting pink solid (**S1** or **S2**) was isolated by centrifugation, rinsed 3 times with deionized water and with CH_3CN (5 mL), and then dried at 38°C for 18 h.

Synthesis of S1-AChE and S2-AChE: In a typical experiment **S1** or **S2** (750 μg) was suspended in TRIS buffer (450 μL, 100 mM, pH = 8.0) and AChE enzyme (300 μL, 2.5 μM) was added. The mixture was stirred for 30 min and then washed 3 times with TRIS buffer (1 mL, 100 mM, pH = 8.0) to eliminate the residual dye and the unattached enzyme.

Enzyme activity assay: Acetylcholinesterase activity on **S1-AChE** and **S2-AChE** was checked by the Ellman's assay. The test is based on the fact that thiols react with Ellman's reagent (5,5'-dithiobis(2-nitrobenzoic acid), DTNB), cleaving the disulfide bond to give 2-nitro-5-thiobenzoate (TNB^{2-}). This TNB^{2-} has a characteristic yellow color that can be monitored by UV-visible spectrophotometry. Acetylthiocholine is used as the enzyme substrate which when hydrolysed produces the resulting thiocholine as the thiol containing molecule. In a typical assay, 900 μL of 100 mM sodium phosphate buffer (pH 7.5), 30 μL 10 mM DTNB solution and 12 μL of acetylthiocholine (75 mM) where placed in a quartz cuvette. Then, 6 μL of either buffer (for blank) or **S1-AChE**/**S2-AChE** nanoparticles (2.7 mg·mL^{-1}) were added. The mixture was shaken and absorbance at 412 nm was monitored.

The acetylcholinesterase activity on **S1-AChE** and **S2-AChE** were estimated to be 1.97 and 2.89 U mg^{-1} respectively, by applying the following formula:

$$\frac{\text{Enzyme Units}}{\text{g}} = \frac{(\Delta - \Delta_{\text{blank}}) * V_T * F_D}{\varepsilon_{TNB} * l * V_{NPs} * C_{NPs}}$$

Where, Δ is the slope of the graph (min^{-1}), V_T is the total volume in the cuvette, ε_{TNB} is the molar extinction of TNB^{2-} at 412 nm (13,700 M^{-1} cm^{-1}), l is the optical path in the cuvette (1 cm) V_{NPs} is the volume of nanoparticles added (mL) and C_{NPs} is the concentration of nanoparticles suspension added (g/mL).

Release experiments of solid S1-AChE and S2-Ach in the presence of neostigmine and DFP: To investigate the gating properties of the solids, 750 µg of nanoparticles were suspended in 600 µL of TRIS buffer (100 mM, pH 8.0) and separated in three aliquots of 200 µL. Both samples were filled to a volume of 1250 µL with the same buffer. 3 µL of DFP were added to one aliquot and filled until a final volume of 1300 µL. For neostigmine 50 µL of solution were directly added. Simultaneously, 50 µL of water (milliQ grade) were added to the remaining aliquot in each case. Both suspensions were stirred at 25ºC for 90 min. Aliquots of 150 µL were taken at several times and centrifuged for 2 min at 12000 rpm (to remove the solid) and the fluorescence of the released rhodamine B was measured at 575 nm (λ_{exc} = 555 nm). The same procedure was used for the release experiments carried out at pH 6.0 (100 mM MES buffer) and 4.0 (100 mM acetic acid/sodium acetate buffer).

Calibration curve of S1-AChE and S2-AChE with DFP or neostigmine: In order to carry out these experiments, 500 µg of **S1-AChE** or **S2-AChE** were suspended in 750 µL of TRIS buffer (100 mM, pH 8.0) and divided into 15 aliquots of 50 µL each. Several water solutions of DFP or neostigmine that fell within a range from 0.06 to 10000 µM were prepared and, instantaneously, 150 µL of each solution were added to the aliquots and stirred for 15 min. One aliquot was reserved to add 150 µL of water (milliQ grade) as a blank. Then suspensions were centrifuged for 2 min at 12000 rpm (to remove the solid) and the fluorescence of the released rhodamine B was measured at 575 nm (λ_{exc} = 555 nm).

Selectivity studies with S1-AChE and S2-AChE: In order to test the selectivity of the solids, 500 µg of nanoparticles were suspended in 1 mL of TRIS buffer (100 mM, pH 8.0) and divided into 10 aliquots of 100 µL. Several water solutions of different organophosphorus compounds (DFP, DCP, DCNP, Pthion, Pox, OP1, OP2, OP3, OP4, OP5, ACh, ASCh, PG and NG) at

a concentration of 5 mM were prepared. Next 200 μL of the prepared solutions were added to each aliquot to obtain a final concentration of 1000 ppm. One aliquot was reserved to add 200 μL of water (milliQ grade) as a blank. After 15 min of stirring samples were centrifuged for 2 min at 12000 rpm (to remove the solid) and the fluorescence of the released rhodamine B was measured at 575 nm (λ_{exc} = 555 nm).

Acknowledgements

Financial support from the Spanish Government and FEDER funds (Project MAT2015-64139-C4-1-R, AGL2015-70235-C2-2-R) and the Generalitat Valencia (Project PROMETEOII/2014/047) is gratefully acknowledged. Ll. P. is grateful to the Universitat Politécnica de Valencia for his grant.

REFERENCES

1 S. Alberti, G. J. A. A. Soler-Illia, O. Azzaroni, *Chem. Commun.* **2015**, *51*, 6050–75.
2 E. Aznar, M. Oroval, L. Pascual, J. R. Murguía, R. Martínez-Máñez, F. Sancenón, *Chem. Rev.* **2016**, *116*, 561–718.
3 C. Coll, A. Bernardos, R. Martínez-Máñez, F. Sancenón, *Acc. Chem. Res.* **2013**, *46*, 339–349.
4 I. I. Slowing, B. G. Trewyn, S. Giri, V. S. Y. Lin, *Adv. Funct. Mater.* **2007**, *17*, 1225–1236.
5 R. Rurack, Knuck Martínez-Mánez, *The Supramolecular Chemistry of Organic-Inorganic Hybrid Materials*, Wiley-VCH Verlag, **2010**.
6 A. B. Descalzo, R. Martínez-Máñez, F. Sancenón, K. Hoffmann, K. Rurack, *Angew. Chem. Int. Ed.* **2006**, *45*, 5924-5948.
7 J. S. Beck, J. C. Vartuli, W. J. Roth, M. E. Leonowicz, C. T. Kresge, K. D. Schmitt, C. T. W. Chu, D. H. Olson, E. W. Sheppard, S. B. McCullen, J. B. Higgins, J. L. Schlenker *J. Am. Chem. Soc.* **1992**, *114*, 10834–10843.
8 G. S. Attard, J. C. Glyde, C. G. Göltner, *Nature* **1995**, *378*, 366–368.

[9] C. T. Kresge, M. E. Leonowicz, W. J. Roth, J. C. Vartuli, J. S. Beck, *Nature* **1992**, *359*, 710–712.
[10] Q. Cai, Z.-S. Luo, W.-Q. Pang, Y.-W. Fan, X.-H. Chen, F.-Z. Cui, *Chem. Mater.* **2001**, *13*, 258–263.
[11] H. B. S. Chan, P. M. Budd, T. Naylor, *J. Mater. Chem.* **2001**, *11*, 951–957.
[12] Z. Li, J. C. Barnes, A. Bosoy, J. F. Stoddart, J. I. Zink, *Chem. Soc. Rev.* **2012**, *41*, 2590.
[13] I. I. Slowing, B. G. Trewyn, S. Giri, V. S.-Y. Lin, *Adv. Funct. Mater.* **2007**, *17*, 1225–1236.
[14] M. Vallet-Regí, F. Balas, D. Arcos, *Angew. Chem. Int. Ed.* **2007**, *46*, 7548–7558.
[15] F. Sancenón, L. Pascual, M. Oroval, E. Aznar, R. Martínez-Máñez, *ChemistryOpen* **2015**, *4*, 418–437.
[16] K. Radhakrishnan, J. Tripathy, D. P. Gnanadhas, D. Chakravortty, A. M. Raichur, *RSC Adv.* **2014**, *4*, 45961–45968.
[17] K. Patel, S. Angelos, W. R. Dichtel, A. Coskun, Y. W. Yang, J. I. Zink, J. F. Stoddart, *J. Am. Chem. Soc.* **2008**, *130*, 2382–2383.
[18] C. de la Torre, L. Mondragón, C. Coll, F. Sancenón, M. D. Marcos, R. Martínez-Máñez, P. Amorós, E. Pérez-Payá, M. Orzaez, *Chem. Eur. J.* **2014**, *20*, 15309–15314.
[19] A. Agostini, L. Mondragón, L. Pascual, E. Aznar, C. Coll, R. Martínez-Máñez, F. Sancenón, J. Soto, M. D. Marcos, P. Amorós, A. M. Costero, M. Parra, S. Gil, *Langmuir* **2012**, *28*, 14766–14776.
[20] I. Candel, E. Aznar, L. Mondragón, C. de la Torre, R. Martínez-Máñez, F. Sancenón, M. D. Marcos, P. Amorós, C. Guillem, E. Pérez-Payá, A. M. Costero, S. Gil, M. Parra, *Nanoscale* **2012**, *4*, 7237–7245.
[21] N. Mas, A. Agostini, L. Mondragón, A. Bernardos, F. Sancenón, M. D. Marcos, R. Martínez-Máñez, A. M. Costero, S. Gil, M. Merino-Sanjuan, P. Amorós, M. Orzaez, E. Pérez-Payá, *Chem. Eur. J.* **2013**, *19*, 1346–1356.
[22] A. Bernardos, E. Aznar, M. D. Marcos, R. Martínez-Máñez, F. Sancenón, J. Soto, J. M. Barat, P. Amorós, *Angew. Chem. Int. Ed.* **2009**, *48*, 5884–5887.
[23] Y. F. Zhu, W. J. Meng, N. Hanagata, *Dalton Trans.* **2011**, *40*, 10203–10208.
[24] A. Agostini, L. Mondragón, A. Bernardos, R. Martínez-Máñez, M. D. Marcos, F. Sancenón, J. Soto, A. Costero, C. Manguan-García, R.

Perona, M. Moreno-Torres, R. Aparicio-Sanchis, J. R. Murguía, *Angew. Chem. Int. Ed.* **2012**, *51*, 10556–10560.

[25] E. Aznar, R. Villalonga, C. Giménez, F. Sancenón, M. D. Marcos, R. Martínez-Máñez, P. Diez, J. M. Pingarron, P. Amorós, *Chem. Commun.* **2013**, *49*, 6391–6393.

[26] M. J. Chen, C. S. Huang, C. S. He, W. P. Zhu, Y. F. Xu, Y. F. Lu, *Chem. Commun.* **2012**, *48*, 9522–9524.

[27] P. Díez, A. Sanchez, M. Gamella, P. Martínez-Ruiz, E. Aznar, C. de la Torre, J. R. Murguia, R. Martínez-Máñez, R. Villalonga, J. M. Pingarrón, *J. Am. Chem. Soc.* **2014**, *136*, 9116–9123.

[28] X. J. Yang, F. Pu, C. E. Chen, J. S. Ren, X. G. Qu, *Chem. Commun.* **2012**, *48*, 11133–11135.

[29] See for example: (a) S. El Sayed, M. MIlani, C. Milanese, M. Licchelli, R. Matínez-Máñez, F. Sancenón, *Chem. Eur. J.* **2016**, *22*, 13935-13945; (b) A. Tukappa, A. Ultimo, C. de la Torre, T. Pardo, F. Sancenón, R. Martínez-Máñez, *Langmuir* **2016**, *32*, 8507-8515; (c) C. Giménez, E. Climent, E. Aznar, R. Martínez-Máñez, F. Sancenón, M. D. Marcos, P. Amorós, K. Rurack, *Angew. Chem. Int. Ed.* **2014**, *53*, 12629-12633; (d) C. de la Torre, A. Agostini, L. Mondragón, M. Orzaez, F. Sancenón, R. Martínez-Máñez, M. D. Marcos, P. Amorós, E. Pérez- Payá, *Chem. Commun.* **2014**, *50*, 3184-3186; (e) M. Oroval, E. Climent, C. Coll, R. Eritja, A. Aviñó, M. D. Marcos, F. Sancenón, R. Martínez-Máñez, P. Amorós, *Chem. Commun.* **2013**, *49*, 5480-5482.

[30] Ll. Pascual, S. El Sayed, R. Martínez-Máñez, A. M. Costero, S. Gil, P. Gaviña, F. Sancenón, *Org. Lett.* **2016**, *18*, 5548-5551.

[31] M. Comes, G. Rodríguez-López, M. D. Marcos, R. Martínez-Máñez, F. Sancenón, J. Soto, L. A. Villaescusa, P. Amorós, D. Beltrán, *Angew. Chem. Int. Ed.* **2005**, *44*, 2918-2922.

[32] D. E. Lorke, M. Y. Hasan, K. Arafat, K. Kuča, K. Musilek, A. Schmitt, G. A. Petroianu, *J. Appl. Toxicol.* **2008**, *28*, 422–429.

[33] H. P. Rang, M. Dale, J. M. Ritter, R. J. Flower, G. Henderson, *Rang & Dale's Pharmacology*, Elsevier Churchill Livingstone, London, England, **2015**.

[34] G. Petroianu, F. Kühn, C. Thyes, V. Ewald, A. Missler, *J. Appl. Toxicol.* **2003**, *23*, 75–79.

[35] S. J. A. Grove, J. Kaur, A. W. Muir, E. Pow, G. J. Tarver, M.-Q. Zhang, *Bioorg. Med. Chem. Lett.* **2002**, *12*, 193–196.

[36] W. S. Augerson in *Chemical and Biological Warfare Agents* (Ed.: W.S. Augerson), RAND, **2000**, pp. 99–189.

[37] J. C. Dacre in *Cholinesterases Fundamental and Applied Aspects* (Eds.: M. Brzin, E.A. Barnard, D. Sket), Walter De Gruyter, New York, **1984**, pp. 415–126.

[38] S. Royo, R. Martínez-Máñez, F. Sancenón, A. M. Costero, M. Parra, S. Gil, *Chem. Commun.* **2007**, 4839-4847.

[39] (a) C. Fan, L. Tsui, M. -C. Liao, *Chemosphere* **2011**, *82*, 229-236; (b) I. S. Fonsgaard, *Int. J. Environ. Anal. Chem.* **1995**, *58*, 231-245.

[40] See for example: (a) J. Turan, M. Kesik, S. Soylemez, S. Goker, S. Coskun, H. E. Unalan, L. Toppare, *Sens. Act. B. Chem.* **2016**, *228*, 278-286; (b) R. Funari, B.Della Ventura, R. Carrieri, L. Mora, E. Lahoz, F. Gesuele, C. Altucci, R. Velotta, *Biosen. Bioelectron.* **2015**, *67*, 224-229; (c) G. Fu, W. Chen, X. Yue, X. Jiang, *Talanta* **2013**, *103*, 110-115; (d) K. Wang, L. Wang, W. Jiang, J. Hu, Talanta 2011, 84, 400-405.

Chapter 5:

Oligonucleotide-capped mesoporous silica nanoparticles as DNA-responsive dye delivery systems for genomic DNA detection

Oligonucleotide-capped mesoporous silica nanoparticles as DNA-responsive dye delivery systems for genomic DNA detection

Lluís Pascual,[a,b,c] Isabel Baroja,[a,b,c] Elena Aznar,[a,c] Félix Sancenón,[a,b,c] M. Dolores Marcos, [a,b,c] Jose Ramón Murguía,[a,b,c] Pedro Amorós,[d] Knut Rurack,[e] Ramón Martínez-Máñeza,[b,c*]

[a] *Centro de Reconocimiento Molecular y Desarrollo Tecnológico (IDM), Unidad Mixta Universidad Politécnica de Valencia-Universidad de Valencia.*

[b] *Departamento de Química, Universidad Politécnica de Valencia, Camino de Vera s/n, 46022, Valencia, Spain.*

[c] *CIBER de Bioingeniería, Biomateriales y Nanotecnología (CIBER-BNN).*

[d] *Institut de Ciència dels Materials (ICMUV), Universitat de València, P.O. Box 2085, 46071 Valencia, Spain*

[e] *Fachbereich 1.9 Sensormaterialien, Bundesanstalt für Materialforschung und -prüfung (BAM), Richard-Willstätter-Straße 11, 12489 Berlin, Germany*

Received: October 21, 2014
Accepted: November 18, 2014
Published online: November 19, 2014

Reprinted with permission from
Chem. Commun. **2015**, *51*, 1414

Abstract

New hybrid oligonucleotide-capped mesoporous silica nanoparticles able to detect genomic DNA were designed.

Nanodevices equipped with molecular gates based on mesoporous silica nanoparticles have proven their potential for use in biological and medical applications.[1] So far, capped materials have been mainly used in drug delivery and their use in sensing protocols is still scarce.[2] For sensing, the mesoporous support is loaded with an indicator before the material is capped with a responsive chemistry. Uncapping and cargo delivery is then selectively achieved only in the presence of a target analyte.[3] In this context we are interested in the use of DNA sequences for the design of gated materials and others and we have recently reported the use of oligonucleotides as caps on mesoporous supports in the context of the detection of biomolecules via delivery of optical or electro-active probes.[4] However, in this context, the detection of genomic DNA using capped materials is still very rare.

Inspired by these preliminary works we report herein a new hybrid gated material with a covalently attached double-stranded DNA (dsDNA) sequence that selectively delivers a dye in the presence of genomic DNA. As a proof of concept the detection of *Mycoplasma* genomic DNA was pursued in this work. Detection of bacteria of genus *Mycoplasma* is of interest in diverse areas. *Mycoplasma* contamination is a common problem in cell culture laboratories of research institutions and hospitals.[5] Moreover, several *Mycoplasma* species are related to the development of certain pathologies such as pneumonia, rheumatoid arthritis and non-gonococcal urogenital diseases.[6]

The approach we followed is depicted in Scheme 1. MCM-41 mesoporous silica nanoparticles of ca. 100 nm of diameter were selected as

inorganic support because of their unique and advantageous properties for the design of capped materials. The MCM-41 support was first loaded with the dye rhodamine B, and then the external surface functionalized with (3-isocyanatopropyl)triethoxysilane yielding solid **S1-I**. For the gating mechanism two single stranded oligonucleotides were selected; i.e. (i) a short DNA sequence, functionalized with an aminohexyl moiety at the 5'-end position (NH_2-$(CH_2)_6$-5'-GAC TAC CAG GGT ATC-3', **O1**) that could be covalently attached to solid **S1-I** via the formation of urea bonds and (ii) a single stranded oligonucleotide (5'-AAG CGT GGG GAG CAA ACA GGA TTA GAT ACC CTG GTA GTC-3', **O2**) which is a highly conserved sequence of the 16S ribosomal subunit of in the *Mycoplasma* species genome.

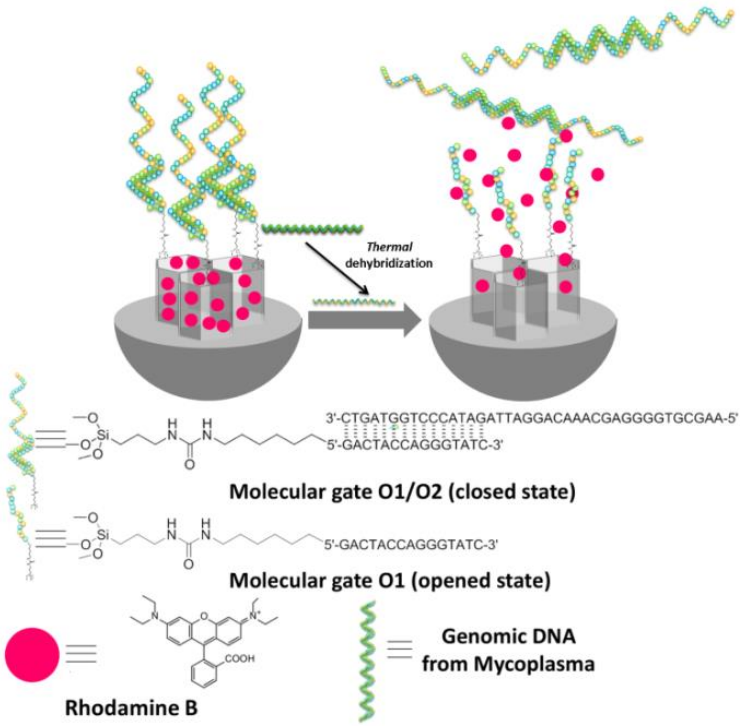

Scheme 1. Representation of the gated material **S1-O1/O2** capped with a dsDNA. Delivery of the entrapped dye (rhodamine B) is selectively accomplished in the presence of a single strand of *Mycoplasma* genomic DNA.

In a typical experiment the two single stranded DNA sequences (**O1** and **O2**) were first hybridized and then covalently attached to the surface of **S1-I** solid, yielding the final material **S1-O1/O2**. The dsDNA, anchored on the mesoporous support was expected to be bulky enough to block the pores and inhibit dye delivery. Moreover it was anticipated that the presence of a single strand of *Mycoplasma* genomic DNA would displace **O2** from the solid with the subsequent pore opening and dye release.

MCM-41 nanoparticles were obtained according to reported procedures. Solid **S1-I** was first loaded with rhodamine B in acetonitrile and then an excess of (3-isocyanatopropyl)triethoxysilane was added to the suspension. Solid **S1-I** was collected by centrifugation, washed with acetonitrile and dried (see Supporting Information for details). For the preparation of the final capped material (i.e. **S1-O1/O2**) **O1** and **O2** were first mixed, heated at 90ºC and then gradually cooled to achieve hybridization of both oligonucleotides. Then the hybridized **O1**/**O2** sequences were anchored onto the outer surface of the **S1-I** solid through the formation of a urea bond by reaction of the amine group in **O1/O2** and the isocyanatopropyl groups attached on **S1-I** (see Supporting Information for further details).

The starting MCM-41-like calcined nanoparticles and **S1-I** were characterized by powder X-ray diffraction, TEM, porosimetry, thermogravimetry and elemental analysis (see Supporting Information for details). Table 1 summarizes the particle diameter, BET specific surface area, pore volumes and pore sizes obtained for the starting nanoparticles and for solid **S1-I**. Moreover, from elemental and thermogravimetric analyses contents of 0.469 and 0.358 mmol g^{-1} for isocyanatopropyl and rhodamine B, respectively were determined in solid **S1-I**. Finally, dynamic light scattering studies in water gave diameters for the MCM-41, **S1-I** and **S1-O1/O2** nanoparticles of 88±2, 114±3 and 154±2 nm, respectively.

Table 1. Main structural properties calculated from TEM and N2 sorption analysis.

Sample	Diameter particle (nm)	S_{BET} (m^2 g^{-1})	Pore Volumea (cm^3 g^{-1})	Pore size[a] (nm)
MCM-41	80 ± 4	1228.2	0.93	2.40
S1-I	80 ± 3	524.9	0.34	2.40

[a] BJH model

The response of **S1-O1/O2** was tested in the presence of *Mycoplasma fermentans* genomic DNA by measuring the emission of rhodamine B dye delivered from the pores of the solid. In a typical experiment 0.2 mg of **S1-O1/O2** were suspended in 400 μL of hybridization buffer (20 mM TRIS-HCl, 37.5 $MgCl_2$, pH 7.5) and separated in 2 aliquots of 200 μL. Both samples were filled to a final volume of 900 μL with hybridization buffer. At the same time a solution of 4000 copies μL^{-1} of *Mycoplasma fermentans* quantification standard in water was heated to 95ºC for 5 min in order to dehybridize the double helix structure and then cooled on an ice bath for 3 min. After cooling, 100 μL of the dehybridized genomic solution was added to one of the aliquots whereas 100 μL of water (that was subjected to the same thermal treatment) were added to the other aliquot. Both suspensions were maintained at 25ºC and, at certain times, fractions were taken and centrifuged to eliminate the solid. Cargo release to the solution was then measured by the rhodamine B fluorescence at 575 nm (λ_{exc} = 555 nm). Figure 1 shows the delivery profile of rhodamine B from solid **S1-O1/O2** in the presence and in the absence of *Mycoplasma fermentans* genomic DNA. As it can be seen, in the absence of the target DNA (Figure 1, curve a) a poor rhodamine B delivery was observed (less than 15% after 1 h) indicative of a

remarkable pore closure. In contrast, in the presence of *Mycoplasma* genomic DNA, the pores were opened due to the displacement of oligonucleotide **O2** from the solid **S1-O1/O2** with the subsequent delivery of dye (Figure 1, curve b). Under these conditions ca. 90% of the maximum delivery of rhodamine B was observed after 30 min.

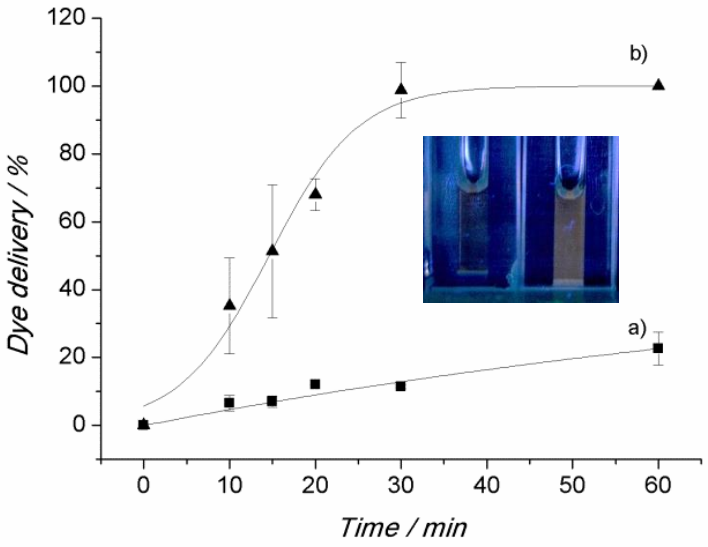

Figure 1. Release of rhodamine B from solid **S1-O1/O2** in a) the absence and b) in the presence of *Mycoplasma fermentans* genomic DNA (4000 copies μL^{-1}) in Tris-HCl buffer at pH 7.5. The inset shows the emission changes (under UV lamp, excitation at 254 nm) of the rhodamine B released from solid **S1-O1/O2** in the absence (left) and in the presence (right) of *Mycoplasma fermentans* genomic DNA (4000 copies μL^{-1}).

The proper performance of solid **S1-O1/O2** pointed toward an effective anchoring of the **O1/O2** dsDNA on the external surface of the inorganic scaffold through the formation of urea bonds. Additional experimental evidences of the correct grafting arose from the fact that solid **S1-O1/O2** was able to deliver rhodamine B in the presence of urease, due to the enzyme-induced hydrolysis of this bond with the subsequent detachment of the **O1/O2** double strand (see Supporting Information). Moreover, in the

presence of DNAse I, a remarkable dye release was also observed indicating the crucial role played by the **O1/O2** sequence in the capping protocol (see Supporting Information).

The next step was to assess the sensitivity of **S1-O1/O2** nanoparticles towards genomic DNA with the determination of the limit of detection. Following a procedure similar to that described above various solutions with different concentrations of *Mycoplasma fermentans* genomic DNA were added to several suspensions of **S1-O1/O2** and the rhodamine B released after 30 min was measured (see Supporting Information). A correlation between the number of copies of *Mycoplasma* genomic DNA added and the rhodamine B delivered was found in agreement with an uncapping process related with the displacement of **O2** from **S1-O1/O2** solid. A limit of detection of ca. 70 DNA copies μL^{-1} was determined (see Supporting Information). The limit of detection following this simple approach is not far from those reported by commercially available PCR *Mycoplasma* detection kits (around ca. 10 copies μL^{-1}),[7] suggesting that this procedure for genomic DNA sensing possesses the potential of finding application in medical diagnosis protocols.

In further studies the selectivity in the detection of *Mycoplasma* genomic DNA of **S1-O1/O2** solid was investigated by carrying out similar experiments in the presence of genomic DNA of the pathogens *Candida albicans* and *Legionella pneumphilla* in amounts of 1000 copies μL^{-1}. The results obtained are shown in Figure 2. As can be seen there were no significant differences between the blank (dye release in TRIS-HCl buffer) and the potentially interfering genomic DNA of *Candida albicans* and *Legionella pneumphilla*. In addition, when a mixture of *Candida albicans*-*Legionella pneumophilla* (each one at a concentration of 1000 copies μL^{-1}) was used no delivery of rhodamine B was observed. Furthermore, when genomic DNA

of *Mycoplasma* was present in the mixture a clear delivery of rhodamine B was found pointing to a high degree of selectivity of the **S1-O1/O2** material.

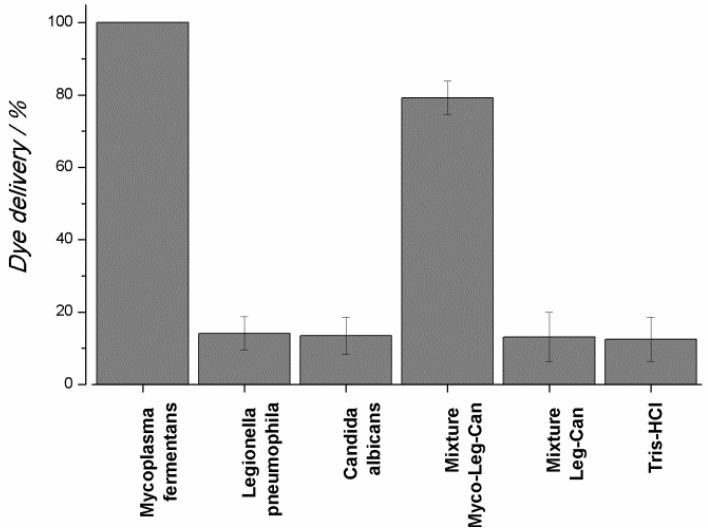

Figure 2. Release of rhodamine B from solid **S1-O1/O2** in the presence of (from right to left): Tris-HCl buffer, a mixture *of Candida albicans-Legionella pneumophilla (Leg-Can)* genomic DNA, a mixture of *Leg-Can* and *Mycoplasma fermentans (Myco)* genomic DNA, *Can* genomic DNA, *Leg* genomic DNA and *Myco* genomic DNA. All DNA were in a concentration of 1000 copies μL^{-1}

In summary, we have prepared mesoporous silica nanoparticles loaded with rhodamine B and capped with a covalently linked double stranded DNA containing a highly conserved sequence of the 16S ribosomal subunit of *Mycoplasma* species genome. The nanoparticles were able to deliver the entrapped dye in the presence of *Mycoplasma fermentans* genomic DNA. A remarkable detection limit of ca. 70 DNA copies μL^{-1} was found. Moreover the selectivity of the system was assessed and for instance addition of *Candida albicans* and *Legionella pneumophilla* genomic DNA were unable to induce dye release. We believe that DNA-based gated materials could be a suitable alternative to the standard bacteria detection techniques such as

PCR and can find application as an alternative rapid point-of-care diagnostic system or in situations and places were sophisticated techniques or equipment are not available.

Financial support from the Spanish Government (Project MAT2012-38429-C04) and the Generalitat Valencia (Project PROMETEOII/2014/047) is gratefully acknowledged. Ll. P. is grateful to the Universidad Politécnica de Valencia for his grant.

REFERENCES

[1] (a) A. Agostini, L. Mondragón, A. Bernardos, R. Martínez-Máñez, M. D. Marcos, F. Sancenón, J. Soto, A. Costero, C. Manguan-García, R. Perona, M. Moreno-Torres, R. Aparicio-Sanchis and J. R. Murguía, *Angew. Chem. Int. Ed.* **2012**, *51*, 10556; (b) Q. Zhang, X. Wang, P.-Z. Li, K. T. Nguyen, X.-J. Wang, Z. Luo, H. Zhang, N. S. Tan and Y. Zhao, *Adv. Funct. Mater.* **2014**, *24*, 2450; (c) C. Chen, J. Geng, F. Pu, X. Yang, J. Ren and X. Qu, *Angew. Chem. Int. Ed.* **2011**, *50*, 882; (d) L. Zhou, Z. Chen, K. Dong, M. Yin, J. Ren and X. Qu, *Adv. Mater.* **2014**, *26*, 2424.

[2] (a) A. Agostini, L. Mondragón, L. Pascual, E. Aznar, C. Coll, R. Martínez-Máñez, F. Sancenón, J. Soto, M. D. Marcos, P. Amorós, A. M. Costero, M. Parra and S. Gil, *Langmuir* **2012**, *28*, 14766; (b) C. Coll, A.Bernardos, R. Martínez-Máñez, F. Sancenón, *Acc. Chem. Res*. **2013**, *46*, 339; (c) E. Climent, R. Martínez-Máñez, A. Maquieira, F. Sancenón, M.D. Marcos, E.M. Brun, J. Soto, P. Amorós, *ChemistryOpen* **2012**, *1*, 251.

[3] (a) M. Oroval, E. Climent, C. Coll, R. Eritja, A. Avino, M. D. Marcos, F. Sancenon, R. Martinez-Manez and P. Amoros, *Chem. Commun.* **2013**,

49, 5480; (b) M. Chen, C. Huang, C. He, W. Zhu, Y. Xu and Y. Lu, *Chem. Commun.* **2012**, *48*, 9522.

[4] (a) E. Climent, R. Martínez-Máñez, F. Sancenón, M. D. Marcos, J. Soto, A. Maquieira and P. Amorós, *Angew. Chem. Int. Ed.* **2010**, *49*, 7281; (b) E. Climent, L. Mondragón, R. Martínez-Máñez, F. Sancenón, M. D. Marcos, J. R. Murguía, P. Amorós, K. Rurack and E. Pérez-Payá, *Angew. Chem. Int. Ed.* **2013**, *52*, 8938; (c) Z. Zhang, D. Balogh, F. Wang, S. Y. Sung, R. Nechushtai and I. Willner, *ACS Nano* **2013**, *7*, 8455; (d) L. Wu, J. Ren and Q. Xiaogang, *Nucleic Acid. Res.* **2014**, *42,* e160.

[5] H. Drexler and C. Uphoff, *Cytotechnology* **2002**, *39*, 75.

[6] (a) L. Matas Andreu, S. Molinos Abós, G. Fernández Rivas, V. González Soler and V. Ausina Ruiz, *Enferm. Infecc. Microbiol. Clin.* **2006**, *24*, 19; (b) Ausina V. *Infecciones causadas por micoplasmas. Medicina Interna Elsevier España* **2004**, *15*, 2362.

[7] (a) http://www.lifetechnologies.com; (b) http://www.sigmaaldrich.com

(c) http://www.lgcstandards-atcc.org (all websites accessed on 01/10/2014).

Supporting Information

Oligonucleotide-capped mesoporous silica nanoparticles as DNA-responsive dye delivery systems for genomic DNA detection

Lluís Pascual,[a,b,c] Isabel Baroja,[a,b,c] Elena Aznar,[a,c] Félix Sancenón,[a,b,c] M. Dolores Marcos, [a,b,c] Jose Ramón Murguía,[a,b,c] Pedro Amorós,[d] Knut Rurack,[e] Ramón Martínez-Máñeza,[a,b,c*]

[a] *Centro de Reconocimiento Molecular y Desarrollo Tecnológico (IDM), Unidad Mixta Universidad Politécnica de Valencia-Universidad de Valencia.*

[b] *Departamento de Química, Universidad Politécnica de Valencia, Camino de Vera s/n, 46022, Valencia, Spain.*

[c] *CIBER de Bioingeniería, Biomateriales y Nanotecnología (CIBER-BNN).*

[d] *Institut de Ciència dels Materials (ICMUV), Universitat de València, P.O. Box 2085, 46071 Valencia, Spain*

[e] *Fachbereich 1.9 Sensormaterialien, Bundesanstalt für Materialforschung und -prüfung (BAM), Richard-Willstätter-Straße 11, 12489 Berlin, Germany*

General techniques: Powder X-ray diffraction (PXRD) and thermogravimetric analysis (TGA), elemental analysis, transmission electron microscopy (TEM), N_2 adsorption-desorption, UV-visible (UV-vis) and fluorescence spectroscopy were employed to characterize the synthesized materials. PXRD measurements were performed on a D8 Advance diffractometer using Cu Kα radiation (Philips, Amsterdam, The Netherlands). Thermogravimetric analyses were carried out on a TGA/SDTA 851e balance (Mettler Toledo, Columbus, OH, USA), using an oxidizing atmosphere (air, 80 mL min^{-1}) with a heating program: gradient of 393-1273 K at 10°C min^{-1}, followed by an isothermal heating step at 1273°C for 30 min. TEM images were obtained with a 100 kV CM10 microscope (Philips). N_2 adsorption-desorption isotherms were recorded with an ASAP2010 automated sorption analyzer (Micromeritics, Norcross, GA, USA). The samples were degassed at 120°C in vacuo overnight. The specific surface areas were calculated from the adsorption data in the low pressure range using the Brunauer, Emmett and Teller (BET) model. Pore size was determined following the Barret, Joyner and Halenda (BJH) method. Fluorescence spectroscopy measurements were carried out on a Felix 32 Analysis version 1.2 (Build 56, Photon Technology International, Birmingham, NJ, USA).

Chemicals: Tetraethylorthosilicate (TEOS), *n*-cetyltrimethylammoniumbromide (CTAB), NaOH, **(**3-isocyanatopropyl) triethoxysilane, rhodamine B, tris(hydroxymethyl)aminomethane (TRIS), hydrochloric acid and oligonucleotides **O1** (NH_2-$(CH_2)_6$-5'-GAC TAC CAG GGT ATC-3') and **O2** (5'-AAG CGT GGG GAG CAA ACA GGA TTA GAT ACC CTG GTA GTC-3') were purchased from Sigma-Aldrich Química (Madrid, Spain). All products were used as received.

Synthesis of MCM-41 mesoporous nanoparticles: NaOH (2.00 mol L^{-1}, 3.5 mL) was added to a solution of CTAB (1.00 g, 2.74 mmol) in deionized H_2O (480 mL). The solution temperature was adjusted to 80°C and then TEOS (5.00 mL, 2.57 × 10^{-2} mol) was added dropwise. The mixture was stirred for 2 h to give a white precipitate. The solid was isolated by centrifugation and washed with deionized H_2O and EtOH and then dried at 60°C for 12 h to give MCM-41. In order to remove the template phase, MCM-41 was calcined at 550°C using an oxidizing atmosphere.

Synthesis of S1-I: In a typical synthesis, calcined MCM-41 (200 mg) and rhodamine B (766.4 mg, 0.16 mmol) were suspended in CH_3CN (10 mL). The suspension was stirred at room temperature for 24 h. Then an excess of (3-isocyanatopropyl)triethoxysilane (247.6 µl , 1.0 mmol) was added, and the final mixture was stirred at room temperature for 5.5 h. The resulting pink solid (**S1-I**) was isolated by centrifugation, washed with CH_3CN (5 mL) and dried at 38°C for 18 h.

Synthesis of S1-O1/O2: A mixture of oligonucleotides **O1** and **O2** (25 µL of each in water at 100 µM concentration) was heated to 90°C and cooled at 25°C slowly in order to achieve DNA hybridization (formation of **O1/O2**). The DNA mixture solution was added to a suspension containing 1 mg of **S1-I**, 50 µL of water, 700 µL of a solution of rhodamine B in CH_3CN (1 mM) and 2 µL of triethylamine. Finally, the mixture was stirred for 18 h at 37°C. The resulting solid was isolated by centrifugation and washed with hybridization buffer (20 mM TRIS-HCl, 37.5 mM $MgCl_2$, pH 7.5) to eliminate the residual dye and unbounded oligonucleotides (see Figure S1).

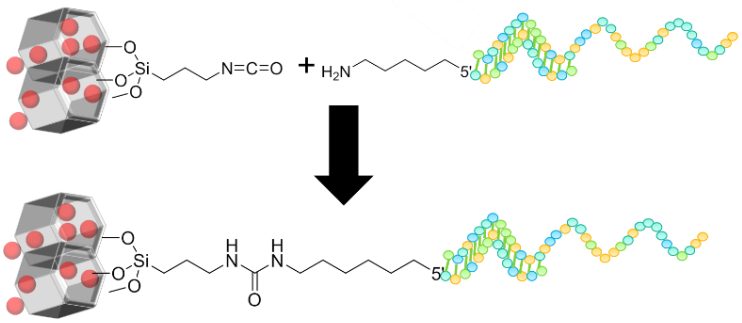

Figure S1. Surface functionalization reaction of **S1-I** via urea bond formation with **O1/O2**.

Characterization of the prepared materials: The MCM-41 scaffold and the mesoporous solid **S1-I** were characterized following standard techniques, including transmission electron microscopy (TEM), powder X-ray diffraction (PXRD) and N_2 sorption analysis**.** PXRD pattern of siliceous MCM-41 nanoparticles as synthesized (Figure S2, curve a) showed four low-angle reflections typical of a hexagonal array, indexed as (100), (110), (200), and (210) Bragg peaks. A significant displacement of 3Å of the (100) peak in the PXRD pattern of the MCM-41 calcined nanoparticles was evident in curve b, related to further condensation of silanol groups during the calcination step. Finally, curve c corresponds to the **S1-I** PXRD pattern. An intensity decrease of the (100) peak and a broadening of the (110) and (200) reflections was observed, related to a loss of contrast due to the filling of the pore voids with the rhodamine B dye.

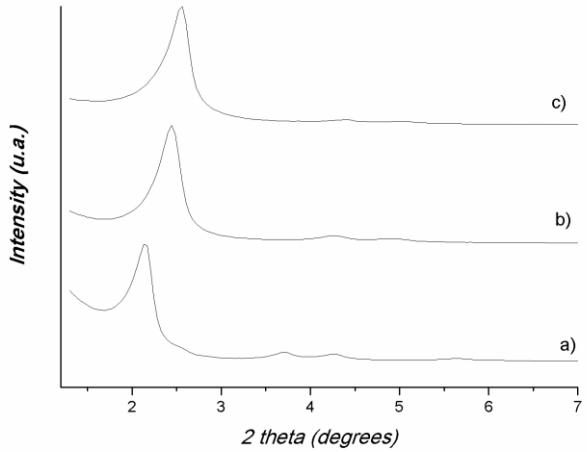

Figure S2. Powder X-ray patterns of the solids (a) MCM-41 as synthesized, (b) calcined MCM-41, and (c) solid **S1-I**.

The presence, in the final functionalized solids, of the mesoporous structure was confirmed by TEM analysis, in which the typical channels of the MCM-41 matrix are visualized as alternate black and white stripes (see Figure S3). The figure also shows that the prepared MCM-41 and solid **S1-I** are obtained as spherical particles with diameters ranging from ca. 80 to 120 nm.

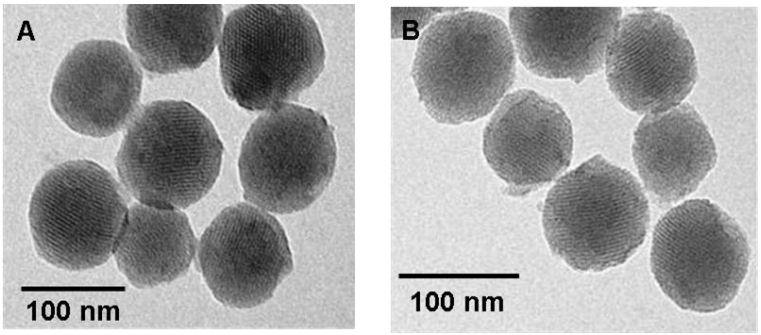

Figure S3. TEM images of calcined MCM-41 sample (A) and solid **S1-I** (B) showing the typical porosity of the MCM-41 mesoporous nanoparticles matrix.

The N_2 adsorption–desorption isotherms of the calcined MCM-41 nanoparticles show an adsorption step at an intermediate P/P_0 value (0.1–0.3) typical of this type of solid (see Figure S4, curve a). A total pore volume of 0.93 cm^3 g^{-1} was calculated by using the BJH model on the adsorption branch of the isotherm. The application of the BET model resulted in a value for the total specific surface of 1228.2 m^2 g^{-1}. From the XRD, porosimetry, and TEM studies a pore diameter of 2.40 nm was determined. The N_2 adsorption–desorption isotherm of **S1-I** (see Figure S4, curve b) is typical of mesoporous systems with filled mesopores, and a significant decrease in the N_2 volume adsorbed (0.34 cm^3 g^{-1}) and surface area (524.9 m^2 g^{-1}) were observed.

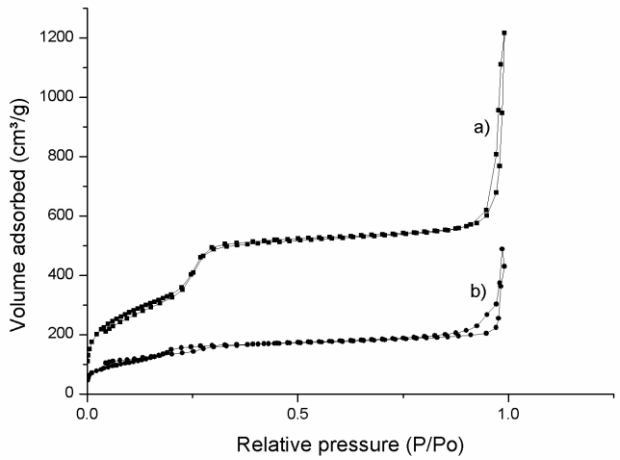

Figure S4. N_2 adsorption-desorption isotherms for calcined MCM-41 nanoparticles (a) and **S1-I** material (b).

The content of **(**3-isocyanatopropyl)triethoxysilane and rhodamine B in the prepared solid **S1-I** was determined by elemental and thermogravimetric analyses (see Table S1). Moreover the diameter of MCM-41, **S1-I** and **S1-**

O1/O2 solids was measured by dynamic light scattering (DLS) studies (see Figure S5 and Table S2).

Table S1. Contents of **(**3-isocyanatopropyl)triethoxysilane and rhodamine B (in mmol/g solid) in the prepared solid **S1-I**.

	$\alpha_{isocyanate}$ (%)	$\alpha_{Rhodamine\ B}$ (%)	$\alpha_{Organic\ matter}$ (%)
Elemental analysis	3.99±0.09	17.16±0.11	21.15±0.10
Thermogravimetry	-	-	26.1±0.2

Table S2. Diameter of MCM-41, **S1-I** and **S1-O1/O2** solids measured by DLS.

	Particle diameter (nm)
MCM-41	88±2
S1-I	114±3
S1-O1/O2	154±2

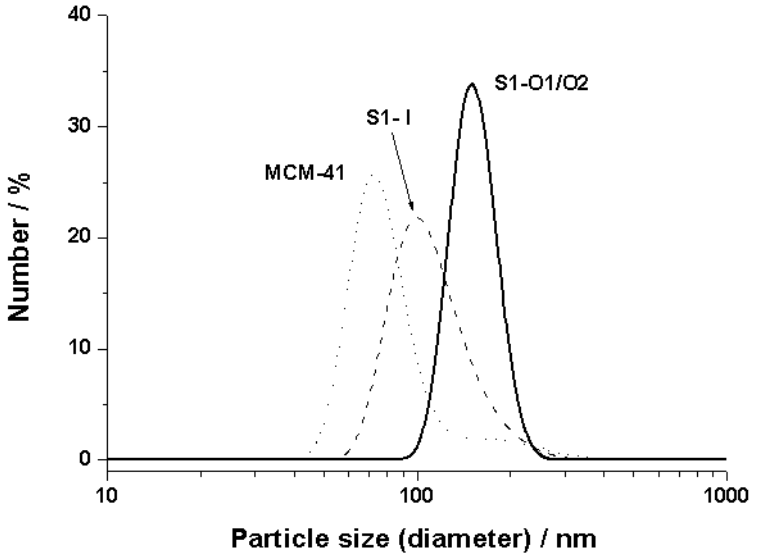

Figure S5. Size distribution by number of particles obtained by DLS studies for calcined MCM-41, **S1-I** and **S1-O1/O2** solids.

Controlled release of solid S1-O1/O2 in the presence of urease and DNAse I enzymes: To confirm the proper anchoring of the double stranded **O1/O2** oligonucleotide, 200 μg of solid **S1-O1/O2** were suspended in 400 μL of the hybridization buffer and separated in 2 aliquots (each of 200 μL). One of the samples was filled to a final volume of 1000 μL with hybridization buffer whereas the other was filled with the same buffer but containing DNAse I enzyme (at a concentration of 10 U/μL). Both suspensions were stirred at 25ºC for 90 minutes. Aliquots of 150 μL were taken at several times and centrifuged 2 min at 12000 rpm (in order to remove the solid) and the fluorescence of the rhodamine B released measured at 575 nm (λ_{exc} 555 nm). The same experimental procedure was used to study rhodamine B release form solid **S1-O1/O2** in the presence of urease. The obtained results are shown in Figure S6.

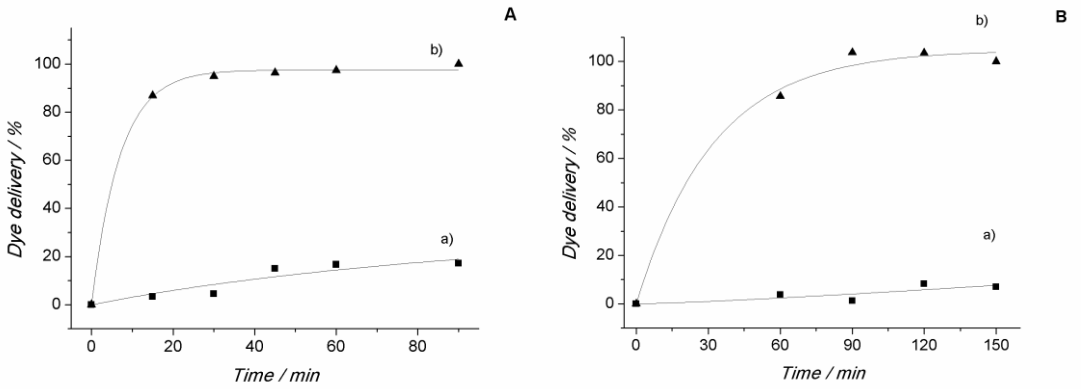

Figure S6. A: Delivery of rhodamine B from solid **S1-O1/O2** in the absence (a) and in the presence (b) of DNAse I; B: Delivery of rhodamine B from solid **S1-O1/O2** in the absence (a) and in the presence (b) of urease.

Release experiments of S1-O1/O2: To investigate the gating properties of **S1-O1/O2**, 200 µg of this solid were suspended in 400 µL of the hybridization buffer and separated in 2 aliquots of 200 µL. Both samples were filled to a volume of 900 µL with hybridization buffer. At the same time a solution of 4000 copies μL^{-1} of *Mycoplasma fermentans* quantification standard in water was heated to 95ºC for 5 min and cooled on ice bath at 0ºC for 3 min (in order to dehybridize the double stranded structure). Then, 100 µL of the genome solution was added to one of the **S1-O1/O2** suspensions. Simultaneously 100 µL of water (milliQ grade) with the same thermal treatment were added to the remaining aliquot. Both suspensions were stirred at 25ºC for 60 min. Aliquots of 150 µL were taken at several times and centrifuged 2 min at 12000 rpm (in order to remove the solid) and the fluorescence of the rhodamine B released measured at 575 nm (λ_{exc} 555 nm).

Calibration curve of S1-O1/O2 with *Mycoplasma fermentans* genomic DNA: In order to carry out these experiments, 120 µL of aqueous solutions containing different number of *Mycoplasma fermentans* DNA copies were heated for 5 min at 95ºC, in order to dehybridize DNA. Then, these solutions

were left cooling for ca. 3 min in ice bath. These samples were added to several aliquots of 60 μL of **S1-O1/O2** (0.2 mg of solid in 400 μL of hybridization buffer). All samples were stirred at 25ºC for 30 min, and after that, were centrifuged 2 min at 12000 rpm in order to remove the solid. The fluorescence of the released rhodamine B was then measured at 575 nm (λ_{exc} 555 nm). The obtained calibration curve is shown in Figure S7. From this curve the limit of detection (ca. 70 DNA copies μL^{-1}) has been calculated based in the intersection point of the two slopes. Moreover a limit of quantification (10σ) of ca. 150 DNA copies μL^{-1} has been determined.

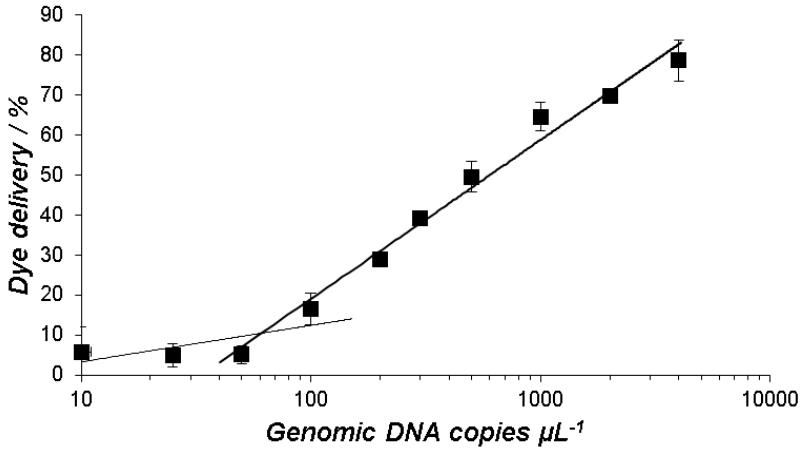

Figure S7. Release of rhodamine B from solid **S1-O1/O2** in the presence of different numbers of *Mycoplasma fermentans* genomic DNA copies in TRIS-HCl buffer (pH 7.5).

Selectivity studies with S1-O1/O2: In order to carry out these experiments, 120 μL of aqueous solutions containing different genome solutions of *Mycoplasma fermentans, Candida albicans, Legionella pneumophilla,* a mixture of *Candida albicans-Legionella pneumophilla* and a mixture of the three genomes (1000 copies μL^{-1}) were heated for 5 min at 95ºC, in order to dehybridize DNA. As control a 120 μL of hybridization buffer received the

same thermal treatment. Then, these samples were left cooling for ca. 3 min in ice bath. These samples were added to several aliquots of 60 μL of **S1-O1/O2** (0.2 mg of solid in 400 μL of hybridization buffer). All samples were stirred at 25ºC for 30 min, and after that, samples were centrifuged 2 min at 12000 rpm in order to remove the solid. The fluorescence of the released rhodamine B was then measured at 575 nm (λ_{exc} 555 nm).

Chapter 6:

MUC1 aptamer-capped mesoporous silica nanoparticles for controlled drug delivery and radio-imaging applications

MUC1 aptamer-capped mesoporous silica nanoparticles for controlled drug delivery and radio-imaging applications

Lluis Pascual,[†, ‡, §] Cristal Cerqueira-Coutinho,[⊥] Alba García-Fernández,[†, ‡, §] Emerson Soares Bernardes,[‖] Marta Souza Albernaz,[▽] Sotiris Missailidis,[○] Ramón Martínez-Máñez, *[,†, ‡, §] Ralph Santos-Oliveira,* [, ▽] and Félix Sancenón[†, ‡, §]

[†] *Instituto Interuniversitario de Reconocimiento Molecular y Desarrollo Tecnológico (IDM). Universitat Politecnica de Valencia, Universitat de Valencia, Spain.*

[‡] *Departamento de Química, Universidad Politécnica de Valencia, Camino de Vera s/n, 46022, Valencia, Spain.*

[§] *CIBER de Bioingeniería, Biomateriales y Nanomedicina (CIBER-BBN).*

[‖] *Centro de Radiofarmácia, Instituto de Pesquisas Energéticas e Nucleares, São Paulo, Brazil*

[⊥] *Federal University of Rio de Janeiro, Faculty of Phamacy, Rio de Janeiro-Brazil*

[▽] *Brazilian Nuclear Energy Commission, Nuclear Engineering Institute, Rio de Janeiro, Brazil*

[○] *Oswaldo Cruz Foundation, Biomanguinhos, Rio de Janeiro, Brazil*

Submited to Advanced Healthcare Materials

Abstract

Mesoporous silica nanoparticles (MSNs) capped with an MUC1 aptamer (S1-apMUC1) have been designed and used for cargo delivery. The pores of MSNs were loaded with safranin O, the external surface functionalised with aminopropyl groups, and nanoparticles gated with the MUC1 aptamer. Laboratory tests demonstrated that solid S1-apMUC1 remained capped, but was able to release safranin O in the presence of DNAse I enzyme (able to hydrolyze the capping aptamer). Confocal microscopy studies showed that the S1-apMUC1 nanoparticles were effectively internalised in MDA-MB-231 cancer cells that overexpress MUC1 receptor with subsequent pore opening and cargo release. The MUC1-mediated internalization of the S1-apMUC1 nanoparticles was corroborated using MCF-10-A cancer cells that do not express MUC1, for which poor internalisation was observed. For imaging applications, the S1-apMUC1-Tc nanoparticles were prepared by radiolabelling the S1-apMuc1 nanoparticles with ^{99m}Tc. *In vivo* imaging studies were performed with MDA-MB-231 tumour-bearing Balb/c mice, and a remarkable ^{99m}Tc signal in the tumour was noted.

6.1 Introduction

Nanotechnology and nanotechnological products are being slowly and noiselessly introduced into our daily lives. Nanotechnology offers myriads of possibilities of developing innovative materials with extended applications in almost countless scientific and technological fields.[1] Perhaps one of the most promising applications of nanotechnology, in the form of smart nanomaterials, is related with nanomedicine.[2] This term covers the medical applications of nanoparticles, biological devices, nanoelectronic

biosensors and biological machines for solving *in vitro* and *in vivo* medical problems.[3]

Among the realm of nanodispositives with powerful applications in medicine, perhaps those related with controlled release are among the most appealing. The possibility of supplying certain drugs or active molecules and biomolecules into the site at which its action is required is expected to drastically reduce side effects.[4] In order to achieve this task, drugs or bioactive agents are normally incorporated into or onto the surface of certain nanomaterials; e.g., micelles, polymers, liposomes or inorganic nanoparticles.[5] The role of these carriers is to protect cargoes from the external environment until target cells/tissues/organs are reached, and then payload release occurs. Loaded nanodevices can also be functionalised with targeting ligands (e.g. polysaccharides, peptides, DNA fragments, antibodies, aptamers) that allow selective internalisation in the cells in which their action is required.[6]

In order to deal with carriers, mesoporous silica nanoparticles (MSNs) have been extensively used in recent years given their remarkable properties, such as homogeneous pore size, large pores, large specific volume and area, good thermal stability, sound biocompatibility and easy functionalisation using trialkoxysilane–based chemistries.[7,8] Notwithstanding, perhaps the most appealing feature of MSNs as carriers is the possibility of functionalising them with molecular/supramolecular ensembles on their external surface to develop gated materials, which ideally show "zero delivery", but release payload on-command in response to specifically designed external stimuli. Several examples of these gated nanoparticles have been reported mainly as drug delivery systems, but also for sensing and diagnostic applications.[9-11]

When dealing with triggering, a number of different external stimuli have been reported to uncap pores and induce cargo release using MSNs. Accordingly, materials triggered by pH changes, redox reactions, light, magnetic fields, ultrasounds, temperature, polarity changes and presence of molecules or biomolecules have been recently described.[9] Yet it was using biomolecules as triggers which was the ultimate proof of the possible application of gated silica mesoporous nanoparticles to biological environments.[12] Among biomolecules, the use of enzymes for uncapping gated materials is appealing if we take into account that employing tailor-made derivatives and specific enzymes is envisioned to have a huge potential, which may provide exquisite selectivity when designing advanced gated devices for the delivery of drugs and active agents. In this field, delivery from MSNs using esterases, glycosidases, peptidases, reductases and DNases has been recently reported.[13-20]

Another biomolecule that has been paid ever-increasing attention in recent years is DNA, used as capping subunits to prepare gated MSNs for controlled delivery applications.[21,22] One specific class of DNAs is aptamers, which are oligonucleotides with a well-known conformation that can bind selectively to certain target small molecules, proteins or ions. Aptamers have been recently used as caps to develop gated materials for drug delivery and sensing.[23-25] Moreover, certain aptamers can used as targeting agents, which make them a valuable alternative to antibodies and peptides and can be used in the design of imaging agents.[26,27]

From another point of view, one of the most powerful imaging techniques is isotopic labeling.[28] This technique consists in marking the (bio)-molecule or nanodevice that we wish to track with selected radionuclides. Decay in the radionuclide emits radiation that can be detected by signalling the presence of the labelled system. In nuclear medicine, a widely used

technique to detect radionuclides is single photon emission computed tomography (SPECT).[29,30] Among various SPECT radionuclides, ^{99m}Tc has been extensively used to develop radiopharmaceuticals because of its ideal nuclear properties and easy low-cost availability.[31-33] Recently certain SPECT radionuclides (^{99m}Tc and ^{188}Re) have been incorporated into specific aptamers and evaluated for their clinical applicability.[34-36] Some of those radionuclide-labelled aptamer probes have shown rapid accumulation rates in tumour, good targeting ability and fast clearance from blood. MSNs have also been radiolabelled with several radioisotopes by different approaches (e.g., direct adsorption onto surfaces, coating nanoparticles with poly(ethylene glycol) conjugated with marked antibodies, functionalising the nanoparticle surface with *t*-cyclooctene derivatives that have undergone 3+2 cycloadditions with labelled tetraazines and grafting complexes through amidation reactions) and have also been used for positron emission tomography (PET) and SPECT imaging.[37-45] However, a typical drawback of some of these labelled systems is poor tumour accumulation.[39,40]

From another perspective, MUC-1 is a mucin glycoprotein expressed in the extracellular matrix by most glandular and ductal epithelial cells, and by several hematopoietic cell lineages.[46] MUC-1 is also highly expressed by the majority of human adenocarcinomas and its presence has been associated with poor clinical prognosis. MUC-1 is shed in the bloodstream of adenocarcinoma patients and is the antigen in commercial serum tumour marker assays.[47] The extracellular presentation of MUC-1, its elongated structure and characteristic under-glycosylation patterns allow the protein core to be exposed in cancer cells, which thus make it a suitable target for immunotherapeutic and targeted radiotherapy approaches.[48] In line with this, MUC-1 aptamers (that bind ligands to the MUC-1 glycoprotein tumour marker) have been functionalised with commercially available chelators,

radiolabelled with ^{99m}Tc and used in biodistribution and imaging studies in xenografted MCF-7 tumour-bearing mice.[49-51] MUC-1 aptamers have also been grafted onto the external surface of silica nanoparticles labelled with fluorophores and the prepared nanodevices used to detect breast cancer cells.[52]

If we take into account all this information, as well as our interest in preparing gated MSNs and applying them to controlled release and signalling applications,[9,11] we show herein the synthesis, characterisation, controlled release features and imaging properties of MSNs loaded with safranin O, capped with an aptamer targeting MUC1 glycoprotein and labelled with ^{99m}Tc. These nanoparticles released the entrapped dye in the presence of DNAse I enzyme and were preferentially internalised by MDA-MB-231 (expresses glycoprotein MUC-1 in the membrane) cancer cells. The radiolabelled nanoparticles, injected into MDA-MB-231 tumour-bearing Balb/c mice, showed remarkable accumulation in tumours in SPECT images. The same accumulation trend was observed in the biodistribution studies.

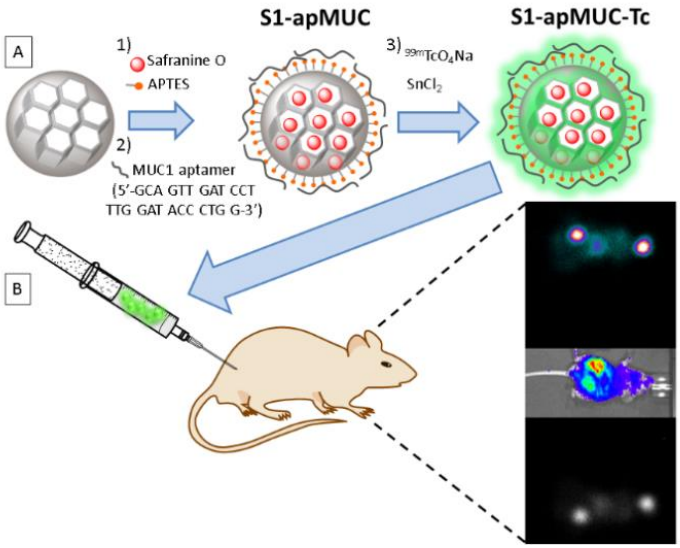

Scheme 1. (A) Synthetic route used to prepare **S1-apMUC1** and **S1-apMUC1-Tc** nanoparticles. (B) Application of **S1-apMUC1-Tc** as a radiolabelling tool.

6.2 Results and discussion

Design and synthesis of aptamer-capped nanoparticles. MSNs were prepared in alkaline media following well-known procedures that use *n*-cetyltrimethylammonium bromide (CTAB) as a directing agent to condense inorganic precursor tetraethylortosilicate (TEOS).[53] The obtained powder was washed and CTAB was removed by calcination. The pores of the calcined MSNs were loaded with safranin O and the external surface of nanoparticles was functionalised with (3-aminopropyl) triethoxysilane (solid **S1**). Aminopropyl moieties were positively charged at a neutral pH and they are known to display electrostatic interactions with negatively charged aptamers. Therefore, the addition of an MUC1 aptamer (5'-GCA GTT GAT CCT TTG GAT ACC CTG G-3') to a suspension of **S1**

nanoparticles resulted in pore capping, which yielded the final material **S1-apMUC1** (see Scheme 1). The **S1-apMUC1** nanoparticles were expected to be effectively internalised by cancer cells that overexpressed glycoprotein MUC1, and to deliver the cargo via the hydrolysis of the capping aptamer by DNAse enzymes (see also Scheme 1). We also labelled the **S1-apMUC1** nanoparticles with the ^{99m}Tc radioisotope to explore the potential use of nanoparticles as a radiopharmaceutical probe (solid **S1-apMUC1-Tc**).

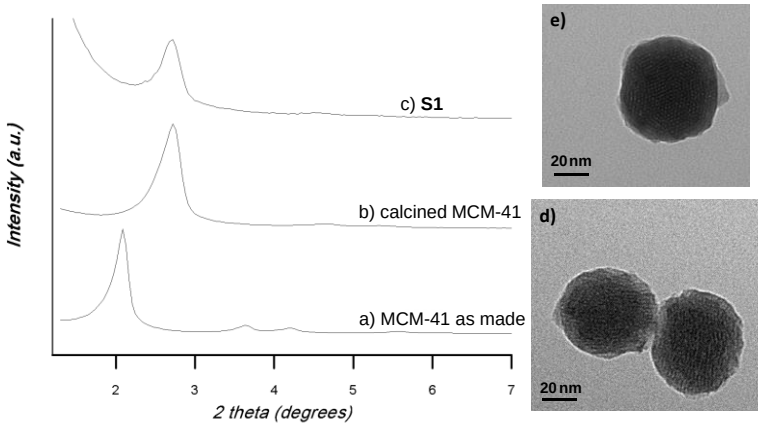

Figure 1. Left: Powder X-ray diffraction patterns of MCM-41 nanoparticles as made (a), calcined MCM-41 nanoparticles (b) and solid **S1** (c). Right: TEM images of the calcined MCM-41 nanoparticles (d) and solid **S1** (e).

Characterisation of gated MSNs. The prepared nanoparticles were characterised by standard techniques. The powder X-ray diffraction of the MCM-41 as-synthesised nanoparticles (curve a in Figure 1) showed four low-angle reflections, typical of a hexagonal mesoporous array that can be indexed as (100), (110), (200) and (210) Bragg peaks. Presence of (100) reflection in the calcined MCM-41 (curve b in Figure 1) and in solid **S1** (curve c in Figure 1) evidenced that loading pores with safranin O and the further functionalisation of the external surface with aminopropyl moieties did not modify the 3D mesoporous structure. Furthermore, an analysis of the TEM

images of the calcined MCM-41 and **S1** nanoparticles confirmed the presence of the mesoporous structure. The typical channels of the mesoporous silica network were visualised as alternate black and white stripes (Figure 1). TEM images also showed that the starting MSNs and solid **S1** consist of spherical particles with a diameter of ca. 100 nm.

N_2 adsorption-desorption studies on the starting MSNs and **S1** were carried out. For both materials, the pore volume was calculated by applying the Barret-Joyner-Halenda (BJH)[54] model on the adsorption branch of the isotherm and the total specific surface was calculated by the Brunauer-Emmet-Teller (BET)[55] model. The values obtained for the calcined MCM-41 and **S1** are listed in Table 1. The calcined MSNs showed a typical curve for this mesoporous support (see Supporting Information), which consisted in an adsorption step at an intermediate P/P_0 value (0.1–0.3). Narrow BJH pore distribution and absence of a hysteresis loop within this interval suggested the existence of uniform cylindrical mesopores (pore diameter of 2.10 nm, pore volume of 0.26 $cm^3\ g^{-1}$, calculated on the adsorption branch of the isotherm). Pore diameter was estimated by analysing the TEM images that agreed with this value. After applying the BET model, a value of 1195 $m^2\ g^{-1}$ was obtained for the total specific surface.

Table 1. BET-specific surface values, pore volumes and pore sizes calculated from the N_2 adsorption-desorption isotherms.

Sample	S_{BET} ($m^2\ g^{-1}$)	BJH pore size[a,b] [nm]	Pore Volume[a] ($cm^3\ g^{-1}$)
Calcined MCM-41	1195	2.51	0.961
S1	66	-	0.036

[a] Pore volumes and pore sizes related only to interparticle mesopores.

[b] Pore sizes estimated by the BJH model applied to the adsorption branch of the isotherm.

The N_2 adsorption-desorption isotherm of solid **S1** was typical of mesoporous systems with filled mesopores, and both the pore volume (0.036 $cm^3\ g^{-1}$) and the specific surface area (66 $m^2\ g^{-1}$) clearly and drastically diminished (see Supporting Information). This reduction in the BET surface, compared with that of the starting MSNs, was attributed to loading pores with safranin O and surface functionalisation with aminopropyl moieties.

The safranin O and aminopropyl contents on solid **S1** were determined by thermogravimetric studies and elemental analyses, which amounted to 0.044 and 1.821 mmol g^{-1}, respectively.

Finally, solid **S1-apMUC1** was prepared in very small quantities, but could not be completely characterized. However, energy dispersive X-ray spectroscopy (EDX, 20 kV) studies on **S1-apMUC1** showed the presence of remarkable amounts of phosphorus atoms (see Supporting Information), which indicated the formation of an MUC1 aptamer shell on the external surface of the **S1-apMUC1** solid.

***In vitro* safranin O release studies form S1-apMUC1.** In a first step, the cargo release from the **S1-apMUC1** nanoparticles alone and in the presence

of DNAse I was studied. In a typical experiment, 100 μg of **S1-apMUC1** were suspended in 400 μL of buffer (20 mM TRIS, pH 7.5; 37.5 mM $MgCl_2$) and then separated into two aliquots. To one of the samples, buffer solution was added until a final volume of 1,000 μL was reached. The other aliquot was also diluted to a final volume of 1,000 μL, but by adding the buffer that contained DNAse I (at the 10 U μL^{-1} concentration). Both suspensions were stirred and aliquots of 150 μL were taken at scheduled times. These aliquots were centrifuged to remove the solid and the emission of the safranin O released at 585 nm (excitation at 520 nm) was measured. The obtained release profiles are shown in Figure 2.

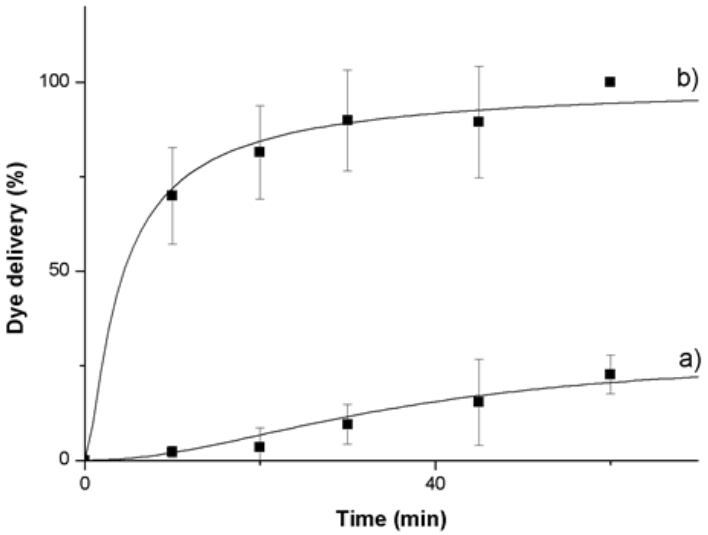

Figure 2. *In vitro* release profiles of safranin O from solid **S1-apMUC** in the absence (a) and presence (b) of DNAse I in TRIS (20 mM pH 7.5) that contained $MgCl_2$ (37.5 mM).

As seen in Figure 2, poor safranin O release was observed (ca. 10% in the first 30 min and reached 20% after 60 min) in the absence of DNAse I.

However when the enzyme was present, a remarkable fast safranin O delivery took place (ca. 90% of the total amount released was found after ca. 30 min). The observed payload release was directly related with the DNAse I-induced hydrolysis of the MUC1 aptamer that allowed pore opening and dye delivery.

Controlled release studies in cells. After conducting studies into the effective safranin O release from **S1-apMUC1** in the presence of DNAse I, our next goal was to prove the possible use of the aptamer-capped nanoparticles as a specific delivery system in cell models. For this purpose, MDA-MB-231 (which expresses glycoprotein MUC-1 in its membrane) and MCF-10-A (which does not express MUC1) cancer cells were selected. The internalisation of the **S1-apMUC1** nanoparticles in cells was assessed by confocal microscopy studies. The MDA-MB-231 and MCF-10-A cell lines were incubated with the **S1-apMUC1** nanoparticles for 2 h and safranine O-associated fluorescence was measured (see Figure 3A). As seen, the MDA-MB-231 cells internalised the **S1-apMUC1** nanoparticles more efficiently than the MCF-10-A cells. In fact strong red fluorescence of the released safranine O was observed in the cytoplasm for the MDA-MB-231 cells, whereas the signal in the MCF-10-A cells was very low under the same conditions. These differences were attributed to the preferential MUC1-mediated internalisation of **S1-apMUC1** in the MDA-MB-231 cells. Quantification of the fluorescence associated with safranine O was determined for each treatment to confirm the results observed in the confocal images. Figure 3B shows a very weak safranine O emission for the MCF-10 cells treated with the **S1-apMUC1** nanoparticles. However, marked safranine O associated fluorescence (4-fold enhancement compared to that

obtained for the MCF.10 cells) was observed for MDA-MB-231 cells treated with **S1-apMUC1**.

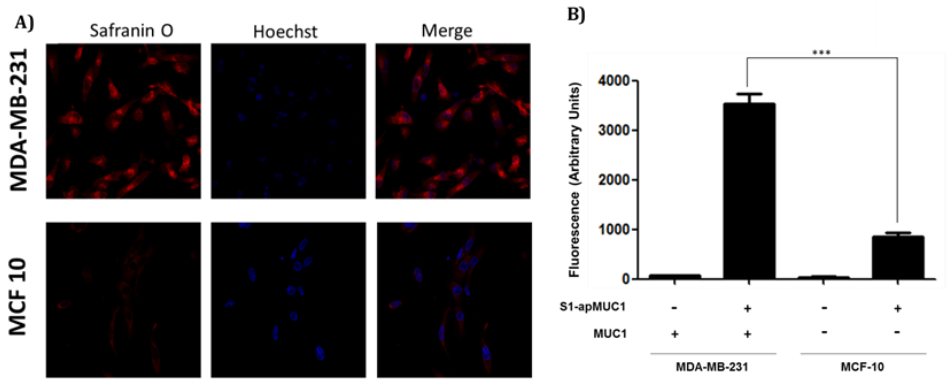

Figure 3. A) Cellular uptake of **S1-apMUC1** in the MDA-MB-231 and MCF-10-A cells. Both cell lines were incubated for 2 h in the presence of **S1-apMUC1** (100 μg/mL). The internalisation of the **S1-apMUC1** nanoparticles was followed by safranin O-associated fluorescence (red) in the presence of DNA marker Hoechst 33342 (blue). Cytoplasmic safranin O-associated fluorescence was observed in the MDA-MB-231 cells that overexpressed MUC1 glycoprotein. The MCF-10-A cells, which lacked the MUC1 glycoprotein, showed poor red fluorescence and only the Hoechst-associated emission was clearly observed. B) Quantification of the safranin O-associated fluorescence intensity for the different treatments. Three independent experiments were done, which gave similar results. Data are expressed as mean±s. Statistically significant differences were found among the different treatments when paired t Student tests were applied ($p < 0.0001$).

Radiolabelling and imaging studies. In order to take another step forward and to impart our nanoparticles with diagnostic features, we studied the labelling of **S1-apMUC1** with the ^{99m}Tc radioisotope. ^{99m}Tc is a metastable isomer of ^{99}Tc used as a radioactive tracer in diagnostic nuclear medicine procedures. It emits easily detectable 140.51 keV gamma rays and has a half-life of 602 h.[56]

In a typical experiment, 150 μg of **S1-apMUC1** nanoparticles were incubated with $SnCl_2$ as the reducing agent and with $Na^{99m}TcO_4$ (300 μL with 100 μCi) for 20 min at room temperature. This result in the production of ^{99m}Tc that labelled the nanoparticles (**S1-apMUC1-Tc**). The small quantity of the prepared labelled solid precluded complete characterisation by standard techniques. Nevertheless, the correct radiolabelling of MSNs was assessed by thin layer chromatography (TLC) using acetone as the mobile phase (see Figure 4). Figure 4 shows that the **S1-apMUC1-Tc** nanoparticles did not migrate in the TLC, but remained in the origin, whereas several weak spots were seen at R_f between 0.5 and 0.7. These spots were tentatively assigned to the unattached aptamer labelled by ^{99m}Tc. Nevertheless, more than 95% of the radiolological signal remained on the original spots, which indicated that most radiation was provided by the **S1-apMUC1-Tc** nanoparticles. Besides, the radiolabelling of nanoparticles remained stable, and it was found that the ^{99m}Tc signal did not lower significantly over time.

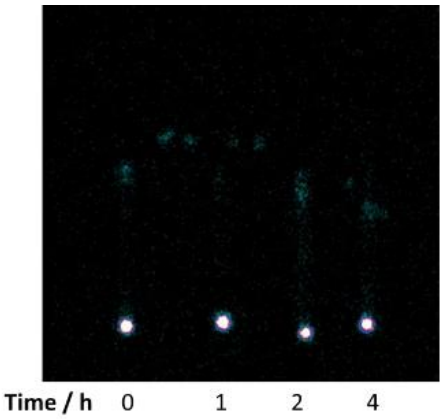

Figure 4. Silica gel TLC carried out after the.labelling reaction of solid **S1-apMUC1** with the ^{99m}Tc radioisotope after different times (acetone was used as the mobile phase).

Once prepared, the labelled **S1-apMUC1-Tc** nanoparticles were tested for *in vivo* imaging using SPECT. For this purpose, a 6-week-old female

MDA-MB-231 tumour-bearing Balb/c mice model was used. **S1-apMUC1-Tc** (3.7 MBq/0.2 mL) was administered to mice by intraocular (retro-orbital) injection. *In vivo* static planar images were obtained with a Millennium Gamma Camera after 90 min in a window centred at 140 keV. The obtained images are shown in Figure 5. As seen in Figures 5A and 5C, the MUC1-positive tumour region showed strong signals (white spots) due to the accumulation of **S1-apMUC1-Tc** nanoparticles at 90 min post-injection. This is a remarkable result which revealed that the accumulation **of S1-apMUC1-Tc** nanoparticles in tumours was significantly larger compared with the bioaccumulation of the free MUC1 aptamer labelled with ^{99m}Tc (*vide infra*).[49-51] Marked accumulation was also observed in the upper part of the image, which correlated with the injection site (retro-orbital). Figure 5B depicts the bioluminescence imaging that indicates the tumour position which correlated with planar images; accumulation of the **S1-apMUC1-Tc** nanoparticles by the tumour, as observed by comparing bioluminescence (red and yellow spots in Figure 5B) and planar images. The high **S1-apMUC1-Tc** accumulation in the tumour was suggested to be partly due to the interaction of the MUC1 aptamer in the functionalised MSNs with the MUC1 glycoprotein overexpressed in the MDA-MB-231 cancer cells. The image clearly collocates with the tumour with a high intensity signal, which suggests **S1-apMUC1-Tc** is a potential candidate for cancer diagnosis by imaging.

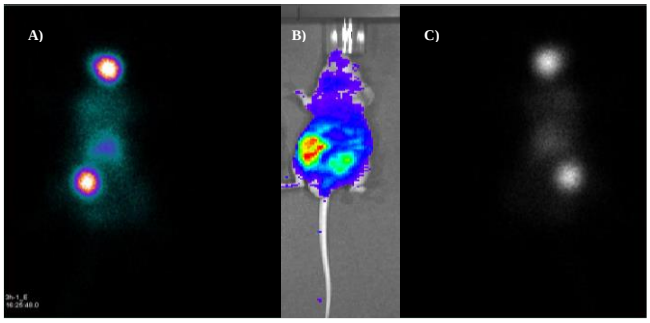

Figure 5. A) Static planar SPECT image of the MDA-MB-231 tumour-bearing Balb/c mice model after administering the **S1-apMUC1-Tc** nanoparticles (3.7 MBq/0.2 mL) at 90 min post-injection. B) Bioluminescence images from mice on day 21 after the intra-ventricular injection of the MDA-MB-231 cancer cells that reveal tumoural lesions. C) Static planar SPECT inverse image of the MDA-MB-231 tumour-bearing Balb/c mice model after administering the **S1-apMUC1-Tc** nanoparticles (3.7 MBq/0.2 mL) at 90 min post-injection.

Biodistribution assays. For the biodistribution assays, mice were sacrificed 120 min after the **S1-apMUC1-Tc** injection, organs were removed, weighed and activity was counted with a gamma counter. The results obtained as a percentage of injected dose per gram and per organ are shown in Figure 6A and 6B respectively. The biodistribution profiles of the **S1-apMUC1-Tc** nanoparticles showed a significant uptake of the nanodevice by tumoural lesions (ca. 20% ID/g and 15% ID). This result once again suggested the targeting abilities of the **S1-apMUC1-Tc** nanoparticles towards the MUC1 glycoprotein overexpressed in the MDA-MB-231 cancer cells. A certain uptake of the labelled nanoparticles by lungs and intestine was observed. These results were expected since the MUC1 glycoprotein ubiquitously spreads throughout the body, especially to intestine and lungs. However, accumulation in tumour was remarkably larger. Besides, the excellent uptake of the **S1-apMUC1-Tc** nanoparticles by kidneys is a desirable feature since radioactive materials have to be excreted from the

body quickly and efficiently. The activity observed in bladder is in accordance with the finding of nanoparticles in kidneys and indicated a non-reabsorption effect of the nanomaterial in kidneys. Another remarkable feature of the biodistribution data is the low uptake percentage observed in the liver and spleen. This low uptake for these two organs suggested that the **S1-apMUC1-Tc** nanoparticles were able to avoid the mononuclear phagocytic system (MPS). This fact was corroborated by presence of radiation in blood, which suggested that nanoparticles have a certain affinity for blood proteins (e.g., albumin) and, consequently, a long-lasting circulation, which agreed with a certain signal in the heart. Finally, it is important to note the negligible uptake by the brain, which is quite a desirable feature for radiopharmaceutical materials and radioactive drugs.

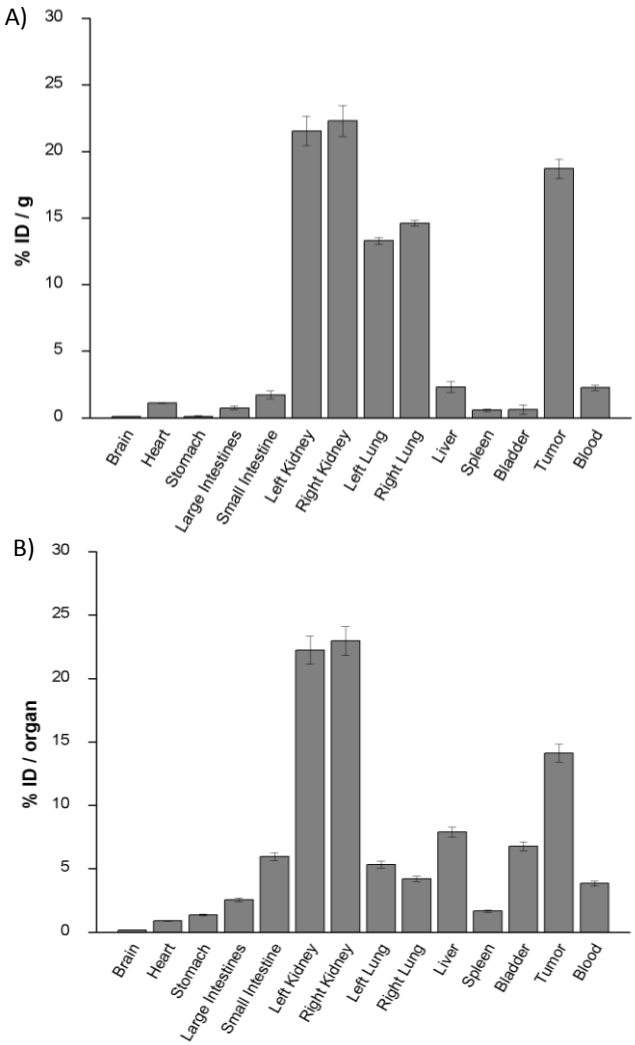

Figure 6. Biodistribution profile of the **S1-apMUC1-Tc** nanoparticles in MDA-MB-231 tumour-bearing Balb/c mice (n = 3) expressed as (A) dose per gram of organ, (B) dose per organ.

It is noteworthy that the biodistribution results obtained with the **S1-apMUC1-Tc** nanoparticles showed remarkable performance in terms of relative accumulation in tumours compared to other systems; e.g., several PET/SPECT nanoparticle-based materials (that involve, or not, aptamer biodirection) or others based on radiolabelled MUC1 aptamers or antibodies,

or even when compared to other aptamer-based radiodiagnosis systems. For instance, it has been reported that MUC-1 aptamers derivatised with a cyclen macrocycle and labelled with ^{99m}Tc show minor tumour accumulation (0.01-0.12% ID/g), with larger amounts located in liver and kidneys.[49] Similarly, radiolabelled bare MSNs have been reported to display a relatively low accumulation of the injected dose in tumours (5.4% ID/g).[37] These results demonstrated that radiolabelling MUC1 aptamer-bearing MSNs offers remarkable performance in imaging terms compared with using the aptamer or MSNs alone. We believe that this approach is general and can be used to design other similar nanoparticles for imaging applications.

6.3 Conclusions

In summary, we have designed, synthesised and characterised MUC1 aptamer-capped MSNs able to preferentially release an entrapped cargo (safranin O) in MDA-MB-231 cells that overexpress glycoprotein MUC-1. Moreover, nanoparticles were also radiolabelled with ^{99m}Tc and used for bioimaging applications. The **S1-apMUC1** nanoparticles showed poor cargo release in the absence of DNAse I, whereas marked safranin O delivery took place when the enzyme was present. Confocal microscopy studies revealed that the **S1-apMUC1** nanoparticles were significantly uptaken by MDA-MB-231 cells and were able to deliver safranin O, whereas a remarkably lower cargo delivery was found for the control MCF-10-A cells. The nanoparticles labelled with the ^{99m}Tc radioisotope (**S1-apMUC1-Tc**) were used in the radioimaging studies on MDA-MB-231 tumour-bearing Balb/c mice. Remarkable tumour signalling and accumulation were observed. **S1-apMUC1-Tc** displayed well-enhanced tumour signalling when compared with other studies in which the MUC1 aptamer or the bare MSNs were also

labelled with ^{99m}Tc. These results indicated that the combination of MSNs capped with aptamers and labelled with radionuclides is a promising candidate for theranostic applications (delivery + imaging). We believe that the results shown herein open up a wide range of new possibilities to develop smart innovative drug delivery and diagnostic nanodevices based on combination of capped mesoporous hybrid materials and radiopharmaceutical techniques.

6.4 Materials and methods

Materials: The chemicals tetraethyl orthosilicate (TEOS), *n*-cetyltrimethylammonium bromide (CTAB), sodium hydroxide, Safranin O, (3-aminopropyl)triethoxysilane, acetonitrile, stannous chloride, sodium hydroxide, Hoechst 33342 and Whatman paper no.1 were purchased from Sigma-Aldrich.

General methods: Powder X-ray diffraction (PXRD), transmission electron microscopy (TEM), scanning Electron Microscopy (SEM), N_2 adsorption-desorption isotherms, fluorescence spectrophotometry, thermogravimetric and elemental analysis were employed for materials characterisation. PXRD measurements were taken on a Seifert 3000TT diffractometer using CuK_α radiation. TEM images were acquired under a JEOL TEM-1010 Electron microscope that worked at 100 kV. SEM images were acquired using a TM 3000 – Hitachi microscope coupled to energy dispersive X-ray spectroscopy (EDX) to analyse the chemical composition of the final materials. The N_2 adsorption-desorption isotherms were recorded in a Micromeritics TriStar II Plus automated analyzer. Fluorescence measurements were taken in a JASCO FP-8500 Spectrophotometer. The thermogravimetric analysis were carried out on TGA/SDTA 851e Mettler

Toledo equipment in an oxidant atmosphere (Air, 80 mL/min) with a heating program that consisted in a heating ramp of 10 °C per minute from 393 K to 1273 K, and an isothermal heating step at this temperature for 30 minutes. An elemental analysis was performed in a CE Instrument EA-1110 CHN Elemental Analyzer. Confocal microscopy imaging was performed with a Leica TCS SPE (Leica Microsystems Heidelberg GmbH) inverted laser scanning confocal microscope using oil objective HC PL APO 40x.

Synthesis of MSNs: *n*-cetyltrimethylammoniumbromide (CTAB, 2 g, 5.48 mmol) was first dissolved in 960 mL of deionised water. Then a solution of NaOH (2 M, 7 mL) in deionised water was added to the CTAB solution and the mixture was heated to 95ºC. TEOS (10.00 mL, 5.14 x 10^{-2} mol) was then added drop-wise. The mixture was left to stir for 2 h to give a white precipitate. Finally, the solid product was centrifuged, washed with deionised water and dried at 60ºC. To prepare the final porous material, the as-synthesised solid was calcined at 550ºC in an oxidant atmosphere for 5 h to remove the template phase.

Synthesis of S1: 200 mg of calcined MCM-41 and 56 mg (0.16 mmol) of safranin O were suspended in 10 mL of anhydrous acetonitrile inside a round-bottom flask. Then the mixture was stirred for 24 hours at room temperature in order to achieve maximum loading in the pores of the MCM-41 scaffolding. Afterward excess (3-aminopropyl)triethoxysilane (0.390 mL, 1.6 mmol) was added, and the suspension was stirred for 5.5 h. Finally, the dark pink solid (**S1**) was filtered off, washed with ethanol and dried at 70°C for 12 h.

Synthesis of S1-apMUC1: 7.5 mg of **S1** were mixed with 5 mg of lyophilised MUC1 aptamer (5′-GCA GTT GAT CCT TTG GAT ACC CTG G-

3′) in 5 mL of buffer solution (20 mM TRIS-HCl, 37.5 mM $MgCl_2$, pH 7.5) and mixed at 37°C for 30 minutes. Final solid **S1-apMUC1** was collected by centrifugation and rinsed 5 times with TRIS buffer solution (33 mM, pH 7.5).

Synthesis of S1-apMUC1-Tc: 150 μg of **S1-MUC1** were incubated with $SnCl_2$ solutions (80 μL/mL) for 20 minutes at room temperature. Then this solution was incubated with 100 μCi (approximately 300 μL) of ^{99m}Tc (IPEN, São Paulo, Brazil) for another 10-minute period to prepare the **S1-apMUC1-Tc** nanoparticles. Thin layer chromatography using Whatman paper no. 1 was carried out to assess the correct labelling of the final nanoparticles.

Tumour xenograft models: MDA-MB-231 cells (American Type Culture Collection, Manassas, VALLC) were cultured in RPMI (Gibco, Life technologies, MD, USA), supplemented with 10% of foetal bovine serum (Gibco, Life technologies, MD, USA) and 50 μg/mL of gentamicin (Gibco, Life technologies, MD, USA). *Mycoplasma* contamination in cultured cells was excluded using the Lonza *Mycoplasma* Detection Kit. Tumours were established by a subcutaneous injection of 2 x 10^6 MDA-MB-231 cells on the backs of 6-week-old female Balb/c nude mice. Tumour size was monitored for 3 weeks and measured by a caliper. Tumour size before imaging was about 2 cm. Balb/c nude mice were bred at the animal facility of the Nuclear Energy Research Institute (IPEN). All the experiments complied with relevant laws and were approved by local animal ethics committees. Mice were observed 3 times a week to evidence any distress, ascites, paralysis or excessive weight loss.

Controlled release of solid S1-apMUC1 triggered by DNAse I: 100 μg of solid **S1-apMUC1** were suspended in 400 μL of buffer solution (20 mM TRIS-HCl, 37.5 mM $MgCl_2$, pH 7.5) and separated into two aliquots (2 x 200

μL). One of the samples was filled to a final volume of 1,000 μL with buffer solution, whereas the other was completed with the same buffer but which contained DNAse I enzyme (at a concentration of 10 U/μL). Both suspensions were stirred at 25ºC for 60 minutes. Next 150 μL aliquots were taken at several times and centrifuged for 2 min at 12,000 rpm to remove the solid. The fluorescence of released safranin O was measured at 585 nm (λ_{exc} 520 nm).

Control release in cells by confocal microscopy studies: Internalisation and cargo delivery using **S1-apMUC1** and the MDA-MB-231 (that expressed MUC1) and MCF-10-A (that did not express MUC1) cell lines were studied by confocal microscopy. Cells MDA-MB-231 and MCF-10-A were cultured in DMEM/F12 that contained 100U/ml of penicillin and streptomycin, and 10% FCS and DMEM/F12 that contained 100U/ml of penicillin and streptomycin, 10% FCS, 10 μg/ml of insulin solution human recombinant from *Saccharomyces Cerevisiae*, 0.5 μg/ml of hydrocortisone, 100 ng/ml of Cholera toxin from *Vibrio cholerae* and 20 ng/ml of EGF recombinant human protein solution respectively. Both cells lines were seeded over glass coverslips at 250,000 cells/ml in 6-well assay plates, incubated at 37ºC. The **S1-apMUC1** nanoparticles were added to cells at 100 μg/ml and were incubated at 37ºC for 2 h. Then cells were washed several times with PBS. Finally, DNA marker Hoechst 33342 was added. Slides were visualized using a confocal microscope Leica TCS SP2 AOBS.

Bioluminescence and imaging: Three female Balb/c nude mice aged 8-9 weeks with breast cancer in the right flank were used for biodistribution and imaging (SPECT). The animals inducted with breast cancer were examined by bioluminesce. Mice were administered D-luciferin (150mg/kg, Promega) by intraperitoneal injection. Immediately after the D-luciferin

injection, photons from each animal's whole body were counted by the IVIS Spectrum imaging system (Xenogen/Caliper Life Sciences, CA) according to the manufacturer`s instructions. Data were analysed by the Living Image 4.3 software (Xenogen). Planar images were obtained 90 min after injecting the **S1-apMUC1-Tc** nanoparticles (3.7 MBq in 0.2 mL) with a Millennium Gamma Camera (GE Healthcare, Cleveland, USA). Counts were acquired for 5 min in a 15% window centred at 140 KeV. Images were processed using the *OsiriX* software, and regions of interest (ROIs) over the tumour were selected for specific analyses. Three inducted mice were imaged separately.

Biodistribution: Mice were maintained at a controlled temperature (23^{o}C±2) with water and food *ad libitum*. No sedative or anaesthetic was used. Labelled samples (3.7 MBq/0.2 mL) were administered by intraocular (retro-orbital) injection. Mice were sacrificed by asphyxiation in a carbon dioxide gas chamber 120 min after administering the **S1-apMUC1-Tc** nanoparticles. Organs (brain, lungs, kidneys, stomach, small and large intestine, bladder, heart and blood pool) were removed, weighed, and the activity in each organ and blood was counted by a gamma counter (Perkin Elmer Wizard® 2470). The results were expressed as a percentage of the injected dose per organ. The Institutional Review Board and the Animal Ethics Committee approved the study protocol.

Author Information

Ramón Martínez-Máñez, e.mail: rmaez@qim.upv.es

Author Contributions

The manuscript was written by contributions made by all the authors. All the authors approved the final version of this manuscript

Acknowledgements

Financial support from the Spanish Government and FEDER funds (Project MAT2015-64139-C4-1) and the Generalitat Valenciana (Project PROMETEOII/2014/047) is gratefully acknowledged. Ll. P. is grateful to the Universitat Politécnica de Valencia for his grant. A.G-F. is grateful to the Spanish government for her FPU grant.

REFERENCES

1 Wilson, M. *Nanotechnology : Basic Science and Emerging Technologies*; Chapman & Hall/CRC, 2002.

2 Sandhya, G.; Kannan, V.; Nandakumar, K. *Adv. Nanomat.* **2015**, 251.

3 Rani, V. *J. Chem. Pharm. Res.* **2015**, *7*, 216.

4 Arias, J. L. *Nanotechnology and Drug Delivery*; Arias, J. L., Ed.; Chapman & Hall/CRC, 2016.

5 Kita, K.; Dittrich, C. *Expert Opin. Drug Deliv.* **2011**, *8*, 329.

6 Du, J.; Lane, L. A.; Nie, S. *J. Control. Release* **2015**, *219*, 205.

7 Slowing, I. I.; Trewyn, B. G.; Giri, S.; Lin, V. S. Y. *Adv. Funct. Mater.* **2007**, *17*, 1225.

8 Rurack, Knuck Martínez-Mánez, R. *The Supramolecular Chemistry of Organic-Inorganic Hybrid Materials*; Wiley-VCH Verlag, 2010.

9 Aznar, E.; Oroval, M.; Pascual, L.; Murguía, J. R.; Martínez-Máñez, R.; Sancenón, F. *Chem. Rev.* **2016**, *116*, 561.

10 Coll, C.; Bernardos, A.; Martínez-Máñez, R.; Sancenón, F. *Acc. Chem. Res.* **2013**, *46*, 339.

11 Sancenón, F.; Pascual, Ll.; Oroval, M.; Aznar, E.; Martínez-Máñez, R. *ChemOpen* **2015**, *4*, 418.

12 Yang, Y.-W. *Med. Chem. Commun.* **2011**, *2*, 1033.

[13] Agostini, A.; Mondragón, L.; Pascual, Ll.; Aznar, E.; Coll, C.; Martínez-Máñez, R.; Sancenón, F.; Soto, J.; Marcos, M. D.; Amorós, P.; Costero, A. M.; Parra, M.; Gil, S. *Langmuir* **2012**, *28*, 14766.

[14] Agostini, A.; Mondragón, L.; Bernardos, A.; Martínez-Máñez, R.; Marcos, M. D.; Sancenón, F.; Soto, J.; Costero, A.; Manguan-Garcia, C.; Perona, R.; Moreno-Torres, M.; Aparicio-Sanchis, R.; Murguía, J. R. *Angew. Chem. Int. Ed.* **2012**, *51*, 10556.

[15] Zhu, Y. F.; Meng, W. J.; Hanagata, N. *Dalt. Trans.* **2011**, *40*, 10203.

[16] Coll, C.; Mondragón, L.; Martínez-Máñez, R.; Sancenón, F.; Marcos, M. D.; Soto, J.; Amorós, P.; Pérez-Payá, E. *Angew. Chem. Int. Ed.* **2011**, *50*, 2138.

[17] Mas, N.; Agostini, A.; Mondragón, L.; Bernardos, A.; Sancenón, F.; Marcos, M. D.; Martínez-Máñez, R.; Costero, A. M.; Gil, S.; Merino-Sanjuan, M.; Amorós, P.; Orzáez, M.; Pérez-Payá, E. *Chem. Eur. J.* **2013**, *19*, 1346.

[18] Patel, K.; Angelos, S.; Dichtel, W. R.; Coskun, A.; Yang, Y. W.; Zink, J. I.; Stoddart, J. F. *J. Am. Chem. Soc.* **2008**, *130*, 2382.

[19] Schlossbauer, A.; Kecht, J.; Bein, T. *Angew. Chem. Int. Ed.* **2009**, *48*, 3092.

[20] Thornton, P. D.; Heise, A. *J. Am. Chem. Soc.* **2010**, *132*, 2024.

[21] Wang, F.; Liu, X.; Willner, I. *Angew. Chem. Int. Ed.* **2015**, *54*, 1098.

[22] Lu, C. H.; Willner, B.; Willner, I. *ACS Nano* **2013**, *7*, 8320.

[23] Oroval, M.; Climent, E.; Coll, C.; Eritja, R.; Avino, A.; Dolores Marcos, M.; Sancenon, F.; Martinez-Manez, R.; Amoros, P. *Chem. Commun.* **2013**, *49*, 5480.

[24] Li, Z. H.; Liu, Z.; Yin, M. L.; Yang, X. J.; Yuan, Q. H.; Ren, J. S.; Qu, X. G. *Biomacromolecules* **2012**, *13*, 4257.

[25] Hernandez, F. J.; Hernandez, L. I.; Pinto, A.; Schafer, T.; Ozalp, V. C. *Chem. Commun.* **2013**, *49*, 1285.

[26] Jayasena, S. D. *Clin. Chem.* **1999**, *45*, 1628.

[27] Ferreira, C. S. M.; Missailidis, S. *Brazilian Arch. Biol. Technol.* **2007**, *50*, 63.

[28] Padmanabhan, P.; Kumar, A.; Kumar, S.; Chaudhary, R. K.; Gulyás, B. *Acta Biomater.* **2016**, *41*, 1.

[29] Chrastina, A.; Schnitzer, J. E. *Int. J. Nanomedicine* **2010**, *5*, 653.

[30] Guo, Z.; Gao, M.; Zhang, D.; Li, Y.; Song, M.; Zhuang, R.; Su, X.; Chen, G.; Liu, T.; Liu, P.; *et al. Sci. Rep.* **2016**, *6*, 1.

[31] Santos-Oliveira, R.; Albernaz, M.; Szwed, M.; Iscaife, A.; Leite, K.; Junqueira, M.; Bernardes, E.; da Silva, E.; Tavares, M. I.; Sarcinelli, M. *Onco. Targets. Ther.* **2016**, *Volume 9*, 5847.

[32] Ligiero, T. B.; Cerqueira-Coutinho, C.; de Souza Albernaz, M.; Szwed, M.; Bernardes, E. S.; Wasserman, M. A. V.; Santos-Oliveira, R.; al, A. M. S. et; al, A. F. et; L, A. R.; *et al. Biomed. Phys. Eng. Express* **2016**, 2, 45017.

[33] Carmo, F. S.; Missailidis, S.; Al-Malki, Y.; Al-Qahtani, M.; Santos-Oliveira, R. *Lat. Am. J. Pharm. Am. J. Pharm* **2016**, *35*, 2056.

[34] Zhang, X. *PLoS One* **2014**, *9*, e90752.

[35] Varmira, K.; Hosseinimehr, S. J.; Noaparast, Z.; Abedi, S. M. *Nucl. Med. Biol.* **2013**, *40*, 980.

[36] Jacobson, O.; Yan, X.; Niu, G.; Weiss, I. D.; Ma, Y.; Szajek, L. P.; Shen, B.; Kiesewetter, D. O.; Chen, X. *J. Nucl. Med.* **2015**, *56*, 616.

[37] Chen, F.; Hong, H.; Goel, S.; Graves, S. A.; Orbay, H.; Ehlerding, E. B.; Shi, S.; Theuer, C. P.; Nickles, R. J.; Cai, W. *ACS Nano* **2015**, *9*, 3926.

[38] Chen, F.; Hong, H.; Shi, S.; Goel, S.; Valdovinos, H. F.; Hernandez, R.; Theuer, C. P.; Barnhart, T. E.; Cai, W. *Sci. Rep.* **2014**, *4*, 5080.

[39] Chen, F.; Hong, H.; Zhang, Y.; Valdovinos, H. F.; Shi, S.; Kwon, G. S.; Theuer, C. P.; Barnhart, T. E.; Cai, W. *ACS Nano* **2013**, *7*, 9027.

[40] Chen, F.; Goel, S.; Valdovinos, H. F.; Luo, H.; Hernandez, R.; Barnhart T. E.; Cai, W. *ACS Nano*, **2015**, *9*, 7950.

[41] Denk, C.; Svatunek, D.; Mairinger, S.; Stanek, J.; Filip, T.; Matscheko, D.; Kuntner, C.; Wanek, T.; Mikula, H. *Bioconjugate Chem.* **2016**, *27*, 1707.

[42] Wuillemin, M. A.; Stuber, W. T.; Fox, T.; Reber, M. J.; Brühwiler, D.; Alberto, R. *Dalton Trans.* **2014**, *43*, 4260.

[43] de Sousa Azevedo, R. C.; Ferreira Soares, D. C.; de Sousa, R. G.; Barros de Sousa, E. M. *J. Biomater. Nanotechnol.* **2012**, *3*, 163.

[44] Cheng, S. -H.; Yu, D.; Tsai, H. -M.; Morshed, R. A.; Kanojia, D.; Lo, L. -W.; Leoni, L.; Govind, Y.; Zhang, L.; Aboody, K. S.; Lesniak, M. S.; Chen, C. -T.; Balyasnikova, I. V. *J. Nucl. Med.* **2016**, *57*, 279.

[45] Branco de Barros, A. L.; de Oliveira Ferraz, K. S.; Soares Dantas, T. C.; Ferreira Andrade, G.; Cardoso, V. N.; Barros de Sousa, E. M. *Mater. Sci. Eng. C, Mater. Biol. Appl.* **2015**, *56*, 181.

[46] Apostolopoulos, V.; Vasso, S.; Gargosky, S. E. *Cell. Mol. Life Sci.* **2015**, *72*, 4475.

[47] Walker, J. M. *Mucins Methods and Protocols, Vol 842*; McGuckin, M. A.; Thornton, D. J., Eds.; Methods in Molecular Biology; Humana Press: Totowa, NJ, 2012; Vol. 842.

[48] Stroopinsky, D.; Kufe, D.; Avigan, D. *Leuk. Lymphoma* **2016**, *57*, 2489.

[49] Da Pieve, C.; Blackshaw, E.; Missailidis, S.; Perkins, A. C. *Bioconjug. Chem.* **2012**, *23*, 1377.

[50] Da Pieve, C.; Perkins, A. C.; Missailidis, S. *Nucl. Med. Biol.* **2009**, *36*, 703.

[51] Da Pieve, C.; Perkins, A.; Missailidis, S. *Eur. J. Cancer Suppl.* **2008**, *6*, 30.

[52] Jo, H.; Her, J.; Ban, C. *Biosens. Bioelectron.* **2015**, *71*, 129.

[53] Kresge, C. T.; Leonowicz, M. E.; Roth, W. J.; Vartuli, J. S.; Beck, J. S. *Nature* **1992**, *359*, 710.

[54] Barrett, E. P.; Joyner, L. G.; Halenda, P. P. *J. Am. Chem. Soc.* **1951**, *73*, 373.

[55] Brunauer S.; Emmet, P. H.; Teller, *J. Am. Chem. Soc.* **1938**, *60*, 309.

[56] Kobayashi, Y. *Curr. Top. Med. Chem.* **2016**, *16*, 2694.

Supporting Information

MUC1 aptamer-capped mesoporous silica nanoparticles for controlled drug delivery and radio-imaging applications

Lluis Pascual,[†,‡,§] Cristal Cerqueira-Coutinho,[⊥] Alba García-Fernández,[†,‡,§] Emerson Soares Bernardes,[‖] Marta Souza Albernaz,[▽] Sotiris Missailidis,[○] Ramón Martínez-Máñez, *[,†,‡,§] Ralph Santos-Oliveira,* [,▽] and Félix Sancenón[†,‡,§]

[†] *Instituto Interuniversitario de Reconocimiento Molecular y Desarrollo Tecnológico (IDM). Universitat Politecnica de Valencia, Universitat de Valencia, Spain.*

[‡] *Departamento de Química, Universidad Politécnica de Valencia, Camino de Vera s/n, 46022, Valencia, Spain.*

[§] *CIBER de Bioingeniería, Biomateriales y Nanomedicina (CIBER-BBN).*

[‖] *Centro de Radiofarmácia, Instituto de Pesquisas Energéticas e Nucleares, São Paulo, Brazil*

[⊥] *Federal University of Rio de Janeiro, Faculty of Phamacy, Rio de Janeiro-Brazil*

[▽] *Brazilian Nuclear Energy Commission, Nuclear Engineering Institute, Rio de Janeiro, Brazil*

[○] *Oswaldo Cruz Foundation, Biomanguinhos, Rio de Janeiro, Brazil*

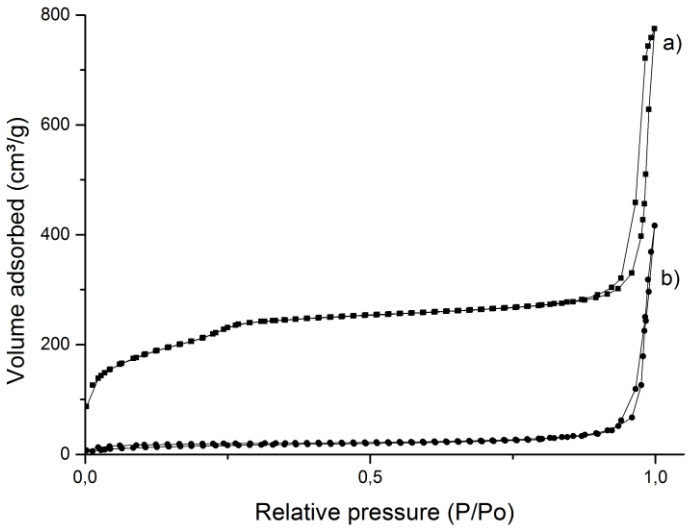

Figure S1. N_2 adsorption-desorption isotherms for (a) calcined MCM-41 nanoparticles and (b) **S1** solid.

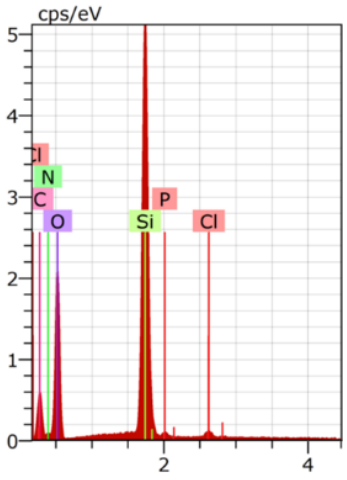

Figure S2. EDX spectrum of **S1-apMUC1** showing the presence of phosphorus atoms in the nanoparticles ascribed to the aptamer coating the external surface of the nanoparticles.

Chapter 7:

General Conclusions and future perspectives

7. General conclusions

Design of functional nanomaterials has been exponentially increasing over the last decades. A significant attention has been focused on developing new hybrid materials for molecular recognition process and to construct therapeutic systems. A great impact has been produced in the fields of sensing systems and in targeted nanomedicine. Silica-based supports stand out due to their versatility, stability and well-known chemistry. This PhD thesis has attempted to contribute to this field with the development of innovative silica-based hybrid materials that used new recognition strategies and with practical applications in sensing and diagnostic protocols. The main conclusions of this PhD thesis are:

The third chapter reports the synthesis and characterization of bifunctionalized (with thiol and polyamine moieties) silica nanoparticles that are used, in an ICS protocol, for the chromogenic recognition of formaldehyde in aqueous environments and in gas phase. The observed chromogenic response is based on the inhibition of thiol-squaraine reaction (coupled with color changes) induced by formaldehyde.

The fourth chapter presents the synthesis of AChE capped mesoporous nanoparticles that are opened in the presence of selected enzyme inhibitors. These nanoparticles are loaded with rhodamine B and functionalized with two pyridostigmine and neostigmine derivatives. Finally, the pores are capped upon addition of AChE. The selective and sensitive detection of DFP using these AChE-capped nanoparticles is achieved.

The fifth chapter describes the preparation of DNA-capped mesoporous silica nanoparticles for the recognition of *Mycoplasma fermentans* genomic DNA. Again, the pores of the mesoporous nanoparticles are loaded with rhodamine B and the external surface functionalized with a single stranded DNA highly conserved sequence of the *Mycoplasma* genome. In the presence of *Mycoplasma fermentans* genomic DNA the pores are opened and rhodamine B released. The prepared nanoparticles showed impressive features in terms of selectivity and sensitivity and are a clear alternative to commercial detection kits and other systems reported.

The sixth chapter reports the synthesis and characterization of mesoporous silica nanoparticles loaded with safranin O and capped with MUC1 aptamer. These nanoparticles are selectively internalized by cancer cells that overexpressed MUC1 glycoportein releasing its cargo. Moreover, MUC1 aptamer-capped nanoparticles are radiolabeled with ^{99m}Tc and used for *in vivo* SPECT imaging of cancerous lesions in mice.

In summary, this PhD thesis presented a new set of hybrid organic-inorganic materials that are successfully applied in molecular recognition protocols in different areas. These or similar materials will be implemented in solid supports (for example in the form of dipsticks) and will be the basis for the development of practical portable new kits for in situ detection of dangerous species or for diagnostic of several diseases. Moreover, the use of enzymes (i.e. tyrosinase, urease or glucose oxidase) as capping agents, will also lead to the preparation of hybrid materials with high degrees of selectivity (with applications in sensing and controlled delivery protocols) taking into account that cargo release will be produced only if the enzyme substrate is present in the environment. Besides, DNA-capped materials will

be used to develop specific quick diagnostic test to detect some DNA strands related to certain diseases. Nearly the same applications will be expected for aptamer-capped nanomaterials due to its targeting features. This ability will be coupled with its easy radiolabeling in order to prepare new radiodiagnostic nanodevices or even theranostic materials (in which the pores of the inorganic support are loaded with therapeutic drugs).

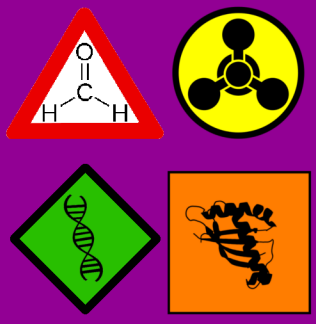
O
C
H
H